Towards Exoplanetary Science in the Era of JWST

Aarynn L. Carter

Submitted by Aarynn Lee Carter to the University of Exeter as a thesis for the degree of Doctor of Philosophy in Physics, June, 2020.

I certify that all material in this thesis which is not my own work has been identified and that no material has previously been submitted and approved for the award of a degree by this or any other University.

Signed: .....

Aarynn L. Carter

Date: 14/08/2020 .....

Abstract

Our understanding of exoplanets has advanced dramatically over the past two decades as we have moved from simply detecting these objects, to performing precise characterisations of their atmospheres. Despite these advancements, many fundamental questions remain, such as: how did these objects form, what is their composition, and what is the overall structure and dynamics of their atmospheres? With the launch of the James Webb Space Telescope (*JWST*) and the advanced observational capabilities it provides, it will be possible to step closer and closer towards the answers to these questions. However, given the lifetime of *JWST* will be limited, as a community we must ensure that the opportunity that it provides is not squandered.

Efficient and effective use of *JWST* cannot be achieved without first understanding the atmospheres of currently known targets to the best of our ability, the overall considerations when performing exoplanet observations, and finally the predicted limitations and feasibility of *JWST* observations in particular. In this work I present a range of studies to further these goals. Firstly, I perform an in-depth and holistic investigation into the atmosphere of the transiting hot Jupiter exoplanet WASP-6b, revealing a host of molecular and atmospheric features and identifying it as a favourable *JWST* target. The impact of stellar heterogeneity of WASP-6 on the overall transmission spectrum is also quantified, revealing measurable biases in the determination of its atmospheric properties without correcting for such effects. Secondly, I perform a range of detailed *JWST* observation simulations of transiting exoplanets, based on state-of-the-art forward model spectra. Specifically, these simulations explore the significance of theorised atmospheric features due to disequilibrium chemistry, the presence of clouds, and the fundamental assumptions of forward models. Finally, I produce the most sophisticated simulations of *JWST* direct imaging to date, incorporating up-to-date estimates of *JWST* performance and the latest planetary evolution models. From these simulations I generate detection probability maps for a range of coronagraphic imaging modes, describing exactly to what degree these modes will be able to explore the known exoplanet population. In particular, I reveal that *JWST* will be best suited towards directly imaging exoplanets as low as 0.1 M_{J} separated further than 100 au from their host star.

Contents

List of Figures

List of Tables

Acknowledgements

As I finish this thesis, and my PhD studies end, there are many people I wish to thank personally for making it all possible. However, I would be remiss not to first acknowledge the immense amount of privilege that has allowed me to be in the position I am today, submitting a thesis on a topic that I am truly passionate about. I know many other people in the world are not so fortunate.

To my joint supervisors Sasha Hinkley and David Sing, thank you for your unwavering support over the past four years. No matter the situation, you've always been willing to give up your time to answer whatever question I might have, be it small or large. You have been exceptional mentors and I honestly feel very lucky to have had the opportunity to work with, and learn from, both of you.

To Nikolay Nikolov, Tom Evans, and Hannah Wakeford, thank you for guiding me through the murky swamp that is transit data reduction and light curve fitting - for a long time I was certain it relied on dark magic.

To Jess Spake, Lis Matthews, and Jayesh Goyal, watching you perform and complete your own PhDs in exoplanetary science has been a real inspiration for me throughout mine. I know that as I watch you continue your academic careers that inspiration will only grow; I can't wait to see what you achieve next.

To my examiners Carole Haswell and Eric Hébrard, thank you for giving up such a considerable amount of your time to review this work.

To Emma Way, Martyn Brake, and Krisztian Kohary, thank you for all the admin and IT support you've given me. Without you all I'm pretty sure I'd be writing this thesis with a pen and paper and submitting it via carrier pigeon to completely the wrong address.

To Adam Finley, Brendan Retter, Mark Phillips, and Tom Bending, I can't think of a better office environment than ours, and I'm really going to miss the Lunch Club sandwiches, toasties, crisps, biscuits, and debates we've had over the years. The G27 spirit will live on within me for the rest of my life!

To all my friends from the Astrophysics group, who number far too many to list individually, thank you for making Exeter such an enjoyable place to be. The coffee time crosswords, lunch time discussions, film nights, game nights, and pub trips were perfect breaks from the pressures of PhD life.

To my family, from dreams of being a zoologist, to an egyptologist, to an astrophysicist, to a particle physicist, and back to an astrophysicist/astronomer, you've always encouraged me to try and achieve whatever I wanted in life, no matter how lofty or outrageous the goal might seem; thank you. In particular, thank you Mum and Dad, you fought to give me every opportunity I needed to succeed, no matter what.

Above all, I must thank my wife Jade. I honestly don't know where, or who, I would be today without you and it is an undeniable fact that I could not have made it this far without your support.

Finally, I will be forever grateful to the UK Science & Technology Facilities Council (STFC) for providing me with the financial support necessary to produce this work, and share it with the world.

Chapter 1

Introduction

1.1 Context and Motivation

With the first discovery of planets beyond our solar system - exoplanets - by Wolszczan and Frail (1992), our perception of these objects shifted from the realm of fiction, to that of reality. Fundamental questions that had burdened philosophers for millennia such as: *"Are we alone?"*, or *"Where did we come from?"*, were now truly approachable. It is therefore no surprise that exoplanetary science has become one of the fastest growing fields in astronomy, representing roughly a quarter of the science cases for large multipurpose observatories despite constituting only 3% of all refereed astronomy articles (Deeg and Belmonte 2018). This growth is mirrored in the discovery of these objects, with over 4000 exoplanets identified to date and many more yet to be unearthed. In fact, it is now known that planets are likely the rule rather than the exception, with current estimates indicating an occurrence rate of at least one planet per star (Cassan et al. 2012). Within this plethora of objects a somewhat surprising diversity has been uncovered, with many exoplanets having no direct solar system analogue. This diversity is a primary driver for the current and future study of exoplanets, not only to understand where our own solar system fits amongst the population, but also to understand the possibilities that exist elsewhere in the universe.

At the forefront of the future characterisation of exoplanets is the *James Webb Space*

Telescope (JWST), scheduled for launch in 2021. *JWST* is envisioned to be the premier observatory of the next decade, succeeding the already hugely successful Hubble Space Telescope (HST). However, unlike HST which has been in operation for over 30 years, *JWST* will have a nominal lifetime of only 5 years and a goal lifetime of 10 years. Furthermore, whilst HST could undergo semi-frequent servicing missions given its low-Earth orbit, *JWST* will be located at the second Lagrangian point, rendering it essentially unserviceable. Under these limitations it is therefore imperative that the predicted capabilities and feasibility of *JWST* observations are well understood, and that currently known exoplanets are characterised to the best of our ability in order to identify those targets best suited for follow-up with JWST. In the absence of such efforts the valuable and limited *JWST* observing time will be at best inefficiently used, and at worst explicitly wasted. Within this work I present a collection of investigations that further these goals, in particular: a robust characterisation of the hazy hot Jupiter WASP-6b, simulated *JWST* spectroscopy of transiting exoplanet atmospheres, and simulated *JWST* coronagraphy of members of nearby young moving groups of stars.

1.2 Observing Exoplanets

The first exoplanets were discovered by Wolszczan and Frail (1992) by observing variations in the timing of the pulsar PSR 1257+12. Whilst a landmark discovery, none of the handful of *"pulsar planets"* detected to date are currently suited for further atmospheric characterisation - although they may still hold atmospheres despite the harsh environments surrounding neutron stars (Patruno and Kama 2017). The first discovery of an exoplanet around a solar-type star did not arrive until a few years later when Mayor and Queloz (1995) detected a Jupiter-mass companion to the star 51 Pegasi, an effort that was recently awarded the 2019 Nobel Prize in Physics. This detection was inferred from periodic variations within the radial velocity signal of the host star, a technique that would dominate early detections of exoplanets. However, this technique was limited as it could not measure the radius of an exoplanet, required a separate measurement of the orbital inclination to infer an exoplanet's mass, and could not directly probe their atmospheres. Fortunately, these limitations can be readily overcome if these exoplanets pass in front of

their host star during their orbit from our line of sight. This crossing, or transit, event results in a drop in the brightness of the host star and was first observed and reported for the hot Jupiter HD 209458b by both Charbonneau et al. (2000) and Henry et al. (2000). This drop in brightness varies as a function of wavelength due to the differential extinction of molecules within an exoplanet's atmosphere and allows more detailed atmospheric characterisations to be performed. Broad field of view searches for transiting exoplanets have been highly successful from both the ground with instruments such as HAT (Bakos et al. 2004), WASP (Pollacco et al. 2006), and KELT (Pepper et al. 2007) as well as space with instruments such as CoRoT (Auvergne et al. 2009), Kepler (Borucki et al. 2009) and TESS (Ricker et al. 2015). Over 3000 of the exoplanets discovered to date have been discovered through transiting observations, however the vast majority of these objects are at separations smaller than 1 AU. Aside from the aforementioned radial velocity planets, only two techniques have been broadly used to observe exoplanets at larger separations. The first of these is gravitational microlensing, which identifies exoplanets through their perturbations on the lensing effect of their host star on a more distant background star and was first used by Udalski et al. (2002) as part of the OGLE project. Whilst useful at probing separations from 1-10 AU, the chance alignments that enable these detections are isolated incidents and cannot be repeated, removing the possibility of further characterisation. For separations further than ~10 AU the most prolific method of detection is through direct imaging. The first reported discovery using this technique was of a multiple Jupiter mass companion to the brown dwarf 2M1207 (Chauvin et al. 2004), however for most direct imaging observations the primary star is not as faint as a brown dwarf and coronagraphic masking or advanced image processing strategies are also required in order to be sensitive to planetary mass companions. The ability of these observations to measure the flux directly from an exoplanet means it is also possible to spectroscopically characterise its atmosphere. The current population of known exoplanets as of March 2020 and their discovery methods are displayed in Figure 1.1 alongside the solar system planets.

JWST will dramatically advance our understanding of exoplanets, however its primary advantage will not be in discovering new objects, but performing atmospheric characterisation of those objects already known. As such the rest of this section will be focused on further describing transit and direct imaging observations - the methods for which at-

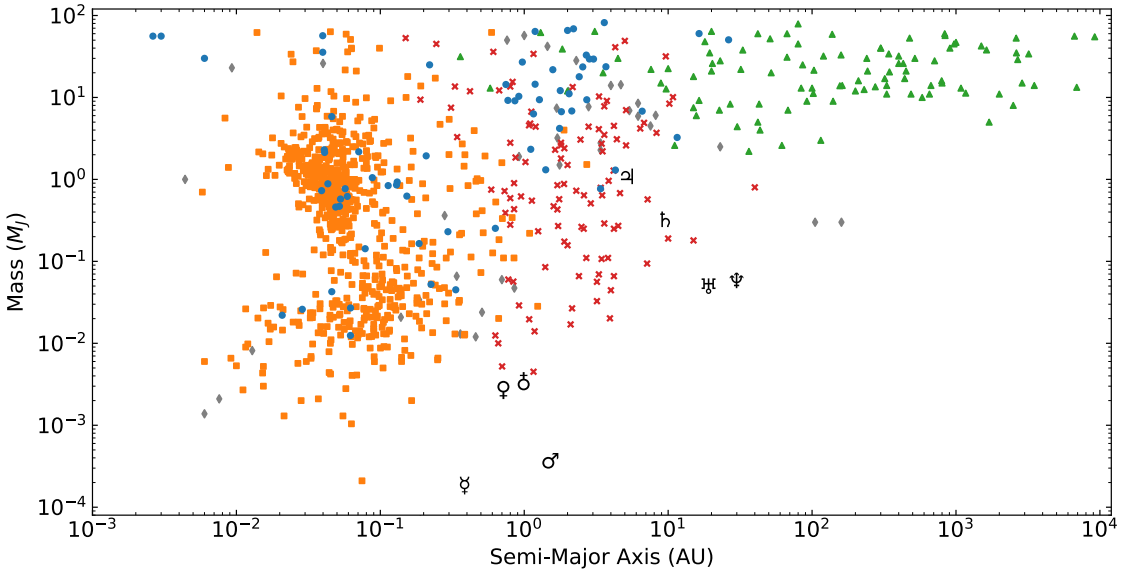

Figure 1.1: The mass-separation population of all currently discovered exoplanets, as retrieved from the exoplanet.eu database on 31/03/2020. Exoplanets are marked and coloured by discovery method with radial velocity as blue circles, transiting as orange squares, microlensing as red crosses, direct imaging as green triangles, and other methods marked as grey diamonds. The solar system planets are also marked by their associated symbol.

mospheric characterisation is possible.

1.3 Transiting Exoplanets

An exoplanetary transit occurs when a planet passes directly in front of its host star from our line of sight, Figure 1.2. This crossing event masks a portion of the stellar disk, producing a distinctive and measurable drop in the overall received flux. The majority of transiting exoplanets also pass directly behind their host star, an event called a secondary eclipse. During secondary eclipse the relatively small amount of planetary emitted flux is completely obscured, resulting in a smaller drop in the overall received flux. During primary transit we observe the night-side of the exoplanet, whereas during secondary eclipse we observe a flux reduction equal to the total day-side emission of the exoplanet and the reflected stellar light. Any variation in day-side to night-side emission can therefore also be probed by measuring variations in the total received flux throughout the orbital phase, more commonly referred to as a phase curve observation. Transit, secondary eclipse, and phase curve observations all provide distinct avenues towards the characterisation of exoplanetary atmospheres and are the reason that transiting exoplanets are arguably the most well studied of the entire population.

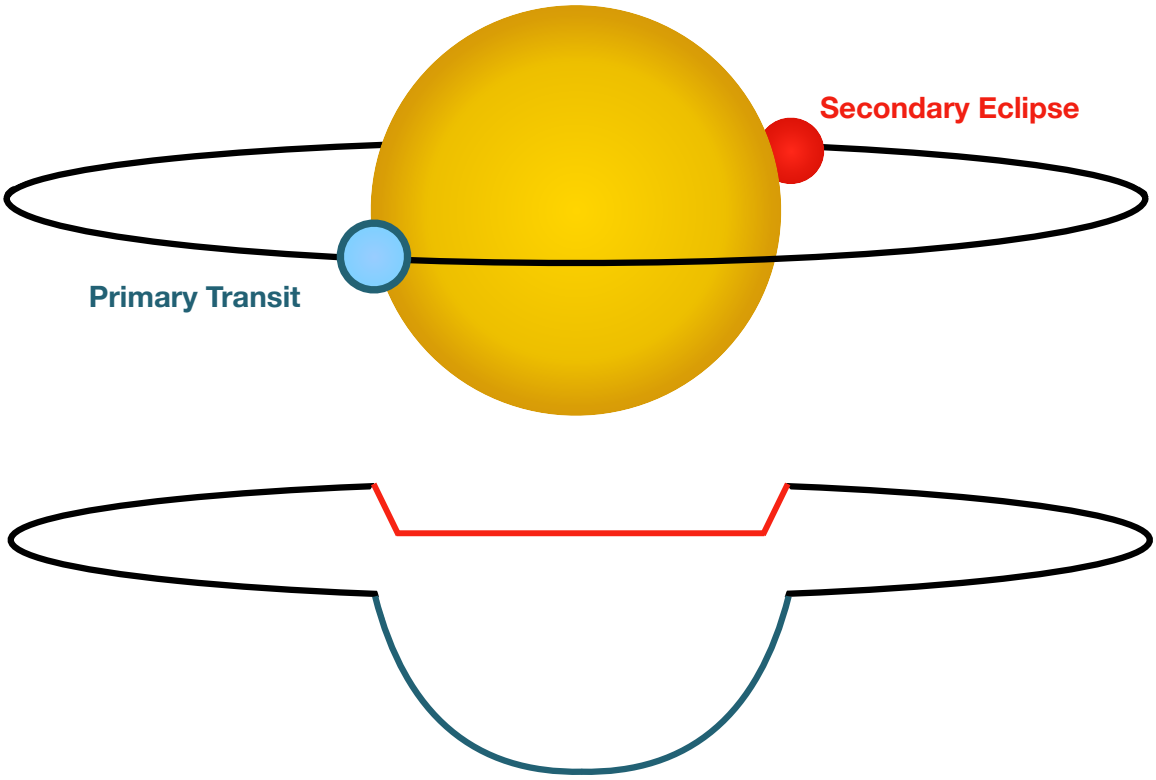

Figure 1.2: A diagram illustrating the geometry of a transiting exoplanet. As the planet passes in front of the host star a primary transit occurs, producing a reduction in the observed flux due to the reduction in observable stellar flux. Conversely, as the planet passes behind its host star the host star masks the relatively small amount of flux emitted from the planet itself, producing a smaller secondary eclipse.

1.3.1 Detection

Before discussing how their atmospheres are probed it is worthwhile to discuss the inherent limitations of the transit discovery method. Transit observations are only possible for objects whose orbits pass in front of their host star from our line of sight, and such an alignment has a typically low geometric probability. Using a diagram of the geometry of a transiting system, such as that in Figure 1.3, it can be seen that given a circular orbit a transit will occur when

$$a \cos i < R_* + R_p, \tag{1.1}$$

where a is the semi-major axis, i is the inclination, R_* is the radius of the star, and R_p is the radius of the planet. The corresponding probability of such an occurrence, p, is

$$p \simeq \frac{R_*}{a}, \tag{1.2}$$

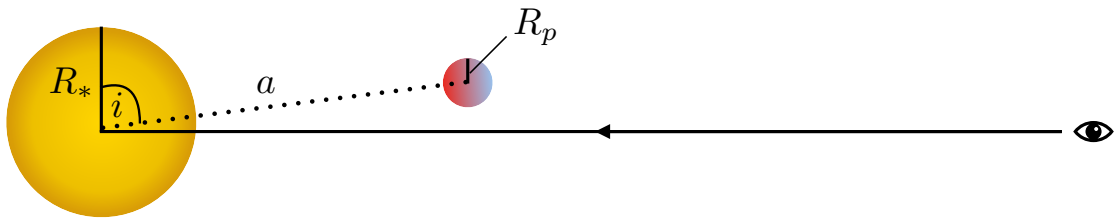

Figure 1.3: A diagram illustrating the geometric properties of an exoplanet transit from our line of sight. R_* is the radius of the star, i is the inclination, a is the semi-major axis, and R_p is the radius of the exoplanet. For a circular orbit, a transit will occur in the event that $a \cos i < R_* + R_p$

as derived by Borucki and Summers (1984). Therefore, transit events are most commonly observed for exoplanets at close separations around larger stars. It is for this reason that the vast majority of discovered transiting exoplanets lie within 1 AU of their host star. Nevertheless, whilst this equation provides the probability of a transit occurring, it does not represent the potential to observe it. During a transit event the partial occultation of a star by a planet results in a characteristic drop in the received starlight. The fractional depth of this reduction in flux is referred to as the transit depth, δ, and is dictated by the projected area of the planet and the star as

$$\delta = \frac{\Delta f}{f} \simeq \left(\frac{R_p}{R_*}\right)^2, \tag{1.3}$$

where Δf is the absolute drop in flux during transit and f is the flux outside of the transit. As larger transit depths are more readily detectable it therefore follows that the more massive, larger radius, exoplanets are more easily identified. This bias drives the large number of discovered hot Jupiter versus Earth mass exoplanets, they are simply easier to find.

1.3.2 Limb Darkening

When performing an analysis of a transit observation, the measurement of the transit depth can be complicated by the effects of limb darkening - the observed dimming of a stellar disk towards its edges. Limb darkening occurs as a result of the non-isothermal temperature profile of a stellar atmosphere. At the centre of the stellar disk, lower and hotter layers of the atmosphere are observed, whereas towards the edges higher and cooler layers are observed. The degree of limb darkening can have significant effects on the shape of a transit light curve as the proportion of blocked stellar emission will vary throughout

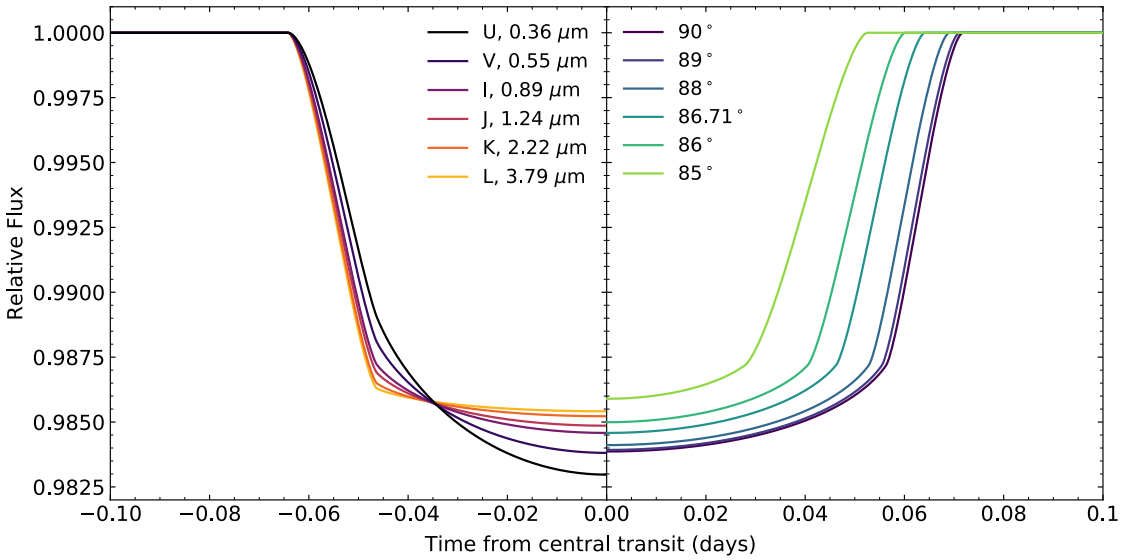

Figure 1.4: Model transit light curves for the hot Jupiter HD 209458b. *Left*: Variation in the light curves for different photometric bands using the non-linear limb darkening coefficients from Hayek et al. (2012). At shorter wavelengths the transit is both deeper and narrower as a result of the more pronounced limb darkening. *Right*: I band variation in the light curves for different orbital inclinations, with the value of 86.71°corresponding to the true value for HD 209458b. An exoplanet with an inclination below 90°will produce a shorter overall transit duration and a shallower transit depth.

the crossing. To further complicate matters, limb darkening varies as a function of wavelength and orbital inclination as shown in Figure 1.4. At shorter wavelengths the limb darkening effect is more pronounced and therefore the centre of the stellar disk takes up a larger proportion of the total emitted stellar flux. This results in deeper and narrower transit light curves that those for the longer wavelengths where the effects of limb darkening are reduced. As inclination varies below 90°, so does the path of a transit across the stellar disk. Naively this only results in shorter transit events, however when including the effects of limb darkening the overall transit depth is also reduced as the exoplanet obscures less of the bright centre of the stellar disk.

These variations mean that to accurately measure the true transit depth it is necessary to model and account for limb darkening. Most commonly limb darkening is modelled through either the quadratic law,

$$I(\mu) = I_0[1 - c_1(1 - \mu) - c_2(1 - \mu)^2], \tag{1.4}$$

or the non-linear law,

$$I(\mu) = I_0[1 - c_1(1 - \mu^{1/2}) - c_2(1 - \mu) - c_3(1 - \mu^{3/2}) - c_4(1 - \mu^2)], \tag{1.5}$$

where $\mu = \cos(\theta)$, with θ being the angle between the normal of the stellar disk and the radial direction of the emitted flux, I_0 is the intensity at the centre of the disk, $I(\mu)$ is the intensity at a desired μ, and c_{1-4} are limb darkening coefficients (Claret 2000). To compute the limb darkening for a given star the limb darkening coefficients are first calculated using a stellar atmosphere model that closely matches the properties of the star. The limb darkening itself can then be included explicitly in an analytical transit model such as that shown in Mandel and Agol (2002) to determine the true transit depth.

1.3.3 Transmission Spectroscopy

In reality most exoplanets are not featureless spheres with a constant radius; they have atmospheres. During a transit, the atmosphere of an exoplanet will partially contribute to the reduction in received stellar flux and it is often useful to redefine Equation 1.3 as

$$\delta = \frac{\Delta f}{f} = \frac{\pi R_p^2 + A}{\pi R_*^2}, \tag{1.6}$$

where R_p is now a reference planetary radius, and A is the area of an annulus which corresponds to the exoplanetary atmosphere. Defining a single point at which a planet ends and its atmosphere begins to obtain a value for A can be difficult, however a good estimation can often be made using the pressure scale height

$$H = \frac{k_B T}{\mu g}, \tag{1.7}$$

where k_B is the Boltzmann constant, T is the atmospheric temperature, μ is the mean molecular weight, and g is the surface gravity. Assuming $H << R_p$ this results in a transit depth of

$$\delta = \frac{\pi R_p^2 + \pi(R_p + H)^2 - \pi R_p^2}{\pi R_*^2} \simeq \frac{R_p^2 + 2R_p H}{R_*^2} \tag{1.8}$$

and an atmospheric transmission signal,

$$\delta_{\text{atm}} = \frac{R_p^2 + 2R_pH}{R_*^2} - \left(\frac{R_p}{R_*}\right)^2 = \frac{2R_pH}{R_*^2}. \tag{1.9}$$

The exoplanets best suited for atmospheric characterisation are those which have the largest atmospheric contributions to the transit depth, as any fractional change of this contribution to the transit depth will be easier to measure. Equation 1.9 therefore demonstrates that smaller stars hosting exoplanets with larger radii, lower surface gravities, higher temperatures, and low mean molecular weights (e.g. H/He dominated gas giants) are the best targets to observe atmospheric features. For most transiting exoplanets R_p, R_*, and g are known quantities and can be readily substituted into Equation 1.9. Assuming perfect heat redistribution, and that a planet absorbs all the incident stellar flux, the atmospheric temperature, T, can be approximated by the equilibrium temperature of the planet

$$T_{eq} = (1/4)^{\frac{1}{4}} T_* \sqrt{\frac{R_*}{a}}, \tag{1.10}$$

where T_* is the stellar effective temperature (Cowan and Agol 2011). Finally, a value of $\mu = 2.3u$ (where u is the unified atomic mass unit) can be assumed for gas giant planets (Fortney 2005). Under these assumptions one can determine δ_{atm} for the majority of transiting objects and identify which are most likely to be accessible via transmission spectroscopy (see Figure 1.5). The most accessible objects are those that lie closest to their host stars and have higher equilibrium temperatures, are not too massive where their surface gravities would be too large, and are massive enough that an observably significant atmosphere can be held. It is for this reason that the vast majority of currently characterised transiting objects lie in the hot Jupiter / hot Saturn regime. As the precision of observations improves in the near future with instruments such as *JWST* it will become increasingly easier to probe the atmospheres of less massive, and even potentially Earth-mass, objects.

When the atmospheres of exoplanets are being observed via transmission spectroscopy it is typical to search for wavelength dependent variations in the transit depth that arise due to the presence of specific atmospheric species. The origin of such a wavelength

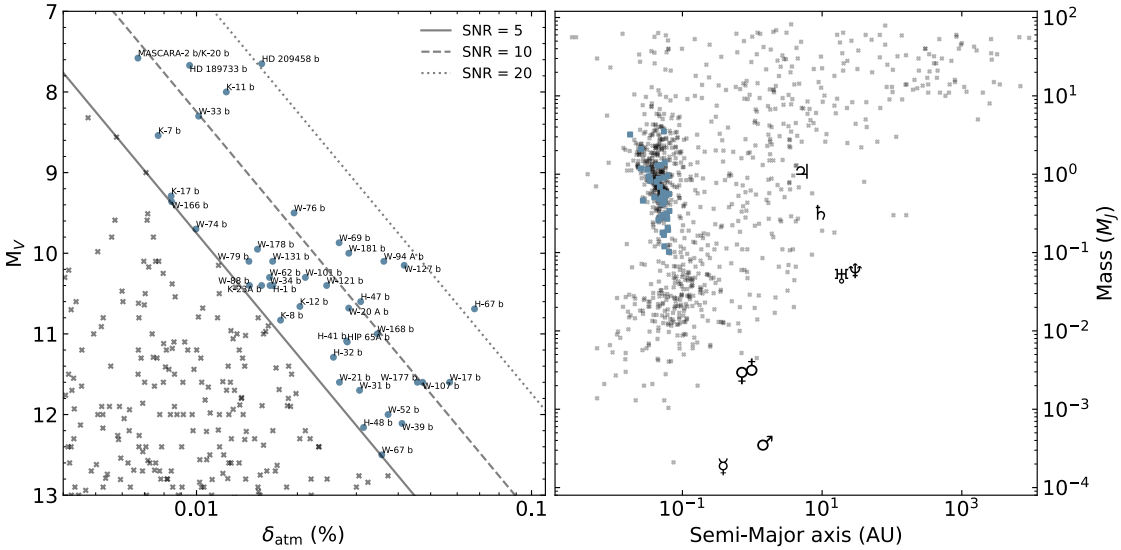

Figure 1.5: *Left*: The atmospheric transmission signal versus host star V-band magnitude. Lines of constant SNR have been approximated assuming photon noise and the precision reported in Kreidberg (2015). Objects with an estimated SNR of >5 are shown individually with abbreviated names. *Right*: As shown in Figure 1.1 except transiting objects with an SNR >5 are marked with blue squares and all other objects are now marked with grey crosses. The majority of objects which are best suited for atmospheric characterisation lie in the lower mass regime of the hot Jupiter / hot Saturn population.

dependence can be understood by looking at the true contribution of the atmospheric annular region to the transit depth, which is equivalent to the integral,

$$A = \int_{R_p}^{\infty} (1 - T) 2\pi r dr, \tag{1.11}$$

where T is the fractional transmittance of stellar light through the atmosphere, and r is the radial distance from the centre of the exoplanet. The transmittance is more aptly described in terms of Beer's law

$$T = e^{-\tau}, \tag{1.12}$$

where τ is the optical depth which can be written in terms of the total attenuation cross-section of the atmosphere, $\sigma_{\text{abs}}(\lambda)$, and its corresponding number density, n_{abs}, as

$$\tau = \int_{-\infty}^{\infty} \sigma_{\text{abs}}(\lambda) n_{\text{abs}} dx, \tag{1.13}$$

where λ is wavelength, and dx is an infinitesimal length along the depth of the atmosphere as viewed at a slant geometry, see Figure 1.6. Crucially, the absorption cross-section of the atmosphere is a function of wavelength due to the different absorption profiles of

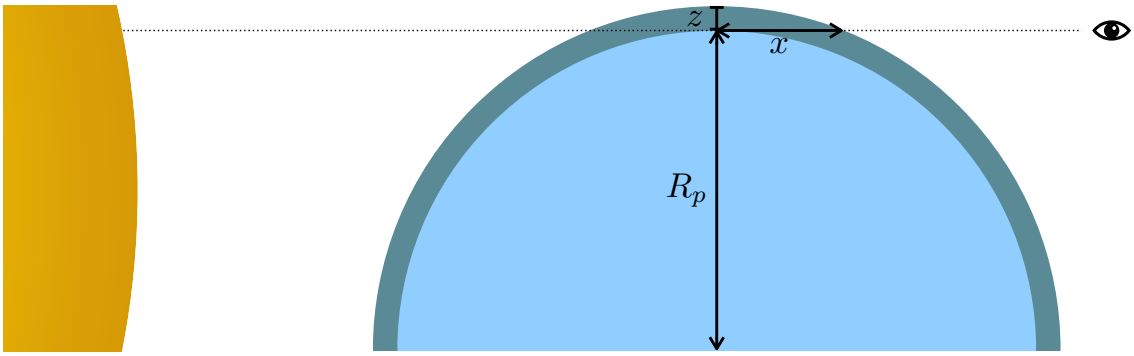

Figure 1.6: Diagram showing the difference between the standard geometry where the atmosphere is viewed at a thickness z, and slant geometry where it is viewed at a thickness x. R_p is the radius at an assumed reference level.

molecular species within the atmosphere. Substituting back into Equation 1.6 gives

$$\delta = \frac{\Delta f}{f} = \frac{\pi R_p^2 + \int_{R_p}^{\infty}(1 - e^{-\int_{-\infty}^{\infty}\sigma_{\text{abs}}(\lambda)n_{\text{abs}}dx})2\pi r dr,}{\pi R_*^2}, \tag{1.14}$$

and therefore variations are expected in the transit depth as a function of wavelength. Furthermore, under the assumption of an isothermal atmosphere, Equation 1.14 simplifies to a representation of the atmospheric "thickness" as a function of wavelength

$$z(\lambda) = H\ln\left(\frac{\sigma_{\text{abs}}(\lambda)\xi_{\text{abs}}P_0}{\tau_{\text{eq}}}\sqrt{\frac{2\pi R_p}{k_B T\mu g}}\right), \tag{1.15}$$

where ξ_{abs} is the number density of only the absorbing species, P_0 is a desired reference pressure, and τ_{eq} is the optical depth at which the atmosphere becomes optically thick (Lecavelier Des Etangs et al. 2008).

The molecular species that are most abundant, or have the most significant impact on the transmission spectrum of an exoplanetary atmosphere are not static. In reality, the presence or significance of a molecule is uniquely tied to the properties of the atmosphere such as: temperature, pressure, nascent molecular abundances, planetary mass, aerosol presence, disequilibrium effects, and solar irradiation. These different properties each impact a transmission spectrum in a unique way, however once they are compounded it becomes increasingly more difficult to disentangle and characterise them. Fortunately, efforts have been made to produce forward model transmission spectra to understand these effects ahead of time, such as those shown in Figure 1.7 (Goyal et al. 2018). In the top panel

of Figure 1.7, broad wavelength variations in the transmission spectrum can be described by the scattering or muting effects of clouds or hazes within the atmosphere. Specifically, at optical to near- infrared wavelengths, clouds are anticipated to impart a muting effect to the transmission spectrum which is wavelength independent, whilst hazes primarily introduce a strongly wavelength dependent slope at optical wavelengths. In the lower panel, the atmospheric temperature strongly determines which molecular species are most abundant. This is readily apparent in the dramatically increased absorption at optical wavelengths due to TiO and VO towards hotter temperatures. It is these variations, in addition to those resulting from other properties, that drive the characterisation of exoplanetary atmospheres through transmission spectroscopy. Through performing broad wavelength observations at a sufficient resolution, it becomes possible to observe spectroscopic features, or lack thereof, and make explicit conclusions about the atmospheric environment. Thus far: a range of molecular species have been detected through this method such as Na (Charbonneau et al. 2002), K (Sing et al. 2011a), H_2O (Deming et al. 2013), He (Spake et al. 2018), or TiO/VO (Evans et al. 2016); signatures have been detected that can be attributed to both clouds (Wakeford et al. 2017a; Alam et al. 2018) and hazes (Pont et al. 2008; Nikolov et al. 2016; Carter et al. 2020); temperature inversions have been constrained in the hottest atmospheres (Madhusudhan et al. 2011a; Evans et al. 2016); and even the effects of host star activity on transmission spectra have been observed (Rackham et al. 2017; Alam et al. 2018; Carter et al. 2020).

An important caveat that must always be remembered when performing transmission spectroscopy observations is that the only part of the atmosphere actually being probed is that at the limb between the day and night side of the exoplanet. This has particularly significant implications for exoplanets that are tidally locked, as the atmosphere may have a vastly different composition from the day to the night side depending on the efficiency of the atmospheric heat redistribution. Furthermore, explicit variations between the eastern and western limbs, and each limb as a function of latitude, may also exist dependent on the overall atmospheric structure. Therefore, given a sufficiently high instrumental precision, some transmission spectrum observations may be better described by an average of multiple 1D forward model spectra, or more advanced 2D or 3D models, as opposed to the single 1D models as displayed in Figure 1.7.

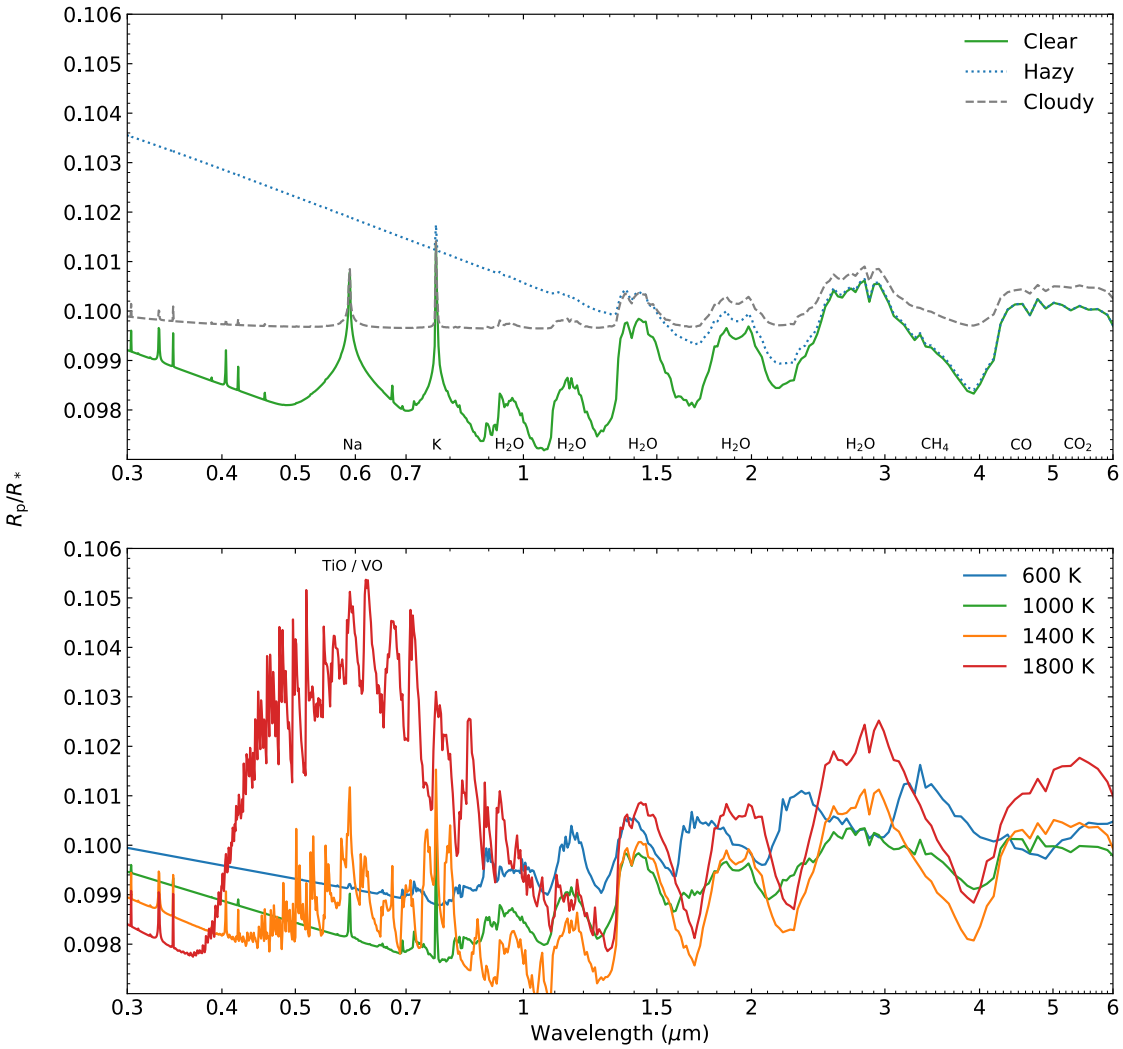

Figure 1.7: Forward model transmission spectra from (Goyal et al. 2018), atmospheric species are marked at the approximate location of their corresponding features, all models are at solar metallicity. The top panel shows a selection of models at $T = 1200$ K for an example clear, cloudy and hazy atmosphere. The bottom panel shows a range of clear models at different effective temperatures.

1.3.4 Emission Spectroscopy

At secondary eclipse, the occultation of an exoplanet by its host star will also produce a characteristic drop in the received flux as shown in Figure 1.2. This reduction is a natural consequence of reflected and emitted light from the day side of an exoplanet being obscured by the stellar disk. However, as stars are typically much more luminous than exoplanets, the average secondary eclipse depth is much shallower than its primary transit counterpart. Nevertheless, for some objects, current instrumental precision is sufficient to measure and detect a secondary eclipse. The amplitude of an eclipse depth, $\delta_{\rm ecl}$, is described as:

$$\delta_{\rm ecl} = \frac{f_{\rm p,d}}{f_*} = \phi_{\rm r} + \phi_{\rm e}, \tag{1.16}$$

where $f_{\rm p,d}$ is the planetary day side flux, f_* is the stellar flux, $\phi_{\rm r}$ is the contribution due to reflected light, and $\phi_{\rm e}$ is the contribution due to emitted light. In this situation, the contribution due to reflected light is a function of the geometric albedo of the exoplanet, G_λ, where

$$\phi_{\rm r} = G_\lambda \left(\frac{R_{\rm p}}{a}\right)^2, \tag{1.17}$$

and as a result will vary dependent on how reflective the atmosphere of the exoplanet is as a function of wavelength. A common way to approximate the emitted flux from the planet itself is to compare the blackbody emission of the star and planet as:

$$\phi_{\rm e} = \frac{B_\lambda(T_{\rm p,d})}{B_\lambda(T_{*,\rm eff})} \left(\frac{R_{\rm p}}{R_*}\right)^2, \tag{1.18}$$

where $B_\lambda(T_{\rm p,d})$ is the blackbody emission from the day side of the exoplanet, $B_\lambda(T_{*,\rm eff})$ is the blackbody emission from the star given its effective temperature. Therefore, by assuming $T_{\rm p,d}$=$T_{\rm eq}$, G_λ=0.5, and substituting in to Equation 1.16, one can estimate the predicted eclipse signal for the known population, as shown in Figure 1.8. In reality, the albedo may differ significantly between planets; stars and planets are not blackbodies, and $T_{\rm eq}$ may not be equal to the day side temperature. However, when taken in reference to the whole population, the estimated eclipse signals can help us understand which exoplanets are likely to be the easiest to detect in secondary eclipse. Interestingly, the best suited targets for eclipse observations are not completely the same as those for transmission observa-

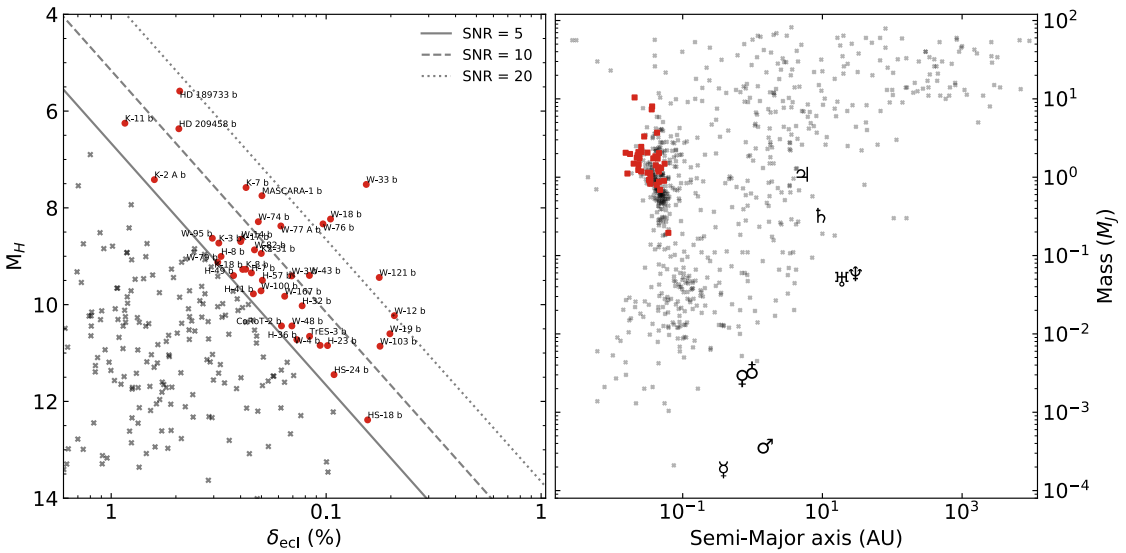

Figure 1.8: *Left*: The eclipse signal versus host star H-band magnitude at a geometric albedo G_λ=0.5. Lines of constant SNR have been approximated assuming photon noise and the precision reported in Stevenson et al. (2014). Objects with an estimated SNR of >5 are shown individually with abbreviated names. *Right*: As shown in Figure 1.1 except transiting objects with an SNR >5 are marked with red squares and all other objects are now marked with grey crosses. The majority of objects which are best suited for atmospheric characterisation lie in the high mass regime of the hot Jupiter.

tions. This is because the eclipse depth has no dependence on surface gravity, which acts to reduce the atmospheric scale height and therefore suppress the corresponding transmission signal. As a result, the targets with the most readily detectable eclipse depths are those that lie in the high mass hot Jupiter regime. In a simplistic case, a larger mass planet is likely to have a larger radius, and therefore a larger surface area to emit and reflect flux over, however larger planets are also more likely to survive the tidal forces at the closest separations where their equilibrium temperatures will be much larger (Equation **??**. For atmospheric characterisation purposes using eclipse spectroscopy, more massive planet may be particularly favourable as they are less likely to have had their atmosphere fully evaporated.

As previously mentioned, exoplanets are not blackbodies. The measured day side flux is uniquely affected by the composition of its atmosphere due to the absorption or emission of individual molecular species. Therefore, in a similar fashion to transmission observations, the eclipse depth will vary as a function of wavelength depending on which specific species are present, and by observing these variations it is possible to constrain atmospheric composition. Similarly, the reflected light component is modulated by the albedo of the exoplanet, as each molecule in the atmosphere will reflect light more or less

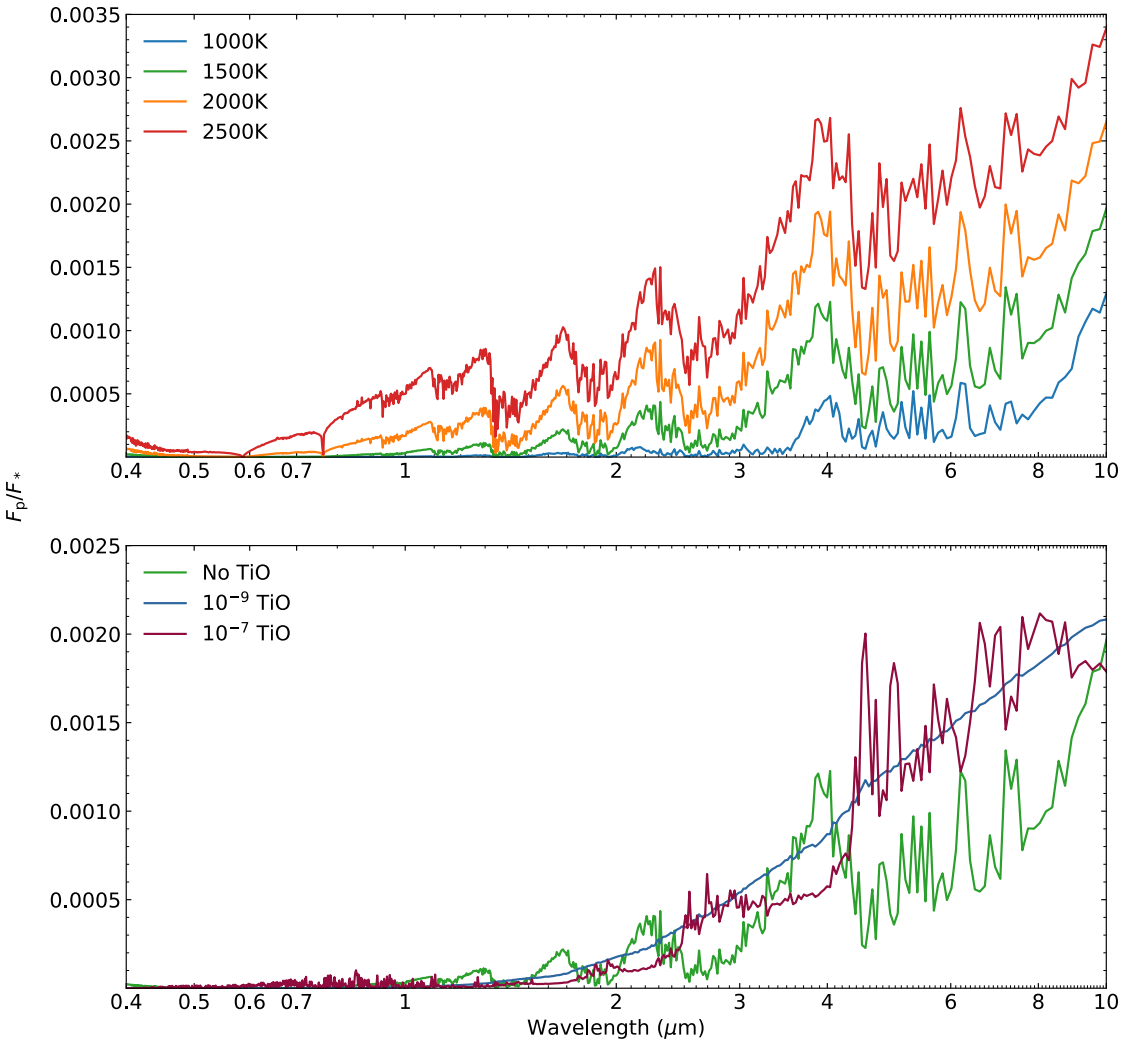

Figure 1.9: Example forward model emission spectra from (Gandhi and Madhusudhan 2017). The top panel displays a range of models without TiO absorption at a range of different effective temperatures. The bottom panel shows how variations in the TiO abundance can have significant implications on the overall emission spectra due to the production of an atmospheric thermal inversion.

efficiently as a function of wavelength. Modelling efforts have also been undertaken in this regard, with different models as a function of temperature and atmospheric composition shown in Figure 1.9 (Gandhi and Madhusudhan 2017).

With increasing temperature, the eclipse depth increases significantly across a broad wavelength range as the intrinsic emitted flux will also correspondingly increase. For the models shown in Figure 1.9, there is not much difference in molecular absorption with temperature, as above 1500 K the atmosphere is similarly dominated by CO and H_2O absorption. An important difference between the spectral absorption features of transmission and emission observations is that absorption increases transit depth, but

decreases eclipse depth. Therefore, absorption due a specific molecular species would appear as a "peak" in transmission, but a "valley" in emission. This can be seen through the H_2O absorption features between 1-4 μm in the top panels of Figures 1.7 and 1.9.

An example of varying atmospheric composition for a 1500 K atmosphere is shown in the lower panel of Figure 1.9. With an increasing TiO abundance the emission spectrum changes dramatically due to the development of a thermal inversion within the atmosphere. As TiO primarily absorbs at optical wavelengths it drives heating of the upper regions atmosphere (Madhusudhan and Seager 2010). Depending on how significant this heating effect is, the spectral features due to other species in the atmosphere can therefore switch from absorption to emission as they re-radiate this accumulated heat. In the case shown in Figure 1.9, with a 10^{-9} fractional abundance of TiO the absorbing and emitting effects almost cancel out and the emission spectrum is similar to a blackbody. As the abundance is increased further to 10^{-7} the emission dominates over the absorption as the spectral features "flip". Such an emission signature was definitively observed for the first time in the atmosphere of WASP-121b by Evans et al. (2017) with *HST*, and subsequently with other instruments (e.g. Kovács and Kovács 2019; Garhart et al. 2020) and for other objects too (e.g. Sheppard et al. 2017; Fu et al. 2020). Thermal inversions are not limited to detection through emission spectroscopy, however the day side is hotter and more strongly irradiated which makes generating such an inversion much easier.

As with transmission spectrum observations, only a portion of the exoplanetary atmosphere is probed when we perform emission spectroscopy. In this case, only the day side contributes to the received signal and as such it may not be descriptive of the entire atmosphere, particularly more so when the planet is tidally locked. Furthermore, emission from the day side of an exoplanet may not necessarily be uniform with latitude and longitude, and 1D models such as those shown in Figure 1.9 may not be suitable comparisons in all scenarios. However, when transmission and emission spectroscopy observations are combined they do provide valuable information on the differences between atmospheric structure and composition between the day and night side.

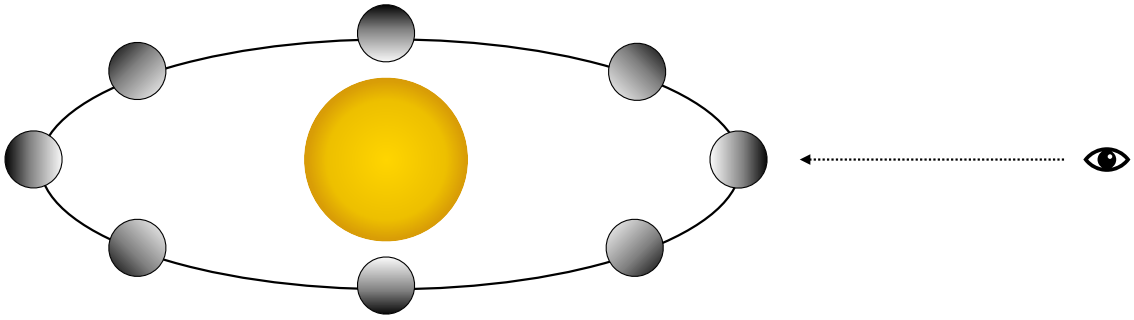

Figure 1.10: A diagram illustrating which area of the exoplanet is viewed as a function of orbital phase. During primary transit only the night side is visible, whilst just before secondary eclipse the day side is predominantly visible.

1.3.5 Phase Curve Observations

As a transiting exoplanet orbits its host star we observe different regions of the planetary surface, or atmosphere (Figure 1.10). Specifically, during the primary transit only the night side is visible, whilst just before secondary eclipse the day side is most visible. As the day side emits and reflects more light than the night side, the flux we receive will vary as a function of orbital phase. The significance of these phase curve variations is primarily linked to the atmosphere's ability to redistribute heat from the day side to the night side and through characterising these variations the 3D properties of the atmosphere can be constrained. This is in stark contrast to solely transmission or emission observations which only probe a portion of the atmosphere at a given time.

Knutson et al. (2007) first performed these observations for the hot Jupiter HD 189733b, revealing a smooth variation in emission as a function of orbital phase (Figure 1.11). Furthermore, these observations indicated that the secondary eclipse did not occur at the peak of the planetary emission, suggesting that the hottest part of the atmosphere was not at the sub-stellar point. Such an offset is a result of the tidally locked nature of HD 189733b, and was in fact predicted prior to the performed observations by Showman and Guillot (2002). Due to the large day to night side temperature contrast, large superrotating jets transport the hottest part of the atmosphere away from the substellar point before it can reradiate the incoming flux. Measuring these offsets can provide powerful insights into the overall radiative and advective properties of the atmosphere. Furthermore, phase curves observations are a powerful constraint for fully 3D models of exoplanetary atmospheres through their ability to probe the full longitudinal atmospheric structure. Due

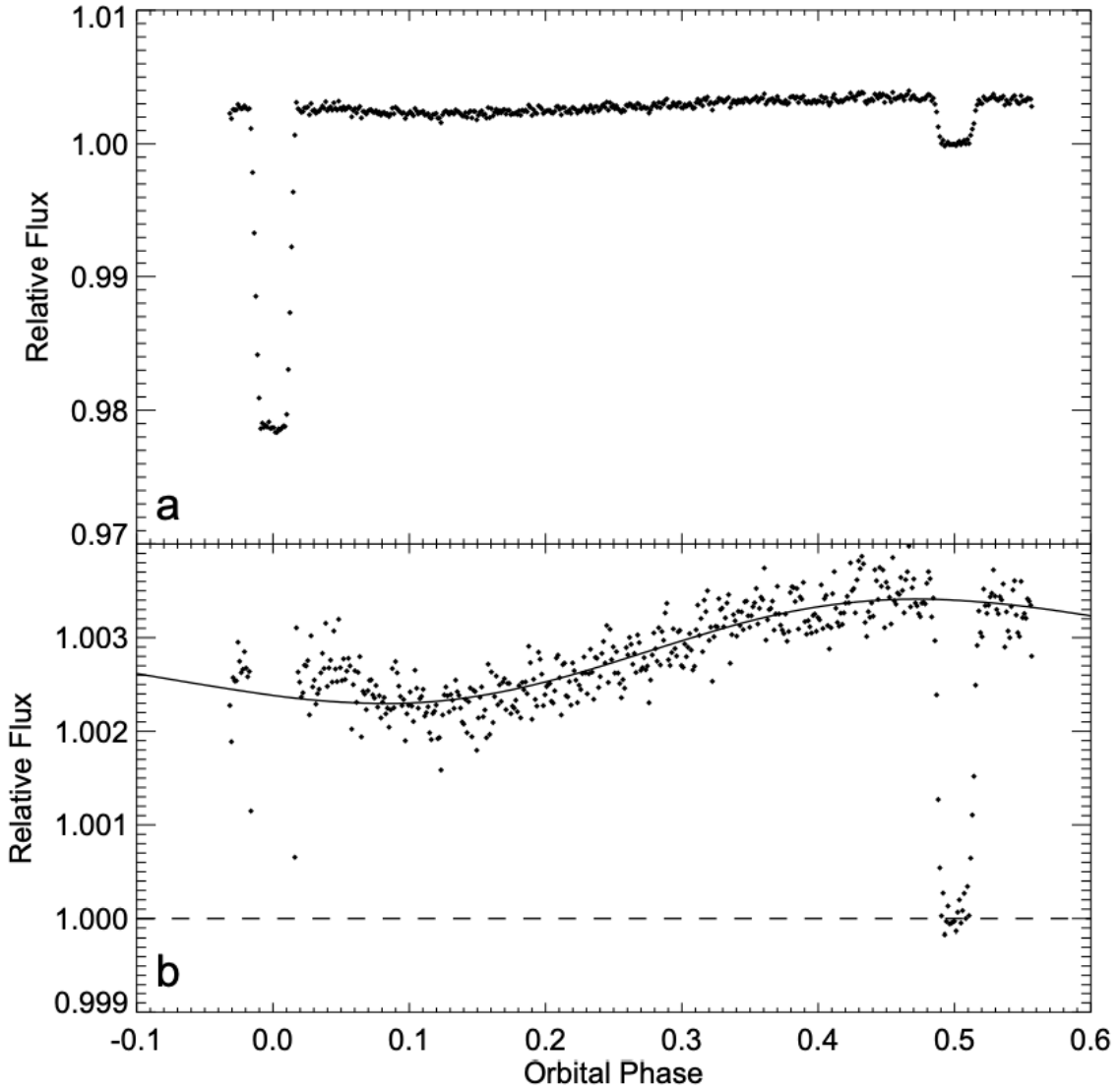

Figure 1.11: The phase curve of the hot Jupiter HD 189733b with *Spitzer* IRAC at 8 μm. The primary transit occurs at zero orbital phase, and the secondary eclipse at 0.5 orbital phase. Figure from (Knutson et al. 2007).

to their expensive nature only a handful of these observations have been performed to date, however the precision and long time baseline provided by *TESS* should increase the number of photometric phase curve observations significantly (e.g. Wong et al. 2020).

1.4 Directly Imaged Planets

Whilst observations of transiting exoplanets are a powerful way to characterise exoplanetary atmospheres, their practicality is limited to a particular range of planetary systems. Exoplanets with large orbital periods will transit very infrequently, making their initial detection and discovery difficult. Furthermore, even if these objects were discovered, it

would likely be a long time before their next transit and efficiently scheduling multiple transmission or emission observations of them would be very difficult. In contrast, and in this respect alone, the limitations towards direct imaging observations are very small. In the event that an exoplanet can be fully resolved from its host star in an image, we do not need to rely on stringent timing restrictions that are common to transiting observations. These observations also facilitate the characterisation of the exoplanetary atmosphere, as the overall emitted spectral energy distribution can be measured using observations performed at different wavlengths. However, these observations are much more easily described than they are performed and have significant limitations of their own.

1.4.1 The Difficulty of Direct Imaging

It is an inescapable fact that planets are much fainter than stars and are therefore harder to observe. However, the primary difficulty in their observation does not come from the fact that they are intrinsically faint, but the fact that they are very closely separated from a much brighter star. At smaller and smaller separations, larger and larger telescopes are necessary to fully resolve the star and planet independently, which in an ideal scenario follows the Rayleigh Criterion:

$$\theta = \frac{1.22\lambda}{D}, \tag{1.19}$$

where θ is the minimum angular separation between the spatial peak of the stellar and planetary emission, λ is the wavelength of the observation, and D is the telescope diameter. Although it is tempting to suggest that observations should be performed at shorter wavelengths, so as to reduce θ, the intrinsic received flux of the planet compared to that of its host star must also be considered. Figure 1.12 shows that the overall planetary fluxes have two distinct peaks: one just below ~1 μm corresponding to the reflected stellar emission, and one towards the mid-infrared corresponding to the inherent thermal emission of the planet. Irrespective of wavelength, the stellar emission dominates, emphasising that not only is sufficient resolution necessary to be able to resolve the planet, but that the observations must be sufficiently precise as to observe variations resulting from a much fainter exoplanet within this emission. Immediately it seems that observations towards the longest wavelengths would be the most optimal, as the contrast between the stellar and planetary flux is at its lowest and the planetary flux can be more easily separated.

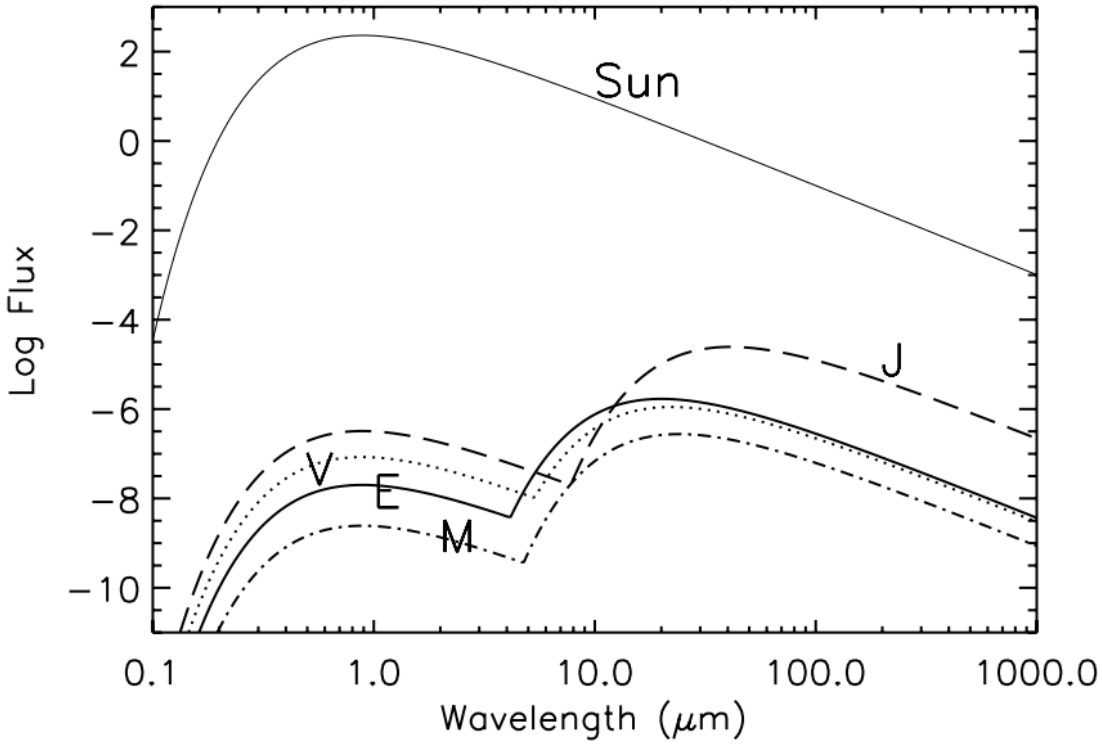

Figure 1.12: Approximate spectral energy distributions for Venus, Earth, Mars, Jupiter, and the Sun as seen at a distance of 33 light years. Figure from Seager (2003).

However, returning to Equation 1.19 it is clear that by observing at longer wavelengths, we reduce the resolution of our observations. The anti-synergistic nature of observing at high resolution, where exoplanets are more readily spatially resolvable, and at longer wavelengths, where exoplanets are at their brightest, is currently the primary limitation towards directly imaging exoplanets. It is for this reason that the direct imaging discoveries to date (see Figure 1.1) occupy a parameter space of the largest separations, and the largest mass exoplanets. We do not currently have a telescope with a sufficient sensitivity to detect the smallest exoplanets at short wavelengths, or a telescope large enough that the closest separation exoplanets can be resolved at longer wavelengths.

The difficulty of directly imaging an exoplanet is already quite clear, however if we broaden our scope from theoretical resolution and contrast limits these observations become even more complex. In reality telescopes are not perfect and small irregularities in the optical elements will lead to significant distortions in the received stellar point-spread function (PSF), more commonly known as speckle noise. Furthermore, at areas on the detector where the distorting effects of these aberrations interfere constructively, individ-

ual "speckles" (Bloemhof et al. 2001) can be produced which have similar intensities to a potentially observable exoplanet. Finally, if one were to observe from a ground-based instrument, the wavefront distorting effects of the atmosphere would even further reduce the clarity of the received image.

1.4.2 Direct Imaging Strategies

Given the inherently difficult nature of direct imaging observations, a variety of strategies have been developed in an effort to characterise and suppress the dominating effects of the stellar PSF and speckle noise in order to separate and identify companion objects.

1.4.2.1 Adaptive Optics

When observing from the ground the effects of atmospheric distortion are a primary concern. Atmospheric turbulence drives significant deviations from a perfect Airy pattern PSF and spreads the incoming stellar flux over a broader spatial region. This limits the area over which companion objects can be readily identified, in addition to restricting our ability to accurately characterise and potentially subtract the stellar PSF. It is therefore desirable to refocus this diffuse light through the use of adaptive optics.

By separating a fraction of the incoming light it is possible to measure the overall atmospheric wavefront distortion. These measures can then be transferred to the controller of a telescope's deformable mirror in order to physically manipulate the shape of the mirror as to counteract the wavefront distortion. An example of the improvement provided under this adaptive optics process is shown in Figure 1.13 for the binary system IW Tau. In the left panel the wavefront distortion has smoothed out the incoming stellar flux, making it almost impossible to discern that there are actually two objects present. In the right panel, the adaptive optics has acted to refocus this light and the two separate objects are resolvable. As the atmosphere itself is not static, this adaptive optics process must be performed quickly and constantly throughout an observation - oftentimes at a frequency of $\sim$1$-$2 kHz (Hardy and Thompson 2000). This somewhat limits our ability to apply these live corrections as there are physical limitations to how quickly the distortion can be measured, or the mirror can be deformed. Furthermore, the scale of the applied

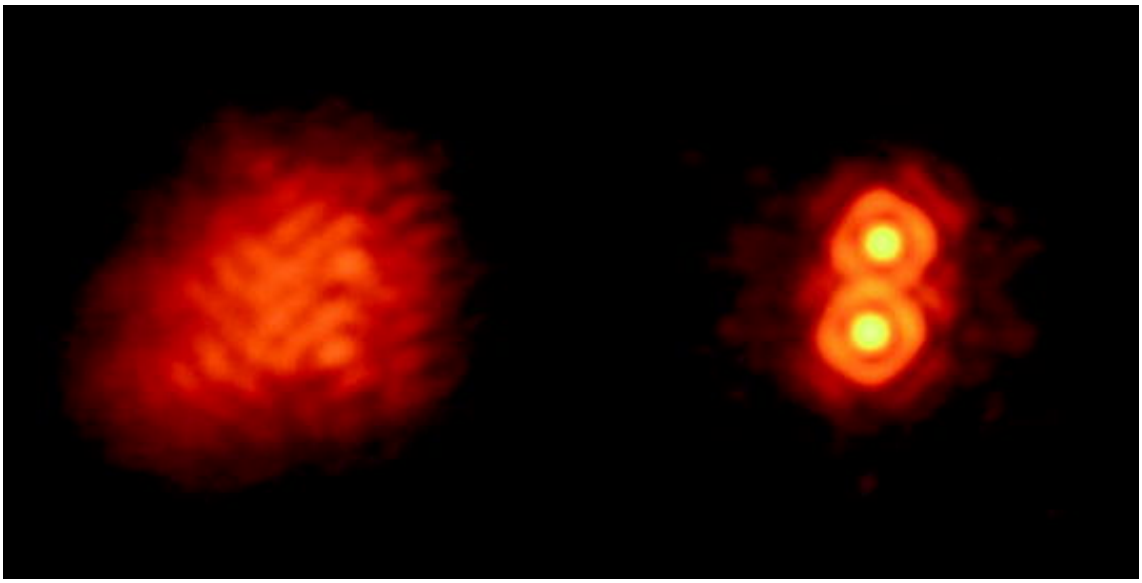

Figure 1.13: The effect of using (right) or not using (left) adaptive optics on an observation of the binary system IW Tau. Image credit: Chas Beichman and Angelle Tanner, NASA/JPL.

distortions is limited by the number of individual actuators behind the mirror. Nevertheless, even though these adaptive optics corrections are not perfect, they provide dramatic improvements over observations without such corrections.

1.4.2.2 Coronagraphy

Irrespective of whether an observation is performed from the ground or space, stellar light dominates the received flux, particularly at the shortest separations. As a result, fainter objects such as exoplanets are very difficult to identify and it is highly desirable to block the stellar light before it reaches the detector. Such a method was first proposed by Lyot (1932), however for observations of the relatively faint coronal emission from the Sun, through coronagraphy. This method is still used today for observations of the Sun, as can be seen for a *SOlar and Heliospheric Observatory* (SOHO) (Domingo et al. 1995) image in Figure 1.14, and has also been adopted for observations of exoplanets.

Conventionally, coronagraphy blocks a significant (~98%) portion of the incoming stellar light through the use of two elements: an occulting mask, and a Lyot stop. The occulting stop acts to completely block the light from the central peak of the stellar Airy disk which is produced after the first lens. The purpose of the Lyot stop is to block the scattered light that results from diffraction at the border of the occulting mask. A schematic

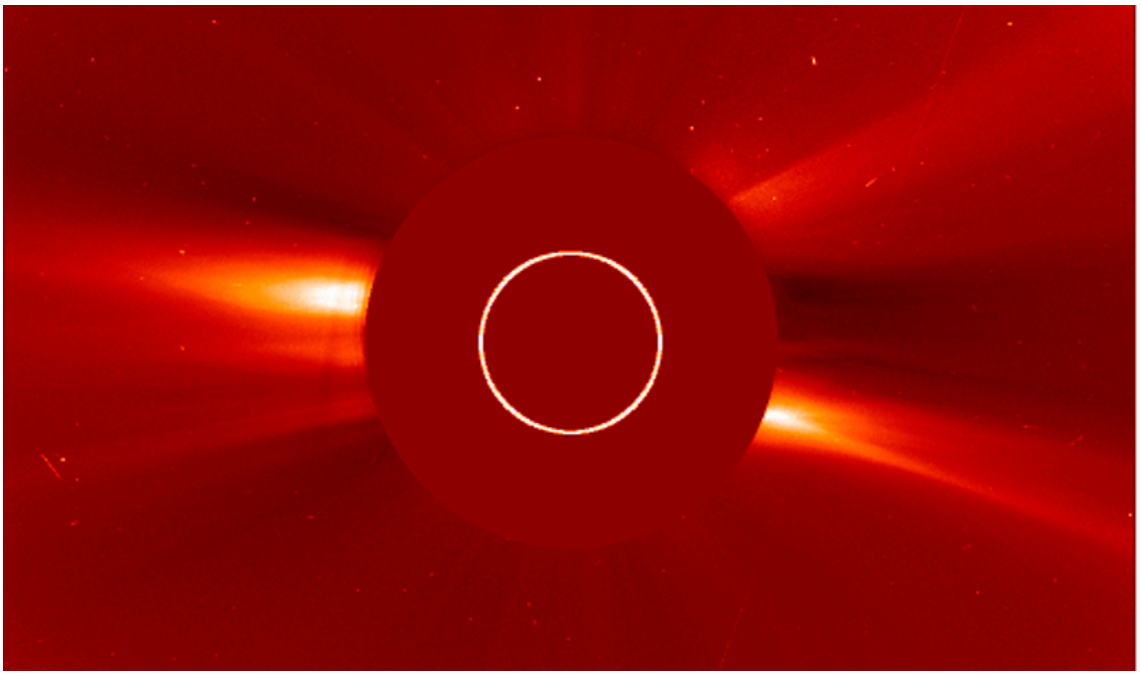

Figure 1.14: A coronagraphic image of the Sun taken with the *SOHO* satellite, the solar disk is marked with a white circle. Suppression of the stellar light enables the fainter solar corona to be observed. Image credit: NASA/ESA

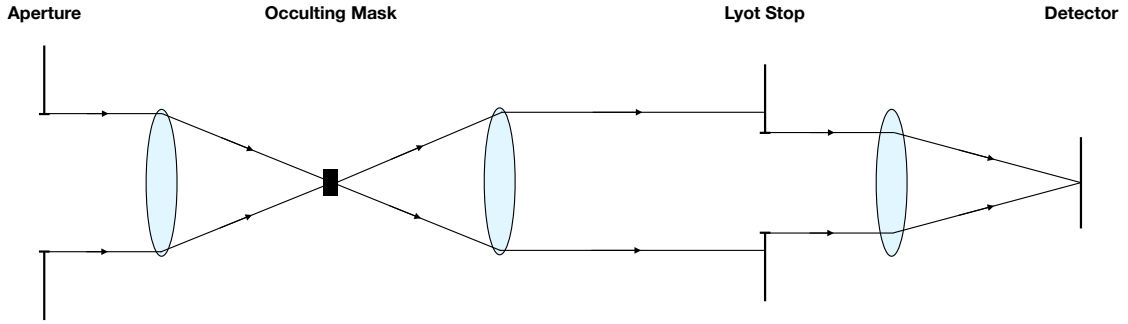

Figure 1.15: A simplistic schematic of a coronagraphic optical train, lenses are pale blue ovals and all other components are labelled. Figure adapted from Sivaramakrishnan et al. (2001).

of a classical Lyot coronagraph is shown in Figure 1.15. Over time other types of coronagraph have been developed, such as apodized pupil Lyot coronagraphs (Soummer 2005) and four-quadrant phase masks (Rouan et al. 2007), however their core application is the same: to block the incoming stellar light.

1.4.2.3 Speckle Noise Suppression

Whilst coronagraphs are effective for the removal of the expected stellar flux, they do not aid in the removal of the speckle noise produced due to instrumental aberrations. Speckle noise is typically quasi-static, with correlation timescales in the range of minutes

to tens of minutes (Hinkley et al. 2007; Milli et al. 2016) and unlike uncorrelated noise sources, such as detector read noise, increasing the exposure time is not a practical or efficient method of accounting for it. Instead, image processing techniques are necessary to separate the speckle noise from potential exoplanetary signals. There are a wide variety of these techniques that can be used, however I describe those that are the most common (and can be used for *JWST* observations) below.

The first and more rudimentary method for removing speckle noise is through reference differential imaging. Due to the quasi-static nature of speckle noise, it is feasible to perform an observation of a target star, then an observation of a reference star, without the underlying speckle noise changing significantly. The reference image can then be subtracted from the target image to remove the speckle noise, potentially revealing planetary companions. The closer in time these observations are performed the better, as the speckle noise will have less time to vary. Ideally, the reference star used must have no evidence of companions itself as to avoid over subtractions in the target image. Furthermore, it is important that the reference star is not too significantly separated from the target. Large telescope slews can lead to significant changes in the overall strain on the telescope elements, in addition to the overall telescope illumination, which can in turn impact the final speckle noise pattern. Finally, the reference star selected should preferably be of a similar spectral type to the host star as the diffraction that drives the speckle noise is a function of wavelength.

Angular differential imaging (Marois et al. 2006) aims to subtract the speckle noise by treating the target star as its own reference through to use of a range of sequenced target image observations at different rotated fields of view. As the telescope and instrument are rotated the position of a potential exoplanet on the detector will also rotate, however, the speckle noise pattern will remain fixed at the same orientation. The speckle noise can therefore be subtracted from a target image by using other images within the observation sequence. As the potential companions have rotated within the image, they will not self-subtract between images with sufficiently different rotations. Finally, the ensemble of target images can then be derotated and aligned to produce a final sequence averaged, speckle noise subtracted, target image. A visual example of this process is displayed in

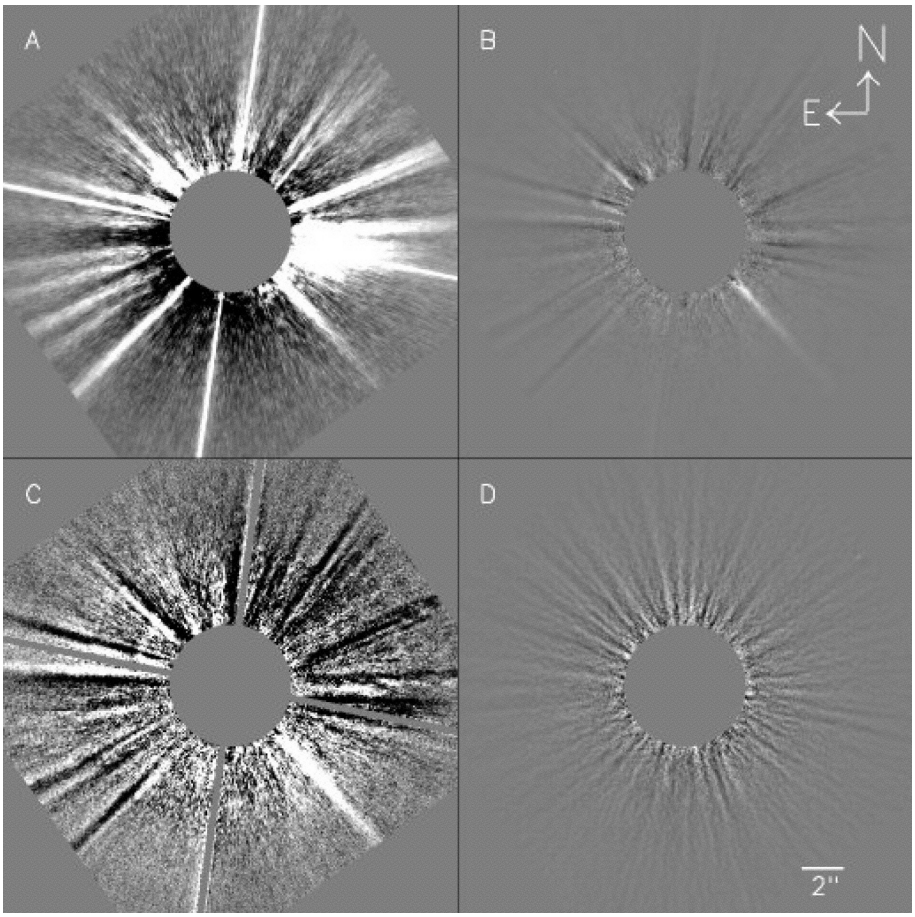

Figure 1.16: Data reduction via angular differential imaging for Vega. *A*: A single target image, *B*: A single ADI differenced target image, *C*: The same as *B*, but with an intensity range 25 times smaller, *D*: The final image following the combination of all individual differenced target images shown on the same intensity range as *C*. Figure from (Marois et al. 2006).

Figure 1.16 for the star Vega, where no companions were observed (Marois et al. 2006).

Whilst the angular differential imaging technique is able to discern the presence of a planetary signal versus that of speckle noise given their unique responses to the observational orientation, it is also possible to discern these two signals due to their similarly unique responses to variations in the observational wavelength. Speckle noise is driven by diffraction and therefore its scale and extent on the detector varies as a function of wavelength, however this noise remains centred at the location of the target star. Conversely, light detected from a companion exoplanet will always be centred at its spatial location, enabling speckle noise subtraction through spectral differential imaging. Using multiple wavelength observations performed simultaneously, such as through integral field spectroscopy, one can exploit the wavelength dependent extent of the speckle noise (Sparks and Ford 2002). Taking a single image, each other image is rescaled so that the extent of

the speckle noise matches between images. Following this, the median combined image can be subtracted from each image to remove the speckle noise. Importantly, potential companions do not get subtracted during this process as the image rescaling acts to radially disperse the companion flux in the median image. By rescaling each image to its original size and co-adding them all together the companion flux can be more readily determined. These images will also exhibit radial subtraction streaks in the same location as imaged companions due to the initial median image subtraction. This technique is best used when the difference in wavelength between each image is small so as to avoid explicit variations in the stellar flux as a function of wavelength.

The methods for speckle noise subtraction described thus far all rely on the subtraction of an image, or median combination of images, from a target image that is assumed to approximately match the observed speckle noise. Given the time and wavelength varying nature of speckle noise, such a method will likely never be able to achieve an optimal subtraction. As a result, a number of efforts have been made to utilise a library of target or reference images in unison to obtain an optimal subtraction image. Most commonly this optimal image is determined algorithmically using either the Locally Optimized Combination of Images (LOCI, Lafrenière et al. 2007) or Karhunen-Loéve Image Projection (KLIP, Soummer et al. 2014) approaches. LOCI operates by determining which combination of library images best matches the science image, whereas KLIP operates by determining which combination of eigenimages determined from the original image library best matches the science image. Such methods typically outperform the more simplistic differential imaging methods previously described by an order of magnitude or more, however a library of reference images may not always be available. An example of the improvement provided by the LOCI algorithm compared to standard reference differential imaging is shown in Figure 1.17 for the exoplanetary system HR 8799. The improvement from LOCI is so drastic that three of the four known exoplanet companions, which were initially unidentifiable, are clearly detected in the final subtracted image.

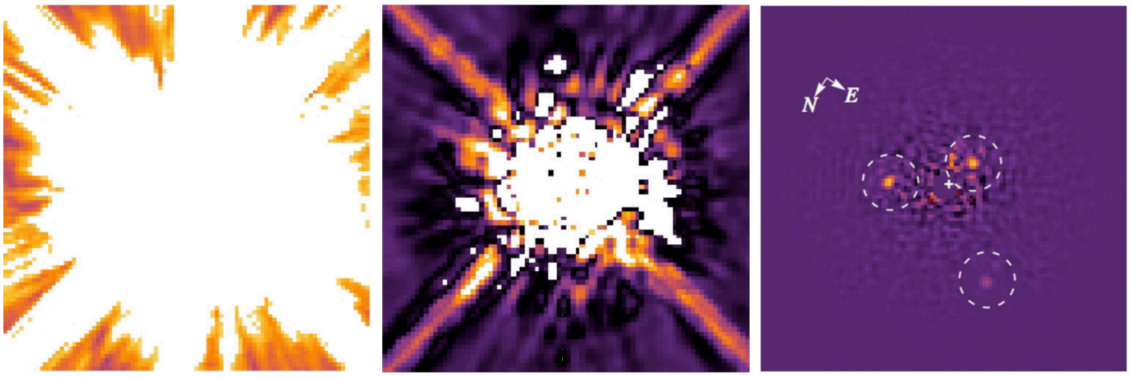

Figure 1.17: Coronagraphic imaging of HR 8799b with *HST* with: no stellar subtraction (left), simplistic reference differential imaging (middle), and subtraction using a LOCI optimised reference image (right). Figure adapted from (Soummer et al. 2011).

1.4.3 Directly Characterising Exoplanets

By directly observing exoplanets at a variety of wavelengths through multiple photometry or spectroscopy, it is possible to characterise their atmospheres in a similar way to transiting exoplanets. However, where transmission and emission spectroscopy observations of transits are indirect measures of the atmospheric properties, direct imaging observations inherently provide direct information from the exoplanet. Unfortunately, this has its own limitations, chief of which being that current telescope resolutions are vastly lower than that necessary to directly measure the planetary radius. This is particularly troublesome as the planetary flux emitted at its surface radius R_p,

$$f_{p,R_p} = f_{p,d}\left(\frac{d^2}{R_p^2}\right), \tag{1.20}$$

where d is the distance, and f_{p,R_d} is the planetary flux received at this distance. Even though the distance can be determined robustly with new data from *Gaia* (Gaia Collaboration et al. 2016; Gaia Collaboration et al. 2018), as the planetary radius is unknown it is difficult to determine the actual emission from the planetary surface. Given a planetary mass and age, it is technically possible for evolutionary models to be used to determine the expected emitted and received flux for a planet of a given radius. Unfortunately, the planetary mass is also very hard to constrain with solely direct imaging observations, and these observations occupy a parameter space currently unreachable by other planetary detection techniques. Furthermore, age is a notoriously difficult parameter to constrain for individual systems (Mamajek and Hillenbrand 2008). Therefore, due to these current

limitations, forward model planetary spectra must be calculated and fit to the data to infer the planetary radius, and other properties such as the temperature and surface gravity.

A collection of forward model spectra as calculated by Phillips et al. (2020) is shown in Figure 1.18 with varying temperature, surface gravity and radius. Variations in temperature make the most significant difference to the emitted spectra, with the hottest temperature model being magnitudes more luminous than the coldest. In contrast, changes due to surface gravity are much more subtle, and primarily affect molecular absorption feature strengths such as the CH_4 feature at ~3.3 μm. Changes to the planetary radius are applied through a scaling of the flux for the nominal 1 R_J model, and result in a wavelength independent increase or decrease to the surface flux. Interestingly, variations in the planetary radius can also vary the surface flux by orders of magnitude. As a result, for observations with limited wavelength coverage there can be sizeable degeneracies between the radius and temperature during model fitting.

In all cases, a rich diversity in molecular absorption features can also be seen, similarly to transmission or emission spectroscopy observations of transiting exoplanets. Therefore, by performing broad wavelength spectroscopic observations of directly imaged planets it is possible to constrain the atmospheric abundances of these molecular species, in addition to bulk planetary properties such as the temperature and radius. Unfortunately, at the wavelength range of an absorption feature less flux will be emitted, making direct imaging characterisation a complex task as planetary mass objects are already 10^4–10^6 times fainter than their host stars (Marois et al. 2008; Macintosh et al. 2015). In some cases the absence of flux can be attributed to absorption from a particular molecular species, but an exact measure of its abundance cannot be obtained aside from an upper limit. To this date only a handful of directly imaged planets have been spectroscopically characterised, and these observations are primarily limited to spectroscopy below 2 μm and photometry below 5 μm (e.g. Zurlo et al. 2016; Samland et al. 2017; Greenbaum et al. 2018; Gravity Collaboration et al. 2019; Cheetham et al. 2019; Stolker et al. 2020).

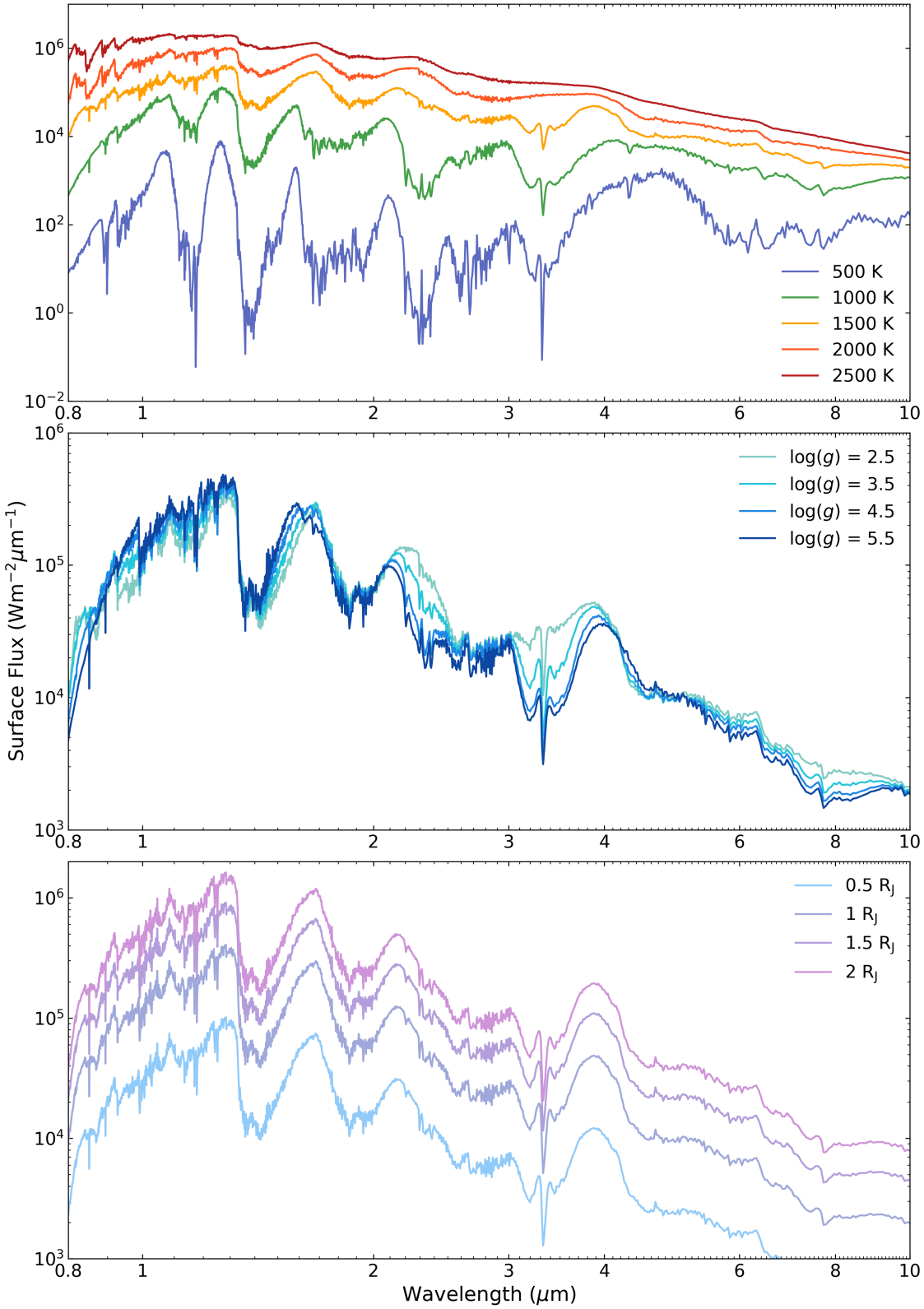

Figure 1.18: Forward model planetary spectra varying in temperature (top), surface gravity (middle), and planetary radius (bottom). Models were obtained from (Phillips et al. 2020) and are all at solar metallicity and chemical equilibrium. For the top panel, all models are at a log(g)=3.5 and a R_p = 1 R_J. For the middle panel, all models are at a T=1500 K and a R_p = 1 R_J. For the bottom panel, all models are at a log(g)=3.5 and a T=1500 K.

1.5 The James Webb Space Telescope

The James Webb Space Telescope (*JWST*) is currently scheduled for launch in 2021 and will provide dramatic advances across the entire field of astronomy and astrophysics. The goals of *JWST* are centred around four primary science themes: first light and reionisation, assembly of galaxies, birth of stars and protoplanetary systems, and planets and the origins of life. As exoplanets straddle both of latter two themes, there is a significant pressure to perform exoplanetary science immediately upon launch.

1.5.1 Capabilities

JWST is an incredibly complex and sophisticated observatory that will significantly push the boundaries of our observing capabilities. However, given its complexity it is not straightforward to understand what drives this improvement. Broadly speaking, the advances that *JWST* will provide are a result of three key qualities: sensitivity, versatility, and wavelength coverage.

One primary advantage of *JWST* is its location: space. From the ground, observations are much more difficult due to the noise inducing effects of the Earth's atmospheric turbulence and the high telluric thermal background. In space, these effects are not present and as a result the explicit noise floor of an observation is reduced. However, space-based observatories are not new, with highly successful missions such as *HST*, *Spitzer* (Werner et al. 2004), and *Chandra* (Weisskopf et al. 2002) making significant scientific discoveries since over the last ~20 years. What sets *JWST* apart is its 6.5 m primary mirror diameter, the largest ever sent to space. In comparison, *HST* has a primary mirror diameter of only 2.4 m, corresponding to a collecting area of ~48 square feet. The collecting area of *JWST* is over 5 times larger than this at ~270 square feet. This increase in collecting area means that *JWST* will be able to conduct highly precise observations of some of the faintest objects in the sky. With regards to transiting exoplanetary observations in particular, this increased sensitivity will enable the characterisation of exoplanets with smaller atmospheric transmission and eclipse signals. For direct imaging observations, smaller and less luminous companions will be much easier to detect.

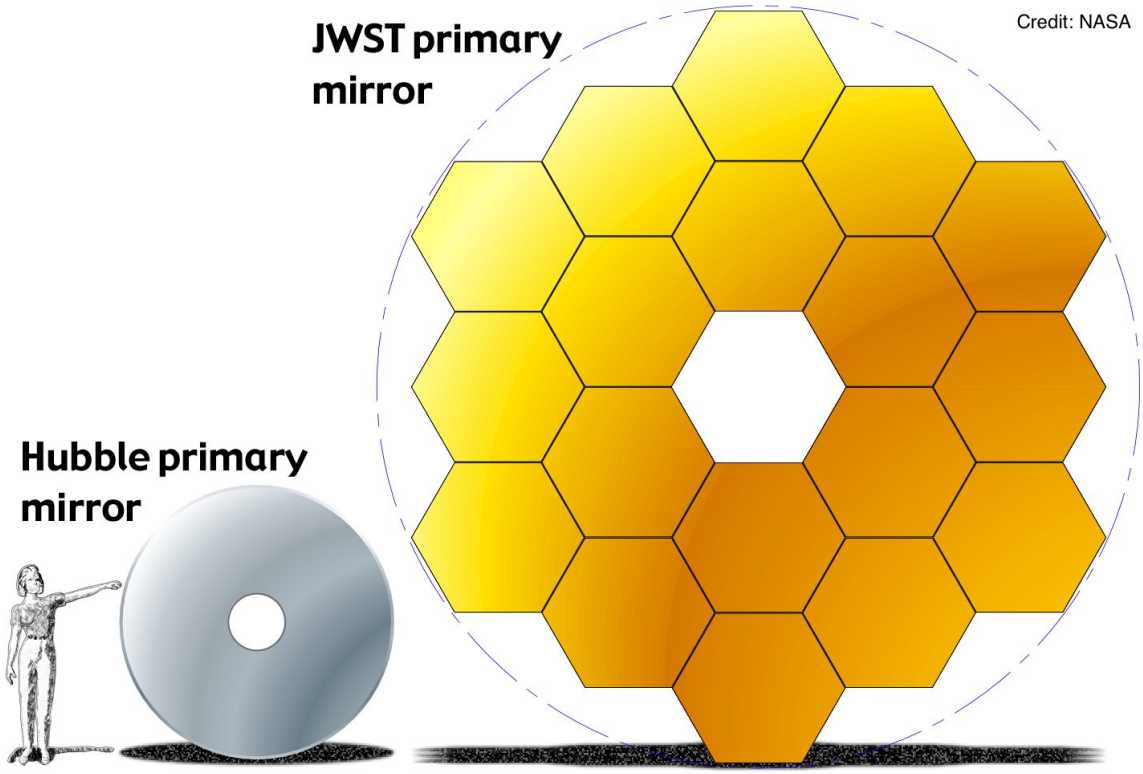

Figure 1.19: A to scale image of the *JWST* primary mirror in comparison to the *HST* primary mirror. Image obtained from the NASA image library.

Four independent instruments will be integrated into *JWST*: the Near-InfraRed Camera (NIRCam) (Rieke et al. 2005), the Mid-InfraRed Imager (MIRI) (Rieke et al. 2015), the Near-InfraRed Imager and Slitless Spectrograph (NIRISS) (Doyon et al. 2012), and the Near-InfraRed Spectrograph (NIRSpec) (Bagnasco et al. 2007). Furthermore, a range of different observing modes can be selected for each independent instrument depending on the desired scientific goals. A brief overview of these modes as a function of wavelength is displayed in Figure 1.20, demonstrating the considerable versatility that *JWST* provides. Importantly, to one degree or another all of the *JWST* instruments have explicit capabilities towards the characterisation of exoplanets through both transit and direct imaging observations.

The third central advantage of *JWST* is its broad wavelength coverage, spanning from 0.6-28.3 μm (see Figure 1.20). From the ground, observations at near- to mid-infrared wavelengths are notoriously more difficult to perform due to the suppressed transmittance of the Earth's atmosphere. Whilst space-based instruments such as *Spitzer* (Werner et al. 2004) and *WISE* (Wright et al. 2010) have been designed to operate at these wave-

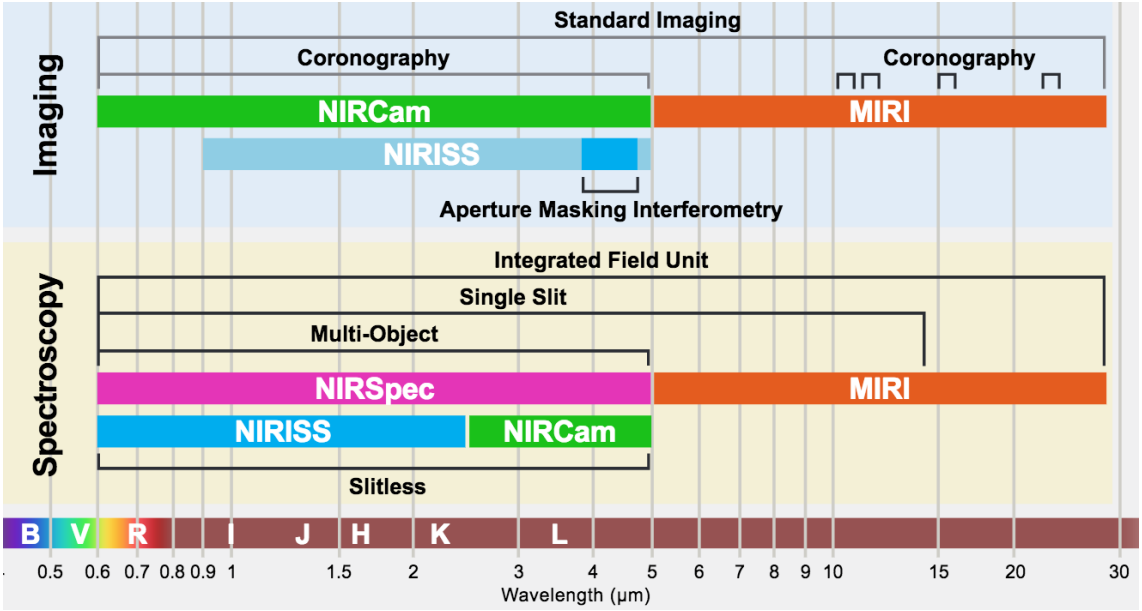

Figure 1.20: Overview of *JWST* observing modes, separated by instrument, and imaging or spectroscopy technique. Credit: STSci.

lengths, they have primarily been limited to broad wavelength photometric observations. *JWST* is a significant improvement from this, with R>1000 spectroscopy possible across its full wavelength range. This is particularly important for the study of exoplanets as thus far these wavelengths have been largely unexplored in such detail. At these wavelengths the blackbodies of lower mass and cooler objects peak, making them easier to detect directly. Furthermore, by characterising the atmospheres of exoplanets over such a broad wavelength range it will be possible to constrain the presence and abundance of a much more diverse variety of molecular species.

When considered in isolation, each of these advantages clearly represents a significant advancement in our observational capabilities. However, it is when these advantages are considered holistically that the strength of *JWST* as the next flagship space observatory can truly be appreciated. *JWST* will not only spectroscopically probe the universe in the near- to mid-infrared for the first time, it will do so with a wide range of unique instrumental modes of observation, each of which representing one of the most sensitive to date.

1.5.2 Transmission and Emission Spectroscopy of Exoplanets with JWST

Each of the four *JWST* instruments has at least one observing mode that can be directly applied to observations of transiting exoplanets. Whilst the photometric observing modes could potentially be used, for transit observations in particular the spectroscopic modes are generally much superior and as such will be the primary focus of this section.

With NIRCam, observations of transiting exoplanets will primarily be performed using its grism time-series observing mode. This mode can be used in conjunction with one of four different filters, spanning approximate wavelength ranges of 2.4-3.1 μm, 2.4-4.0 μm, 3.1-4.0 μm, and 3.9-5.0 μm. The resolution of these grism observations varies as a function of wavelength, with resolutions of $R \simeq 1100$ at 2.4 μm up to $R \simeq 1700$ at 5.0 μm, a significant increase over the current *HST* Wide-Field Camera 3 resolution of $R \sim 200$ (Bohlin and Deustua 2019). However, previous observations with *HST* (e.g. Kreidberg 2015) have demonstrated that binning of the spectra are necessary to improve the precision of transit depth measurements, reducing its practicable resolution. As a result, all *JWST* spectra may also require similar binning, and its achievable resolution for transmission or emission spectra observations may be reduced.

The NIRSpec instrument also hosts a variety of spectroscopic capabilities in the near-infrared, however these span a slightly broader wavelength range than NIRCam of 0.6-5.3 μm. All of these observations are performed in the Bright Object Time Series (BOTS) mode, which utilises a specialised 1.6"x1.6" aperture to reduce the effects of slit light losses. NIRSpec provides a diverse range of disperser and filter combinations that can be used to probe different regions of wavelength space. Specifically, there are four combinations that can be used at either a medium ($R \sim 1000$) or high ($R \sim 2700$) resolution across approximately 0.8-1.3 μm, 1.0-1.8 μm, 1.7-3.0 μm, or 2.9-5.1 μm, in addition to a low resolution Prism ($R \sim 100$) mode spanning the full 0.6-5.3 μm range. Whilst the lowest resolution mode seems superior it terms of observing efficiency, it saturates more quickly than the other modes and is therefore not practical for every transiting exoplanet target.

The NIRISS instrument only has one mode that is directly compatible with direct imaging observation, Single Object Slitless Spectroscopy (SOSS). The SOSS mode spans

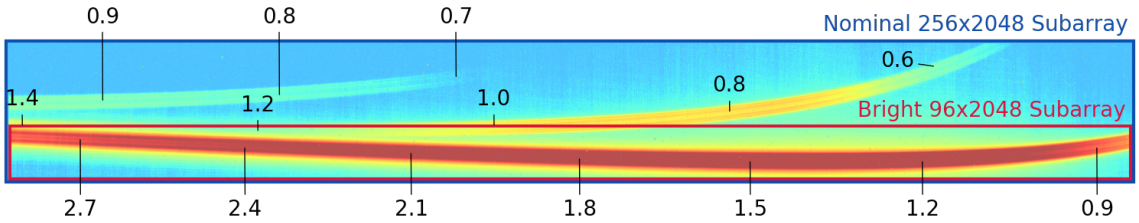

Figure 1.21: Example NIRISS SOSS spectrum as obtained during observatory testing, wavelength in microns at specific dispersion points are marked. Credit: STSci.

a wavelength range of 0.6-2.8 μm across two cross-dispersed spectral orders at a modest resolution of (R~700). A particularly interesting consideration for NIRISS is its unique and complex spectral dispersion (Figure 1.21). These distinct and overlapping spectral orders mean that data analysis will be considerably more complex and will likely be the most immediate challenge to performing transit observations with this mode.

The final instrument, MIRI, is the only instrument with observational capabilities at wavelengths beyond 5 μm. Whilst nominally MIRI can reach wavelengths up to ~28 μm, for transit observations the only practical spectroscopic observing mode is slitless Low Resolution Spectroscopy (LRS) from 5-12 μm at a resolution of R~ 40 at 5 μm up to R~ 160 at 10 μm. Spectroscopy beyond 12 μm can only be achieved used the MIRI Medium Resolution Spectroscopy (MRS) Integral Field Units (IFUs). Transit observations with IFUs have been particularly difficult in the past (Angerhausen et al. 2006) and therefore standard MIRI photometry will likely be the only way to characterise exoplanetary atmospheres with *JWST* beyond 12 μm.

Whilst MIRI is clearly the instrument of choice beyond 5 μm, in the near-infrared it is much more difficult to know which instrument or mode is best suited for a given observation. A robust assessment of which mode is most optimal will require on-sky observations, where the true systematic intricacies of each instrument can be understood. However, in an effort to predict which mode is most scientifically profitable Batalha and Line (2017) have performed an information content analysis of *JWST* transit specific modes. They find that in general, a combination of the NIRISS SOSS and the NIRSpec grating from 2.9-5.1 μm is optimal for scientific return, however if the target is faint enough the NIRSpec Prism can be used as a more efficient alternative.

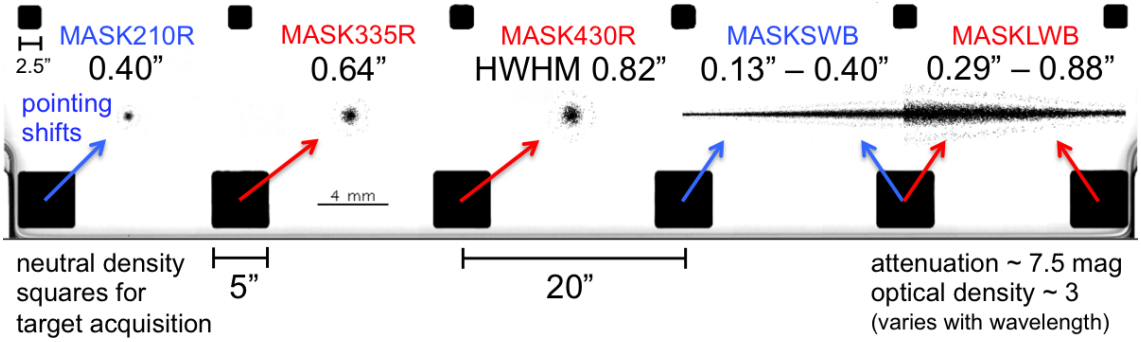

Figure 1.22: The five NIRCam coronagraphic masks, with half-width half-maximum inner working angles labelled. Blue corresponds to those masks that can be used at short wavelengths (<2.4 μm) whilst red corresponds to those masks that can be used at long (>2.4 μm) wavelengths. Credit: STSci.

1.5.3 Direct Imaging of Exoplanets with JWST

Similarly to transiting exoplanets, each of *JWST*'s instruments possesses an observing mode that can be used for direct imaging observations of exoplanets. However, given the significant challenges inherent to these observations, the most suitable observing modes will be those that are photometric in nature and will therefore be the focus of this section. The NIRCam instrument will be the primary workhorse instrument towards directly imaging exoplanets in the near-infrared due to its coronagraphic capabilities. NIRCam has five unique coronagraphic masks as displayed in Figure 1.22, three of which are tuned to be used with 12 different filters from 2.4-5.0 μm, with the remaining two compatible with the five different short wavelength filters from 1.6-2.4 μm. There is further variation amongst these masks: two are of a bar design to improve the achievable inner working angle, whilst three are of a spot design to reduce the total obscured detector area. Unlike standard coronagraphic designs, there are no “spiders” necessary to hold the coronagraphic masks in the focal plane as they are built directly into a transparent substrate material. A robust discussion of the sensitivity limits for NIRCam coronagraphic observations is presented in Chapter 4.

The primary method for characterising directly imaged planets with NIRSpec is through IFU spectroscopy. The IFU observations are performed over a 3"x3" field of view and enable both spatial and spectral information to be obtained simultaneously. Similarly to the NIRSpec BOTS mode outlined earlier, these observations can be performed in a wide range of filter and disperser combinations. To reiterate, there are four combina-

tions that can be used at either a medium (R~1000) or high (R~2700) resolution across approximately 0.8-1.3 μm, 1.0-1.8 μm, 1.7-3.0 μm, or 2.9-5.1 μm, in addition to a low resolution Prism (R~100) mode spanning the full 0.6-5.3 μm range. Although the NIRSpec IFU offers powerful capabilities towards the spectral characterisation of exoplanets, as it has no coronagraph it can only be used for those objects sufficiently separated from their host star that the diffuse stellar light does not greatly impact the underlying noise. As the sample of directly imaged planets is already relatively modest, the necessity that an object is significantly separated likely means that the NIRSpec IFU will likely remain a more niche, but still powerful, mode for exoplanetary characterisation.

NIRISS has a unique capability towards the direct imaging of exoplanets with its aperture masking interferometry (AMI) mode. AMI turns *JWST* into a makeshift interferometer by placing an opaque mask with seven holes into the path of the incoming light. This produces an interferogram on the detector which can later be converted to an image of the target object. Whilst this mask greatly suppresses the number of detected photons, interferometry allows objects at much closer separations to be resolved. Specifically, the AMI mode is capable of imaging exoplanetary companions separated by 0.07"-0.4" that are approximately 9 magnitudes fainter than their host star. Whilst this range may seem comparable to the shorter wavelength NIRCam coronagraphic inner working angles, NIRISS only operates at longer wavelengths through three filters at ~3.8, 4.3 and 4.8 μm. At these wavelengths the NIRCam inner working angles are much larger and as such NIRISS AMI is the best mode for observations of the closest separation companions. However, its sensitivity is less than that of NIRCam or MIRI and will therefore not be able to detect the lowest mass objects.

Much like NIRCam, MIRI's primary ability to image exoplanets comes through its coronagraphic modes. MIRI has four unique coronagraphs, each tied to a specific filter at 10.65, 11.40, 15.50, or 23.00 μm. Unfortunately, the coronagraphic mask at 23 μm has a very large inner working angle of 2.16" which is generally unsuitable for imaging of exoplanetary companions and therefore *JWST* coronagraphic observations are limited to below ~15.50 μm. A robust discussion of the sensitivity limits for MIRI coronagraphic observations is also presented in Chapter 4. Much like NIRSpec, MIRI has IFU capabili-

ties through its Medium Resolution Spectroscopy (MRS) mode. Whilst this mode could potentially be able to spatially resolve and characterise a sufficiently separated companion exoplanet, the limited potential sample of objects that can be observed this way prevents the MRS from being a workhorse mode for *JWST* exoplanet characterisation.

In general, the picture for which mode is most optimal for a desired direct imaging observation of an exoplanet is much clearer than for transiting exoplanet observation. In almost all cases, characterisation and detection efforts should be performed with NIRCam and MIRI due to their coronagraphic capabilities. However, if it is preferable to trade sensitivity towards the lowest mass exoplanets for an improved inner working angle the NIRISS AMI mode should be used at near-infrared wavelengths. Finally, if a target companion was known to be sufficiently separated from its host star that stellar flux contamination would not be an issue, the NIRSpec and MIRI IFU spectroscopic modes would provide the best characterisation potential.

1.5.4 Potential Advancements

The previously outlined capabilities of *JWST* demonstrate that it will be an exceptional tool for the detection and characterisation of exoplanetary objects. Even though it is not possible to precisely predict the exact scientific achievements *JWST* will make ahead of time, by understanding and forecasting its expected capabilities it is possible to ascertain some of the developments it may bring to the field of exoplanetary science in particular.

1.5.4.1 Infrared Observations of Exoplanets

The ability of *JWST* to observe in the near- to mid-infrared is vital for future detections of lower mass exoplanets through direct imaging. Towards the infrared, stellar emission begins to dramatically reduce whilst the exoplanetary emission begins to peak due to their different effective temperatures. As a result, the overall contrast between a star and an exoplanet is its lowest at these wavelengths, making separating the emitted planetary flux from the stellar noise much easier. This is particularly important for objects at cooler temperatures, as the peak of their blackbody spectral energy distributions lie the furthest into the infrared and are therefore particularly difficult to detect at shorter wavelengths

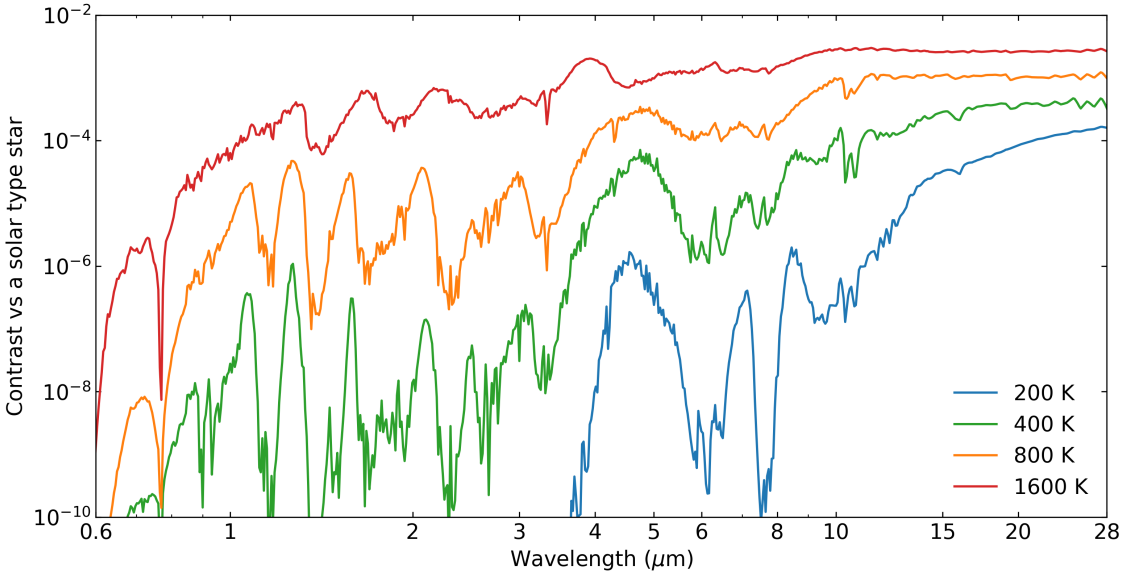

Figure 1.23: The contrast ratio for a Jupiter-like object orbiting a solar type star. Towards the near- to mid-infrared the contrast is greatly reduced due to the drastically reduced stellar emission at these wavelengths. Plot generated using the `ATMO` models of Phillips et al. (2020) and the `PHOENIX` stellar models of Husser et al. (2013).

(Figure 1.23). Whilst the temperature of a planetary mass object can depend on a variety of properties such as its age, separation, evolution, and stellar irradiation, at young ages the temperature of a planet primarily increases as a function of its mass due to the larger amounts of energy released from the gravitational infall of material during formation. Therefore, the infrared not only opens the door to the direct characterisation of cooler objects, but also of objects at a lower mass. As direct imaging observations have thus far been limited to observations of multiple-Jupiter mass objects, *JWST* will image the lowest mass exoplanets to date. A detailed discussion and analysis of these capabilities is presented in Chapter 4.

Currently, the combined capabilities of ground- and space-based observations of exoplanets can typically only provide spectroscopy below ~2 μm and photometry out to ~5 μm. Therefore, the spectroscopic capabilities of *JWST* will enable the first detailed characterisations of exoplanetary atmospheres at near- to mid-infrared wavelengths rich with spectral features, as demonstrated by Figures 1.7, 1.9, 1.18, and 1.23. The ability to characterise such a broad wavelength range has significantly diverse implications for our overall understanding of exoplanetary atmospheres, a subset of which are discussed in the following sections.

1.5.4.2 Planetary Evolution and Formation

One primary advantage that *JWST* will provide is the ability to detect and measure the strength of infrared spectroscopic features resulting from dominant carbon bearing species such as CH_4, CO_2, and CO for the first time. Such measurements are vital to accurately and precisely measure the C/O ratio of an exoplanetary atmosphere, which could potentially act as an indicator for the overall planetary formation and evolution.

Currently there are two primary suggested pathways for planetary formation: core accretion (Pollack et al. 1996) and gravitational instability (Boss 1997). In brief, core accretion proceeds through the coalescence of solid dust grains into planetesimals followed by pairwise collisions into protoplanets, and potential runaway gas accretion into gas giants. The second pathway is similar to the formation of stars and brown dwarfs, in this case gravitational instabilities far out in the protoplanetary disk can lead to fragmentation and an immediate accumulation of a large of amount of material capable of forming a planet. These formation pathways have distinct interactions with solids and gas in the protoplanetary disk and as such will uniquely affect the resulting atmospheric C/O ratio (Öberg et al. 2011; Öberg and Bergin 2016) (Figure 1.24). Generally, it is expected that stellar C/O ratios correspond to planets formed via gravitational instability, where all material is mixed during formation, or for all planets forming very close to the host star, where all the volatile species are in the gas phase. A sub-stellar C/O ratio could be an indicator that a large amount of icy solids polluted the atmosphere following gas accretion. Finally, super-stellar C/O ratios are consistent with planetary formation outside of the water snowline (Öberg et al. 2011).

In reality these connections between C/O ratio and planetary formation may not be so simplistic, and events throughout a planet's history such as outwards or inwards migration, collisions, or atmospheric escape could significantly affect the atmospheric composition. However, patterns in the C/O ratio may be evident across the full exoplanetary population. Specifically, how do the C/O ratios of the massive, wide separation, directly imaged exoplanets compare to the transiting exoplanet population? Or, how does the C/O ratio vary amongst the hot Jupiter population, and is it indicative of their migration history? With *JWST*, the first steps towards answering these questions can be made.

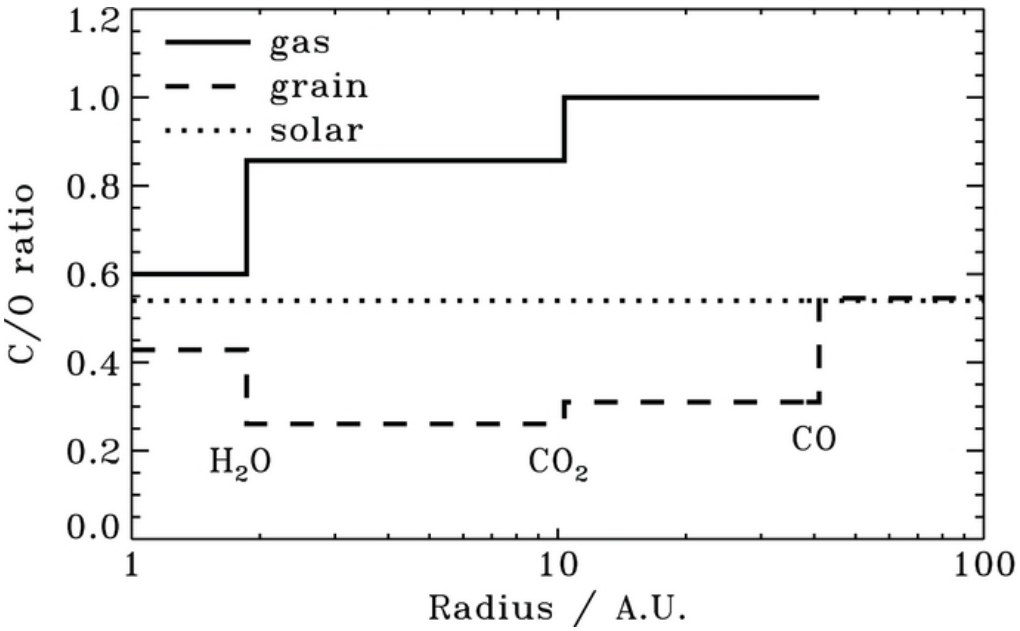

Figure 1.24: The C/O ratio of the gas and grain material within a protoplanetary disk as a function of orbital radius, molecular snow lines are marked by their respective molecule. Figure from Öberg et al. (2011).

1.5.4.3 Cloud and Haze Aerosol Species

Current observations have demonstrated that the presence of cloud or haze species can have significant effects on the overall atmospheric spectrum. In transmission spectroscopy observations this is primarily observed through a steep optical slope attributed to haze, or broad wavelength muting attributed to clouds. On the other hand, when observing via emission spectroscopy or direct imaging, the effects are primarily seen through the redistribution of flux from shorter to longer wavelengths. Importantly, all of these described effects are indirect measures of the presence of clouds or haze, and to robustly constrain their properties it is necessary to explicitly measure absorption from their constituent molecular species. Unfortunately, both the most commonly predicted haze species (hydrocarbons) and cloud species (silicates) do not exhibit significant absorption features at currently examinable wavelengths.

With *JWST* the characterisation of haze species will be expanded primarily through its ability to constrain the molecular abundance of haze precursor species at infrared wavelengths. It is most commonly suggested that the haze species within exoplanetary atmospheres are formed via photodissociation of atmospheric species such as CH_4 and HCN by the incident stellar UV flux. This dissociation enables the formation and enrichment

of more complex species such as C_2H_2, C_2H_4, and C_2H_6 (e.g. Yung et al. 1984; Moses et al. 2011; Morley et al. 2013). Performing spectroscopic observations in the infrared with *JWST* will enable more precise constraints on the haze precursor species such as CH_4 and HCN. Specifically, it is predicted that these features may be somewhat muted compared to a haze-free atmosphere due to their dissociation (Kawashima et al. 2019).

Whilst clouds produce a primarily grey muting effect to transmission spectra at currently observable wavelengths, it is predicted that towards the mid-infrared it will be possible to observe actual absorption from the cloud species themselves (Wakeford and Sing 2015). Commonly predicted silicate cloud species such as SiO, SiO_2, $MgSiO_3$, and $MgSiO_4$ in particular display absorption at ~9-12 microns (e.g. Wakeford and Sing 2015; Lines et al. 2018a, Figure 1.25). As a result, *JWST* MIRI observations will likely offer the first ever direct observations of exoplanetary clouds. A more thorough description of this predicted cloud absorption and *JWST* capabilities is presented in Chapter 3. Such features will likely also be observable in both emission spectroscopy and direct imaging observations both directly through this silicate absorption, but also indirectly due to cloud driven flux redistribution (Morley et al. 2012; Charnay et al. 2018).

1.5.4.4 Broad Spectroscopic Coverage, Variability, and Stellar Activity

A subtle advantage of *JWST*'s spectroscopic modes is that they enable characterisations across broad (a few μm) regions of wavelength space within a single observation. Current characterisations of exoplanetary atmospheres are typically piecemeal, with the underlying observations being made by multiple instruments, at vastly different epochs, with wavelength ranges of less than 1 μm in scale. As we know from the solar system, planetary atmospheres evolve over time and are not static, and therefore piecing together multiple epoch observations may not be entirely correct. Furthermore, there is often no spectroscopic overlap between these observations. As a result there may be systematic induced offsets between different portions of the data, limiting our ability to accurately compare to forward models. With *JWST*, different epoch observations will still be necessary, however the spectroscopic modes of *JWST* share significant wavelength overlaps, allowing for the correction of these potential systematic offsets. An example of this overlap is shown in Figure 1.26.

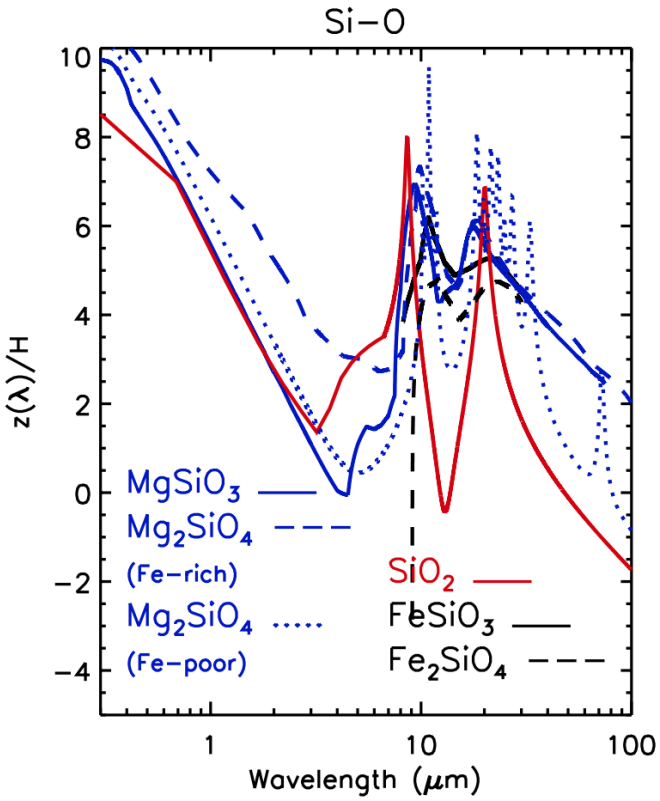

Figure 1.25: Model transmission spectra based on the hot Jupiter exoplanet HD 189733b with absorption from different silicate cloud species included. Figure from (Wakeford and Sing 2015).

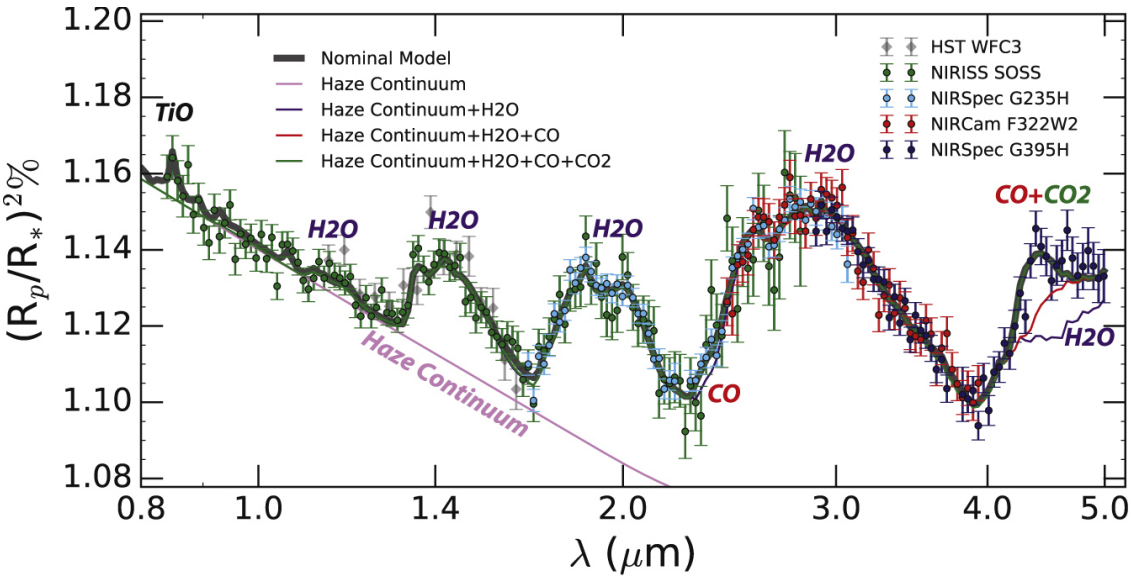

Figure 1.26: *JWST* observations of the exoplanet WASP-79b as part of the Transiting Community Early Release Science Program, clear overlap between different spectroscopic modes can be seen. Figure from Bean et al. (2018).

This broad coverage and spectroscopic overlap also aids observations of exoplanets around relatively active host stars. Spots on the stellar surface act to modulate the overall emitted stellar flux as a function of wavelength, with potentially significant implications for the study of transiting exoplanet atmospheres (e.g. Rackham et al. 2017; Alam et al. 2018; Carter et al. 2020). With a sufficiently broad wavelength coverage, it will therefore be much easier to characterise and correct for these effects. A more detailed discussion of this effect is provided in Chapter 2. Furthermore, given that the stellar spot coverage likely also varies over time, similarly to the sun, this may introduce epoch dependent variations in the overall transmission spectrum. Due to the spectroscopic overlap of *JWST* modes it may also be possible to identify if such variations occur and account for them.

1.6 Chapter Overview

In this thesis, I present a collection of studies towards the characterisation and detection of exoplanets, with a focus towards the future with *JWST*. In Chapter 2, I present the most up-to-date transmission spectrum of the hazy hot Jupiter WASP-6b, identifying it as a favourable *JWST* target. In Chapter 3, I describe an ensemble of transiting exoplanet modelling efforts and their implications for future observations with *JWST*. In Chapter 4, I present the latest simulations of *JWST* coronagraphy and provide specific predictions for its overall mass sensitivity as a function of host star separation. At the start of each of these chapters I detail my contribution to the respective work, in addition to any significant co-author contributions. Finally, I provide a conclusion and summary in Chapter 5.

Chapter 2

The Complete Transmission Spectrum of WASP-6b

2.1 Statement of Contribution

Chapter 2 has previously been published in (Carter et al. 2020). In this work, A. L. Carter led the data analysis and interpretation, and wrote the manuscript. T. M. Evans and N. Nikolov provided template data reduction codes which were adapted, heavily built upon, and utilised by A. L. Carter. G. W. Henry performed the stellar activity monitoring with *AIT*, M. K. Alam calculated the stellar heterogeneity correction, and D. K. Sing performed the retrieval analysis.

2.2 Introduction

Transiting exoplanets currently present one of the best options towards studying the atmospheres of planets outside of the Solar System through observations of wavelength-dependent variations in their apparent radii as they occult their host star. These variations are intrinsically linked to the composition and structure of an exoplanetary atmosphere, as the starlight transmitted through the planetary limb is strongly modulated by the wavelength dependent opacities of its constituent molecular species (Seager and Sasselov 2000). Tracing these variations as a function of wavelength, known as transmission

spectroscopy, has already been successfully applied across a range of both ground- and space-based observatories, unveiling a host of atomic and molecular species in the atmospheres of exoplanets (e.g. Charbonneau et al. 2002; Redfield et al. 2008; Snellen et al. 2008; Sing et al. 2011a; Deming et al. 2013; Spake et al. 2018; Evans et al. 2018) as well as providing strong insights into their bulk atmospheric properties (e.g. Madhusudhan et al. 2011a; Evans et al. 2017; Wakeford et al. 2018). In particular, Sing et al. (2016) show a large diversity in the atmospheres of a sample of ten hot Jupiter exoplanets, revealing a continuum in the obscuring effects of haze and clouds on molecular absorption features present in their transmission spectra. Of the ten exoplanets displayed by Sing et al. (2016), WASP-6b and WASP-39b were lacking in near-infrared observations between 1-2 μm, a region abundant in potential water absorption features. Wakeford et al. (2018) reported such observations for WASP-39b, providing a strong constraint on the water abundance in its atmosphere. In this study we present these observations for WASP-6b, completing the search for water absorption features across this sample of exoplanets.

Space-based observations, such as those performed with the *Hubble Space Telescope* (*HST*) and *Spitzer*, have thus far proven to be the most prolific method towards the broad spectrophotometric characterisation of exoplanet atmospheres (e.g. Charbonneau et al. 2002; Deming et al. 2013; Sing et al. 2016). However, ground-based characterisation through multi-object differential spectrophotometry with the *Very Large Telescope* (*VLT*) FOcal Reducer and Spectrograph (FORS2) (Appenzeller et al. 1998), has recently been able to produce *HST*-quality transmission spectra for a variety of exoplanets (Bean et al. 2011; Nikolov et al. 2016; Gibson et al. 2017; Sedaghati et al. 2017; Nikolov et al. 2018). As part of a small survey to test the performance of FORS2 and assess the validity of previously observed spectroscopic features with *HST*, the optical spectra of WASP-31b, WASP-39b and WASP-6b have been observed. In the case of WASP-39b and WASP-31b, these results have already been reported in Nikolov et al. (2016) and Gibson et al. (2017) respectively. In this study we report the results for WASP-6b, the final target from our ground-based comparative program.

WASP-6b is an inflated hot Jupiter with a mass of 0.485 $M_{\rm Jup}$, a radius of 1.230 $R_{\rm Jup}$ and an equilibrium temperature of 1184 K (Tregloan-Reed et al. 2015) discovered by the

Wide Angle Search for Planets (*WASP*) ground-based transit survey (Pollacco et al. 2006; Gillon et al. 2009). WASP-6b orbits with a period of $P \simeq 3.36$ d at a separation $a \simeq 0.041$ AU around a mildly metal-poor G8V star (Gillon et al. 2009; Tregloan-Reed et al. 2015). Ibgui et al. (2010) demonstrate that the planet's inflated radius could be due to tidal-heating brought on by a non-zero eccentricity reported in Gillon et al. (2009). Whilst further radial velocity data from Husnoo et al. (2012) demonstrated that this eccentricity is not significantly non-zero, as initially inferred, it does not necessitate a circular orbit and as such the true cause of the inflation has yet to be definitively determined. Doyle et al. (2013) refine the bulk properties of the host star WASP-6 through spectroscopy, providing measurements of $T_{\rm eff}$ = 5375 ± 65, log(g) = 4.61 ± 0.07 and [Fe/H] = -0.15 ± 0.09. Finally, Tregloan-Reed et al. (2015) demonstrated that fluctuations in multiple transit light curves of archival photometry of WASP-6b could be attributed to a single star spot anomaly. This enabled a more precise measurement on the sky-projected spin-orbit alignment of $\lambda = 7.2° \pm 3.7°$ in agreement with Gillon et al. (2009).

The atmosphere of WASP-6b was initially probed spectrophotometrically in the optical with the ground-based IMACS instrument on the 6.5-m *Magellan Telescope* by Jordán et al. (2013) who observed a decrease in transit depth as a function of wavelength, characteristic of a scattering haze, and no evidence of the Na I and K I absorption lines. Subsequent observations performed in the optical with *HST*'s Space Telescope Imaging Spectrograph (STIS) and *Spitzer*'s InfraRed Array Camera (IRAC) (Nikolov et al. 2015) also demonstrated evidence of a scattering haze, however the Na I and K I lines were resolved in this case with significance levels of 1.2σ and 2.7σ respectively. WASP-6b's atmosphere has also been observed at secondary eclipse as the planet passes behind its host star from our point of view with *Spitzer* IRAC, providing day side temperature estimates of 1235^{+70}_{-77} K and 1118^{+68}_{-74} K for the 3.6 and 4.5 μm channels respectively (Kammer et al. 2015).

We present new spectrophotometric observations from 1.1 to 1.7 μm using the *HST* Wide Field Camera 3 (WFC3) instrument with the G141 grism for the exoplanet WASP-6b, the final object in the Sing et al. (2016) study without observations in this wavelength range. Additionally, we present new spectrophotometric observations from 0.4 to 0.8 μm performed from the ground using *VLT* FORS2. Recent photometric observations of WASP-

6b performed from space with the Transiting Exoplanet Survey Satellite (*TESS*) (Ricker et al. 2014) are also included in our study. These datasets were analysed in tandem with a reanalysis of the archival STIS and *Spitzer* datasets on a common Gaussian Process (GP) framework (Gibson et al. 2012b). We also perform light-curve corrections to account for the effects of stellar heterogeneity on the perceived transmission spectrum of WASP-6b, the presence of which can act to mimic the signatures of scattering hazes (McCullough et al. 2014; Rackham et al. 2018; Pinhas et al. 2018; Alam et al. 2018; Rackham et al. 2019).

Descriptions of our observations and the necessary data reduction are shown in Section 2.3. All light curve fitting and analysis is presented in Section 2.4. An accounting of the effects of stellar heterogeneity is shown in Section 2.5. The resultant transmission spectra and the conclusions drawn from them using both forward and retrieval based models are described in Section 2.6. Finally, we summarise our results in Section 2.7.

2.3 Observations and Data Reduction

2.3.1 *VLT* FORS2

We obtained observations of two primary transits of WASP-6b using the *VLT* FORS2 GRIS600B (G600B) and GRIS600RI (G600RI) grisms in multi-object spectroscopy mode on 2015 October 3 and 2015 November 9 respectively as part of program 096.C-0765 (PI: Nikolov). These observations utilise a mask with broad slits centred on WASP-6 and a nearby reference star (2MASS J23124095-2243232), all slits had a width of 25", the slit lengths used in the G600B and G600RI observations were 31" and 90" respectively. On the night of the G600B observations conditions began clear (less than 10 per cent of the sky covered in clouds, transparency variations under 10 per cent) and moved to photometric (no clouds, transparency variations under 2 per cent) approximately half way through the observations. The exposure time was set at 100 seconds per exposure for a total of 152 exposures. During this night observations were halted for ~30 minutes during transit ingress as the target passed through the zenith and was outside the observable region of the telescope. On the night of the G600RI observations, conditions began clear but moved to photometric for the bulk of the observation and the exposure time was set to 60 seconds per exposure for a total of 184 exposures. Towards the end of the transit an earthquake

caused a guide star loss and as such observations were halted for ~15 minutes.

We begin the data reduction by performing bias- and flat-field corrections on the raw data frames, followed by cosmic ray correction using two iterations of the `L.A.Cosmic` algorithm (van Dokkum 2001). Background flux subtraction for each spectrum was conducted using the median of a box of pixels outside of each spectral trace. Spectra were then extracted using the `APALL` procedure within the `IRAF` package (Tody 1993). Aperture widths for the spectral extraction were varied and values of 14 and 15 pixels were selected as they minimised the dispersion in the out-of-transit flux for the G600B and G600RI white light curves respectively. We produce a wavelength solution for both observations using the spectra of an emission lamp taken with the calibration mask following each observation. In particular, a low-order Chebyshev polynomial was fit to a multitude of emission lines, the centres of which were determined through individual Gaussian fits. This wavelength solution was then applied to a single data frame to produce a reference spectrum for each observation. Finally, each extracted spectrum was then cross-correlated against its respective reference to account for sub-pixel shifts in the dispersion direction, the maximum resultant shifts were ~1.2 pixels and ~0.3 pixels for the G600B and G600RI datasets respectively. Representative spectra of both WASP-6 and the reference star are shown in Figure 2.1 for both the G600B and G600RI observations.

2.3.2 *HST* WFC3

A primary transit of WASP-6b was also observed using the *HST* WFC3 G141 grism on 2017 May 6 as part of General Observer (GO) program 14767 (PI: Sing and López-Morales). All exposures were taken in sequence across five *HST* orbits, with 13 exposures per orbit, except for the first orbit which only consisted of 10 exposures. Each exposure was performed in forward spatial scanning mode (McCullough and MacKenty 2012), where the telescope slews in the cross dispersion axis during the exposure, allowing for longer exposure times whilst avoiding saturation on the detector. For the first orbit the exposure times were set to ~184 seconds, whilst the remaining orbits had exposure times of ~138 seconds. All exposures employed the SPARS25 readout mode and used a scan rate of ~0.46 pixels per second.

Reduction of the spectra began with the `.ima` files output from the `CALWF3` pipeline. Each `.ima` file contains multiple reads for each individual spatial scan, up to the final full scan image. We do not however perform spectral extraction on the final frame of each scan but rather the sum of differenced frames, following Deming et al. (2013). This has the advantage of reducing the impact of cosmic rays and hot pixels, whilst also reducing the overall sky background. For each differenced read, pixels beyond a mask of 35 pixels above and below the centre of the spectral trace were zeroed before extraction of the differenced frame following (Evans et al. 2016). Finally, we then sum all of the differenced frames for each spatial scan to produce a final differenced frame scan. To perform cosmic ray correction these frames were stacked into a single cube so that the variation of each pixel could be tracked as a function of time. Each pixel was smoothed temporally with a Gaussian filter and pixel deviations between this and the initial datacube larger than 8σ were flagged as cosmic rays. Static bad pixels were also flagged by searching for deviations greater than 10σ between each individual unsmoothed pixel and the median of a span of 5 pixels in the cross-dispersion direction, centred on the initial pixel. These cosmic rays and static pixels were then replaced by a linear interpolation of the pixel to the PSF of the same median span. Using a second mask of 50 pixels above and below the centre of the final scans, the 2D spectra were summed along the cross-dispersion axis to produce a 1D spectrum for each scan. This mask width was selected as it provided the minimal white light curve out-of-transit scatter across a range of 30 to 80 pixels in steps of 5 pixels. The background was subtracted from each spectrum using the median of a box of pixels in a region of the detector unpolluted by the diffuse light from the edges of the spatial scan.

Wavelength solutions were obtained by cross-correlating each individual spectrum with an `ATLAS`[1] (Kurucz 1993) stellar spectrum, with parameters similar to WASP-6 (T_{eff}=5500K, log(g)=4.5, [M/H]=-0.2), convolved with the throughput of the G141 grism. Before cross-correlation, both spectra were smoothed with a Gaussian filter to inhibit the effects of spectral lines and focus the correlation on the steep edges of the G141 throughput. This process revealed shifts in the dispersion direction across the course of observation within ~0.12 pixels. An example 1D spectrum from the G141 observations is shown in Figure 2.1.

1. http://kurucz.harvard.edu/

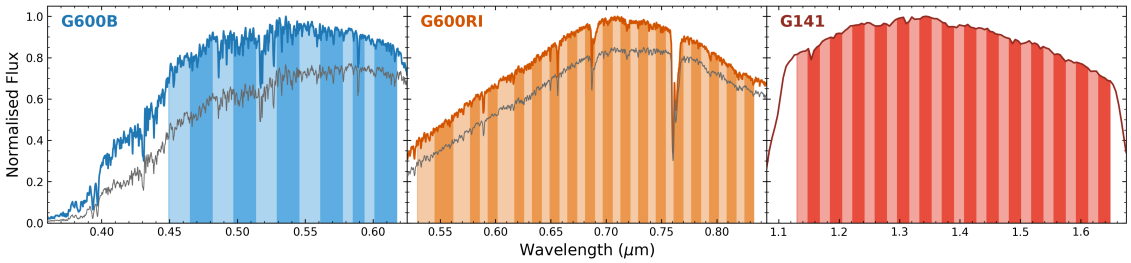

Figure 2.1: Representative observed spectra for the FORS2 G600B, FORS2 G600RI and WFC3 G141 grisms, the thicker coloured lines indicate spectra of WASP-6 whilst thinner grey lines correspond to that of the reference star, both target and reference spectra are normalised to the maximum of the target spectrum for that observation. Shaded bands indicate the selected wavelength binning for each grism.

2.3.3 *TESS*

The *Transiting Exoplanet Survey-Satellite* (*TESS*) is currently performing an all sky search for transiting exoplanets in a single broadband filter from 0.6 to 1.0 μm (Ricker et al. 2014). Due to the broad $24° \times 96°$ field of view, *TESS* holds enormous potential not only for discovering new exoplanets, but also observing transits of already known transiting systems. With the public release of the *TESS* Sector 2 data, 7 clear transits of WASP-6b can be readily identified from 2018 Aug 23 to 2018 Sep 19.

To obtain the *TESS* light curve spanning this time period we initially used the pre-calibrated and extracted light curve held in the `lc.fits` file. However, on closer inspection we found indications of a non-optimal pipeline correction and as such choose to perform our own correction on the uncorrected light curve in the same file. We follow a Pixel Level Decorrelation (PLD) systematics removal method on the raw data as implemented by the `lightkurve` python package (Lightkurve Collaboration et al. 2018). Rather than explicitly correlate overall systematic variations in the stellar brightness to variations in the estimate of the centroid of the stellar PSF, the PLD technique instead relies on variations in the individual pixel flux intensities. This technique has clear advantages through it ability to account for red noise and flat fielding inaccuracies, and has already been used successfully as a systematics correction technique on both *Spitzer* (Deming et al. 2015) and K2 data (Luger et al. 2016; Luger et al. 2018). Finally, to prepare for the transit light curve analysis, we extract seven separate portions from the complete light curve, each centred on one of the observed transits. Each individual extracted light curve spans from roughly 5 hours pre-transit to 5 hours post transit to facilitate an effective out-of-transit baseline

determination.

2.3.4 Archival Data

In order to fully exploit the data that are available to us we opt to perform a reanalysis of the previously reported *HST* STIS and *Spitzer* IRAC data (Nikolov et al. 2015). Specifically, there were two spectroscopic transit observations with the STIS G430L grism from 0.33-0.57 μm, one spectroscopic transit using the STIS G750L grism from 0.55-1.03 μm, and one photometric transit for each of the *Spitzer* IRAC 3.6 and 4.5 μm bandpasses. Performing such a reanalysis can account for transit depth baseline offsets between these datasets and those in this study by fitting all light curves under a common set of prior system parameters. Furthermore, the implementation of a stellar heterogeneity correction, and its changes to the system parameters (Section 2.5) necessitates further light curve fitting. A complete reanalysis ensures that any comparisons between the spot corrected and uncorrected datasets are not influenced by the differing light curve fitting methodologies of this study and that of Nikolov et al. (2015).

With respect to the data reduction of the observations themselves, all light curves were extracted following the same methodology outlined in Nikolov et al. (2015). For the STIS data this involves spectral extraction following the `APALL` procedure in `IRAF` (Tody 1993), and photometry is performed for the *Spitzer* data through time-variable aperture extraction. For the *Spitzer* IRAC light curves there are thousands of independent photometric measurements throughout each observation and to reduce the computational intensity of the light curve fitting procedure described in Section 2.4 we bin each light curve into 1000 bins, corresponding to a cadence of ~15 and ~16 seconds for the 3.6 and 4.5 μm bands respectively.

2.4 Light Curve Analysis

White light curves for the G600B, G600RI and G141 datasets were produced by summing the flux for each individual spectrum along the dispersion axis from 0.449 to 0.617 μm, 0.529 to 0.833 μm, and from 1.0 to 1.8 μm respectively. Spectrophotometric light curves were produced for the G600B, G600RI, and G141 datasets by summing the flux within 12,

34, and 28 respective bins across the wavelength ranges displayed in Figure 2.1.

Below ~ 0.45 μm the G600B flux levels are the lowest of both of the FORS2 datasets and inherently contain a limited amount of information due to the higher photon error. Whilst using a larger bin size could alleviate this, the contribution of differential extinction due to a spectral type mismatch between the target and reference must also be considered. In the case of our observations such a mismatch is evident in the different spectral profiles of the target and reference star in Figure 2.1. The flux of the reference star from 0.40 to 0.45 μm is 50% that of the target, whereas at 0.6 μm this value is 80%. Therefore, the data below 0.45μm not only contain the lowest flux levels of our FORS2 observations, but their accuracy is impacted the most by the differential extinction. Furthermore, including such a wavelength range would also impart further differential extinction effects on every other spectrophotometric bin in the G600B dataset due to the nature of the common-mode, white-light correction performed during the light curve fitting. In an effort to mitigate the impact of differential extinction on our final transmission spectra we therefore choose to exclude the G600B data below ~0.45 μm.

In the case of the G600B and G600RI observations, all light curves were also produced for the reference star. Before fitting any of the G600B or G600RI light curves, we first correct for dominant atmospheric effects by dividing the raw flux of the target by that of the corresponding wavelength range reference. The spectrophotometric bins for all observations are displayed in Figure 2.1. As the *TESS* observations are photometric they hold no spectral information and were treated as white light curves in terms of fitting. Finally, we obtain the archival STIS and *Spitzer* light curves across identical wavelength ranges as described in Nikolov et al. (2015).

During both the G600B and G600RI observations, the target needed to be reacquired and as such all light curves suffer from incomplete phase coverage, this also results in the separate pieces of each light curve exhibiting differing systematic effects. Throughout our analyses we were unable to accurately and effectively account for these systematic offsets due to the significant, or complete, absence of in transit observations for one piece of each light curve. As such, in the analysis presented here we exclude the pre-ingress data for the G600B observation and the post-egress data for the G600RI observation. The first

orbit, and first spectrum of all other orbits, of the G141 observation exhibit much stronger systematics than the other obtained spectra due to charge trapping in the detector (Zhou et al. 2017). We therefore opt to remove these data from our analysis in line with many other studies (e.g. Knutson et al. 2014; Sing et al. 2016; Wakeford et al. 2018; Mikal-Evans et al. 2019) that have been performed since the first spatial scanning WFC3 transit observations were made (Deming et al. 2013).

2.4.1 White Light Curves

To perform all lightcurve fitting we follow Gibson et al. (2012b), accounting for the transit and instrumental signals simultaneously by treating the data for each light curve as a Gaussian process (GP) using the Python library `George` (Ambikasaran et al. 2014). GP fitting methodologies have been successfully applied to a range of transit observations (Gibson et al. 2012b; Gibson et al. 2012a; Gibson et al. 2017; Evans et al. 2013; Evans et al. 2015; Evans et al. 2016; Evans et al. 2017; Evans et al. 2018; Mikal-Evans et al. 2019; Cartier et al. 2017; Kirk et al. 2017; Kirk et al. 2018; Kirk et al. 2019; Louden et al. 2017; Sedaghati et al. 2017) from both the ground and space and enable the measurement of the systematic signal without assuming any prior knowledge on its functional form. We obtain the best fit model to each light curve by marginalising over the constructed GP likelihoods using Markov chain Monte Carlo (MCMC) as implemented by the Python library `emcee` (Foreman-Mackey et al. 2013). When executing each MCMC, we first initialised a group of 150 walkers near the maximum likelihood solution, identified using a Nelder-Mead simplex algorithm as implemented by the `fmin` function within the `scipy` library. We run a group for 500 samples and then use the best run to initialise a second group of 150 walkers in a narrow space of this solution. This second group was then run for 3000 samples, with the first 500 samples being discarded as burn-in.

We list the individual subtleties for each dataset throughout the GP fitting procedure below, however there are some aspects which remained unchanged regardless of the dataset. For the GP covariance amplitudes of all datasets we utilise gamma priors of the form $p(A) \propto e^{-100A}$ as in Evans et al. (2018) to favour smaller correlation amplitudes and reduce the effects of outliers. Additionally, we follow previous studies and fit for the natu-

ral logarithm of the inverse length scale hyperparameters (e.g. Evans et al. 2017; Gibson et al. 2017; Evans et al. 2018), but limit these quantities with a uniform prior ranging between the cadence of the observation and twice the length of the observation. This prescription encourages the GP to fit the broader systematic variations that occur during the transit, with shorter variations described by white noise and longer variations accounted for by the linear baseline trend. Finally, in all cases the orbital period was held fixed to the value of $P = 3.36100239$ d from Nikolov et al. (2015) and the eccentricity was held fixed to the value of $e = 0.041$ from Husnoo et al. (2012).

2.4.1.1 G600B & G600RI

To describe the mean function of the GP we use the model transit light curves of Mandel and Agol (2002) generated using the `batman` Python library (Kreidberg 2015) multiplied by a linear airmass baseline trend. We initially tested a time baseline trend however found that this restricted the final GP fitting of shorter frequency variations within the light curves, by utilising a linear airmass baseline trend the non-linear sloping of the light curves was better matched and the GP had more freedom to fit these shorter frequency variations. Whilst the observed airmass trend can be included in the GP directly as a decorrelation parameter we found this necessitated stricter priors on the length scale hyperparameters and did not measurably improve the fitting. As such, we opt to include this term through the baseline trend. To construct the covariance matrix of the GP we use the Matérn $\nu = 3/2$ kernel, with time as the decorrelation parameter. Other decorrelation parameters were also tested both individually and in combination such as: spectral dispersion drift, cross-dispersion drift, full-width half maximum, ambient temperature, ambient pressure, and telescope rotation angle. Despite this, no clear correlations were observed and therefore we excluded these parameters from the final analysis.

Unlike the other datasets, for the FORS2 analysis we account for limb-darkening following the two-parameter quadratic law. The treatment is different as these observations were performed from the ground where the Earth's atmosphere acts as an filter for the incoming light. Crucially, the response of the atmosphere is a function of wavelength and varies as a function of the zenith distance, which varies throughout the observations. Instead of making explicit assumptions about this atmospheric transmission and includ-

ing it directly in our determination of the precomputed limb darkening coefficients we choose to fit for the coefficients themselves. We select the quadratic limb darkening law to improve computational efficiency by reducing the number of fit parameters whilst still providing an accurate description for the true limb darkening of WASP-6 given its temperature (Espinoza and Jordán 2016).

For the G600RI observation we allow the transit depth R_p/R_*, inclination i, normalised semi-major axis a/R_*, transit central time T_0, linear trend parameters and quadratic limb darkening parameters c_1 and c_2 to vary throughout the fit. However, in the case of the G600B observation, we found that the paucity of transit coverage provided imprecise determinations of i and a/R_* and as such perform a simpler fit after retrieving the weighted average best fit parameters, see Section 2.4.1.5.

The presence of high frequency variations from ~2-3 hours and ~0-1 hours after mid-transit for the G600B and G600RI light curves, respectively, strongly constrain the hyperparameters of the GP fit which leads to over fitting of other variations within the light curve. To assess the impact on the fit transit parameters we restricted the priors on these hyperparameters such that the high frequency variations could no longer bias the GP fitting. Whilst this significantly reduced the perceived overfitting, we find that all fit transit parameters are unaffected by this change and lie within 1σ of the original fit. Therefore, and in addition to the lack of prior knowledge on these hyperparameters, we opt not to perform such a restriction for any of the final white light curve fits.

2.4.1.2 STIS & G141

The mean function of the GP is described identically to the G600B and G600RI mean functions, except using a linear time baseline trend. To construct the covariance matrix of the GP we use the Matérn $\nu = 3/2$ kernel, with *HST* orbital phase, dispersion shift and cross dispersion shift identified as the optimal decorrelation parameters. Limb darkening was accounted for through the four-parameter non-linear law. During the fitting we allow the transit depth R_p/R_*, inclination i, normalised semi-major axis a/R_*, transit central time T_0 and linear trend parameters to vary throughout the fit and we fixed all four non-linear limb darkening values to values calculated from the ATLAS model described in Section

	Uncorrected	*TESS* Corrected	*AIT* Corrected
i (°)	$88.78^{+0.13}_{-0.13}$	$88.73^{+0.13}_{-0.12}$	$88.72^{+0.013}_{-0.012}$
a/R_*	$11.154^{+0.049}_{-0.072}$	$11.135^{+0.050}_{-0.072}$	$11.123^{+0.050}_{-0.072}$

Table 2.1: Weighted average values of the orbital inclination and normalised semi-major axis for the uncorrected and spot corrected light curve analyses.

2.3, following Sing (2010). Finally, as there are two independent light curves in the STIS G430L observations we performed a joint fit between them, only allowing the transit central time for each light curve to vary independently.

2.4.1.3 Spitzer

The mean function of the GP is described identically to the G600B and G600RI mean functions, except using a linear time baseline trend. We construct the covariance matrix following Evans et al. (2015). Specifically, we construct a kernel $k = k_{xy} + k_t$ where k_{xy} is a squared exponential kernel, with the photometric centroid x and y coordinates as the decorrelation parameters, and k_t is a Matérn $\nu = 3/2$ kernel, with time as the decorrelation parameter. Constructing such a kernel allows us to account for the smooth variations in pixel sensitivities as well as residual correlated noise in the light curve. Limb darkening was accounted for through the four-parameter non-linear law. During the fitting we allow the transit depth R_p/R_*, inclination i, normalised semi-major axis a/R_*, transit central time T_0 and linear trend parameters to vary throughout the fit and we fixed all four non-linear limb darkening values similarly to the STIS and G141 observations.

2.4.1.4 TESS

The mean function of the GP is described identically to the G600B and G600RI mean functions, except using a linear time baseline trend. To construct the covariance matrix of the GP we use the Matérn $\nu = 3/2$ kernel, with time as the decorrelation parameter. Limb darkening was accounted for through the four-parameter non-linear law. During the fitting we allow the transit depth R_p/R_*, inclination i, normalised semi-major axis a/R_*, transit central time T_0 and linear trend parameters to vary throughout the fit and we fixed all four non-linear limb darkening values similarly to the STIS and G141 observations.

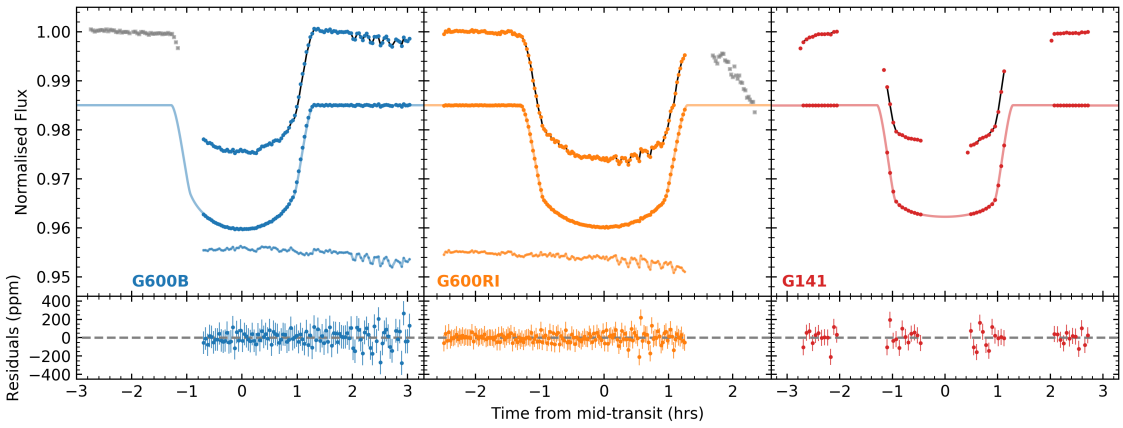

Figure 2.2: Normalised white light curves and residuals of WASP-6b for the G600B, G600RI and G141 grism observations as labelled. *Left:* Data shown from top to bottom are: the raw light curve following reference star correction (grey squares indicating the excluded sections of the light curve) with the black line indicating the GP transit plus systematic model fit, the light curve after removal of the GP systematic component overplotted with the best fitting transit model from Mandel and Agol (2002), and the computed common-mode correction following division of the raw data by the best fitting transit model. *Centre:* As in the left panel. *Right:* The upper light curve is the raw flux with the black line indicating the GP transit plus systematic model fit, whilst the lower is the light curve after removal of the GP systematic component overplotted with the best fitting transit model from Mandel and Agol (2002). All lower panels display residuals following subtraction of the corresponding corrected light curves by their respective best fitting models.

2.4.1.5 Best Fit Models

To obtain the best fit model to each dataset we determine the weighted average values of the orbital inclination and the normalised semi-major axis (Table 2.1). Using these values we performed the fit to the G600B dataset, where we allowed the transit depth R_p/R_*, transit central time T_0, linear trend parameters, and the quadratic limb darkening parameters u_1 and u_2 to vary. In addition, we repeat the fit for each light curve, with the orbital inclination and normalised semi-major axis fixed to the weighted average values and the transit central time to that of its respective original fit. The G600B, G600RI and G141 light curves, alongside the systematics corrected light curves are displayed in Figure 2.2, all *TESS* light curves are displayed in Figure 2.3, all STIS light curves are displayed in Figure A.1, all *Spitzer* light curves are displayed in Figure A.2, and all relevant MCMC results are displayed in Table 2.2.

2.4.2 Spectrophotometric Light Curves

Prior to the full spectrophotometric fits, we correct all of the spectrophotometric light curves for wavelength independent (common-mode) systematics. In the case of the G600B and G600RI datasets we follow Nikolov et al. (2016) and determine a common-mode cor-

Instrument	R_p/R_*	T_0 (MJD)	i (°)	a/R_*	c_1	c_2	c_3	c_4
Uncorrected								
G600B	$0.14425^{+0.00161}_{-0.00176}$	$57298.172234^{+0.000549}_{-0.000516}$	-	-	$0.510^{+0.117}_{-0.122}$	$0.126^{+0.272}_{-0.252}$	-	-
G600RI	$0.14602^{+0.00057}_{-0.00058}$	$57335.146823^{+0.000173}_{-0.000172}$	$88.67^{+0.53}_{-0.38}$	$10.98^{+0.19}_{-0.20}$	$0.469^{+0.054}_{-0.054}$	$0.004^{+0.088}_{-0.086}$	-	-
STIS430 V1	$0.14618^{+0.00065}_{-0.00061}$	$56088.216349^{+0.000183}_{-0.000155}$	$89.38^{+0.41}_{-0.54}$	$11.33^{+0.10}_{-0.21}$	0.4593	-0.0641	0.8327	-0.3729
STIS430 V2	$0.14618^{+0.00065}_{-0.00061}$	$56094.937530^{+0.000263}_{-0.000250}$	$89.38^{+0.41}_{-0.54}$	$11.33^{+0.10}_{-0.21}$	0.4593	-0.0641	0.8327	-0.3729
STIS750	$0.14505^{+0.00058}_{-0.00060}$	$56131.906130^{+0.000306}_{-0.000292}$	$89.17^{+0.54}_{-0.74}$	$11.33^{+0.17}_{-0.38}$	0.6068	-0.1441	0.4857	-0.2312
$TESS_1$	$0.14315^{+0.00127}_{-0.00126}$	$58357.394027^{+0.000429}_{-0.000446}$	$88.35^{+1.07}_{-0.91}$	$10.91^{+0.45}_{-0.67}$	0.6990	-0.4538	0.9531	-0.4668
$TESS_2$	$0.14336^{+0.00115}_{-0.00116}$	$58360.755834^{+0.000405}_{-0.000381}$	$88.68^{+0.83}_{-0.88}$	$10.99^{+0.31}_{-0.56}$	0.6990	-0.4538	0.9531	-0.4668
$TESS_3$	$0.14653^{+0.00124}_{-0.00124}$	$58364.116237^{+0.000384}_{-0.000391}$	$88.62^{+0.90}_{-0.91}$	$10.91^{+0.34}_{-0.59}$	0.6990	-0.4538	0.9531	-0.4668
$TESS_4$	$0.14538^{+0.00112}_{-0.00114}$	$58370.838845^{+0.000401}_{-0.000390}$	$88.37^{+0.99}_{-0.83}$	$10.93^{+0.45}_{-0.59}$	0.6990	-0.4538	0.9531	-0.4668
$TESS_5$	$0.14303^{+0.00106}_{-0.00108}$	$58374.199389^{+0.000365}_{-0.000353}$	$88.66^{+0.86}_{-0.87}$	$11.03^{+0.32}_{-0.57}$	0.6990	-0.4538	0.9531	-0.4668
$TESS_6$	$0.14467^{+0.00112}_{-0.00112}$	$58377.559940^{+0.000384}_{-0.000389}$	$88.45^{+0.91}_{-0.85}$	$10.91^{+0.40}_{-0.59}$	0.6990	-0.4538	0.9531	-0.4668
$TESS_7$	$0.14193^{+0.00124}_{-0.00122}$	$58380.922042^{+0.000420}_{-0.000426}$	$89.24^{+0.50}_{-0.77}$	$11.34^{+0.18}_{-0.36}$	0.6990	-0.4538	0.9531	-0.4668
G141	$0.14374^{+0.00048}_{-0.00041}$	$57880.135381^{+0.000057}_{-0.000061}$	$88.64^{+0.20}_{-0.17}$	$11.09^{+0.12}_{-0.10}$	0.5692	0.1519	-0.2305	0.0672
Spitzer CH1	$0.14124^{+0.00142}_{-0.00132}$	$56313.405391^{+0.000244}_{-0.000246}$	$89.37^{+0.44}_{-0.59}$	$11.26^{+0.11}_{-0.22}$	0.4839	-0.3558	0.3447	-0.1402
Spitzer CH2	$0.14148^{+0.00191}_{-0.00187}$	$56306.683284^{+0.000335}_{-0.000358}$	$88.44^{+0.85}_{-0.65}$	$10.95^{+0.41}_{-0.48}$	0.5652	-0.7296	0.7488	-0.2845
Corrected *TESS*								
G600B	$0.14330^{+0.00156}_{-0.00177}$	$57298.172253^{+0.000552}_{-0.000527}$	-	-	$0.513^{+0.118}_{-0.123}$	$0.123^{+0.270}_{-0.254}$	-	-
G600RI	$0.14513^{+0.00055}_{-0.00057}$	$57335.146826^{+0.000178}_{-0.000178}$	$88.57^{+0.53}_{-0.37}$	$10.93^{+0.22}_{-0.20}$	$0.474^{+0.053}_{-0.054}$	$-0.006^{+0.087}_{-0.086}$	-	-
STIS430 V1	$0.14518^{+0.00062}_{-0.00063}$	$56088.216348^{+0.000171}_{-0.000168}$	$89.35^{+0.40}_{-0.51}$	$11.32^{+0.09}_{-0.20}$	0.4593	-0.0641	0.8327	-0.3729
STIS430 V2	$0.14518^{+0.00062}_{-0.00063}$	$56094.937581^{+0.000267}_{-0.000254}$	$89.35^{+0.40}_{-0.51}$	$11.32^{+0.09}_{-0.20}$	0.4593	-0.0641	0.8327	-0.3729
STIS750	$0.14424^{+0.00056}_{-0.00059}$	$56131.906148^{+0.000305}_{-0.000289}$	$89.19^{+0.55}_{-0.69}$	$11.33^{+0.16}_{-0.35}$	0.6068	-0.1441	0.4857	-0.2312
$TESS_1$	$0.14211^{+0.00121}_{-0.00119}$	$58357.393949^{+0.000410}_{-0.000412}$	$88.13^{+1.09}_{-0.80}$	$10.77^{+0.54}_{-0.61}$	0.6990	-0.4538	0.9531	-0.4668
$TESS_2$	$0.14214^{+0.00110}_{-0.00111}$	$58360.755686^{+0.000364}_{-0.000375}$	$88.63^{+0.90}_{-0.86}$	$10.98^{+0.34}_{-0.56}$	0.6990	-0.4538	0.9531	-0.4668
$TESS_3$	$0.14564^{+0.00119}_{-0.00118}$	$58364.116453^{+0.000370}_{-0.000363}$	$88.78^{+0.79}_{-0.91}$	$11.06^{+0.29}_{-0.56}$	0.6990	-0.4538	0.9531	-0.4668
$TESS_4$	$0.14399^{+0.00108}_{-0.00108}$	$58370.839042^{+0.000375}_{-0.000386}$	$88.19^{+0.93}_{-0.73}$	$10.79^{+0.50}_{-0.54}$	0.6990	-0.4538	0.9531	-0.4668
$TESS_5$	$0.14249^{+0.00107}_{-0.00106}$	$58374.199361^{+0.000358}_{-0.000368}$	$88.47^{+0.94}_{-0.83}$	$10.94^{+0.40}_{-0.58}$	0.6990	-0.4538	0.9531	-0.4668
$TESS_6$	$0.14371^{+0.00110}_{-0.00108}$	$58377.560027^{+0.000382}_{-0.000383}$	$88.61^{+0.91}_{-0.84}$	$10.98^{+0.34}_{-0.55}$	0.6990	-0.4538	0.9531	-0.4668
$TESS_7$	$0.14139^{+0.00123}_{-0.00122}$	$58380.922106^{+0.000422}_{-0.000431}$	$89.27^{+0.49}_{-0.73}$	$11.28^{+0.17}_{-0.32}$	0.6990	-0.4538	0.9531	-0.4668
G141	$0.14305^{+0.00046}_{-0.00041}$	$57880.135372^{+0.000058}_{-0.000061}$	$88.59^{+0.20}_{-0.17}$	$11.06^{+0.12}_{-0.11}$	0.5692	0.1519	-0.2305	0.0672
Spitzer CH1	$0.14078^{+0.00138}_{-0.00132}$	$56313.405403^{+0.000243}_{-0.000244}$	$89.31^{+0.47}_{-0.63}$	$11.25^{+0.12}_{-0.27}$	0.4839	-0.3558	0.3447	-0.1402
Spitzer CH2	$0.14114^{+0.00194}_{-0.00186}$	$56306.683297^{+0.000339}_{-0.000359}$	$88.41^{+0.82}_{-0.62}$	$10.93^{+0.41}_{-0.47}$	0.5652	-0.7296	0.7488	-0.2845
Corrected *AIT*								
G600B	$0.14280^{+0.00161}_{-0.00175}$	$57298.172246^{+0.000556}_{-0.000532}$	-	-	$0.512^{+0.118}_{-0.125}$	$0.125^{+0.275}_{-0.256}$	-	-
G600RI	$0.14464^{+0.00055}_{-0.00055}$	$57335.146821^{+0.000176}_{-0.000174}$	$88.54^{+0.47}_{-0.35}$	$10.91^{+0.19}_{-0.20}$	$0.472^{+0.054}_{-0.054}$	$-0.000^{+0.087}_{-0.085}$	-	-
STIS430 V1	$0.14469^{+0.00069}_{-0.00065}$	$56088.216337^{+0.000175}_{-0.000161}$	$89.32^{+0.42}_{-0.58}$	$11.32^{+0.10}_{-0.24}$	0.4593	-0.0641	0.8327	-0.3729
STIS430 V2	$0.14469^{+0.00069}_{-0.00065}$	$56094.937540^{+0.000279}_{-0.000251}$	$89.32^{+0.42}_{-0.58}$	$11.32^{+0.10}_{-0.24}$	0.4593	-0.0641	0.8327	-0.3729
STIS750	$0.14379^{+0.00058}_{-0.00060}$	$56131.906103^{+0.000310}_{-0.000298}$	$89.24^{+0.51}_{-0.71}$	$11.35^{+0.15}_{-0.34}$	0.6068	-0.1441	0.4857	-0.2312
$TESS_1$	$0.14171^{+0.00122}_{-0.00122}$	$58357.393948^{+0.000398}_{-0.000399}$	$88.14^{+1.05}_{-0.80}$	$10.78^{+0.52}_{-0.61}$	0.6990	-0.4538	0.9531	-0.4668
$TESS_2$	$0.14170^{+0.00112}_{-0.00110}$	$58360.755698^{+0.000377}_{-0.000372}$	$88.61^{+0.85}_{-0.85}$	$10.96^{+0.34}_{-0.56}$	0.6990	-0.4538	0.9531	-0.4668
$TESS_3$	$0.14528^{+0.00118}_{-0.00118}$	$58364.116468^{+0.000370}_{-0.000364}$	$88.81^{+0.79}_{-0.91}$	$11.07^{+0.28}_{-0.56}$	0.6990	-0.4538	0.9531	-0.4668
$TESS_4$	$0.14353^{+0.00109}_{-0.00108}$	$58370.839017^{+0.000381}_{-0.000367}$	$88.20^{+0.96}_{-0.72}$	$10.80^{+0.50}_{-0.54}$	0.6990	-0.4538	0.9531	-0.4668
$TESS_5$	$0.14211^{+0.00107}_{-0.00109}$	$58374.199350^{+0.000362}_{-0.000371}$	$88.54^{+0.91}_{-0.85}$	$10.98^{+0.38}_{-0.58}$	0.6990	-0.4538	0.9531	-0.4668
$TESS_6$	$0.14332^{+0.00108}_{-0.00111}$	$58377.559989^{+0.000382}_{-0.000377}$	$88.49^{+0.97}_{-0.83}$	$10.92^{+0.38}_{-0.57}$	0.6990	-0.4538	0.9531	-0.4668
$TESS_7$	$0.14096^{+0.00124}_{-0.00121}$	$58380.922103^{+0.000422}_{-0.000428}$	$89.29^{+0.48}_{-0.72}$	$11.29^{+0.16}_{-0.32}$	0.6990	-0.4538	0.9531	-0.4668
G141	$0.14280^{+0.00048}_{-0.00042}$	$57880.135374^{+0.000059}_{-0.000059}$	$88.59^{+0.19}_{-0.16}$	$11.05^{+0.11}_{-0.10}$	0.5692	0.1519	-0.2305	0.0672
Spitzer CH1	$0.14060^{+0.00145}_{-0.00134}$	$56313.405406^{+0.000240}_{-0.000239}$	$89.30^{+0.48}_{-0.61}$	$11.25^{+0.12}_{-0.26}$	0.4839	-0.3558	0.3447	-0.1402
Spitzer CH2	$0.14098^{+0.00185}_{-0.00188}$	$56306.683310^{+0.000341}_{-0.000353}$	$88.50^{+0.91}_{-0.65}$	$10.99^{+0.40}_{-0.47}$	0.5652	-0.7296	0.7488	-0.2845

Table 2.2: Measured parameters for WASP-6b from fits to the photometric *TESS* and *Spitzer* light curves, and the white light curves of the G600B, G600RI, STIS430, STIS750 and G141 datasets. Transit depths are those calculated following the fixing of the system parameters to the weighted average values.

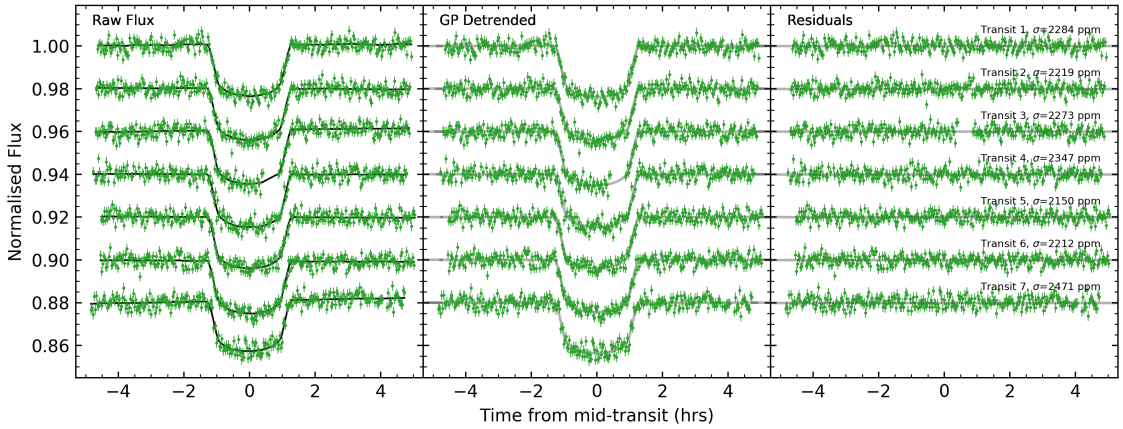

Figure 2.3: Normalised *TESS* photometric light curves multiplied by an arbitrary constant. *Left:* Raw extracted light curves with black lines indicating the GP transit plus systematic model fits. *Centre:* Light curves after removal of GP systematic component. The best fitting transit models from Mandel and Agol (2002) are displayed in grey. *Right:* Residuals after subtraction of best fitting models from the GP systematic corrected light curves.

rection by dividing each uncorrected transit white light curve by its final best fit transit model. To apply the correction we divide all spectrophotometric light curves by the common-mode calculated from their parent white light curve. For the G141 dataset we correct for common-mode systematics following the shift-and-fit method of Deming et al. (2013). In this case a reference spectrum was first produced by averaging all of the out-of-transit spectra. Each individual spectrum was then matched against this reference through stretching vertically in flux and shifting horizontally in wavelength following a linear least-squares optimisation. We then separate the spectral residuals of the previous fit into 28 wavelength bins spanning 1.13 to 1.65 μm. Each spectrophotometric residual was then added to a transit model constructed using the best fit parameters from the white light curve fit and limb-darkening calculated for the relative wavelength bin to produce the spectrophotometric light curves. All corrections can be seen under each systematics corrected light curve in Figure 2.2.

All spectrophotometric light curves were then fit following the same process as their corresponding white light curves. In each case however, the inclination and normalised semi-major axis were fixed to the weighted average values calculated from the white light curve fits and the transit central time was fixed to that of each respective white light curve fit. Additionally, for the G600B and G600RI light curves the quadratic limb darkening parameter u_2 was fixed to a value calculated from the ATLAS model described in Section 2.3

for each individual wavelength bin. The results for all best fit transit depths are displayed in Tables A.1 and A.2 and all spectrophotometric light curves for the G600B, G600RI, G141 and STIS datasets are displayed in Figures 2.4, 2.5, 2.6 and A.3 respectively.

The initial transmission spectrum of these spectrophotometric light curves revealed an offset in transit depth between the G600B and G600RI datasets. Whilst activity of the host star can lead to such offsets, the stellar variability monitoring performed in Nikolov et al. (2015) shows that potential offsets are of a magnitude $\Delta R_p/R_* \simeq 0.00022$, much too small to account for the observed offset of $\Delta R_p/R_* \sim 0.002$. Furthermore, the very good agreement of the G600RI dataset with the STIS measurements (Section 2.6.1) of Nikolov et al. (2015) demonstrates that the cause of this offset most likely lies with the G600B dataset. Due to the poor phase coverage of the G600B dataset there are almost no observations during ingress, this produces a large uncertainty in the transit central time and subsequently the absolute transit depth, which may be responsible for the offset we see. Therefore, to account for this offset we apply a vertical shift to the G600B dataset by performing a weighted least-squares minimisation on the difference between the spectrophotometric bins in the overlapping region between the G600B and G600RI datasets, leaving the relative vertical shift of the G600B dataset as a free parameter in the minimisation. This results in a shift of $\Delta R_p/R_* = 0.00248$, equivalent to $\sim 1.5\sigma$ of the error on the transit depth of the G600B white light curve. A full transmission spectrum with this offset included is shown in Figure 2.7.

2.5 Correcting for Stellar Heterogeneity

Stellar activity leads to the presence of heterogeneities on stellar surfaces through the magnetically driven formation of cooler regions known as star spots and hotter regions known as faculae. The presence of spots (or faculae) on the surface of a star results in a wavelength dependent variation in the stellar baseline flux due to the respective differences in the emission profiles of the relatively cool spot (or relatively hot faculae) and the stellar surface itself. As the stellar baseline flux is crucial in determining transit depth, the presence of an unocculted star spot during a transit observation will necessarily produce a wavelength dependent variation in the measured transit depth (Rackham et al. 2018,

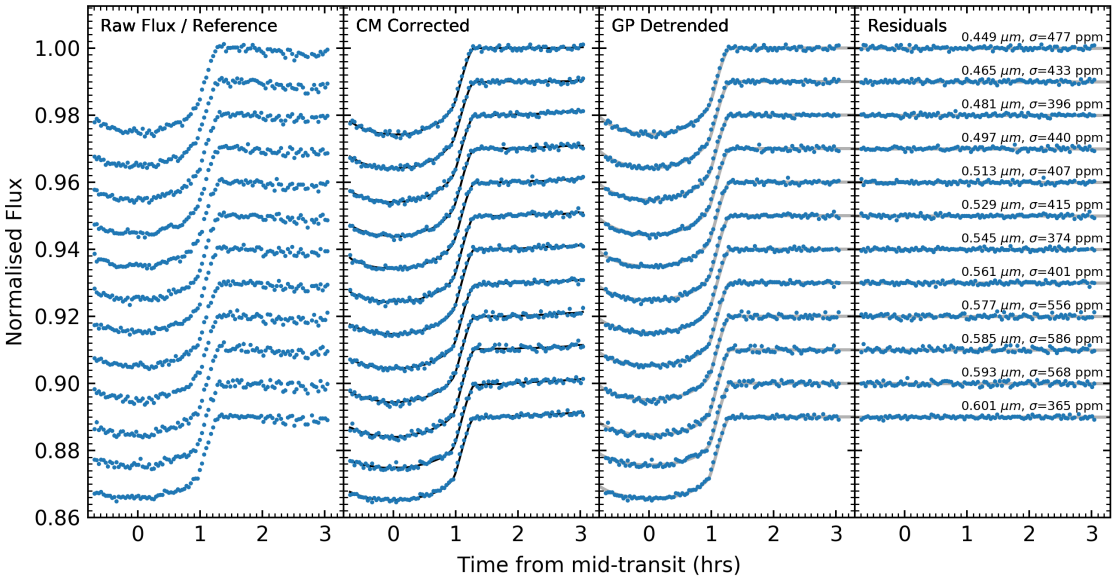

Figure 2.4: Normalised spectrophotometric light curves for the G600B dataset of WASP-6b, light curves are offset from one another by an arbitrary constant. *Left:* Raw light curves following reference star correction. *Centre-Left:* Light curves after common-mode correction with black lines indicating the best GP transit plus systematic model fit. *Centre-Right:* Light curves after common-mode correction and removal of GP systematic component. The best fitting transit models from Mandel and Agol (2002) are displayed in grey. *Right:* Residuals following subtraction of best fitting model.

2019). If significant enough, this variation can produce an artificial slope in the optical region of the final measured transmission spectrum, potentially mimicking the effects of haze in the atmosphere (Pont et al. 2008; Sing et al. 2011b; McCullough et al. 2014; Alam et al. 2018; Pinhas et al. 2018). These wavelength dependent variations can also impact individual spectral features due to the differential emission of specific stellar lines. Previous studies have displayed small decreases in the amplitude of Na I absorption following a stellar heterogeneity correction (e.g. Sing et al. 2011b; Alam et al. 2018), however this effect is typically secondary to the artificially induced optical slope.

To estimate the impact surface stellar heterogeneities may have on our observations we obtained a proxy of the magnetic activity level of WASP-6 using a measurement of $\log(R'_{HK})$. This value has been previously quoted without uncertainties as -4.741 in Sing et al. (2016), however analysis of the emission cores of the Ca II H and K lines in the HARPS spectra of Gillon et al. (2009) results in a direct measurement of -4.511 ± 0.037, indicating that WASP-6 is a moderately active star compared to the broader population of cool stars (Boro Saikia et al. 2018). We therefore endeavour to account for the effects of unocculted star spots following the methodology of Alam et al. (2018).

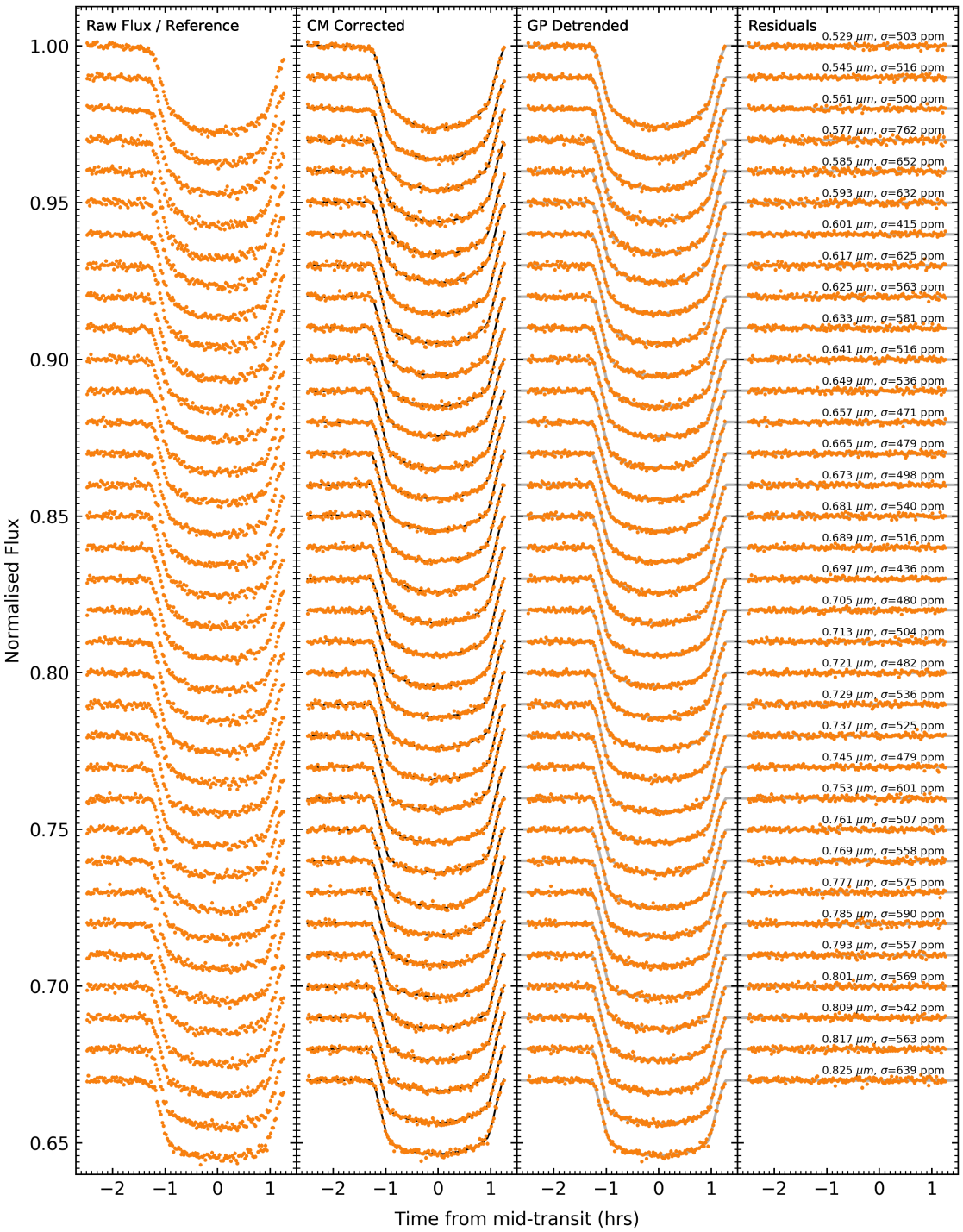

Figure 2.5: As in Figure 2.4, but for the G600RI dataset.

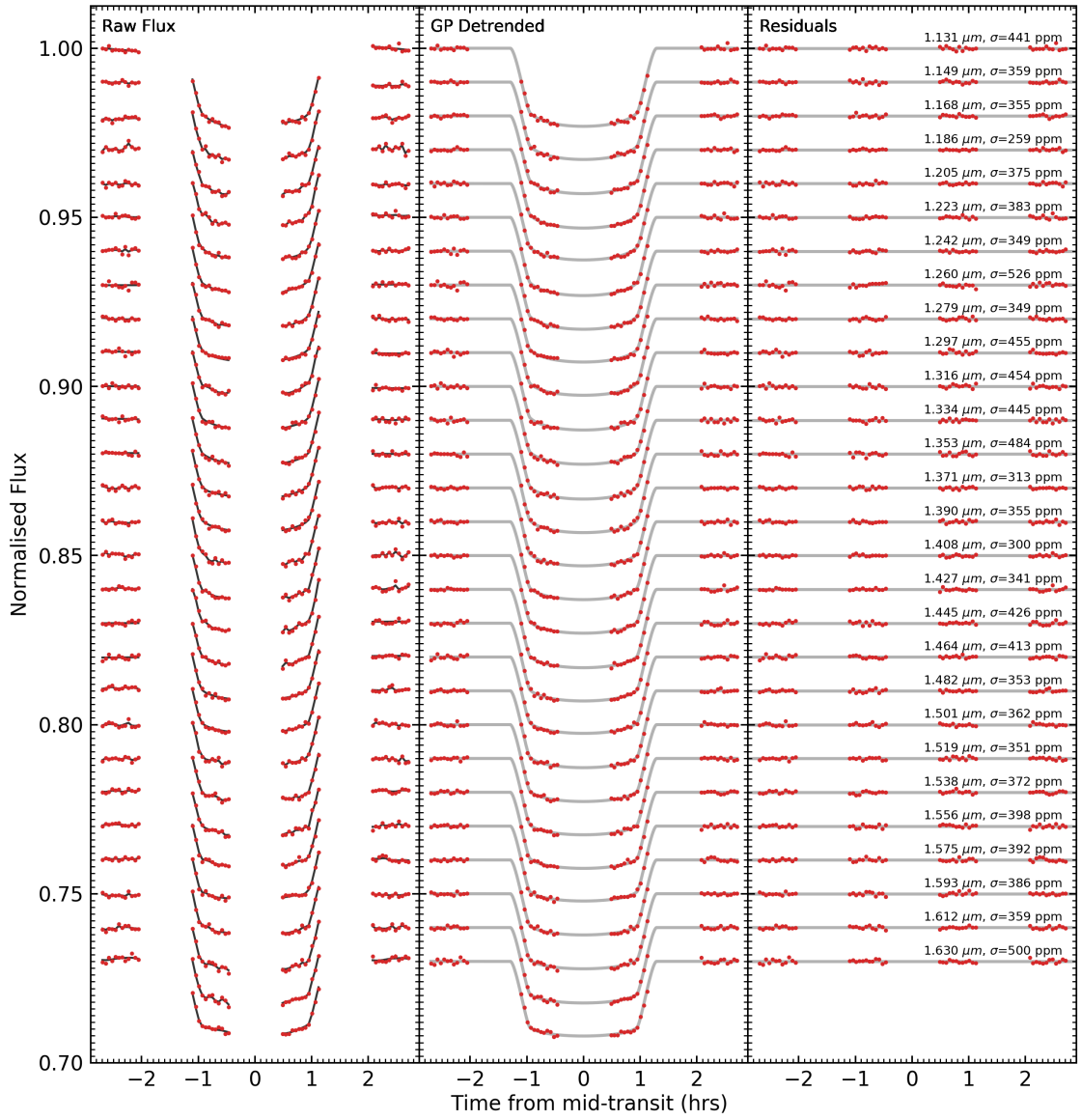

Figure 2.6: Normalised spectrophotometric light curves for the G141 dataset of WASP-6b, light curves are offset from one another by an arbitrary constant. *Left:* Raw extracted light curves with black lines indicating the GP transit plus systematic model fit. *Centre:* Light curves after removal of GP systematic component. The best fitting transit models from Mandel and Agol (2002) are displayed in grey. *Right:* Residuals following subtraction of best fitting model.

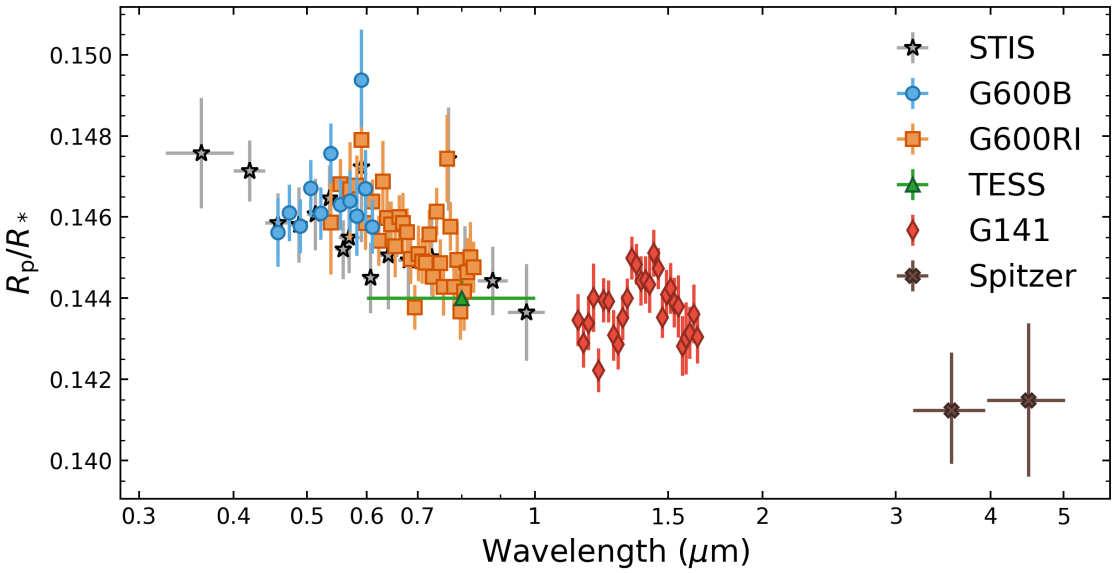

Figure 2.7: The measured transmission spectrum of WASP-6b obtained from the G600B, G600RI, *TESS*, STIS, G141 and *Spitzer* datasets.

2.5.1 Photometric Monitoring of WASP-6

We estimate the long baseline variability of WASP-6 by considering all 18,317 images from the *TESS* observations previously described in Section 2.3.3 in addition to 435 *R*-band images from the Tennessee State University 14-inch Celestron *Automated Imaging Telescope* (*AIT*) taken from September 2011 to January 2019 (Figure 2.8). Initially, we also incorporated 738 *V*-band images taken from November 2013 to July 2018 as part of The Ohio State University *All-Sky Automated Survey for Supernovae* (*ASAS-SN*) (Shappee et al. 2014; Jayasinghe et al. 2018) into our photometric monitoring dataset as in Alam et al. (2018). However, on comparing the contemporaneous *ASAS-SN* and *TESS* data we find a ~4 times larger photometric scatter in the *ASAS-SN* dataset compared to the more precise *TESS* sample and, as such, exclude it from our analysis to avoid influencing the variability amplitude estimation with such a noise-dominated dataset.

2.5.2 The Stellar Rotation Period

To perform an accurate fit to the photometric monitoring data, it is necessary to have a measurement of the stellar rotation period. However, a range of rotation periods have been reported for WASP-6. In particular, Jordán et al. (2013) find a period of 16 ± 3 d based on the $v\sin I = 2.4 \pm 0.5$ km s^{-1} measurement from Doyle et al. (2013), Nikolov et al. (2015)

determine a period of 23.6 ± 0.5 d from a portion of their *AIT* photometric monitoring, and by tracking transit star spot crossings Tregloan-Reed et al. (2015) find a period of 23.80 ± 0.15 d, assuming the star had rotated only once between successive observed crossings.

We also perform a measurement of this rotation period through virtue of the very high cadence *TESS* observations. Even from an initial inspection of the light curve shown in Figure 2.8 a clear sinusoidal variation can be seen. In order to determine that this variation is not due to an instrumental effect we inspect the light curves and background flux of the four closest neighbouring stars to WASP-6 with *TESS* light curve observations. We find that none of the stars exhibit the same sinusoidal variation as WASP-6, and they all exhibit similar variations in their background flux. To determine the rotation period itself, we perform a least-squares minimisation using a simplistic sinusoidal model on the data with all transit events removed. This resulted in an inferred period of 12.18 ± 0.05 d.

Even though this method of model fitting is quite rudimentary, the determined period is clearly in contradiction to current estimates of the stellar rotation period. This contradiction suggests that the variability observed is likely not that of a single spot feature rotating with a period equal to that of the stellar rotation period. Alternatively, the perceived *TESS* period can be explained by the spot coverage during the *TESS* epoch being concentrated on opposite hemispheres of the star, rather than one single hemisphere. During a period of *AIT* photometry performed shortly after the *TESS* observations from September 2018 to January 2019 we find a standard deviation of 3.8 mmag, in contrast to previous seasons where this reached up to 8.1 mmag. This reduced variability is further justification of the measured *TESS* period being a result of hemispherically varying star spot coverage and not intrinsic to the *TESS* instrument itself. Further high-quality photometric monitoring will likely be necessary to fully resolve the discrepancy between these observations. For subsequent analysis however, we adopt the stellar rotation period of 23.6 ± 0.5 d from Nikolov et al. (2015) as this estimate was made over much longer timescales compared to the estimates of Jordán et al. (2013) and Tregloan-Reed et al. (2015).

2.5.3 Modelling and Correction of Unocculted Star Spots

The variability of WASP-6 was modelled following the methodology of Alam et al. (2018). We perform a Gaussian process (GP) regression model fit to the photometric monitoring data constructed with a three component kernel which models: the quasi-periodicity of the data, irregularities in the amplitude, and stellar noise. A gradient based optimisation routine was used to locate the best-fit hyperparameters and a uniform prior was placed on the stellar rotation period, centred on the value of 23.6 ± 0.5 d from Nikolov et al. (2015) with a width three times that of the standard deviation. The *TESS* bandpass ranges from 0.6-1.0 μm and is less susceptible to active photometric variations compared to the *AIT R*-band observations. This should not affect the wavelength dependence of our determined spot correction however, as the estimated variability amplitude is ultimately used as a reference to normalise the true model wavelength-dependent correction factor (Equation 2.1). Despite this, the discrepancy of the measured *TESS* period from the measured period in other studies (Jordán et al. 2013; Nikolov et al. 2015; Tregloan-Reed et al. 2015), and the reduced variation in a subset of *AIT* data described in Section 2.5.2, does indicate that the variability of the star as a whole was also lower during this epoch. Because the variability amplitude is crucial in determining the spot correction, we opt to perform separate fits to the *TESS* and *AIT* datasets. To avoid influencing the GP fitting with the lower variance *AIT* data, we exclude 41 measurements obtained shortly after the *TESS* epoch which correspond to the subset described in Section 2.5.2. Due to the large size of the *TESS* dataset (~18,000 data points) we bin the data down by a factor of 10 to make the GP fitting computationally tractable.

Whilst the *TESS* data is well sampled and more precise than the *AIT* data, we may be perceiving a lower level of variability due to the *TESS* bandpass or the lower intrinsic variability of WASP-6 during the *TESS* epoch (Section 2.5.2). Comparatively, the *AIT* data has a much broader temporal coverage and could therefore be more indicative of the longer-term variability of WASP-6, though as there are no contemporaneous measurements with the *TESS* dataset their accuracy is not guaranteed. The *TESS* and *AIT* model fits therefore provide respectively more conservative or realistic estimates of the true stellar variability. All such fits to the photometric monitoring data are displayed in Figure 2.8.

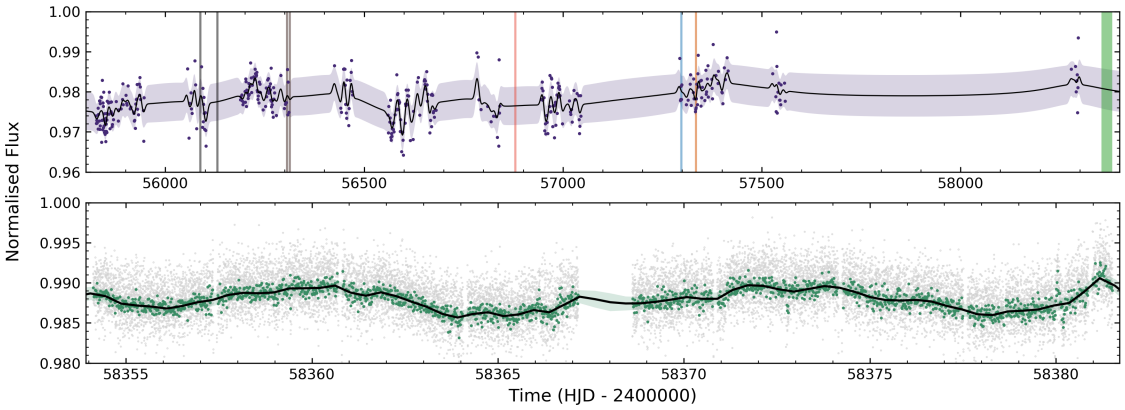

Figure 2.8: Photometric monitoring and modelling of the stellar variability of WASP-6. *Top*: *AIT* monitoring data prior to the *TESS* epoch(purple dots) with best fit GP model represented by the solid black line, the shaded area represents the 1σ confidence region. Additional vertical lines are plotted corresponding to the best fit transit central times of each observation as shown in Table 2.2, the broader green region nearest the latest observations corresponds to the full *TESS* epoch. *Right:* Unbinned (grey) and binned (cyan) *TESS* monitoring data with best fit GP model represented by the solid black line, the shaded area represents the 1σ confidence region. For both the *AIT* and *TESS* datasets the flux has been normalised with the maximum stellar flux obtained from their respective GP model fits corresponding to unity.

We are then able to correct for the unocculted spots in the transit light curves following Huitson et al. (2013). Under the assumption that there is always some level of spot coverage on the stellar surface, the maximum observed stellar flux does not correspond to the flux emitted by an entirely unspotted surface. Using the amplitude of the GP fit to both the *TESS* and *AIT* photometric monitoring data we determine different estimates for the unspotted stellar flux $F' = \max(F)+k\sigma$, where F is the observed photometric monitoring data, σ is the dispersion of these photometric measurements, and k is a value fixed to unity. Whilst an accurate value of k can be difficult to determine a $k = 1$ has been shown to be suitable for active stars (Aigrain et al. 2012). Furthermore, varying the chosen value of k does not significantly influence the wavelength dependence of the correction and mainly influences the offset of the transmission spectrum baseline (Alam et al. 2018). For each estimate, the fractional dimming due to stellar spots was then calculated as $f_{\rm norm} = \overline{F/F'}$, giving the amplitude of the spot correction at the variability monitoring wavelength as $\Delta f_0 = 1 - f_{\rm norm}$.

To determine each wavelength dependent spot correction we must compute the wavelength-dependent correction factor shown in Sing et al. (2011a):

$$f(\lambda, T) = \left(1 - \frac{F_{\lambda, T_{\rm spot}}}{F_{\lambda, T_{\rm star}}}\right) \Bigg/ \left(1 - \frac{F_{\lambda_0, T_{\rm spot}}}{F_{\lambda_0, T_{\rm star}}}\right) \tag{2.1}$$

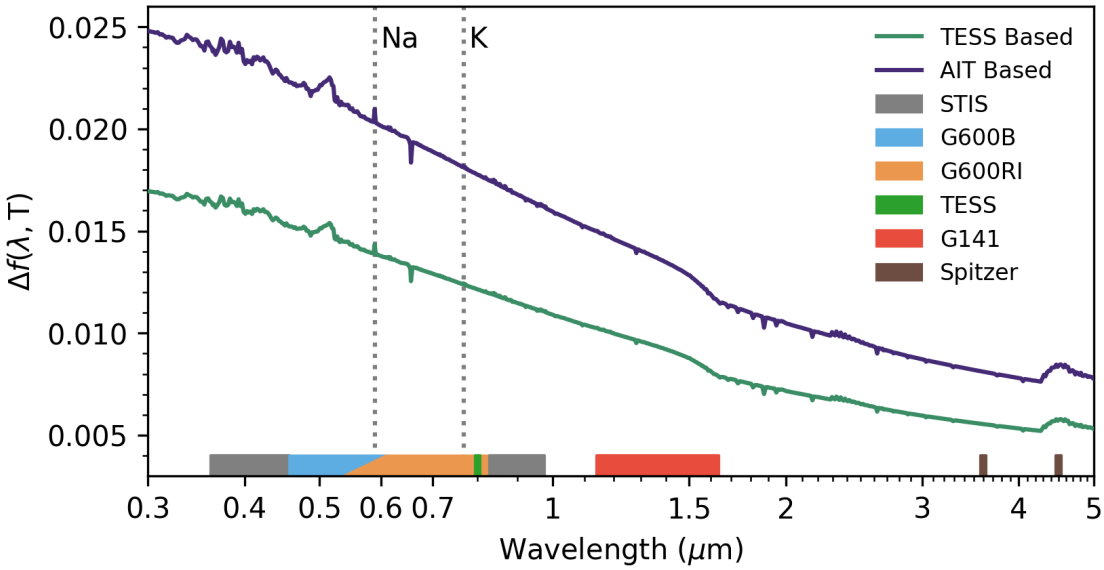

Figure 2.9: Calculated spot corrections based on the *TESS* (teal, bottom) and *AIT* (purple, top) photometric data. Regions of wavelength coverage for all observations performed in this study are also shown, the photometric *TESS* and *Spitzer* data points are represented as lines at the centre of their respective bandpasses.

where $F_{\lambda,T_{\rm spot}}$ is the wavelength dependent stellar flux at temperature $T_{\rm spot}$, $F_{\lambda,T_{\rm star}}$ is the wavelength dependent stellar flux at temperature $T_{\rm star}$, $F_{\lambda_0,T_{\rm spot}}$ is the stellar flux at the wavelength of the photometric monitoring data at temperature $T_{\rm spot}$, and $F_{\lambda_0,T_{\rm star}}$ is the stellar flux at the wavelength of the photometric monitoring data at temperature $T_{\rm star}$. To determine the stellar and spot fluxes described we use the `ATLAS` stellar model described in Section 2.3. The only difference between the stellar flux and spot models is that they differ by a temperature of 1500K, assumed from an empirically determined relation (Berdyugina 2005). Finally, we compute wavelength dependent spot corrections based on both the *AIT* and *TESS* photometry following $\Delta f = \Delta f_0 \times f(\lambda, T)$ (Figure 2.9).

Each spot correction was then independently applied to both the white and spectrophotometric light curves using:

$$y_{\rm corr} = y + \frac{\Delta f}{(1 - \Delta f)} \overline{y_{\rm oot}} \tag{2.2}$$

where $y_{\rm corr}$ is the corrected light curve flux, y is the uncorrected flux, and $\overline{y_{\rm oot}}$ is the out-of-transit mean flux. These corrected light curves, informed by either the *TESS* or *AIT* photometry, were then refit following the same method as demonstrated in Section 2.4 and are hereafter defined as the *TESS* corrected or *AIT* corrected datatsets. Both *TESS*

and *AIT* corrected G600B spectrophotometric light curves exhibited comparable offsets to the uncorrected dataset (Section 2.4.2) of $\Delta R_p/R_* = 0.00244$ and 0.00242 respectively and thus similar vertical shifts are performed. All best fit parameters from the white light curve fits are displayed in Tables 2.1 and 2.2, and all best fit spectrophotometric transit depths are displayed in Table A.1 and A.2.

2.6 Discussion

The observed transmission spectrum of WASP-6b reveals a variety of spectroscopic features present both in the uncorrected and spot corrected analyses (Figure 2.10). In particular, the broad absorption feature at 1.4 μm indicates the presence of H_2O in the atmosphere. Additionally, narrow band absorption features at 0.589 and 0.767 μm due to Na I and K I are also evident in the optical. Finally, a distinct increase in transit depth across optical wavelengths is seen, indicative of a scattering haze and in agreement with Nikolov et al. (2015). The primary difference between the uncorrected and spot corrected datasets is the presence of a vertical offset across the full wavelength range. This offset is not wavelength independent however and the spot correction has acted to slightly reduce the gradient across the optical slope. This wavelength dependence is clearly identified by the difference in transit depth between the uncorrected and *AIT* corrected datasets at the shortest wavelength bin compared to that of the longest wavelength.

2.6.1 Archival Data Comparisons

The transmission spectrum of WASP-6b had already been measured using the available *HST* STIS and *Spitzer* IRAC datasets (Nikolov et al. 2015). In order to compare our independent reduction against these results we overplot both the uncorrected transit depths from this study, with those from this prior published study (Figure 2.11). The different reductions agree quite well, with all measurements within 1σ of one another. A minor discrepancy in transit depth is seen for the longest wavelength STIS bins and the *Spitzer* photometry. These discrepancies are likely due to the slightly different measured system parameters which were held fixed during the independent fittings in addition to slight differences in the adopted stellar limb darkening parameters. The error bars for the re-

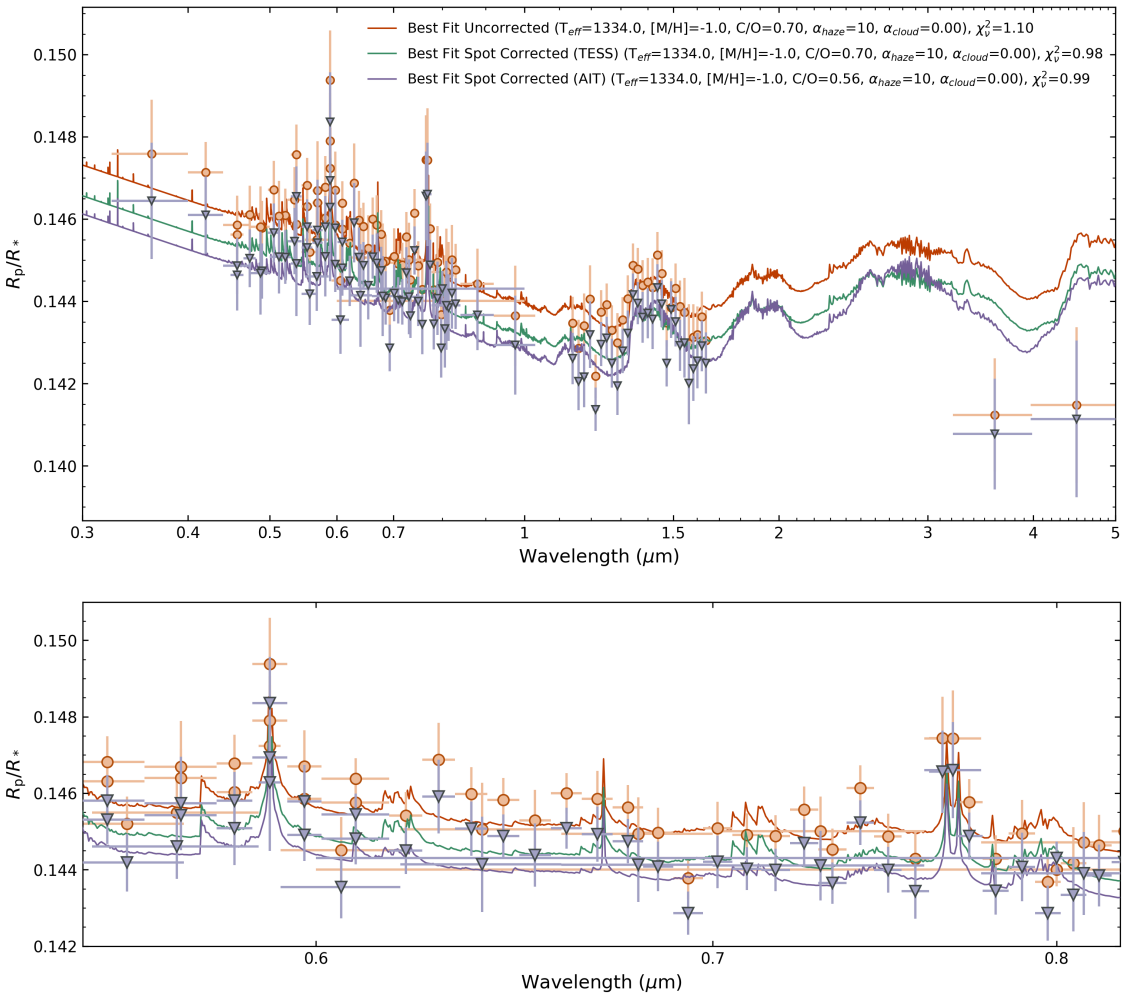

Figure 2.10: *Top*: The uncorrected (orange circles) and *AIT* spot corrected (purple triangles) transmission spectra of WASP-6b as determined from the performed G600B, G600RI, G141, *TESS*, and archival STIS and *Spitzer* observations with the best fit models from the Goyal et al. (2018) forward grid. For reasons of clarity the *TESS* spot corrected dataset is not shown, however the best fit model is displayed to demonstrate the differences in transit depth. *Bottom*: As in the top panel, except zoomed in to the wavelength region spanning the Na I and K I lines

duction performed in this study are larger than those of those from the original reduction, primarily due to the difference between the model marginalisation and Gaussian process approaches towards light curve fitting.

As the STIS and *VLT* FORS2 datasets have a broad overlapping wavelength range we reproduce the *VLT* FORS2 transmission spectrum using an identical wavelength binning as the *HST* STIS measurements to facilitate a comparison between the results (Figure 2.11). It is evident from this comparison that whilst our results agree very well at the shortest and longest wavelengths, there is a small disparity in the measurements centred around the Na I absorption line. We calculate a weighted average transit depth across 5 wavelengths bins centred on the Na I absorption line for the G600RI dataset and the STIS dataset, resulting in R_p/R_*'s of 0.14628±0.00031 and 0.14520±0.00043 respectively. We exclude the G600B dataset from the calculation to avoid any bias due to the applied vertical shift as described in Section 2.4.

As the offset reduces proportionally with separation from the Na I line center, this signal could be indicative of an observation of the pressure-broadened wings from the full Na I feature in the FORS2 datasets. Such wings have recently been definitively observed in the atmosphere of the hot Jupiter WASP-96b (Nikolov et al. 2018). Given these wings are not present in the STIS dataset, this could suggest we are observing variability in the atmosphere of WASP-6b. However, this offset being of an instrumental or systematic origin cannot be excluded, particularly as the FORS2 observations are taken from the ground where systematic variations are not as well understood and harder to model. The possibility that this discrepancy has been caused by the STIS observations in particular also cannot be excluded as there exists robust evidence that systematics in STIS observations resulted in a spurious detection of K in WASP-31b (Gibson et al. 2017; Gibson et al. 2019). The true cause of the discrepancy, be it physical or systematic, can not be determined with these data and additional observations at higher signal to noise and over long timescales will be required to investigate this further.

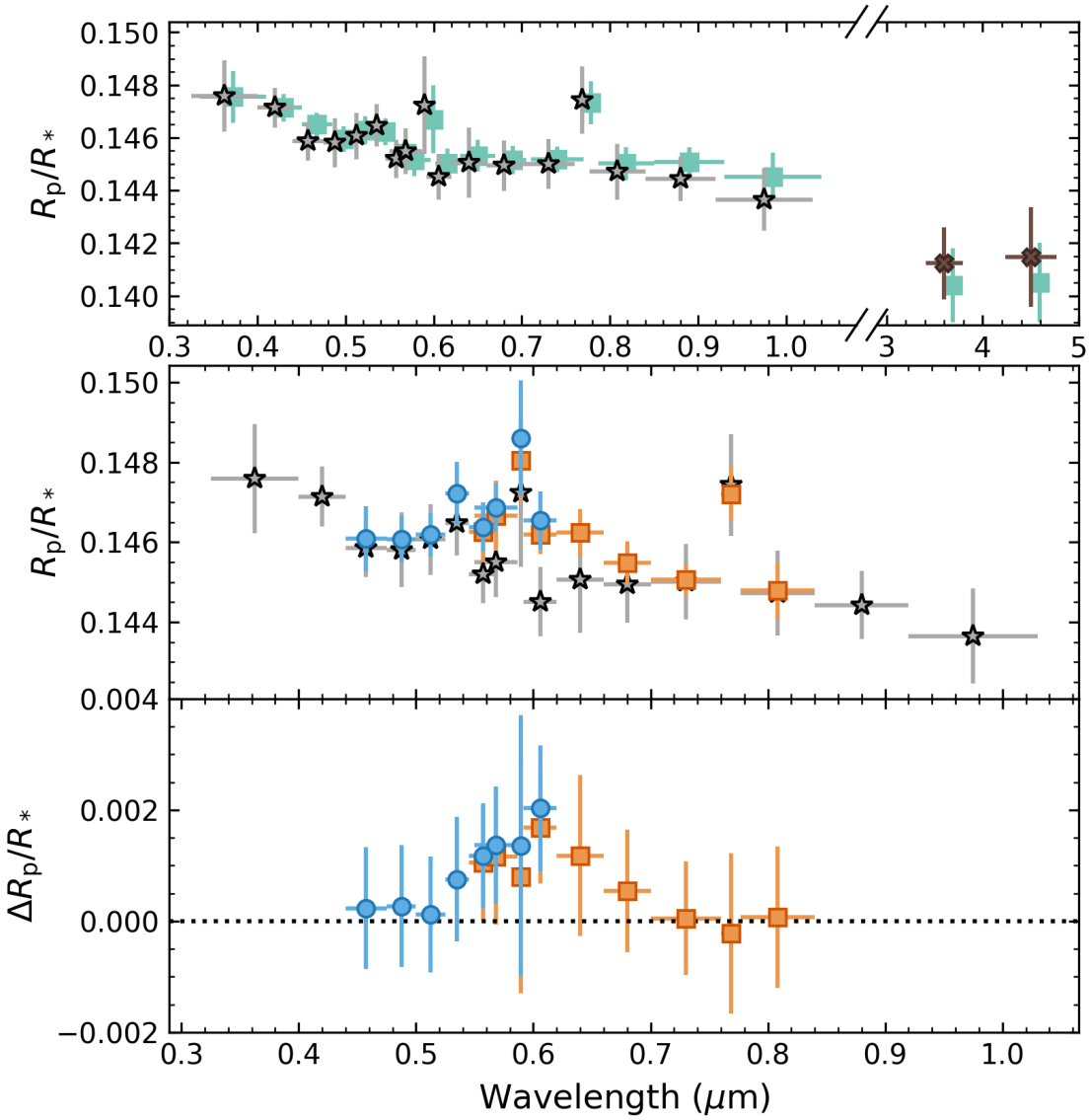

Figure 2.11: *Top*: A comparison of the measured STIS and *Spitzer* transit depths from this study (grey stars/brown crosses) and those published in Nikolov et al. (2015) (teal squares). A small wavelength offset has been added to the literature datasets for clarity. *Middle*: The measured uncorrected transit depths of the STIS (grey stars) dataset in comparison to the G600B (blue circles) and G600RI (orange squares) datasets, binned down to an identical resolution where possible. *Bottom*: Differenced transit depths following subtraction of the STIS dataset from the G600B and G600RI datasets, a slight disparity is seen within the Na I line.

2.6.2 Goyal Forward Models

To explore the bulk properties of WASP-6b we fit the observed transmission spectrum to a grid of forward models (Goyal et al. 2018; Goyal et al. 2019b). These models are generated using the 1D radiative-convective equilibrium code `ATMO`. Initially we opted to use the more recent generic model grid (Goyal et al. 2019b) in our analysis as it allowed for a broader coverage of the parameter space than the WASP-6b specific grid from Goyal et al. (2018). However, as sub-solar metallicity forward models have yet to be implemented into the generic grid our ability to accurately fit the observed data was ultimately restricted. As such, we used the WASP-6b specific grid (Goyal et al. 2018) in order to cover the sub-solar metallicity range of parameter space.

With the arrival of the *Gaia* Data Release 2 (Gaia Collaboration et al. 2018) the distance to WASP-6 has been more accurately determined as $d = 197.1^{+0.4}_{-1.6}$ pc (Bailer-Jones et al. 2018), significantly different to the prior measurement of 307 pc. This re-estimation has significant effects on the inferred stellar radius of WASP-6 which in turn affects the estimation of planetary radius from the observed transit depths. A mismeasurement of the planetary radius naturally leads to a mismeasurement of the planetary gravity, a currently fixed parameter for the planet specific forward model grid of Goyal et al. (2018). Following the methodology of Morrell and Naylor (2019), we performed spectral energy distribution (SED) fitting on WASP-6 using NUV, optical and NIR broadband photometry. The fitted integrated flux allows us to measure its luminosity, and the shape of the SED determines its so-called $T_{\rm SED}$ (see Morrell and Naylor 2019, for details). By combining this with the revised distance measurement, we obtained an updated estimate of the radius of WASP-6, and subsequently the radius of WASP-6b. This radius results in a new value for the planetary gravity of $g = 10.55^{+0.19}_{-0.39}$ ms^{-2}, notably different from the previous estimate of $g = 8.71 \pm 0.55$ ms^{-2} (Gillon et al. 2009). Changes in gravity can have significant effects on the computed forward models (Goyal et al. 2018; Goyal et al. 2019b) and therefore to fit our observed data we use a more updated forward model grid for WASP-6, identical to the original shown in Goyal et al. (2018) except recomputed for a value of $g = 10.5$.

The model grid used consists of 3920 different transmission spectra varying in temperature, metallicity, C/O ratio, scattering haze and uniform cloud. The scattering haze

is implemented through the use of a haze enhancement factor α_{haze} which simulates an increase in the total scattering of small aerosol particles in the atmosphere. Similarly, the uniform cloud is implemented through a variable cloudiness factor α_{cloud}, which produces the effects of a cloud deck through a modification to the wavelength dependent scattering using the strength of grey scattering due to H_2 at 350 nm. Irrespective of the true cloud composition, implementing a grey cloud is appropriate for our observations as at the observed wavelengths Mie scattering predicts essentially grey scattering profiles (Wakeford and Sing 2015). Further details on the grid parameters, including their ranges and implementations, can be found in Goyal et al. (2018).

Each model spectrum was fit in turn by producing a binned version of the spectrum which matches the selected spectrophotometric bands from the data reduction and then averaged to produce a single value of transit depth in each bin. A χ^2 measurement between the observed and model data was then computed following a least-squares minimisation scheme with a varying wavelength-independent vertical offset. These fits were performed for both the uncorrected and both spot corrected transmission spectra and the best fitting models for each are presented in Figure 2.10.

For the uncorrected and the *TESS* corrected transmission spectra we find a best fitting model of $T = 1334$ K, sub-solar metallcity [M/H] = −1.0, slightly super-solar C/O ratio of [C/O] = 0.70, moderate hazes $\alpha_{\text{haze}} = 10$ and no evidence of clouds $\alpha_{\text{cloud}} = 0$ corresponding to a $\chi^2_\nu = 1.10$ and 0.98 respectively. For the *AIT* corrected transmission spectrum however, we find a best fitting model of $T = 1334$ K, sub-solar metallcity [M/H] = −1.0, solar C/O ratio of [C/O] = 0.56, moderate hazes $\alpha_{\text{haze}} = 10$ and no evidence of clouds $\alpha_{\text{cloud}} = 0$ corresponding to a $\chi^2_\nu = 0.99$. To explore the discrepancies and commonalties between the grid fits to the uncorrected and corrected datasets we produce χ^2 contour maps (Madhusudhan and Seager 2009) as shown in Figure 2.12. We begin by constructing 2D grids of every possible pair of model parameters. In each separate grid, and at every individual grid point dictated by the resolution of the model parameters, we vary all the remaining model parameters in turn and determine the model with the smallest χ^2. Across these new χ^2 spaces we determine contours which correspond to models in the parameter space which are N-σ from the overall best fit model following Goyal et al. (2018).

The primary differences between the datasets are the existence of subsets of model fits more favoured by the lowest metallicities and the highest haze enhancement factors for only the uncorrected dataset. These subsets are present because the wavelength dependence of stellar heterogeneity acts to increase the gradient of the optical slope in the observed data, an effect that is somewhat degenerate with lower metallicity and hazy atmospheres (Goyal et al. 2018). Whilst both the lowest metallicities and highest haze enhancements factors are not as favoured in tandem, they both correspond to model fits favouring a lower level of C/O ratio. This is because both low metallicity and high haze enhancement factor act to suppress the H_2O absorption features beyond the constraints set by the G141 dataset and as such the C/O ratio must be reduced to re-inflate the H_2O features to match the observations. In summary, the χ^2 contour map for even the conservative *TESS* corrected dataset indicates that these highest haze enhancement factors, lowest metallicities, and lowest C/O ratios are likely effects of stellar heterogeneity on the transmission spectrum of WASP-6b and not truly symptomatic of its atmosphere. However, a moderate haze enhancement of at least $\alpha_{\text{haze}} = 10$ is strongly constrained, and a preference towards sub-solar metallicities is still evident, independent of the addition of a spot correction.

Whether or not a spot correction is used, temperatures of 1334 K are primarily preferred for each grid fit. Comparatively, the measured dayside temperatures for WASP-6b are 1235^{+70}_{-77} and 1118^{+68}_{-74} from the 3.6 and 4.5 μm *Spitzer* IRAC channels respectively (Kammer et al. 2015). As these values are within $\sim 1\sigma$ they do not suggest a disagreement, however, it is worthwhile assessing the source of the slight preference of the grid model fits towards limb temperatures higher than that measured from the dayside. As the model grid varies in temperature steps of 150 K the model cannot settle on a precise temperature estimate and is therefore likely to be somewhat discrepant from the true value. However, there are models at a temperature $T = 1184$ K which should in theory match the true temperature of WASP-6b's limb more accurately. Looking to Figure 2.12, the preferred temperature is strongly constrained below the 1484 K grid models, as at approximately this temperature absorption features due to TiO and VO start to become significant in the optical (Fortney et al. 2008) and are strongly disfavoured by the observed FORS2 and STIS datasets. As temperature acts to increase the gradient of the optical slope (Goyal et

Dataset	Na I Significance	K I significance
Uncorrected	4.2 σ	3.5 σ
TESS Corrected	3.9 σ	3.2 σ
AIT Corrected	3.9 σ	3.4 σ

Table 2.3: Sigma confidence levels of the Na I and K I line detections with respect to the model baseline level.

al. 2018) it is also degenerate with the effects of stellar heterogeneity. Therefore the models at 1334 K are the most favoured as it is the highest temperature, and thus steepest slope, that the model grid can produce without generating conflicting TiO and VO features. Figure 2.12 demonstrates this as the model preferences for the highest temperatures are slightly reduced upon application of the spot corrections, with the most significant difference being for the *AIT* corrected dataset. As the best fit temperature for the *AIT* correction is still beyond what we would expect given the day side temperatures already reported it could even suggest that the spot correction used has been underestimated. However, a subset of 1184 K models are comfortably within the 2σ region for every dataset and therefore conclusively determining the true effect of stellar heterogeneity on the best fit model temperature will require further investigation with observations at a higher signal to noise.

To determine the significance of the perceived detections of the Na I and K I features we begin by performing a quadratic interpolation of the baseline of the best fit model to each dataset from 0.4-0.9 μm using regions of the optical slope with no clear absorption features as anchors for the interpolation. The interpolation then served as a comparison against the weighted mean value of the G600B, G600RI, STIS 430 and STIS 750 data contained with the Na I and K I lines. Detection significances are summarised in Table 2.3, these values indicate at least a 3σ detection of the Na I and K I narrow line signatures in the atmosphere WASP-6b, irrespective of an applied spot correction.

2.6.3 `ATMO` Retrieval Modelling

The previously available transmission spectra of WASP-6b has been the subject of multiple retrieval based model analyses thus far. Firstly by Barstow et al. (2017) who utilize the `NEMESIS` retrieval code to demonstrate that the atmosphere of WASP-6b is best described by Rayleigh scattering clouds at high altitudes. In addition, Pinhas et al. (2018) perform

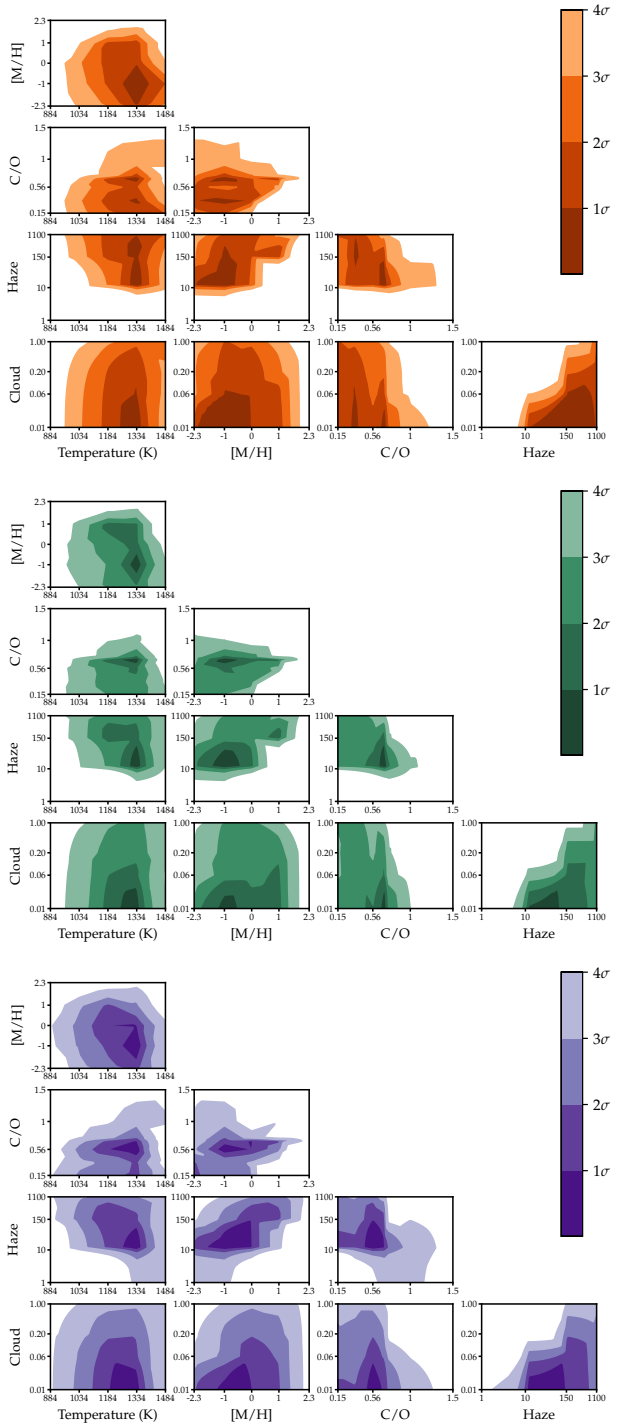

Figure 2.12: χ^2 contour maps produced when fitting the complete transmission spectrum of WASP-6b to forward model grids of Goyal et al. (2018) considering **(a)** no correction for stellar heterogeneity, **(b)** correction using *TESS* photometry, and **(c)** correction using *AIT* photometry. Shaded regions indicate models in the parameter space which are at least $N - \sigma$ from the best fit model. Preferences towards the lowest metallicity, highest haze enhancement factors, and lower C/O ratios are present for the uncorrected dataset, whereas this is not the case for the *TESS* or *AIT* spot corrected datasets.

a retrieval using the `AURA` code, demonstrating that the atmosphere of WASP-6b is best described as a combination of the effects of stellar heterogeneity and atmospheric hazes. However, in an effort to fit the widely disparate STIS and *Spitzer* points this retrieval predicts a very low H_2O abundance, a claim that has not been possible to verify or refute until the recent acquisition of *HST* WFC3 data from this study.

Due to the wealth of new data available with the addition of the FORS2, WFC3 and *TESS* observations we perform our own atmospheric retrieval on the uncorrected and spot corrected datasets using the `ATMO` Retrieval Code (`ARC`) which has already been used for a variety of transmission spectra to date (Wakeford et al. 2017b; Wakeford et al. 2018; Nikolov et al. 2018; Spake et al. 2018; Evans et al. 2018). For the retrieval model, the relative elemental abundances for each model were calculated in equilibrium. For each model, equilibrium chemistry was calculated on the fly, using input elemental abundances fit by assuming solar values and we allowed for non-solar scaled elemental compositions by fitting the carbon, oxygen, sodium, and potassium elemental abundances ([C/H], [O/H], [Na/H], [K/H]), which can potentially all be constrained by the transmission spectrum. We fit all remaining species by varying a single quantity for the trace metallicity, $[M_{trace}/H]$. Throughout this study, all abundances are quoted as [X/H] which is logarithmic relative to the Sun, with all solar abundances taken from Asplund et al. (2009). The resulting chemical network consisted of 175 neutral gas phase species, 93 condensates, and the ionized species e^-, H^+, H^-, He^+, Na^+, K^+, C^+, Ca^+, and Si^+. By varying both C and O separately, we mitigate several important modelling deficiencies and assumptions compared to varying the C/O ratio as a single parameter (Drummond et al. 2019). For the spectral synthesis, we included the spectroscopically active molecules of H_2, He, H_2O, CO_2, CO, CH_4, NH_3, Na, K, Li, TiO, VO, FeH, and Fe. The temperature was assumed to be isothermal, fit with one parameter, and we also included a uniform haze fit with the enhancement factor. A differential-evolution MCMC was used to infer the posterior probability distribution which was then marginalised (Eastman et al. 2013), we ran twelve chains each for 30,000 steps, discarding the burn-in before combining them into a single chain. Uniform priors were adopted, with the $\log_{10}$ abundances allowed to vary between -12 and -1.3.

Dataset	T_{eq} (K)	$\log(M_{trace}/H)$	Radius (R_J)	Haze Opacity $\ln(\frac{\sigma}{\sigma_0}$ -1)	log(C/H)	log(O/H)	log(Na/H)	log(K/H)
Uncorrected	1312^{+91}_{-89}	$-1.30^{+0.59}_{-0.45}$	$1.140^{+0.005}_{-0.003}$	$3.85^{+0.59}_{-0.83}$	<0.26	$-0.99^{+0.31}_{-0.31}$	$1.33^{+0.42}_{-0.67}$	$0.22^{+0.65}_{-0.74}$
TESS Corrected	1202^{+80}_{-74}	$-1.04^{+0.71}_{-0.61}$	$1.133^{+0.003}_{-0.003}$	$3.72^{+0.69}_{-0.62}$	<0.26	$-0.83^{+0.31}_{-0.29}$	$1.37^{+0.38}_{-0.48}$	$0.44^{+0.57}_{-0.65}$
AIT Corrected	1199^{+94}_{-80}	$-1.10^{+0.80}_{-0.56}$	$1.132^{+0.006}_{-0.005}$	$3.08^{+0.89}_{-0.92}$	<0.64	$-0.84^{+0.40}_{-0.39}$	$0.83^{+0.67}_{-0.80}$	$-0.12^{+0.71}_{-0.74}$

Table 2.4: Mean retrieved parameters for the uncorrected and corrected datasets using ARC. All abundances are quoted relative to the solar abundances of (Asplund et al. 2009) and as the log(C/H) abundances are largely unconstrained, we quote 3σ upper limits.

The resulting best fit retrieval models for the uncorrected, *TESS* corrected, and *AIT* corrected datasets all provide good fits to the data, with $\chi^2 = 75, 71$, and 73 respectively for 86 degrees of freedom. We show a visual representation of the retrieval for the *AIT* corrected dataset in Figure 2.13 and the mean values for each individual retrieval are shown in Table 2.4. To facilitate comparisons between the uncorrected and corrected datasets we plot the retrieval posteriors for each together in Figure 2.14. As with the forward model grid fits shown in Section 2.6.2 there are clear differences between the uncorrected and spot corrected datasets, particularly for the temperature, radius, and haze opacity. The difference in radius is a natural result of performing the spot correction, as this results in a wavelength dependent shift in the transmission baseline to lower transit depths. Given the square root of the transit depth $\sqrt{\delta} = R_p/R_*$, and that the stellar radius is fixed during the retrieval, any decrease in the transit depth will subsequently produce a decrease in the estimated planetary radius. In a similar fashion to the forward model grid fits, the highest temperatures and highest levels of haze opacity are favoured by the uncorrected dataset, the cause of which being the degeneracy between these properties and the effects of stellar heterogeneity on the uncorrected transmission spectrum. Upon performing a spot correction, the best fit temperature and haze opacity falls as the gradient of the optical slope has been reduced. However at least a moderate amount of haze is still required irrespective of spot correction.

Due to the freedom of the retrieval analyses we were also able to investigate the specific elemental abundances inferred from the measured transmission spectra. Firstly, as the C, O, Na, and K abundances were fit independently throughout the retrieval analysis the measured metallicity only encompasses the other elemental constituents of the atmosphere. The sub-solar metallicity measured across all retrieval analyses therefore show that no other substantial absorber is required to fit the measured transmission spectra. The *Spitzer* data points are the only observations sensitive to carbon bearing species in

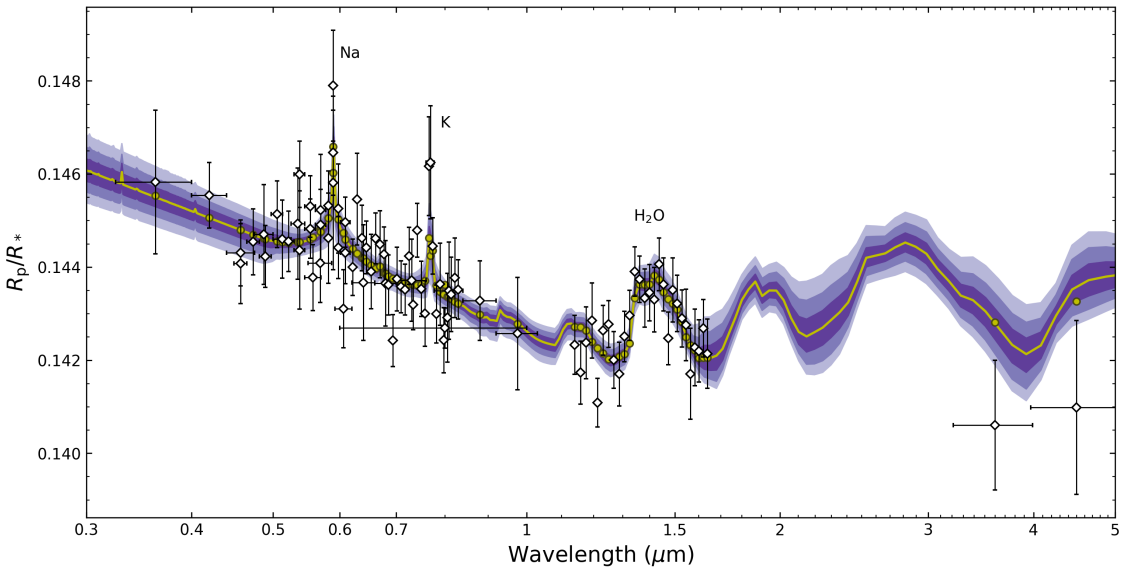

Figure 2.13: The measured *AIT* spot corrected transmission spectrum of WASP-6b (white diamonds) in addition to the best fit ARC retrieval model (yellow line) and its corresponding 1, 2 and 3σ bounds (purple shaded regions).

the atmosphere such as CH_4, CO and CO_2, however, given their non-negligible uncertainties and minimal relative offset the retrieved carbon abundance is largely unconstrained and merely represents an upper limit. This is true across all datasets as the addition of a stellar heterogeneity correction has a marginal effect towards the infrared. We constrain the carbon abundance to sub-solar at 3σ for the uncorrected and *AIT* datasets, and at 2σ for the *TESS* dataset. Our limit on the carbon abundance suggests that H_2O is the primary oxygen-bearing species, and from the observed feature we constrain the oxygen abundance to a sub-solar value, irrespective of a spot correction. For the best fit retrieval model to the *AIT* corrected dataset our oxygen abundance corresponds to a water abundance of log(H_2O) = -4.87. Given the lack of WFC3 data available to previous studies of WASP-6b this water abundance is the first to be informed by an observed water absorption feature in transmission. Furthermore, given the extensive optical data from FORS2 and STIS, this result is robust to previously observed degeneracies of water abundance and reference pressure (Griffith 2014; Pinhas et al. 2018). Contrasting to oxygen, the Na and K abundances are relaxed to lower values following the application of a spot correction as the lone Na I and K I absorption features lie in the optical region where stellar heterogeneity has a significant effect on the observed slope. Upon a reduction in the slope opacity, these abundances must necessarily drop to fit the observed data. Specifically for the *AIT*

correction, we see variations in sodium of super-solar, [Na/H] = $1.33^{+0.42}_{-0.67}$, to solar/super-solar, [Na/H] = $0.83^{+0.67}_{-0.80}$, and potassium of solar/super-solar, [K/H] = $0.22^{+0.65}_{-0.74}$, to sub-solar/solar, [K/H] = $-0.12^{+0.71}_{-0.74}$. Given the measurement precision we cannot explicitly quantify the impact of the correction as both the [Na/H] and [K/H] abundances lie within 1σ of their inferred uncorrected abundances. Despite this, the broader shifts of their full retrieved distributions (Figure 2.14) indicate that neglecting to account for the affects of stellar heterogeneity in future, higher precision, observations may lead to strictly incorrect determinations of their abundances.

As the metallicity we retrieve excludes C, O, Na, and K, we cannot perform a comparison to the [M/H] distributions obtained as part of the forward model analysis in Section 2.6.2. However, comparing the retrieved [O/H] to the forward model [M/H] we see similar distributions indicating a sub-solar metallicity. Additionally, whilst the slightly super-solar abundances of [Na/H] and [K/H] do not completely agree with the sub-solar [M/H] the large uncertainties of these distributions indicate that an overall sub-solar metallicity cannot be ruled out.

2.6.4 WASP-6b In Context

Our determined, spot corrected, oxygen abundance of [O/H] = $-0.84^{+0.40}_{-0.39}$ and sodium abundance of [Na/H] = $0.83^{+0.67}_{-0.80}$ are slightly disparate to the determined sub-solar metallicity of the host star of [Fe/H] = -0.15 ± 0.09 (Doyle et al. 2013), whilst the potassium abundance is in good agreement at [K/H] = $-0.12^{+0.71}_{-0.74}$. Variations in these elemental abundances relative to the host star could be indicative of formation history (e.g. Öberg et al. 2011), however in the case of WASP-6b the current uncertainties are not sufficiently constrained to make such determinations, with all values lying within 2σ of the host star metallicity. Further observations of the atmosphere of WASP-6b will be necessary to provide more detailed constraints on these elemental abundances. In particular, due to the presence of carbon-bearing molecular features beyond 2 μm such as CO, CO_2, and CH_4, spectroscopic observations with *JWST* will provide stronger constraints on the carbon abundance, of which this study could only provide an upper limit. This in turn will enable robust constraints on the C/O ratio and progress our understanding of the formation

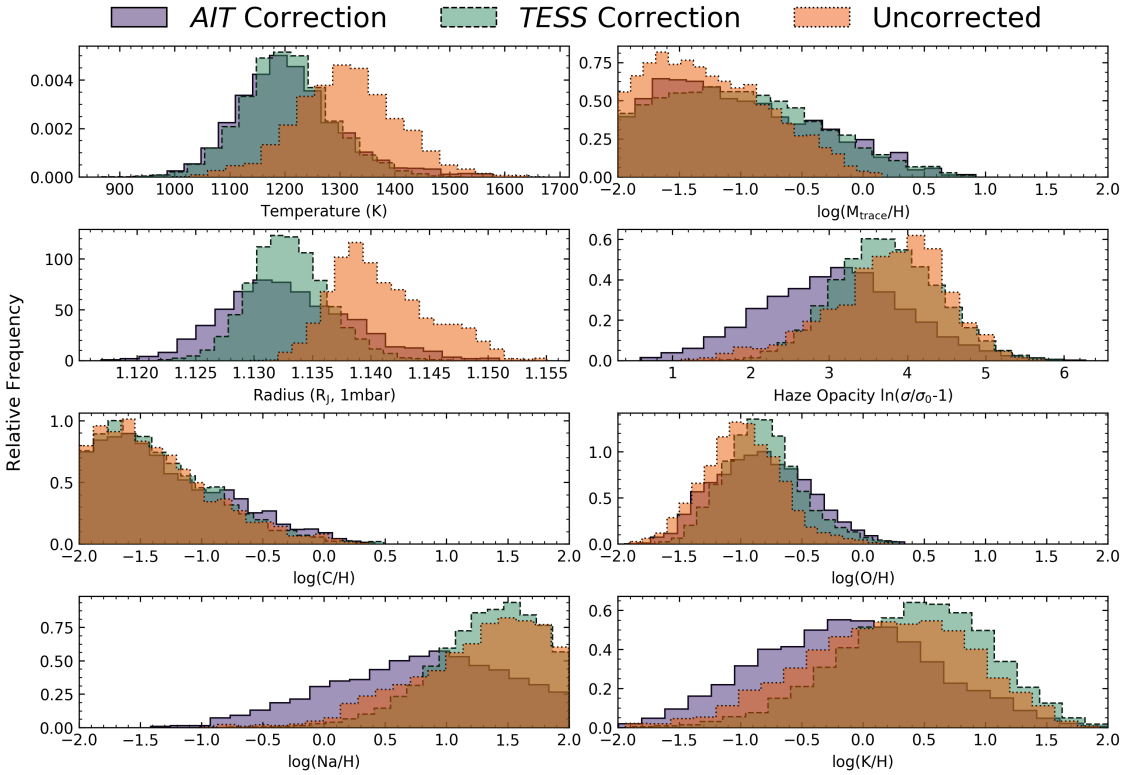

Figure 2.14: Retrieval posteriors from the ARC analysis of the uncorrected (orange, dotted line), *TESS* spot corrected (teal, dashed line) and *AIT* spot corrected (purple, solid line) datasets for WASP-6b. The metallicity and abundances of Na, K, C, and O are given with reference to solar values as taken from Asplund et al. (2009). All distributions have been normalised so that their integral is equal to unity.

history of WASP-6b.

Irrespective of the application of a stellar heterogeneity correction, both the forward and retrieval models require some level of haze opacity enhancement to describe the steep optical slope of the transmission spectrum. In the context of hot Jupiter atmospheres, this haze is often thought of as either photochemically produced, or condensate dust, scattering species within the atmosphere (Marley et al. 2013). In the case of the condensate species it is thought that the lofting of particles from deeper atmospheric cloud decks can serve to populate the upper atmosphere and lead to the observed scattering we see (e.g. Parmentier et al. 2013). Despite this, the most recent simulations of condensate particle formation in the atmosphere of the hot Jupiter HD 189733b (Bouchy et al. 2005) fail to fully reproduce its observed scattering slope (Lee et al. 2017; Powell et al. 2018). At the temperature of WASP-6b, generation of hydrocarbons through photochemistry was initially thought to be inhibited (Liang et al. 2004) and whilst sulphur photochemistry may play a role (Zahnle et al. 2009), it primarily induces a scattering slope below 0.45 μm, whereas the observed slope of WASP-6b extends further into the optical. However, recent laboratory experiments have shown that hydrocarbons may form not just in cool exoplanet atmospheres (Hörst et al. 2018; He et al. 2018), but also in hot atmospheres beyond 1000 K with a sufficiently high [C/O] = 1 (Fleury et al. 2019), a possibility our observations cannot definitively rule out. Additionally, the effects of wind-driven chemistry act to homogenise the atmospheres of tidally locked hot Jupiters such as WASP-6b and can lead to significant increases in the abundance of CH_4 compared to standard equilibrium models (Drummond et al. 2018a; Drummond et al. 2018b). Given photolysis of CH_4 can drive the formation of haze precursors (Lavvas et al. 2008), this increase in abundance may naturally lead to their more efficient production. Furthermore, of the well characterised hot Jupiter atmospheres, WASP-6b and HD 189733b present an interesting comparison as they have similar temperatures, both orbit active stars ($\log(R'_{HK})$ = -4.511 and -4.501 respectively), and both exhibit strong haze scattering slopes across the optical (Sing et al. 2016). Recent simulations of HD 189733b by Lavvas and Koskinen (2017) have shown that the formation of photochemical haze "soots" higher in the atmosphere are not excluded and can match its observed transmission spectrum. Moreover, the increased UV flux that these two planets are subject to due to their large host star activity levels is likely acting to en-

hance the rate of photochemical haze production in their atmospheres (Kawashima and Ikoma 2019). Possible evidence to this conclusion is seen in the potential trend towards stronger scattering haze signatures with reducing $\log(R'_{HK})$ (increasing activity) observed in the hot Jupiter population study of Sing et al. (2016). An exact determination of whether the haze produced in the atmosphere of WASP-6b is of photochemical origin, condensate dust origin, or a combination of the two, was not possible as part of this study due to their similar opacities at the wavelengths of these observations (e.g. Nikolov et al. 2015). In future analyses however, the relative contributions of both photochemical and condensate haze components should be considered to describe this observed scattering.

Amongst the population of spectroscopically studied exoplanets, the atmosphere of WASP-6b is one of the haziest. Previous studies of its atmosphere predicted a small (Nikolov et al. 2015; Sing et al. 2016) amplitude H_2O feature at 1.4 μm, however the feature observed as part of this study is slightly larger than anticipated. This increase is likely due to the seemingly small *Spitzer* transit depths biasing the model estimates prior to the acquisition of the FORS2 and WFC3 datasets. To quantify the size of the H_2O feature relative to an assumed clear atmosphere for WASP-6b we determine the scaled amplitude of the water feature following Wakeford et al. (2019). Specifically, we begin by taking a clear atmosphere forward model from the grid used throughout this paper (Goyal et al. 2018) with: the equilibrium temperature of WASP-6b, solar metallicity, solar C/O ratio, and no haze or cloud opacity components. We then scale this model to fit the data using a model defined as $S1 = (S0 \times p_0) + p_1$, where $S0$ is the clear atmosphere model, p_0 is the model amplitude scale factor and p_1 is a baseline offset. For the *AIT* corrected dataset we determine $p_0 = 64 \pm 12$ per cent, in contrast to the median amplitude across the observed population of $p_0 = 33 \pm 24$ per cent (Wakeford et al. 2019). These new observations indicate that despite the presence of haze, WASP-6b remains a favourable target for atmospheric characterisation, particularly with *JWST*. This potential for *JWST* to characterise hazy hot Jupiters such as WASP-6b is in contrast to those who exhibit flat, cloudy spectra such as WASP-31b (Gibson et al. 2017) and WASP-101b (Wakeford et al. 2017a).

2.7 Conclusion

We present the most complete optical to infrared transmission spectrum of the hot Jupiter WASP-6b to date utilising new observations performed with *HST* WFC3, *VLT* FORS2 and *TESS* in addition to reanalysed existing *HST* STIS and *Spitzer* IRAC data. The impact of host star heterogeneity on the transmission spectrum was investigated and we correct the observed light curves to account for these effects under different assumptions for the level of stellar activity. All reduced transmission spectra then undergo a retrieval analysis fitting in addition to being fit to a grid of forward atmospheric models.

Across all datasets we find clear evidence for Na I, K I and H_2O within the atmosphere of WASP-6b in addition to a steep increase in transit depth towards the optical. After applying both forward model and retrieval analyses we find that at least a moderate haze enhancement is required to describe the optical slope, however when neglecting even a conservative stellar heterogeneity correction, higher and potentially erroneous haze enhancement factors are more preferred. An analogous effect is also seen in the estimated temperature, where higher and potentially unphysical temperatures are preferred when there is no stellar heterogeneity correction. Both of these effects likely stem from the degeneracy of these properties and the impact of stellar heterogeneity towards increasing the optical slope of the transmission spectrum.

Whilst the precision of current observations is not sufficient to definitively estimate the impact of stellar heterogeneity on the transmission spectrum of WASP-6b, the parameter differences observed upon the application of a stellar heterogeneity correction indicate that its effect should not be neglected for future observations of exoplanetary atmospheres around moderately active stars. Despite the presence of haze in its atmosphere, WASP-6b remains a favourable target for further characterisation. Contemporaneous and broader wavelength measurements of its transmission spectrum with missions such as *JWST* will enable a more detailed characterisation of its atmosphere in addition to precisely determining the effects stellar heterogeneity has on its appearance. The first true estimates of *JWST* performance with regards to transiting observations will come from the Director's Discretionary Early Release Science Program 1366, *The Transiting Exoplanet Community Early Release Science Program* (PI: N. Batalha), at which point it will be much

easier to quantify which expected atmospheric species can be detected, and which bulk atmospheric properties can be inferred, from further observations of WASP-6b.

Chapter 3

JWST Simulations of Transiting Exoplanet Atmospheres

3.1 Statement of Contribution

Chapter 3 is based on the previous published work of Drummond et al. (2018a), Lines et al. (2018a), and Drummond et al. (2019). In each of these works the respective lead author performed the model calculations, analysis, and wrote the manuscript. A. L. Carter fulfilled a co-authorship role through simulating *JWST* data from the output forward model spectra and providing descriptions of the simulations.

3.2 Simulating *JWST* Transiting Exoplanet Data

Until *JWST* has officially launched and performed its first observations, simulations are the only way to estimate the expected data output throughout the course of an exoplanetary transit observation. Using simulated data, it is possible to make a more concrete judgement of what features one might expect to be detectable given the observation structure, instrumental mode, or target. In the case of *JWST*, making these estimations is particularly valuable given its relatively short nominal lifetime of only 5 years. *JWST* observing time will be highly competitive and robust simulations will be necessary to demonstrate the feasibility of proposed observations ahead of time. Furthermore, performing these simu-

lations in combination with the latest modelling studies allows us to assess the potential limitations of our current models, and forecast what new scientific discoveries we might expect, or should target.

With regards to transiting exoplanets, the primary method for simulating *JWST* data is through the use of the `PandExo` PYTHON package (Batalha et al. 2017). `PandExo` is based on the official *JWST* exposure time calculator `Pandeia` (Pontoppidan et al. 2016) and allows for the calculation of transiting exoplanet specific simulated data products for all of *JWST*'s time series modes, in addition to the *HST* Wide Field Camera 3 (WFC3) grisms. To perform a `PandExo` simulation, a variety of input parameters must be provided, including: a stellar spectrum, an exoplanet spectrum, the stellar apparent magnitude, the observing mode of interest, the transit duration, the observation duration, a desired noise floor, and a desired detector saturation limit. There are a variety of choices possible for the observation duration, however typical observations call for at least an equal amount of time during and outside of the transit event to ensure that an accurate baseline trend can be measured. The true noise floor of *JWST* will be difficult to determine until launch and commissioning has been completed. Until then, the best estimates indicate noise floors of 20 ppm for NIRISS, 30 ppm for NIRCam and NIRSpec, and 50 ppm for MIRI (Greene et al. 2016). Reducing the detector saturation limit from 100% can reduce the impact of detector non-linearity effects, however as these effects can be well characterised from the ground it may be possible to correct for them (e.g. Canipe et al. 2017). The remaining input values are tied to the exoplanetary system of interest. From all of these input parameters, `PandExo` first calculates the difference between the in- and out-of-transit fluxes for a desired observation as a function of wavelength. This difference can be used as a reasonable proxy for the transit depth, however does not include the effects of limb darkening. Fortunately, as limb darkening is strongest towards shorter wavelengths, and *JWST* primarily operates in the near- to mid-infrared, these effects are not as significant. However, caution should be exercised for the shortest wavelengths where this is not the case. With this assumed transit depth and the duration of the observation, `PandExo` is able to compute the predicted shot noise, read noise and background noise, and finally calculates the propagated error at each spectroscopic wavelength. Using this error, it is then possible to generate synthetic data and estimate whether certain spectral features will be observable.

3.3 Modelling Studies

In this section, I present an ensemble of three independent studies towards the forward modelling of transiting exoplanetary atmospheres: the effect of 3-dimensional wind driven advection (Drummond et al. 2018a), the effect of 3-dimensional kinetic cloud formation (Lines et al. 2018a), and the effect of model C/O parameterisation (Drummond et al. 2019). Specifically, I place my focus on the simulated *JWST* data presented in these studies, and its implications for future transiting observations.

3.3.1 Wind Driven Chemistry

Typically, the modelling of chemical kinetics in exoplanetary atmospheres is limited to 1-dimensional prescriptions due to issues of complexity, and computational tractability. However, even under this limited framework, many studies have demonstrated that vertical transport of chemical species throughout the atmosphere can lead to departures from chemical equilibrium (e.g. Moses et al. 2011; Venot et al. 2012; Drummond et al. 2016). Towards hotter and deeper atmospheric regions the timescale for chemical kinetics is typically faster than that of vertical mixing timescale and thermochemical equilibrium is maintained. In contrast, at cooler and higher regions of the atmosphere the timescale for chemical kinetics is reduced, allowing material deposited through vertical mixing from the deeper atmosphere to enrich the upper atmosphere (Visscher and Moses 2011). Additional efforts have been made to investigate these effects at higher dimensions for hot Jupiter exoplanets, in particular Agúndez et al. (2014) in pseudo-2D using a 1-dimensional kinetics models and a time-varying temperature pressure profile, and Cooper and Showman (2006) using a 3-dimensional atmospheric circulation model coupled with both a chemical and temperature relaxation scheme. However, these studies provide contrasting results, with Agúndez et al. (2014) suggesting that horizontal mixing is more important due to the transport of material from the cooler night-side of the planet, whilst Cooper and Showman (2006) suggest that vertical mixing remains the dominant effect.

Recently, Drummond et al. (2018a) also performed such an investigation for the hot Jupiter HD 209458b to compare the disequilibrium effects of both vertical and horizontal mixing to the more simplistic equilibrium prescription. However, this study differs from

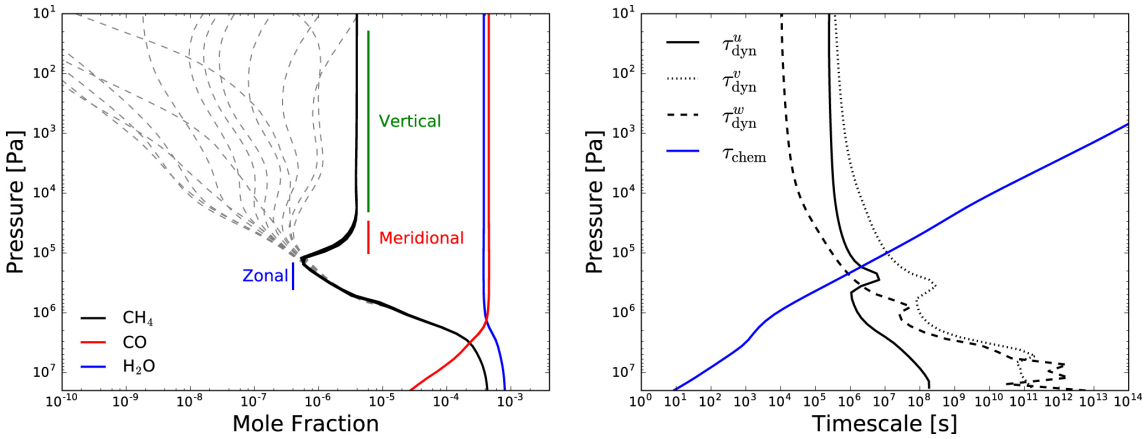

Figure 3.1: *Left*: Vertical abundance profile for water, methane, and carbon monoxide under both the equilibrium (dashed) and relaxation (solid) simulations at a series of longitudinal points at the equator. *Right*: Estimated chemical kinetic and dynamical mixing timescales, where τ_{chem} corresponds to the chemical kinetic timescale and τ^{u}_{dyn}, τ^{v}_{dyn}, τ^{w}_{dyn} correspond to the zonal, meridional, and vertical mixing timescales respectively. Figure from (Drummond et al. 2018a).

the previous multi-dimensional studies of Cooper and Showman (2006) and Agúndez et al. (2014) as it utilises the Met Office Unified Model 3-dimensional general circulation model (Mayne et al. 2014), consistently coupled with both the chemical relaxation scheme of Cooper and Showman (2006) and the SOCRATES radiative transfer scheme (Edwards 1996; Edwards and Slingo 1996). The results of these simulations (Figure 3.1) demonstrate that both vertical and horizontal mixing influences the overall chemical composition in hot Jupiter atmospheres. In comparing to the equilibrium abundance profiles it is clear that this mixing leads to homogenisation of the atmospheric CH_4 abundance at all longitudes. In particular, the most upper regions of the atmosphere at pressures below $\sim 10^4$ Pa are primarily influenced by vertical mixing, whilst the region between $\sim 10^6 - 10^4$ Pa is primarily influenced by horizontal mixing. At pressures higher than this, the chemical kinetic timescale is much smaller than the mixing timescales and the equilibrium and disequilibrium simulations are in agreement.

Potential variations in the CH_4 abundance in the upper atmosphere are highly significant for both transmission and emission spectrum observations of hot Jupiter exoplanets. In particular, increases in the CH_4 abundance due to disequilibrium processes should enhance the absorption within the CH_4 spectral bands. The significance of these effects was investigated by computing forward model transmission and emission spectra for the simulations as shown in Figure 3.2. Variations between the two simulations are imme-

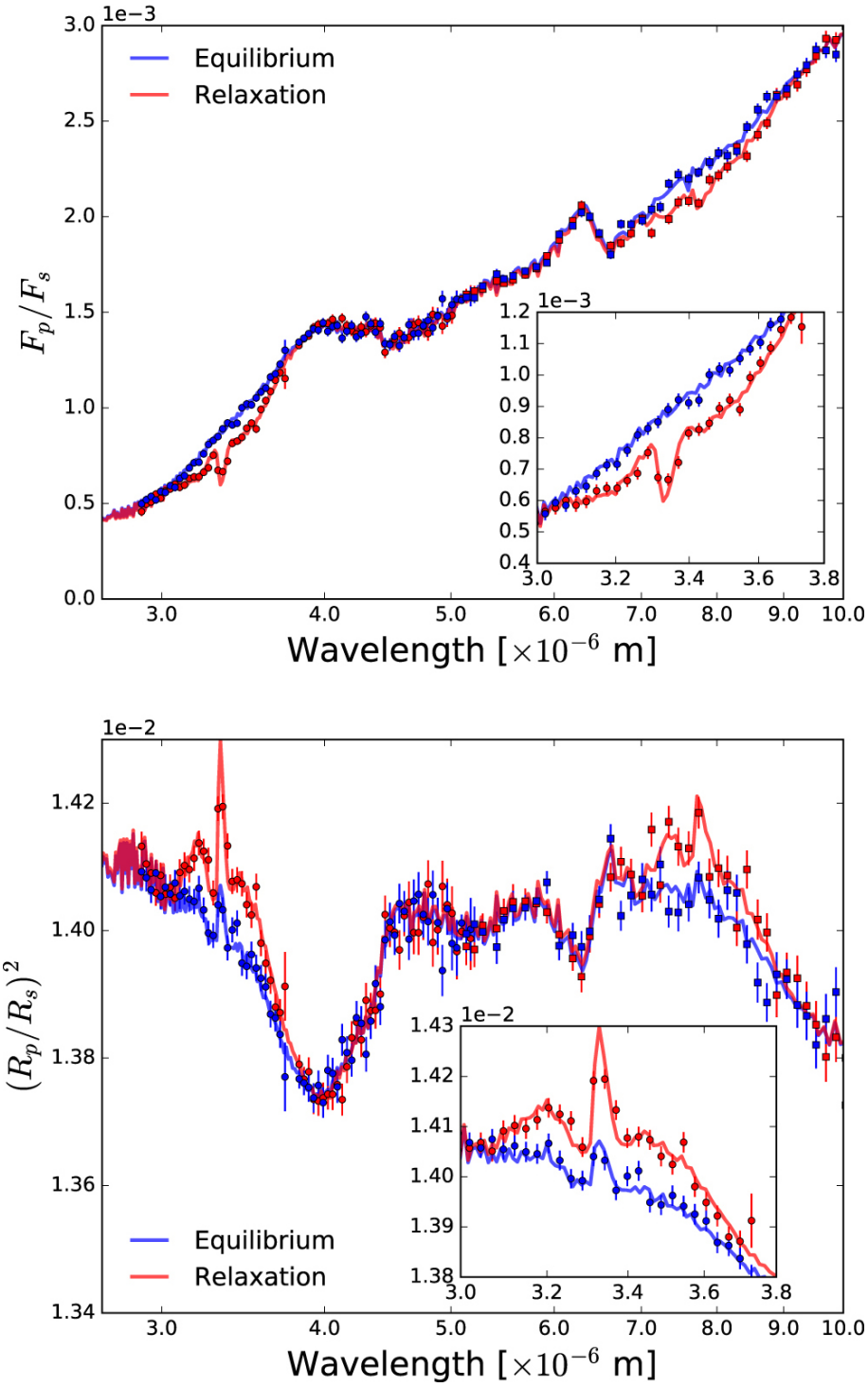

Figure 3.2: Emission (*Top*) and transmission (*Bottom*) spectra of the simulations. In each case, `PandExo` simulated data are also plotted for the NIRSpec G395H (circles) and MIRI LRS (squares) modes, binned down to resolutions of R =60 and R =30 respectively. Clear and measurable deviations can be seen between the two different simulated scenarios. Figure from (Drummond et al. 2018a).

diately evident at the CH_4 absorption bands between 3-4 μm and 7-9 μm. To determine whether these effects would be observable with *JWST*, we also produced a `PandExo` simulation. Specifically, the simulations were performed for a single occultation of HD 209458b in both transmission and emission using the NIRSpec G395H and MIRI LRS modes. An equal amount of in- to out-of-transit time, a noise floor of 50 ppm, and detector saturation set at 80% was adopted. The stellar and planetary parameters necessary for the simulation were retrieved from the TEPCAT[1] database (Southworth 2011) and the stellar spectrum used was identical to the one used in the simulation. All instrument related parameters were kept at the `PandExo` defaults. Finally, to improve the precision of these measurements, the data were binned down to a resolution of $R = 60$ and $R = 30$ for the NIRSpec and MIRI data respectively.

The resultant simulated data demonstrates that these variations will be very easy to observe with *JWST* (see Figure 3.2). In the aforementioned CH_4 absorption bands between 3-4 μm and 7-9 μm the signal- to-noise and resolution of the data are more than sufficient to visually discern between the two scenarios. However, there are many other effects that could potentially lead to variations in the CH_4 abundance such as the intrinsic atmospheric C/O ratio, metallicity, and temperature. As a result, it would be necessary to obtain similar constraints on molecular abundances such as CO and H_2O to definitively determine that disequilibrium processes were driving this increased absorption. Fortunately, as *JWST* is capable of performing transiting exoplanet observations from ~0.6-12 μm, expected features due to these species will be readily accessible. Additionally, some of these constraints have already been made using instruments such as *HST* and *VLT* in the optical to near-infrared (e.g. Wakeford et al. 2017a; Evans et al. 2018; Nikolov et al. 2018; Carter et al. 2020). Finally, comparisons of *JWST* data to 1D models must be made with careful consideration of which 3D effects are potentially being neglected to avoid biases in the measured atmospheric properties.

3.3.2 Silicate Cloud Features

Clouds are observed on every solar system planet that hosts an atmosphere, and may similarly exist in the atmospheres of exoplanets. With recent transmission spectroscopy ob-

1. Transiting ExoPlanet CATalogue; https://www.astro.keele.ac.uk/jkt/tepcat/

servations, evidence towards this hypothesis has been found in the form of muted spectral features, attributed to an increased, broad-wavelength, cloud opacity (e.g. Sing et al. 2016; Wakeford et al. 2017a; Alam et al. 2018; Wakeford et al. 2019). This muting effect significantly hampers our ability to effectively characterise exoplanetary atmospheres, and as a result the inclusion of clouds within forward model spectra is crucial towards understanding exactly how our data are being affected. Ensembles of such models have been produced (e.g. Goyal et al. 2018; Goyal et al. 2019a) with varying degrees of "cloudiness" and have proved successful in fitting both clear (Nikolov et al. 2018) and cloudy atmospheres (Alam et al. 2018). A clear atmosphere does not mean that the atmosphere is devoid of clouds entirely, but rather that the pressure level at which clouds are formed is likely below the region from which the observed photons are being detected. The majority of current forward model spectra are computed in 1D, and rely on simple parameterisations of the cloud opacity. In reality, the presence and absorption of clouds is tightly connected to the atmospheric thermochemical conditions and circulation. As a result, a number of efforts have been made to include the effects of clouds within 3D global circulation models of exoplanetary atmospheres (e.g. Parmentier et al. 2013; Parmentier et al. 2016; Lee et al. 2016; Lines et al. 2018b) to better understand the overall cloud dynamics, radiative feedback, and impact on observables. In particular, the work of Lines et al. (2018b) couples the Met Office Unified Model (Mayne et al. 2014) to the SOCRATES radiative transfer scheme (Edwards 1996; Edwards and Slingo 1996) and a state-of-the-art disequilibrium cloud formation model which incorporates the nucleation, growth and evaporation of seed cloud particles in addition to cloud particle advection, or precipitation through gravitational settling (Helling et al. 2008; Lee et al. 2016).

In Lines et al. (2018a) the work of Lines et al. (2018b) is extended to produce the first ever model transmission spectra of a hot Jupiter from a fully 3D global circulation model with radiatively active clouds. The specific cloud dust species used in these models are TiO_2, SiO, SiO_2, $MgSiO_3$, and $MgSiO_4$, which are predicted to be the most abundant in hot Jupiter atmospheres (Helling et al. 2008). All models are generated for the prototypical transiting hot Jupiter HD 209458b with: a clear atmosphere, a transparent cloudy atmosphere that includes only the radiative effects of clouds, a cloudy atmosphere which excludes scattering effects, a cloudy atmosphere which excludes absorption effects, and

a full opacity cloudy atmosphere. In addition, models are produced for the full opacity cloudy atmosphere at varying levels of cloud opacity by scaling the absorption and scattering coefficients. All of these models are displayed in Figure 3.3. In the transparent cloudy case, simply the presence of clouds has acted to cool the atmosphere, increasing the abundance of CH_4 as evident in the spectral features at 3.3 and 7.8 μm. In the full cloudy simulation the spectrum is flattened from ~0.3-5 μm due to the greatly enhanced Mie scattering from the cloud particles. Further into the infrared, absorption from the cloud species plays a more significant role and produces a distinctly broad and almost flat feature, peaking at approximately 9 μm. In reality, this broad feature is a mixture of absorption features due to the different absorption profiles of the produced cloud species (Lines et al. 2018a). For the lower opacity cloudy models the absorption feature at 9 μm becomes clearer due to the reduced Mie scattering at the longer wavelengths, however at wavelengths below 1 μm this scattering is still strong and the features due to Na, K, and H_2O are still heavily muted.

As current instrumentation limits transmission spectrum observations to wavelengths shorter than ~5 μm for photometry and ~2 μm for spectroscopy, all detections of clouds within exoplanetary atmospheres have been indirectly assumed from flat spectra attributed to Mie scattering. As the models in this study show, in addition to other previous studies (e.g. Wakeford and Sing 2015), direct absorption from cloud species can only be readily identified towards mid-infrared wavelengths beyond 5 μm. Therefore, *JWST* presents the closest and best opportunity to directly detect cloud species for the first time.

To determine whether the cloud absorption seen in these models would be observable with *JWST*, we also produced a `PandExo` (Batalha et al. 2017) simulation for each model as shown in Figure 3.4. Specifically, the simulations were performed for a single occultation of HD 209458b in both transmission and emission using the NIRSpec G395H and MIRI LRS modes. An equal amount of in- to out-of-transit time, a noise floor of 50 ppm, and detector saturation set at 80% was adopted. The stellar and planetary parameters necessary for the simulation were retrieved from the TEPCAT database (Southworth 2011) and the stellar spectrum used was identical to the one used in the simulation. All instrument related parameters were kept at the `PandExo` defaults. To improve the pre-

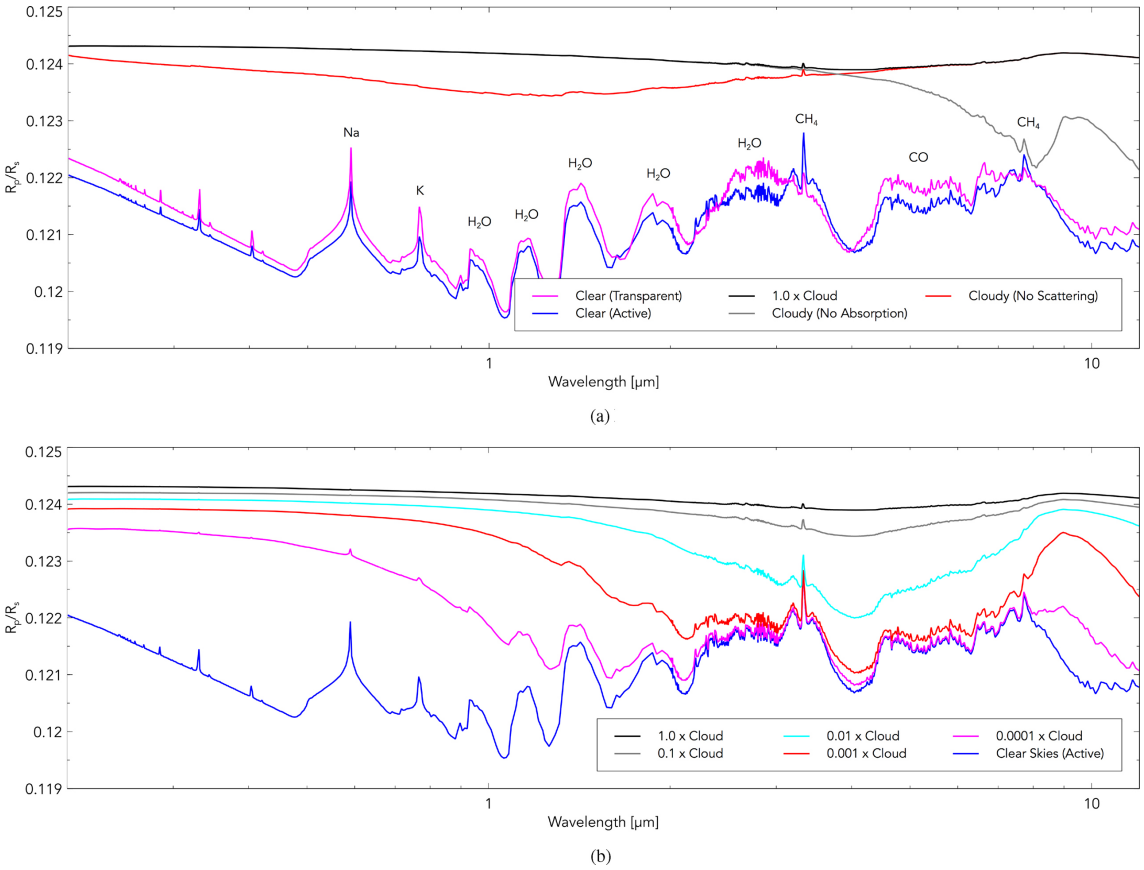

Figure 3.3: Forward model transmission spectra. *Top*: Models of clear-sky transmission (magenta), a clear-sky transmission from a cloudy atmosphere (blue), full cloudy atmosphere (black), cloudy atmosphere without scattering (red), cloudy atmosphere without absorption (grey). *Bottom*: Models from a clear-sky transmission with a cloudy atmosphere (blue), in addition to a fully cloudy atmosphere with a varying scale factor for the cloud opacity. Figure from (Lines et al. 2018a)

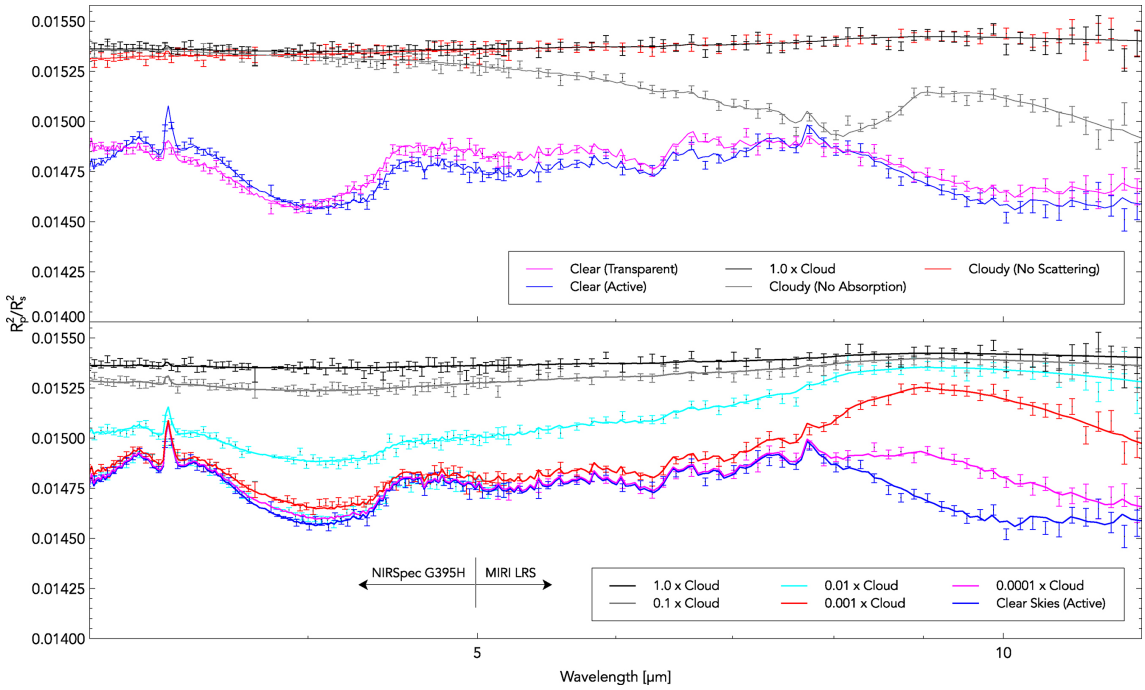

Figure 3.4: The same models as in Figure 3.3, expect with additional simulated *JWST* data. Figure from (Lines et al. 2018a)

cision of these measurements, the data were binned down to a resolution of $R = 60$ and $R = 30$ for the NIRSpec and MIRI data respectively. For the full opacity cloudy simulation the absorption feature peaking at 9 μm is 70 ppm in scale, larger than the estimated MIRI noise floor. However, even if the MIRI noise floor were higher, the feature is broad enough that as an ensemble the data would likely be more than sufficient to detect it. We estimate the significance of the detection by comparing the simulated data to both the model it was generated from, and a number of different flat, "grey", spectra across a range transit depths through a collection of χ^2 tests. For the cloudy model we obtain a $\chi^2_{\rm cloudy}$=117 and for the best fit grey spectra we obtain a $\chi^2_{\rm grey}$=228, each with 122 degrees of freedom. This difference rules out a grey atmosphere at 5.6σ and suggests that detecting this cloud absorption feature will be possible with *JWST*. Towards lower cloud opacities the absorption feature only becomes more distinct, and as a result will be even easier to measure. Furthermore, whilst the transmission spectra of the 1x, 0.1x, and 0.01x cloudy opacity models are very similar from the optical to the near-infrared, they differ significantly near the 9 μm feature. As a result, it will likely also be possible to assess the strength of the cloud absorption opacity with *JWST*.

3.3.3 Modelling Assumptions of the C/O Ratio

The intrinsic C/O ratio of an exoplanetary atmosphere will have dramatic effects on the composition, and relative abundances, of molecular species within it (Madhusudhan 2012; Moses et al. 2013b). Additionally, due to the different radial distribution of gas and dust species within a protoplanetary disk, the atmospheric C/O ratio is uniquely tied to the formation and evolutionary history of the exoplanet as a whole (Öberg et al. 2011; Öberg and Bergin 2016). By observing the atmospheres of transiting exoplanets through transmission and emission spectroscopy to constrain the C/O ratio, it may also be possible to constrain its formation pathway (e.g. via gravitational instability (Boss 1997) or core accretion (Pollack et al. 1996)). Unfortunately, it has proven quite difficult to obtain robust constraints of the C/O ratio of exoplanets due to the observational limitations at longer wavelengths where absorption features due to carbon-bearing species such as CH_4, CO, and CO_2 are more significant. However, with the advent of *JWST*, and the improved resolution at near- to mid-infrared wavelengths that it will provide, it will be possible to obtain these constraints for the first time through data comparisons to forward model or retrieval transmission and emission spectra.

Within a simulation of an exoplanetary atmosphere, one can theoretically vary the C/O ratio by either varying the carbon abundance relative to hydrogen (C/H) or the oxygen abundance relative to hydrogen (O/H). As the C/H and O/H ratios independently drive further variations in the chemical equilibrium composition of an atmosphere, simply choosing to vary one of these quantities over the other to modulate the C/O ratio could result in biases in forward model spectra. However, of the many studies that have investigated the precise effects of C/O variations on the atmospheric composition and structure, a number fix O/H and vary C/H (Helling and Lucas 2009; Madhusudhan et al. 2011b; Moses et al. 2013b; Tsai et al. 2017), whilst in contrast many fix C/H and vary O/H (Moses et al. 2013a; Mollière et al. 2015; Goyal et al. 2018). To determine the degree to which these assumptions affect forward model transmission and emission spectra, we investigate the effect of varying either the C/H or the O/H ratio when generating simulations at C/O ratios equal to 0.1 and 2.0 Drummond et al. (2019). Specifically, these models are produced using the 1D atmospheric model `ATMO` (Tremblin et al. 2015; Drummond

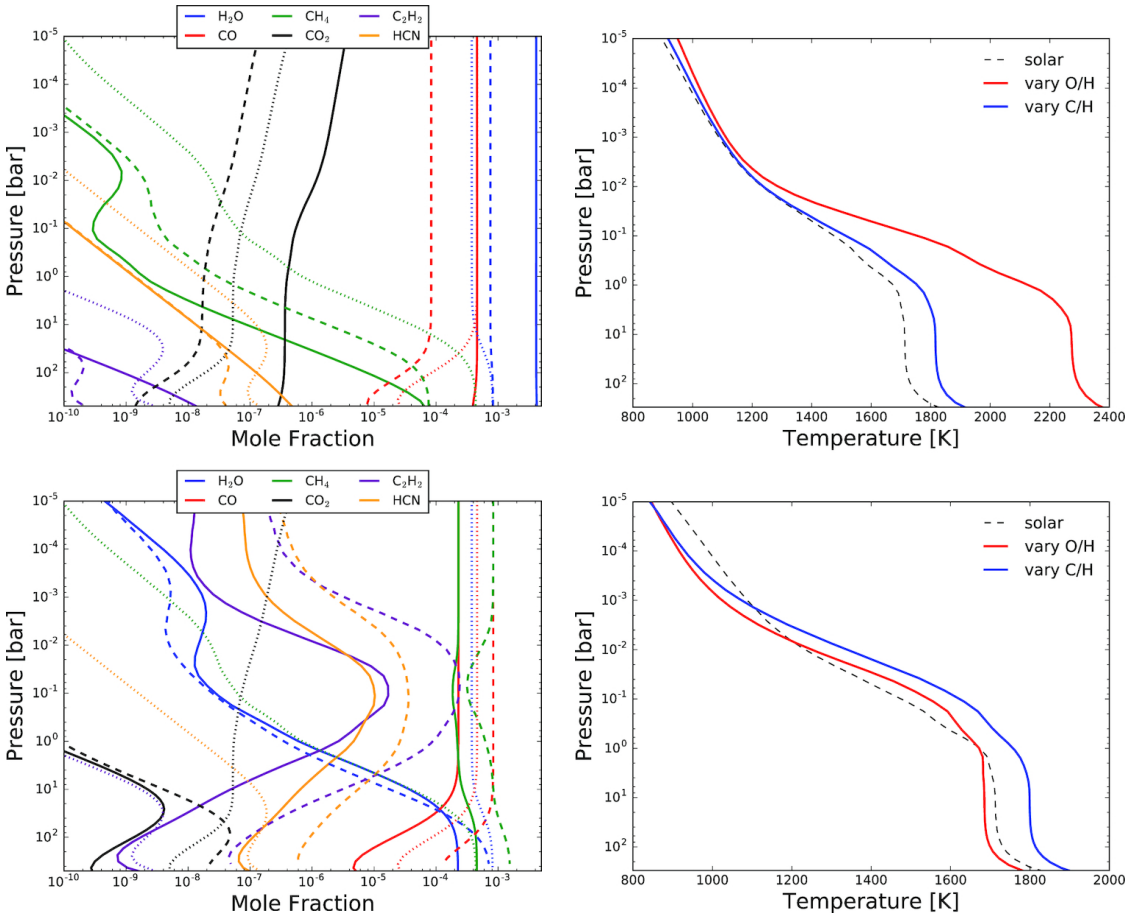

Figure 3.5: *Left*: Mole fractions of the most abundant species for the hot atmosphere at a C/O ratio of 0.1 (top) and 2.0 (bottom). The simulation with varying O/H are represented by solid lines, the simulation with varying C/H are represented by dashed lines, and mole fractions assuming solar abundance are represented by dotted lines. *Right*: Pressure temperature profiles for the hot atmosphere simulations at a C/O ratio of 0.1 (top) and 2.0 (bottom). Figure from (Drummond et al. 2019).

et al. 2016; Goyal et al. 2018; Goyal et al. 2019a) for both a "warm" atmosphere where CH_4 is the most abundant carbon species, and a "hot" atmosphere where CO is the most abundant carbon species. These simulations are meant to serve as approximations to the warm Neptune GJ 436b and the hot Jupiter HD 209458b, however they should not be interpreted as predictions for their atmospheres in particular. Figures 3.5 and 3.6 display the vertical distributions of the most abundant molecular species alongside temperature pressure profiles from these simulations for the hot and warm atmospheres respectively. In all cases the temperature pressure profiles are affected by the variation in C/O ratio from solar, and uniquely affected dependent on whether the C/H or O/H ratio was varied to reach this value of C/O.

For the hot atmosphere, C/O=0.1 scenario, the reduced carbon abundance means

that more oxygen is available to form H_2O as opposed to being locked up in CO. This heats the atmosphere as H_2O has many absorption bands across a broad wavelength range, driving the pressure temperature profiles away from the solar abundance case. However, the simulations demonstrate that this effect is much more significant for the case when O/H is varied in comparison to C/H. For the hot atmosphere, C/O=2.0 scenario, in both the case where the C/H is varied or O/H is varied, the reduced oxygen abundance means that excess carbon is available to produce carbon species other than CO, such as CH_4, CO_2, C_2H_2, and HCN, and less oxygen is available to form H_2O. The reduction in H_2O abundance acts to cool the atmosphere, however variations in carbon bearing species also affect the temperature profile. At pressures below $\sim 10^{-2}$ bar, the reduced H_2O cooling dominates, however between $\sim 10^{-2}$ bar and $\sim 10^{0}$ bar heating due to absorption from C_2H_2 and HCN counteracts and even overcomes this cooling. At pressures above $\sim 10^{0}$, the reduced oxygen in the case where O/H is varied also reduces the overall CO abundance, further cooling the atmosphere. This is in contrast to the case where C/H is varied and the overall CO abundance increases, heating the atmosphere and is the reason these temperature pressure profiles lie above and below the solar abundance case.

For the warm atmosphere, C/O=0.1 scenario, heating due to increased H_2O abundance is also observed, however only for the case where O/H is varied. At these temperatures CH_4 is already the dominant carbon bearing species and the vast majority of oxygen is already held in H_2O, therefore in the case when C/H is varied an insignificant amount of oxygen is freed and the H_2O abundance does not significantly increase. Instead, when the C/H abundance is varied the abundance of CH_4 is decreased and an overall cooling effect is observed. For the warm atmosphere, C/O=2.0 scenario, an inverse process occurs. When O/H is varied less oxygen is available to form CO and H_2O and an overall cooling effect is observed. Conversely, when C/H is varied more carbon is available for the formation of carbon species, primarily CH_4, slightly heating the atmosphere.

As the abundance of these molecular species varies, so does the overall absorption of the atmosphere as a function of wavelength. To assess the significance of these differences, forward model transmission and emission spectra were computed for the warm and hot atmospheres at C/O ratios of 0.1 and 2.0, for both the case where C/H is varied, and where

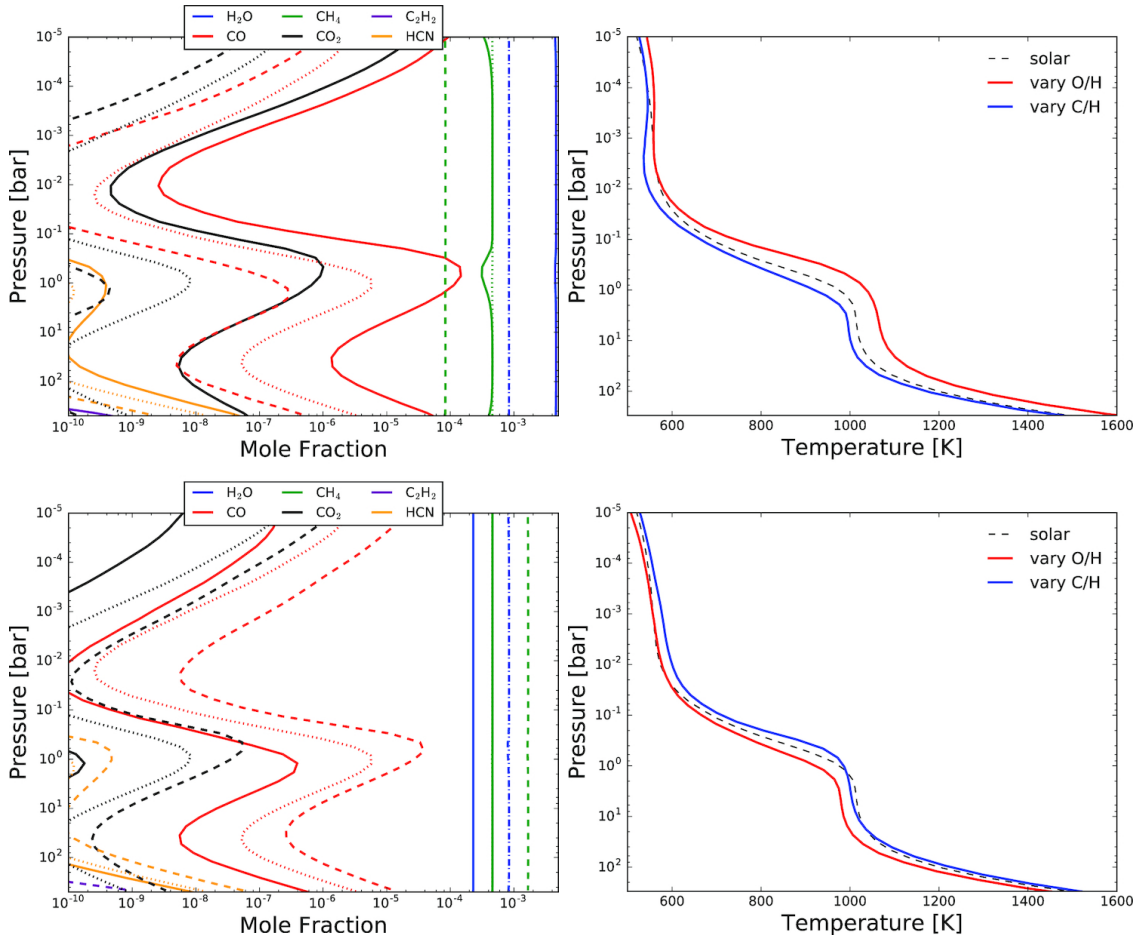

Figure 3.6: As in Figure 3.5 but for the warm atmosphere. Figure from (Drummond et al. 2019).

O/H is varied (Figures 3.7, 3.8). To compare the transmission models more effectively, a vertical shift is applied to approximately align the solar abundance case to the cases where C/H and O/H are varied along the optical scattering slope. We predict whether any of the observed differences would be significant, given the precision of *HST* and *JWST*, by producing corresponding `PandExo` (Batalha et al. 2017) simulations for each forward model. For the transmission spectra we simulate data in the *HST* WFC3 G102 and G141 modes, in addition to the *JWST* NIRSpec G140H, G235H, G395H, and MIRI LRS modes. As the emission signal is relatively weak below ~3μm, for the emission spectra we only simulate data in the NIRSpec G395H and MIRI LRS modes. In all simulations a noise floor of 50 ppm was adopted for each mode, the detector saturation level was set to 80%, and an equal amount of in- to out-of-transit was used. For the hot atmosphere the signal is sufficiently large that only one transit or eclipse is necessary, however for the warm atmosphere two eclipses were used for the emission spectra. The stellar and planetary

properties for the hot and warm atmosphere cases were taken from the TEPCAT database (Southworth 2011) entry for HD 209458b and GJ 436b respectively. For the *HST* WFC3 simulations, all necessary orbital and exposure parameters were taken from Deming et al. (2013) for the hot atmosphere case (corresponding to HD 209458b) and from Knutson et al. (2014) for the warm atmosphere case (corresponding to GJ 436b). For the *JWST* simulations, all instrument parameters were kept at the `PandExo` defaults.

In the hot atmosphere transmission spectra at C/O=0.1 there is a broadly wavelength independent increase in the overall transit depth for both the case where C/H is varied and O/H is varied. This is a result of the increased H_2O abundance as seen in Figure 3.5, which drives further absorption over this H_2O feature dominated wavelength range. Aside from this, differences in the absorption at ~4.3 μm are observed due to the respective increase, or decrease, in the CO_2 abundance for the cases where O/H or C/H are varied. In the C/O=2.0 transmission simulations, significant differences appear between the solar case and both the cases where C/H or O/H are varied due to the depletion of H_2O and increase in CH_4 absorption. Between the C/H and O/H cases there is however still an offset, resulting from the increased abundance of CH_4 in the case where C/H is varied compared to the case where O/H is varied (Figure 3.5). For the hot atmosphere emission spectra at C/O=0.1 an overall decrease in eclipse depth is evident. This stems again from the increased H_2O absorption which reduces the emitted flux from the deeper, hotter, atmosphere. Similarly to the transmission case, differences are observed at 4.3 μm due to variations in CO_2 absorption. Finally, for the emission spectra at C/O=2.0 dramatic differences are also seen due to CH_4 replacing H_2O as the dominant absorbing species, with the C/H case having its emitted flux reduced the most owing to slightly larger CH_4 and H_2O abundances.

For the warm atmosphere transmission spectra at C/O=0.1, the absorption at all wavelengths in the case where O/H is varied is increased primarily due to the increased H_2O abundance (Figure 3.6). Conversely, in the case where C/H is varied there is a clear decrease in transit depth which stems from the reduced CH_4 absorption. Variations between the two models can also be seen due to their differing CH_4 abundances, in addition to an offset at 4.3 μm resulting from their differing CO_2 abundances. In the C/O=2.0 trans-

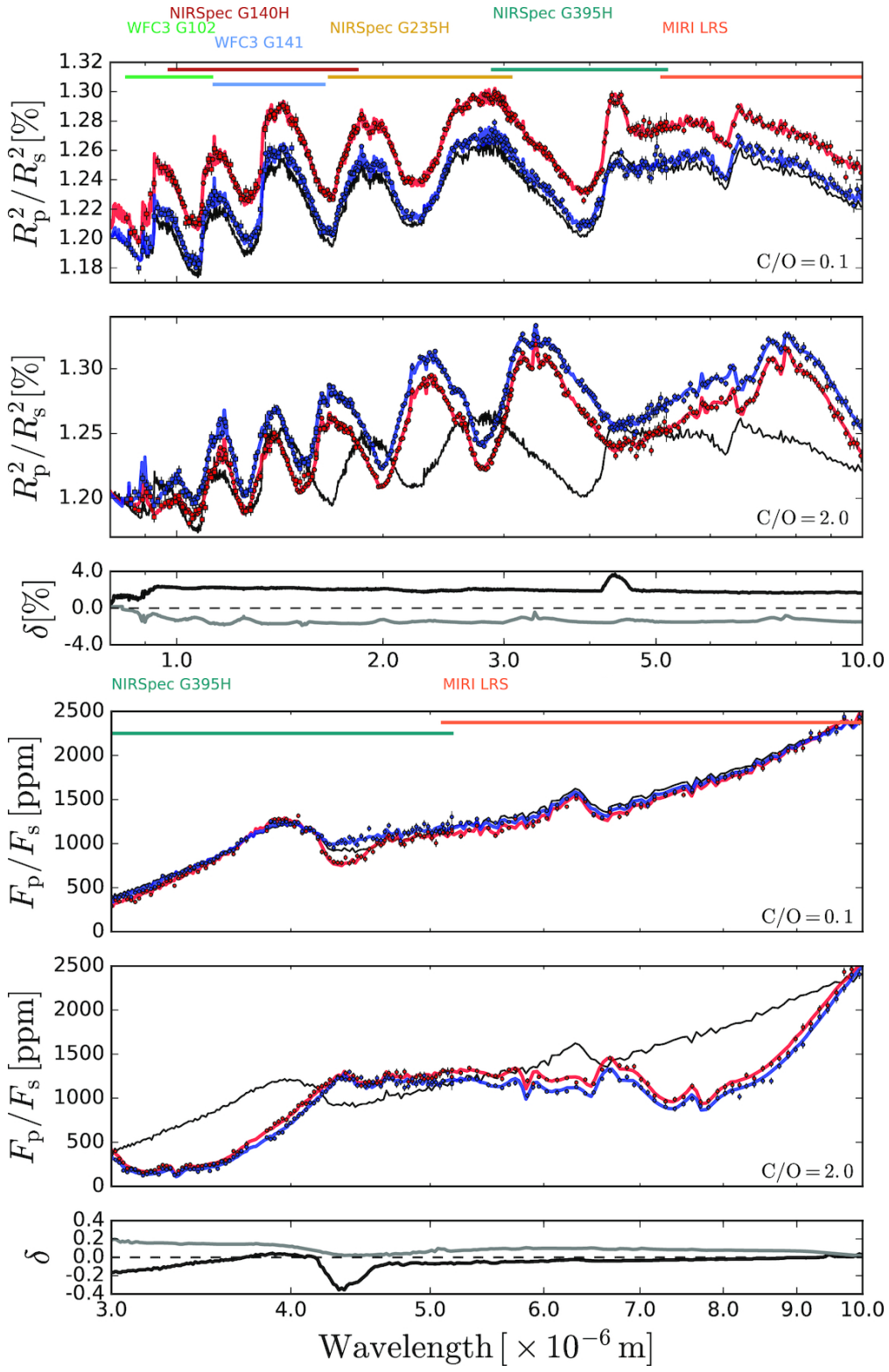

Figure 3.7: Transmission and emission spectra for the hot atmosphere simulations. The top two panels represent the transmission spectra for both the C/O=0.1 and C/O=2.0 scenarios for the case where C/H is varied (blue lines), the case where O/H is varied (red lines), and the solar abundance case (black lines). In the third panel the fractional difference between the C/H and O/H case are shown for the C/O=0.1 scenario (black line), and the C/O=2.0 scenario (grey line). The bottom three panels are similar to the top three panels, however they instead show the emission spectra. Figure from (Drummond et al. 2019).

mission case, there is almost no difference between the solar case and the case where O/H is varied as the abundance of CH_4, which is the dominant absorber, does not vary between them. However, for the case where C/H is varied, the CH_4 abundance also increases and the absorption is greater than the solar case. For the warm atmosphere emission spectrum at C/O=0.1, when C/H is varied the competing effects of the reduced CH_4, CO and CO_2 abundances (which increases the emitted flux from deeper and hotter regions of the atmosphere) and the overall cooler atmosphere (Figure 3.6), drive small negative and positive variations in the eclipse depth as a function of wavelength. A similar but opposite effect is observed for the case where O/H is varied. For the C/O=2.0 emission spectra, very little difference can be seen between the C/H, O/H, or solar cases.

As a complete ensemble, the cases where C/H is varied and the cases where O/H is varied produce fundamentally different transmission and emission spectra. The discrepancies between these scenarios are consistently larger than the predicted precision of *JWST* observations as assumed from `PandExo` simulations. Even in the C/O=2.0 emission spectra, whilst differences between the spectra may not be evident by eye, across the broad wavelength range provided by *JWST* the difference is statistically significant. In particular, data generated from the model where C/H is varied gives a χ^2=172 for that model, compared to a χ^2=1205 for the model where O/H is varied. As a result, to avoid biases when modelling the transmission and emission spectra of transiting exoplanets, it is crucial to examine the full set of elemental abundances respective to hydrogen, as opposed to ratios such as the C/O ratio. This is particularly relevant when comparing models to observations, as it may result in incorrect determinations of atmospheric properties.

3.3.4 Conclusions

This chapter covers a collection of three independent studies into the detectability of 1D and 3D modelling effects in *JWST* transmission and emission spectroscopy observations of transiting exoplanets. In the first study, performed by Drummond et al. (2018a), a 3D GCM with consistent radiative transfer, chemistry, and hydrodynamics is used to explore the effect of wind-driven disequilibrium chemistry for the hot Jupiter HD 209458b. The combined effects of horizontal and vertical mixing act to drive an increase in the methane

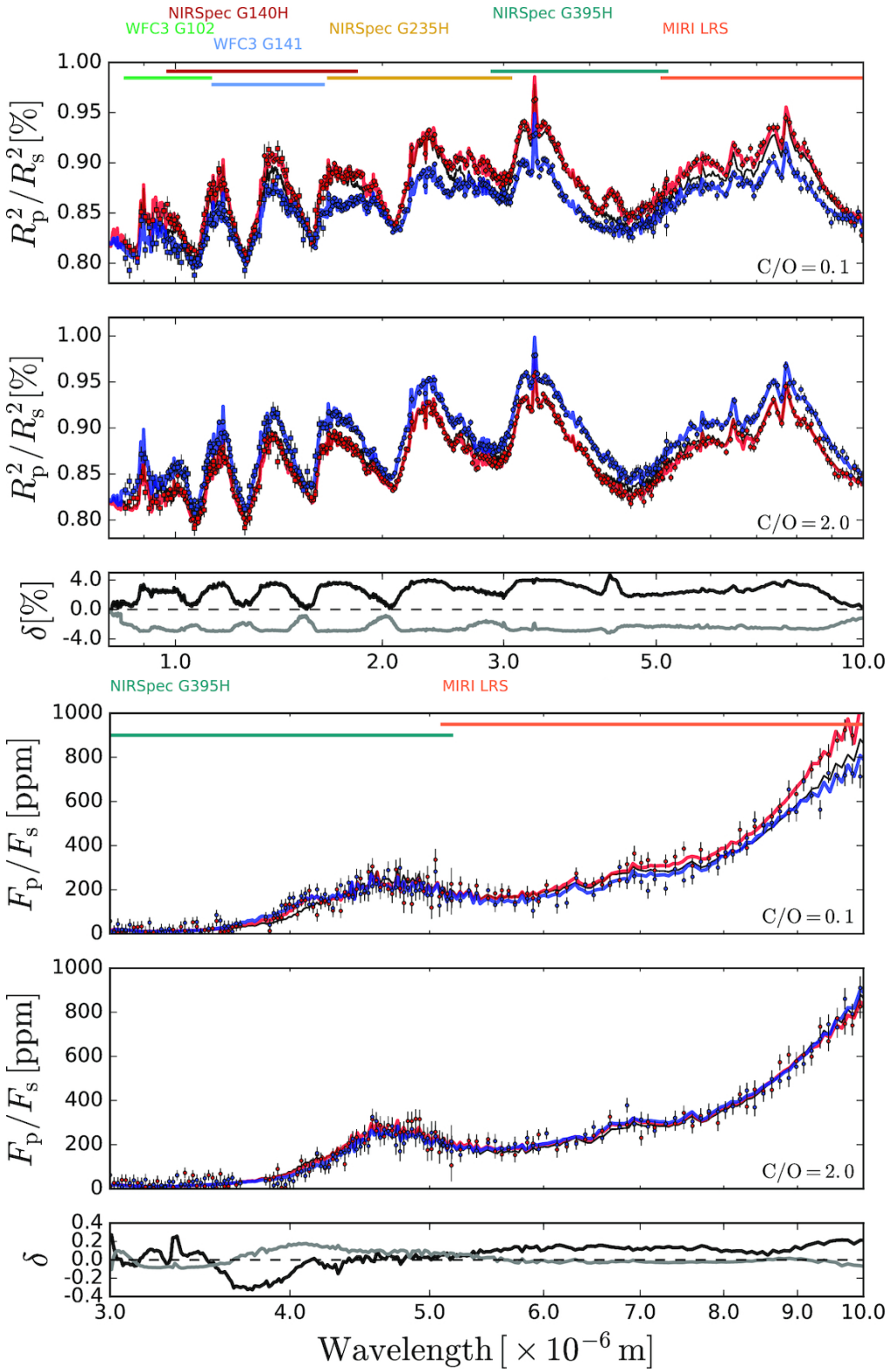

Figure 3.8: As in Figure 3.7, but for the warm atmosphere. Figure from (Drummond et al. 2019).

abundance which produces variations in the observable transmission and emission signatures of carbon species compared to that of a typical equilibrium model. In the second study, performed by Lines et al. (2018a), the first transmission spectrum from a 3D GCM including radiatively active clouds is produced for the hot Jupiter HD 209458b. Due to their large vertical extent, the produced clouds act to mask any molecular absorption features. However, the model does indicate a broad absorption feature due to absorption of mixed-composition cloud species that differentiates it from a typical "grey" cloud prescription. Finally, the third study performed by Drummond et al. (2019) investigates the methodological effect of varying the C/H or O/H abundance when introducing variations to the bulk atmospheric C/O ratio in 1D forward models. For both cases of a prototypical hot Jupiter and warm Neptune, the independent variations in the C/H and O/H abundance necessary to achieve an identical C/O ratio result in distinctly different atmospheric compositions, temperature-pressure profiles, transmission spectra, and emission spectra. For each of the aforementioned studies, the produced transmission and emission spectra were provided to the *JWST* transiting exoplanet simulation tool PandExo. In all cases the described variations or features are above the limiting sensitivity of the simulated observations and should be considered when interpreting true *JWST* data.

A key advantage of the first two studies by Drummond et al. (2018a) and Lines et al. (2018a) is that they are computed using 3D models. As a result they provide a more physically accurate description of how the global atmosphere of an exoplanet will be affected by different model assumptions compared to that of a more computationally tractable 1D atmospheric model. Furthermore, in some cases such as the study by Drummond et al. (2018a), a 1D model is simply not able to encapsulate the physical processes of interest, and a 3D model is a necessity. With the advent of *JWST* and its increased precision and resolution, more simplistic descriptions using 1D models are likely to be less useful and models that can incorporate multi-dimensional effects will be necessary in order to fully describe observed transmission and emission spectra. However, whilst 3D forward models are powerful predictive tools, they are very computationally intensive and in some cases it may not be practical, or even possible, to perform them for a broad range of desired initial conditions. In addition to this computational intensity, the complexity of 3D models makes exploring the interaction between modelling effects - such

as gas phase chemistry, cloud phase chemistry, disequilibrium processes, full chemical kinetics, and more - inherently challenging. Towards the future, 3D models will be valuable tools for understanding the atmospheres of exoplanets, however it will likely also be necessary for the more parameterised 1D models to increase in complexity in order to incorporate the known 3D effects and match *JWST* spectra as accurately as possible without requiring large amounts of computational time.

The final study by Drummond et al. (2019) illustrates that even when using the most up-to-date models, fundamental assumptions regarding their construction and execution can affect the resultant transmission spectrum. With the data quality that *JWST* will provide, these differences could be so significant as to drive variations in the determined atmospheric composition and bulk properties. Therefore, as it becomes necessary to include more complicated physical processes into forward models, it will also be necessary to constantly reflect on the assumptions that go into these models to ensure that the conclusions that are made are not fundamentally biased.

Chapter 4

JWST Coronagraphy of Exoplanets in Nearby Young Moving Groups

4.1 Statement of Contribution

Chapter 4 is based on a currently unpublished study, A. L Carter et. al (in preparation). In this work, A. L. Carter designed and performed the simulations, calculated the contrast curves, and wrote the manuscript. M. Bonavita performed the conversion from mass sensitivity to detection probability map.

4.2 Introduction

The direct imaging of exoplanetary companions remains a critical avenue towards our understanding of planetary formation and evolution due to its ability to probe the widest separations of exoplanetary systems, a region of parameter space largely inaccessible to the more prolific transit or radial velocity methods. Over the last decade, direct imaging surveys have optimised their target selection to maximise the detection of exoplanetary mass companions (e.g. Nielsen et al. 2013; Vigan et al. 2017; Stone et al. 2018; Nielsen et al. 2019). In particular, focus is placed on the distance and age of the target systems. For stars closer to us, the angular scales explored in a high-contrast observation correspond to physical separations where planetary companions are more common (Mordasini 2018). Younger

stars are preferable targets as at early ages exoplanets are more luminous and therefore easier to distinguish (Burrows et al. 1997; Baraffe et al. 2003; Phillips et al. 2020). Furthermore, at the earliest ages it is much easier to distinguish between different scenarios for the initial entropy conditions and in turn more robustly measure the exoplanetary mass (Marley et al. 2007; Spiegel and Burrows 2012; Marleau and Cumming 2014). However, obtaining precise ages for individual stellar systems is particularly challenging (Mamajek and Hillenbrand 2008; Soderblom 2010), and significantly limits our ability to select optimal survey samples.

Fortunately, this limitation can be overcome by selectively observing objects within nearby young moving groups, coeval associations of stars that share the same galactic space motion. These associations provide a unique advantage as the ages of their constituent members can be determined more robustly (within a few Myr) by combining typical indicators of youth with their 3-dimensional galactic motions (Bell et al. 2015). Young moving groups remain a principal area of exploration towards directly imaging exoplanets, and a number of surveys have focused their attention at least partially towards them (e.g. Lafrenière et al. 2007; Biller et al. 2013; Brandt et al. 2014; Chauvin et al. 2015; Bowler et al. 2015; Galicher et al. 2016; Nielsen et al. 2019). In fact, a large proportion of the known directly imaged exoplanets have been discovered around stars within young moving groups (Bowler 2016).

Discovering and further characterising exoplanetary companions through direct imaging is most readily accomplished with near- to mid-infrared observations. It is at these wavelengths that the spectral energy distributions of cooler, lower mass, objects peak and the contrast between companion and host star is at its lowest (Skemer et al. 2014). Additionally, these wavelengths are rich with spectral absorption features that enable us to probe atmospheric structure, dynamics, and composition, in addition to the overall formation and migration history of an exoplanet (Madhusudhan 2019). Thus far the overwhelming majority of direct imaging surveys have been performed from the ground – where it is feasible to build a telescope with a spatial resolving power large enough at these wavelengths to detect exoplanetary companions. However, these observations are not without limitations. The effect of Earth's atmosphere is significant: advanced adap-

tive optics techniques must be used to account for atmospheric wavefront distortion, only particular wavelength regions can be observed due to the atmospheres inherent transmittance, and day-to-day weather variations reduce observing efficiency. Furthermore, the increasing noise resulting from the thermal emissivity of the telescope itself compounds with the intrinsically larger sky thermal background beyond ~3 μm. It has therefore become more and more desirable to conduct these observations from space.

Currently scheduled for launch during 2021, the *James Webb Space Telescope* (*JWST*) (Gardner et al. 2006) will significantly transform our ability to both detect and characterise exoplanets through direct imaging. *JWST* will be host to a diverse range of observing modes across its four instruments, enabling a similarly diverse range of observations to be performed. Crucially, *JWST* will have the largest aperture of any space telescope to date, alleviating all ground-based concerns of the Earth's atmosphere and allowing it to reach an unprecedented level of sensitivity. Furthermore, as *JWST* is located in space it is able to have a very broad functional wavelength range, spanning from ~0.6−28 μm. When considering only the observing modes relevant to direct imaging of the closest separation exoplanets, this range is reduced to ~1−16 μm. However, this is still a significant increase over current instruments which are constrained below ~5 μm.

Given the relatively short amount of time until the launch of *JWST*, it is prudent to assess the predicted capabilities of its direct imaging modes towards exoplanet detection. Such an analysis was initially performed by Beichman et al. (2010), however the understanding of *JWST* performance has increased significantly over the last decade due to a variety of observatory tests and the creation of more robust simulation tools. Furthermore, new and sophisticated exoplanet atmosphere and evolutionary models have been produced (e.g. Phillips et al. 2020), enabling a more accurate determination of their predicted luminosities. Recently, Perrin et al. (2018) provided a significant, target unspecific, update to the contrast predictions for *JWST*, Sallum and Skemer (2019) gave a recent account of the non-redundant masking and kernel phase capabilities of *JWST*, and finally Brande et al. (2020) have assessed the feasibility of *JWST* mid-infrared coronagraphic imaging of field-aged exoplanets at short separations around the nearest stars. With these studies in mind, we focus our efforts towards determining the overall limits of *JWST* coro-

nagraphic imaging for a set of observations of the previously discussed nearby young moving groups.

In Section 4.3 we discuss our choice of young moving groups and the objects within them, in Section 4.4 we describe the performed simulations. Our primary results are shown in Section 4.5, and finally we summarise our conclusions in Section 4.6

4.3 Young Moving Group Selection

As there are currently 26 known, well defined, associations younger than ~ 200 Myr within 150 pc (Gagné et al. 2018b; Gagné et al. 2018a; Zuckerman 2019; Meingast et al. 2019; Curtis et al. 2019), it is necessary to select the young moving groups among this sample that will be best suited for searches of wide separation companions through direct imaging. Specifically, throughout this study we focus our efforts on the TW Hya Association (TWA) (Kastner et al. 1997; Gagné et al. 2018b) and the β Pictoris Moving Group (βPMG) (Zuckerman et al. 2001; Gagné et al. 2018b). Both of these moving groups occupy a unique region of parameter space, with ages old enough that planetary formation processes have largely ended due to disk clearing (Haisch et al. 2001), ages young enough that any potentially formed planets have retained a significant amount of heat from their initial gravitational contraction and are therefore more luminous (Baraffe et al. 2003; Phillips et al. 2020), and distances close enough to probe the innermost architectures of planetary systems through direct imaging. Although many other moving groups fulfil one or even two of these qualities (Gagné et al. 2018b), currently TWA and βPMG present the best opportunity to fulfil all three at once and are hence chosen for this investigation.

Whilst there is a known distribution in the distances of individual young moving group members, generally the members of TWA lie ~60 pc away, whereas the members of βPMG lie ~30 pc away. Therefore, observations of βPMG members are more likely to probe smaller physical separations where planetary formation is more common (Mordasini 2018). However, TWA has an estimated age of 10 ± 3 Myr, whereas βPMG has an estimated age of 24 ± 3 Myr (Malo et al. 2014; Bell et al. 2015). Observations of TWA members are therefore likely to be more sensitive to lower mass planets, as they have recently

formed and are naturally more luminous (Baraffe et al. 2003; Phillips et al. 2020).

As the known populations of both TWA and βPMG have grown since their original classifications, we use the on-going compilation of members based on Gagné et al. (2018b) (updated with *Gaia* DR2 astrometry and kinematics from Gaia Collaboration et al. 2016; Gaia Collaboration et al. 2018) to select objects for this study. Specifically, we select objects that: have a high membership probability of >90%, have at least two complementary measurements from radial velocity, parallax, or youth, and are the primary object within their respective system. Following this selection, we obtain 30 sample objects for TWA and 64 sample objects for βPMG. Each individual object and its properties are listed in Tables A.3 and A.4, and the distribution of these samples in distance and spectral type is shown in Fig. 4.1.

4.4 *JWST* Coronagraphic Imaging Simulations

Of the four instruments aboard *JWST*, three have direct imaging capabilities. Namely, the Near-InfraRed Camera (NIRCam) (Rieke et al. 2005) has five separate coronagraphic masks, the Mid-InfraRed Imager (MIRI) (Rieke et al. 2015) has four coronagraphic masks, and the Near-InfraRed Imager and Slitless Spectrograph (NIRISS) (Doyon et al. 2012) has aperture masking interferometry capabilities through the use of a non-redundant mask (Sivaramakrishnan et al. 2012) (see the Introduction for more details). For NIRCam and MIRI in particular, we show the photon conversion efficiencies (PCEs) of the filters that can be paired with these masks as calculated by the *JWST* exposure time calculator `Pandeia` (Pontoppidan et al. 2016) in Fig. 4.2. The PCE describes the fraction of incoming photons that will be detected in the final science field of view, and includes the effects of the optical telescope element, detector efficiency, filter throughput, and coronagraph transmission.

Of the five NIRCam masks, we do not consider the two bar masks due to their potential to completely obscure normally detectable objects at position angles that lie underneath the mask. Additionally, we do not consider the MASK210R round mask as it is only compatible with filters below 2.3 μm, a wavelength range that ground-based telescopes are likely to have superior performance across. Of the two remaining round masks we select

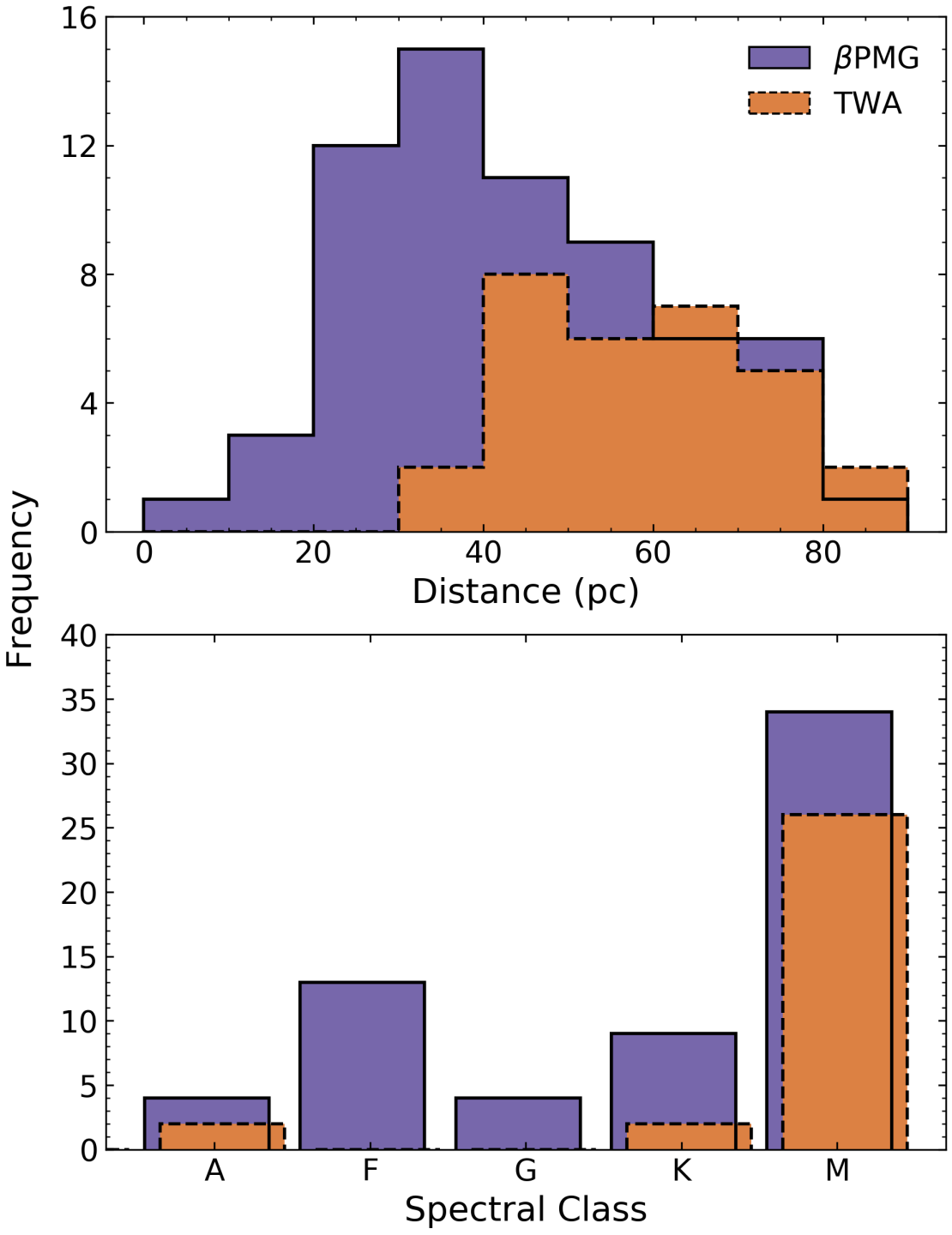

Figure 4.1: Overlapping histograms of the selected βPMG (purple, solid line) and TWA (orange, dashed line) populations in both distance (top) and in spectral class (bottom).

the MASK335R for all of the NIRCam simulations due to its superior inner working angle (IWA) compared to the MASK430R and with the knowledge that any potential improvement in contrast with the MASK430R is relatively small following PSF subtraction (Perrin et al. 2018). As there are a large number of filters compatible with NIRCam coronagraphic imaging (Fig. 4.2), we only select the broad F356W and F444W filters to be simulated in this study. From a subset of preliminary simulations similar to those described in Section 4.4.2, we find that the F444W filter is generally the best suited of the NIRCam filters to identify the lowest mass objects. In a small number of cases however, the F460M and F480M filters perform just as well, if not slightly better (~0.02 M_J greater mass sensitivity). The F444W filter is selected in particular for this study as we are primarily interested in the broad, population based, sensitivity limits of *JWST* coronagraphic imaging, and not those of a small subset of targets. In contrast, the F356W filter lies directly on a broad CH_4 absorption band and is therefore much less suitable for direct imaging of the lowest mass companions. Nevertheless, we find that it is the most optimal filter between $3-4$ μm and select to include it as a comparison to the F444W filter.

Three of the four MIRI coronagraphic masks are of a four-quadrant phase mask (4QPM) design at 10.65, 11.40 and 15.50 μm, with the final mask of a classical Lyot design at 23 μm Fig. 4.2. The mask at 23 μm has a large IWA of 2.16" which makes it typically unsuitable for exoplanet observations and is therefore not considered as part of this work. All three of the 4QPMs utilise a specific paired filter to optimise the cancellation of stellar light at the centre of the mask and the choice of mask is therefore tied to the wavelength of interest. For this investigation, we select the F1140C and F1550C mask/filter combinations. Only the F1140C filter is selected of the two filters between $10-12$ μm as the F1065C filter is designed to probe an NH_3 absorption band and will therefore be less able to detect cooler (lower mass) exoplanets as NH_3 is more abundant in their atmospheres.

The method of direct imaging performed by NIRISS is vastly different to that performed by traditional coronagraphy. NIRISS utilises a non-redundant mask to convert the full *JWST* aperture into an interferometric array. This allows NIRISS to perform observations at a higher angular resolution than *JWST* coronagraphy, but only at separations shorter than ~400 mas (Sivaramakrishnan et al. 2009). Given the significantly different

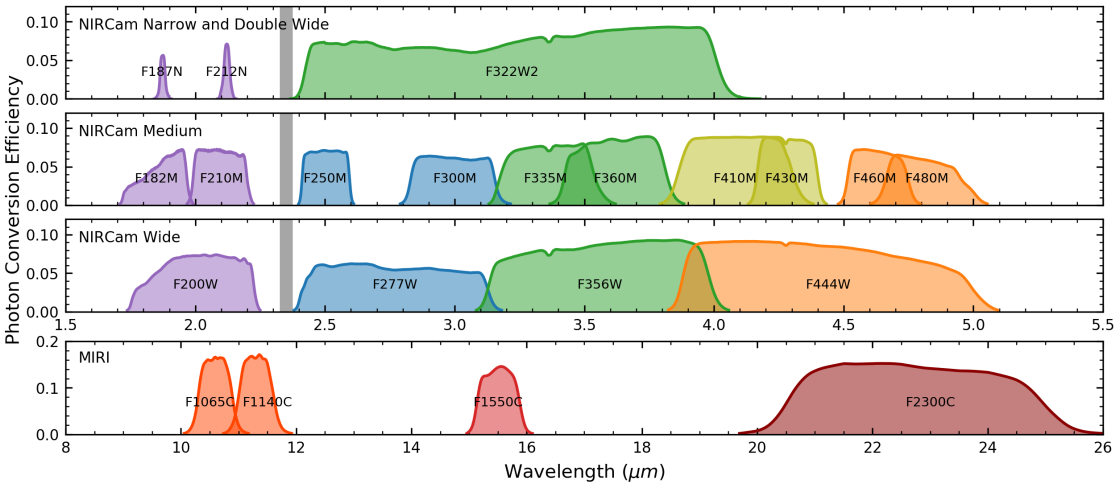

Figure 4.2: All *JWST* filters that are compatible with its coronagraphic imaging modes and the corresponding photon conversion efficiencies (PCEs) for an observation in such a setup. Grey lines indicate the gap in wavelength coverage between the short and long wavelength channels of the NIRCam detectors. All short wavelength channel NIRCam PCEs are computed using the throughput of the MASK210R round mask, and all long wavelength channel NIRCam PCEs are computed using the MASK335R round mask. All PCEs are determined using the *JWST* exposure time calculator, `Pandeia` (Pontoppidan et al. 2016).

method of operation versus that of standard coronagraphy and the unique techniques required for their simulation, we do not incorporate any NIRISS observations into this study. However, a recent account of NIRISS detection limits performed by Sallum and Skemer (2019) suggests that in the F430M and F480M filters, NIRISS will be able to detect objects seven magnitudes fainter than their host star beyond ~100 mas. The mass sensitivity limits corresponding to this detection limit are dependent on the age and magnitude of the observed system, but could potentially reach sub-Jupiter mass companions around a 1 Myr object at 140 pc, with an absolute stellar magnitude below ~3 in the F430M/F480M filters (Sallum and Skemer 2019).

4.4.1 SED Selection

Prior to performing imaging simulations on each individual target in the sample it is necessary to generate their corresponding spectral energy distributions. This process begins by matching the *Gaia B-R* colour (Gaia Collaboration et al. 2016; Gaia Collaboration et al. 2018) of each target to a corresponding effective temperature ($T_{\rm eff}$) and $\log(g)$ using theoretical stellar isochrones. The isochrones used are those from Baraffe et al. (2015), covering $0.07 - 1.4\ M_{\odot}$, and Haemmerlé et al. (2019) covering $0.8 - 120\ M_{\odot}$. In order to retrieve as accurate a value as possible, each set of isochrones are interpolated to the age

of the system of interest before the values of $T_{\rm eff}$ and $\log(g)$ are determined. Additionally, for those objects that lie in the overlapping region between the two models we compute a weighting

$$\alpha = \frac{G_{B-R,\rm target} - \max(G_{B-R,\rm Haemmerle})}{\min(G_{B-R,\rm Baraffe}) - \max(G_{B-R,\rm Haemmerle})} \tag{4.1}$$

where $G_{B-R,x}$ is the *Gaia B-R* colour for a target or model x. This weighting is then used to compute the values of $T_{\rm eff}$ and $\log(g)$ for these objects using the linear relation

$$Q = \alpha Q_{\rm Baraffe} + (1-\alpha) Q_{\rm Haemmerle} \tag{4.2}$$

where Q is the value of interest, and $Q_{\rm Baraffe}$ and $Q_{\rm Haemmerle}$ are the corresponding model values given an initial $G_{B-R,\rm target}$ value. Examples of these isochrones for βPMG, including the linear relation for the overlapping region, are shown in Fig. 4.3.

SEDs for each object are then found by matching the determined $T_{\rm eff}$ and $\log(g)$ values to theoretical spectra. As Haemmerlé et al. (2019) do not provide spectra corresponding to their evolutionary models, for any objects with temperatures above the ~7000 K limit of the Baraffe et al. (2015) models we instead use the BOSZ models of Bohlin et al. (2017) (see also Mészáros et al. 2012). In all cases we assume solar metallicity during the spectral selection. Finally, each SED is normalised to its respective target's magnitude in the *WISE W2* bandpass (Wright et al. 2010; Cutri and et al. 2013).

4.4.2 `PanCAKE` Simulations

All simulations are performed using the PYTHON package `PanCAKE`[1] (Van Gorkom et al. 2016; Perrin et al. 2018; Girard et al. 2018), which is based on the official *JWST* exposure time calculator `Pandeia` (Pontoppidan et al. 2016). Given a desired input scene, `PanCAKE` is capable of producing corresponding 2D simulated images for all coronagraphic observations with the NIRCam and MIRI instruments aboard *JWST*. For every object in the sample we simulate observations using NIRCam's MASK335R with the F356W and F444W filters, and MIRI's F1140C and F1550C masks. A block diagram demonstrating the steps performed in these observations alongside example images from the F444W simulations are displayed

1. Pandeia Coronagraphy Advanced Kit for Extractions; https://github.com/spacetelescope/pandeia-coronagraphy

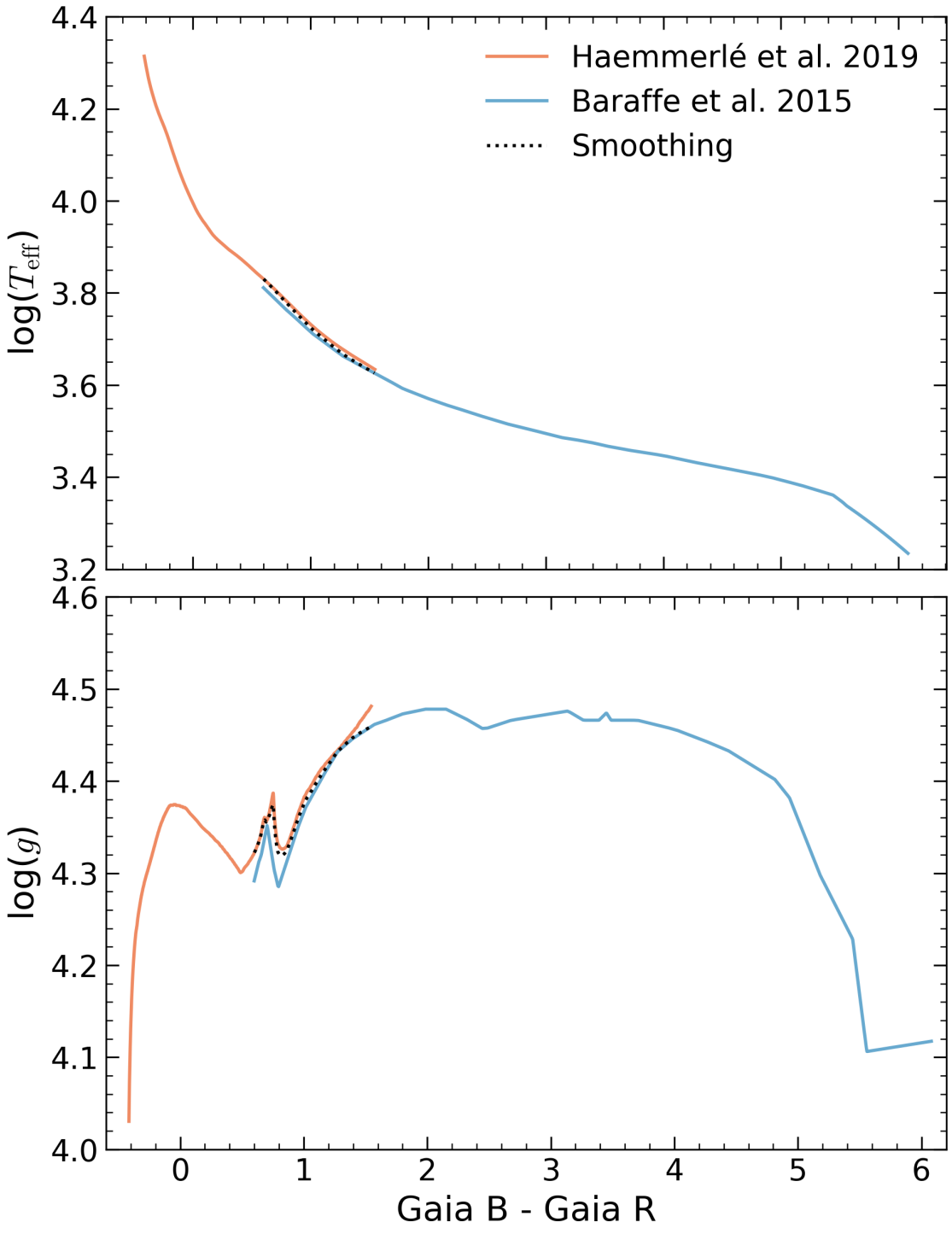

Figure 4.3: 24 Myr isochrones of log($T_{\rm eff}$) and log(g) versus *Gaia* $B - R$ colour corresponding to βPMG from the (Baraffe et al. 2015) (blue) and (Haemmerlé et al. 2019) (orange) evolutionary models. Similar curves for TWA are not displayed for clarity, but exhibit very similar variations. The black dotted lines indicate the smoothing of the two models in their overlapping region.

in Figure 4.4 and described in detail below.

4.4.2.1 Target and Reference Observations

For each target, simulated observations are performed on the target star and a reference assumed to be identical in spectral type and magnitude to that of the target. Whilst mismatches in spectral type can lead to non-optimal PSF subtraction, differences on the order of a few subtypes are unlikely to significantly impact the estimated contrast performance (Perrin et al. 2018) and we therefore assume that a viable reference can be found for every target in the sample. Unlike the target observations, we repeat the reference star observations nine times following a circular small-grid dither (SGD) pattern. Despite the time intensive nature of such a procedure, utilising a SGD technique significantly improves the contrast performance of *JWST* observations (Soummer et al. 2014; Lajoie et al. 2016) and as such will likely be necessary to reach the true contrast limits for *JWST* coronagraphy. Furthermore, the expensive nature of these observations may be mitigated somewhat during a true observation by selecting a reference star brighter than that of the target.

In reality it is not possible to centre the target or reference behind the coronagraphic mask due to the intrinsic pointing accuracy of *JWST*. We include this effect in the simulations by applying a target acquisition error equal to a random draw from a normal distribution with a standard deviation equal to 5 mas. However, these offsets between target and coronagraphic mask lead to unique variations in the resultant simulated image and therefore biases in the determination of the simulated contrast curve. In these simulations we mitigate such affects by repeating each individual simulation 10 times to generate a statistical sample from which the contrast curve can later be determined.

When performing a default simulation, the `PanCAKE` package utilises a library of PSFs which are precomputed across the coronagraphic field of view. As a result, variations in the simulated images due to small offsets such as the target acquisition error will not be accurately represented. We remedy this issue in our simulations by enabling the `on_the_fly_PSFs` setting within `PanCAKE`. This setting circumvents the use of the precomputed library and instead calculates the precise PSF using the `WebbPSF` dependency (Perrin et al. 2014). To make the simulations computationally tractable we reduce the wavelength

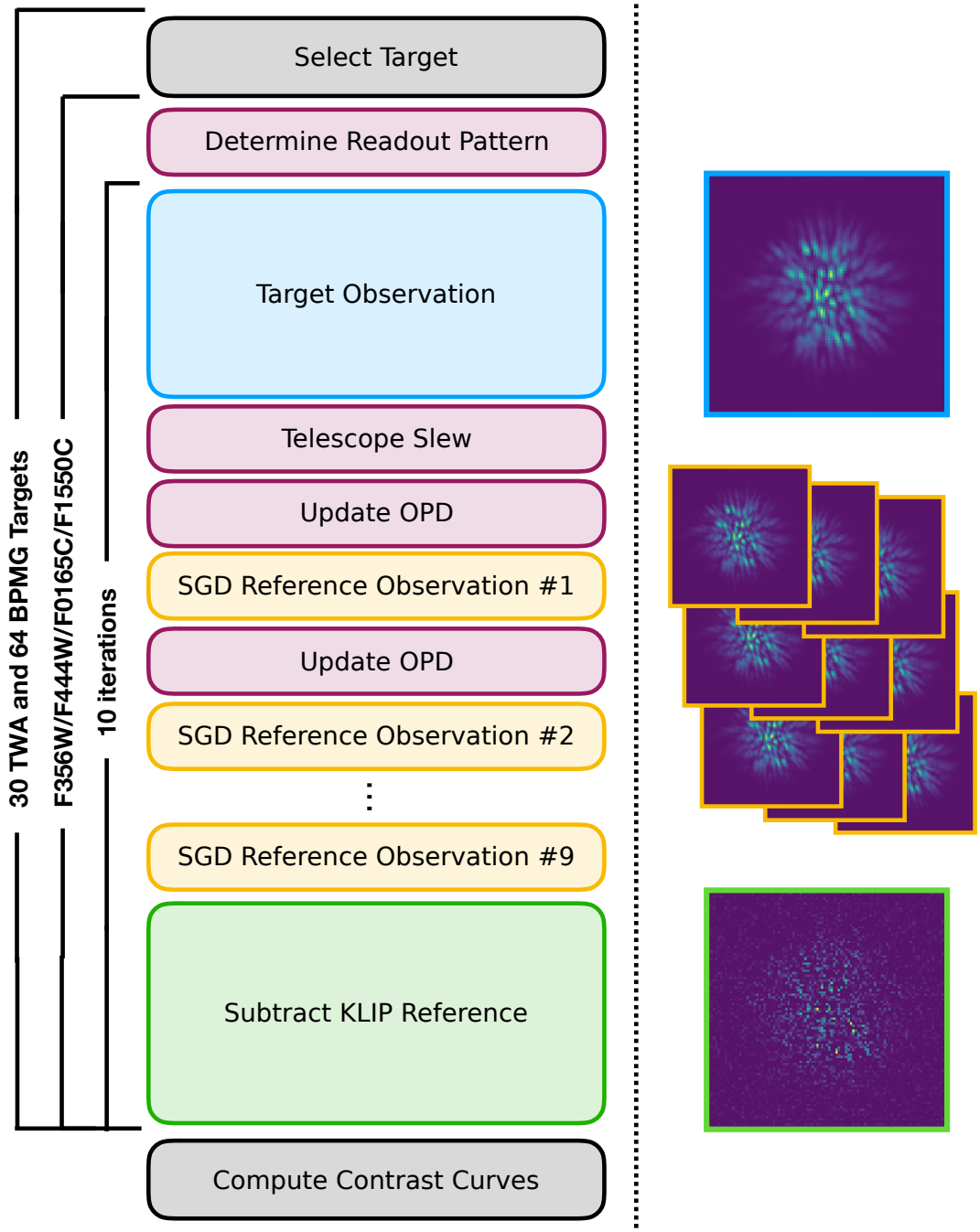

Figure 4.4: A block diagram representation of the simulated `PanCAKE` observations. Example images for one simulation in the NIRCam F444W filter are also provided. The intensity scale for the subtracted image is 100 times smaller than that of the target and reference images in order to display the signal-to-noise variations.

sampling from the default of 150, to 41 through the `wave_sampling` setting. Despite this reduction, variations from the true PSF are on the order of <1% (Marshall Perrin, private communication).

For both the NIRCam and MIRI simulations we selected an observation duration of ~3600 s. This duration is short enough to be observationally feasible, yet long enough that we do not observe any appreciable improvement to the final simulated contrast with an even longer observation. The simulations shown in this study therefore represent an estimate of the practicable sensitivity limits of *JWST* coronagraphy. We stress that for an actual observation the duration should be carefully selected to reach a desired sensitivity limit for the specific target of interest.

4.4.2.2 Readout Specifications

The NIRCam detectors host a broad range of readout modes, with nine distinct readout patterns and up to either 10 or 20 groups per integration. Whilst this provides significant versatility, finding the optimal readout mode for a desired observation can be a non-trivial task. Although it is technically possible to perform the simulation for every possible readout mode to assess which performed the best, this is very computationally intensive and hence not practical. Alternatively, we estimate the optimal readout mode using the `ramp_optimize` function of the `pyNRC` software package (Leisenring et. al, in preparation[2]). Given a NIRCam observational setup and a desired integration time, this function can quickly estimate the achievable SNR of a target object for each possible readout mode. We use this function to select the input readout mode for every `PanCAKE` simulated target by finding the corresponding `ramp_optimize` mode which: provides the maximal SNR of a synthetic companion object 20 magnitudes fainter than the target star, has a total integration time less than 3600 s, and does not saturate the detector. The choice of such a faint companion is made as this preferentially selects readout modes best for observing objects with the largest contrast to their host stars.

For the MIRI simulations we instead perform a custom optimisation to determine the optimal readout parameter for every target in the sample. The MIRI detector only

2. https://pynrc.readthedocs.io/en/latest/

has two possible readout patterns – SLOW or FAST – and the SLOW pattern is only recommended for parallel observations where the overall data volume in the FAST pattern would be too high. Therefore only the number of groups (NG) and integrations (NI) needs to be optimised for the simulations (see Ressler et al. (2015) for further discussion on MIRI readout specifications). For each target object we begin by determining the fraction of detector saturation for a desired MIRI filter using a simplistic `PanCAKE` simulation with a FAST readout pattern, NG=5, and NI=1. This fraction is then inverted to determine the maximal NG without going beyond a saturation fraction of 80%. For maximal NG values $\leq$100 we determine the maximal NI that corresponds to a total observation time less than 3600 s and adopt these maximal values as the input values of the simulation. The reason for such a cutoff is to avoid non-ideal detector effects which are more pronounced for shorter integrations (Ressler et al. 2015). For maximal NG values >100 we instead adopt the highest NG value possible that: a) results in individual integration times less than 280 s, and b) has a corresponding NI value that results in a total observation time between 3580 and 3600 s. The first restriction will be necessary for true on-sky observations as long integrations will be more significantly affected by cosmic rays, with every pixel being affected, either directly or indirectly, by ~1000 s[3]. The second restriction ensures that all of the observations have approximately similar integration times.

4.4.2.3 Accounting for Thermal Drifts

The slew performed by *JWST* when moving from target to reference star will inherently cause a variation in the observatory pitch angle relative to the Sun. This variation leads to a difference in the overall illumination of the observatory between observations and will induce a thermally driven wavefront drift which is currently expected to be the primary driver of variations in *JWST* optical telescope element (Perrin et al. 2018). Any such variations will inhibit the ability to perform an accurate PSF correction and therefore will affect the achievable contrast.

We include the effects of thermal drifts throughout the simulated observations using the `thermal_slew` function included in the `webbpsf` PYTHON software package (Perrin

3. https://jwst-docs.stsci.edu/mid-infrared-instrument/miri-observing-strategies/miri-cross-mode-recommended-strategies

et al. 2014). By providing a desired slew start pitch angle, end pitch angle, and the elapsed time, this function can model the variation in the optical path difference (OPD) map of each primary mirror segment which in turn can be provided to the `PanCAKE` simulation. During these simulations the OPD map is updated after the target observation and then after every consecutive dither for the reference star observation.

Selecting a slew start pitch angle is not straightforward, as the observatory pitch angle can vary between 45° and −5°. Furthermore, not every object in the sky can be observed at the maximum pitch angle. Assuming an approximate average declination of −51° and −34° for βPMG and TWA respectively, their corresponding maximum observable pitch angles are ~39° and ~45°. We assume average yearly pitch angles for the slew start angles by taking the midway point between these maximum observable pitch angles and the minimum pitch angle of −5°. To determine the slew end angle we must first assume an offset angular distance between the target and reference star. As we do not explicitly select real reference stars for each of the targets it is necessary to instead determine a "typica" angular offset. To approximate this for the simulations we take the average offset for all *JWST* Early Release Science (ERS) and Guaranteed Time Observer (GTO) coronagraphic observations, resulting in a value of ~6.6°. However, given that the observatory can rotate a full 360° in the axis perpendicular to the pitch axis, the average angular offset does not directly correspond to an average change in pitch angle between target and reference. In such a case this average is actually half of this value, i.e. 3.3°, and this is treated as the difference between the slew start and end pitch angles. Whilst it is possible to add or subtract this value from the slew start pitch angle to obtain a slew end pitch angle, we do not observe any measurable difference in the final contrast curve and as such opt to add it.

To determine the elapsed time between the slew start pitch angle and the slew end pitch angle we refer to the official *JWST* slew times[4]. An overall slew distance of 6.6° corresponds to a total slew time of ~980 s, including 284 s for a necessary guide star reacquisition. In the simulations we adopt a slightly more conservative value of 1000 s for the elapsed time between the end of the target observation and the start of the reference

4. https://jwst-docs.stsci.edu/jppom/visit-overheads-timing-model/slew-times

observation to account for target acquisition procedures. Finally, after each subsequent dithered reference observation, we recompute the OPD map by adding one hour to the elapsed time.

4.4.2.4 Contrast Curve Determination

Following the generation of all of the 2D simulated images, it is necessary to compute corresponding contrast curves which show the limiting sensitivity of the synthetic observations. As 10 realisations of simulated target and reference images were produced for each object in the sample, it is first necessary to subtract a stellar PSF from each of the target images. This subtraction is performed for each target image realisation using a synthetic PSF generated from its corresponding reference star images following the KLIP algorithm of Soummer et al. (2012), as implemented by the `klip_projection` function within `PanCAKE`. An estimation of the radial contrast curve for each target is then calculated using the default `Pandeia` correlation matrix method on the remaining ensembles of subtracted images as described in Appendix A.2.2.

To reduce computational intensity the observed field of view in `PanCAKE` simulations is reduced to 6.3″×6.3″ and 8.8″×8.8″ from 20″×20″ and 24″×24″ for NIRCam and MIRI respectively. Additionally, the estimated contrast at the widest simulated separations is imprecise as it is calculated from only a few pixels in the image. To alleviate these effects we extend each NIRCam and MIRI contrast curve to 10″ and 12″ respectively, assuming that the contrast at separations beyond 90% of the widest simulated separation is constant and equal to the contrast at 90% of the widest simulated separation. Whilst larger radial separations are possible, exoplanets at these separations would not be observable at all roll angles. To avoid any overestimation of the detection probability maps determined in Section 4.5 we do not include these widest separations in our analysis. Each contrast curve is then divided by its respective coronagraphic transmission profile to incorporate the intrinsic IWA restrictions of these observations. Finally, all contrast curves are converted from angular separation to physical separation using the reported *Gaia* distances (Gaia Collaboration et al. 2016; Gaia Collaboration et al. 2018) for each individual target.

At this stage it is common to calculate a final contrast curve for a given observa-

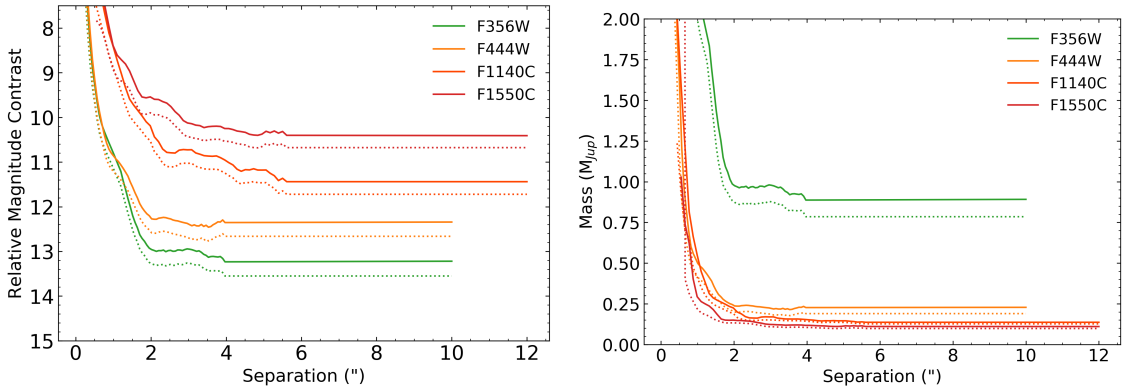

Figure 4.5: *Left*: Example 95% completeness (solid) and classical 5σ (dotted) simulated contrast curves for the F356W, F444W, F1140C, and F1550C filters for a single target within the sample. *Right:* As in the left panel, but with the magnitude contrast converted into a corresponding mass sensitivity limit using the `ATMO` and `BEX` evolutionary models. Contrasts at separations beyond the simulated field of view, yet still within the observationally possible field of view, are assumed to be constant and equal to the contrast at 90% of the widest simulated separation.

tion in terms of an integer multiplication, n, of the base contrast curve, representing the threshold at which at object would be n times brighter than the noise, σ. However, such a measure fails to account for the limitations of the small number statistics at the innermost separations (Mawet et al. 2014), and irrespective of the value of n, corresponds to a fraction of true positive detections of only 50% (Jensen-Clem et al. 2018). We therefore perform a final correction to the simulated contrast curves following the more modern prescription detailed in Ruane et al. (2017) and Stone et al. (2018), using a true positive detection fraction of 95% and a total of 0.01 false detections per image. As the nature of this correction is intrinsically linked to the number of available resolution elements, which is a function of observation wavelength, it is unique to each simulated filter. In general, these corrections are on the order of -0.27 to -0.33 magnitudes at the widest separations, and up to ~1 magnitude at the very innermost separations.

An example set of the 95% completeness contrast curves are plotted alongside the more classical 5σ contrast curves for a single object within the sample in Fig. 4.5. In all of the simulations the NIRCam observations reach a superior contrast than the MIRI observations. However, as the SED of both a star and planet vary as a function of wavelength, the relative magnitude contrast between them will also vary. Therefore, to assess which filter is best suited towards detecting the lowest mass exoplanets, these limits must be calculated in terms of mass.

4.5 Results

4.5.1 Mass Sensitivity Estimation

To estimate the detectable mass limits of *JWST* coronagraphy it is necessary to convert the determined contrast curves from the standard representation in terms of magnitude, to one in terms of mass. To do so we make use of planetary evolution models, which predict the magnitude of an object within a filter of interest given its mass. Specifically, we rely on the latest models of cold, low mass objects spanning $\sim 5 M_{\rm E} - 2 M_{\rm J}$ from Linder et al. (2019) (`BEX`), and more massive giant planets and brown dwarfs spanning $\sim 0.5 M_{\rm J} - 75 M_{\rm J}$ from Phillips et al. (2020) (`ATMO`).

In the case of `ATMO`, evolutionary models have already been computed for all *JWST* coronagraphic filters, including those used as part of this study. Additionally, `ATMO` offers three different sets of evolutionary models: one at chemical equilibrium, and the other two at chemical disequilibrium assuming different strengths of vertical mixing. Given that all of the `BEX` models are computed at chemical equilibrium, we do not explore the effects of disequilibrium chemistry on *JWST* sensitivity limits as part of this study and select the equilibrium models at solar metallicity.

Similarly to `ATMO`, `BEX` offers a range of different sets of evolutionary models based on different atmospheric models: one using the `Ames-COND` grid (Allard et al. 2001), 14 based on the `petitCODE` grid (Mollière et al. 2015; Samland et al. 2017), and one using the `HELIOS` grid (Malik et al. 2017). As `petitCODE` has recently been benchmarked against `ATMO` (Baudino et al. 2017), we select these models for this study. Of the 14 evolutionary model sets produced from the `petitCODE` grid, many incorporate varying levels of metallicity or clouds. Only Na_2S and KCl clouds are included in these models and therefore water clouds, which are expected to impact the spectra of objects with temperatures $\lesssim$400 K (Morley et al. 2014), are neglected. Furthermore, recent work has suggested that the high nucleation energy barrier of Na_2S strongly inhibits its formation and therefore its inclusion as a dominant cloud species may not be strictly accurate (Gao et al. 2020). For these reasons, and as none of the `ATMO` models of Phillips et al. (2020) include the effects of cloud opacity, we select the solar metallicity `petitCODE` models without any cloud opacity and retain

model consistency between mass ranges.

As we are unable to simultaneously include both cloud formation and disequilibrium chemistry processes with the chosen evolutionary models, it is not straightforward to determine exactly how their complex interplay would affect the overall mass sensitivity calculations presented in this work. However, as these processes play a significant role in the overall structure and composition of sub-stellar atmospheres, differences will likely exist.

The presence of a silicate or alkali cloud deck acts to limit the atmospheric depth from which flux can readily emerge, primarily resulting in reductions of the ~1−2 μm emission for objects with temperatures <1300 K. This flux is then redistributed, producing an opposing increase in emission at wavelengths beyond ~2 μm (Morley et al. 2012; Charnay et al. 2018). However, for objects at temperatures below 400 K, which represent our best case limiting mass sensitivity, this increase is negligible (Morley et al. 2012). In contrast, the formation of water clouds below ~400 K can substantially affect the emitted flux at infrared wavelengths. In the case of a large fractional cloud coverage of 80% at a 200 K effective temperature, the emitted flux could be reduced by approximately half an order of magnitude at ~4.5 μm, and increased by approximately two orders of magnitude at ~3.5 μm (Morley et al. 2014). Nevertheless, these effects become less significant with increasing temperature, or decreasing cloud coverage. Whilst we do not aim to specifically quantify the overall impact of clouds on our simulations, in a qualitative sense, and in this respect alone, the estimates of the limiting mass sensitivity in the F356W and F444W filters may therefore be considered somewhat pessimistic or optimistic respectively.

Disequilibrium chemistry is primarily considered through enrichment of molecular species in the upper atmosphere through upwards vertical mixing from deeper and hotter regions of the atmosphere. Recently, such an effect has been inferred ubiquitously in a sample of the coolest brown dwarf atmospheres, ranging from 250 − 750 K in effective temperature, through the enhancement of CO absorption from ~4.5−5.0 μm in their *M*-band spectra (Miles et al. 2020). Among these brown dwarfs the scale of the absorption varies from object to object, although in general it results in reductions in the emitted flux by approximately a factor of two compared to an equilibrium model. However, CO is

likely not the only species that may be enhanced through disequilibrium chemistry, and species such as CO_2, HCN, C_2H_2, PH_3, and GeH_4 may also reduce the emitted flux at infrared wavelengths (Morley et al. 2018). Unfortunately, observations of disequilibrium chemistry in exoplanetary atmospheres are still relatively sparse, and its significance and nature as a function of planetary mass and temperature is still not well understood. We therefore do not attempt to quantify exactly how disequilibrium processes may affect our simulations either. Nonetheless, in the absence of disequilibrium enhanced absorption it can be assumed that the limiting mass sensitivities for all of the simulated filters are likely more optimistic.

For the `BEX` models in particular, only a subset of the *JWST* photometric filters have been computed. To compute new `BEX` evolutionary magnitude tracks we first calculate the synthetic magnitude in all the coronagraphic filters used throughout this study for each of the chosen `petitCODE` models. The full throughputs used in this process are equal to the PCEs as calculated from the *JWST* exposure time calculator `Pandeia`, and are displayed in Fig. 4.2. For each filter, we produce a corresponding 2-dimensional interpolation over these magnitudes in $T_{\rm eff}$–$\log(g)$ space. For each mass division in the existing `BEX` evolutionary tracks, we obtain the corresponding value of $T_{\rm eff}$ and $\log(g)$ and then pass these values to the previously described interpolations to determine the corresponding magnitudes for all filters used in this study at these mass divisions. To verify this method we also compute these magnitudes for the already calculated F356W photometric filter shown Linder et al. (2019). The resulting differences between our calculation and that of Linder et al. (2019) are <0.07 mag in all cases and are likely a result of different interpolation methods, or even the precision of the astronomical constants used in the underlying calculations.

As both of these evolutionary models are computed across a range of specific ages, all of the following analyses were performed using interpolations to these models at the nominal ages of βPMG and TWA (see Section 4.3). First, the apparent magnitude of each target star in each of the used coronagraphic filters is added to its corresponding contrast curve as produced in Section 4.4.2.4. These magnitudes are computed using the SEDs generated in Section 4.4.1 and the PCEs as shown in Fig. 4.2, and are displayed in Tables

A.3 and A.4. In essence, this process converts the contrast curves from a relative magnitude contrast, to an absolute detectable magnitude limit. This limit can then be readily converted to an absolute detectable mass limit using the interpolation between mass and magnitude in a desired filter from the aforementioned evolutionary models. An example set of these absolute detectable mass limits for a single object within the sample are shown in Fig. 4.5.

Similarly to the stellar evolutionary models in Section 4.4.1, there is an overlap in mass between the the `ATMO` and `BEX` models from 0.5–2 M_J. However, for many of the simulations this overlap is too small to produce an effective smoothed model in a similar fashion to that shown in Section 4.4.1. To account for the overlapping region, we instead take the average between the `ATMO` and `BEX` interpolations as a function of semi-major axis. As the `ATMO` and `BEX` models are not perfectly congruent, this averaging produces discontinuities in the mass sensitivity curves as some values of the `ATMO` mass interpolation that are not in the averaged region will lie below the maximum averaged value. Similarly, some values of the `BEX` mass interpolation that are not in the averaged region will lie above the minimum averaged value. Whilst we do not seek to assess and account for the discrepancy between these evolutionary models explicitly, it is desirable to remove these discontinuities when determining the final mass sensitivity limits. This is performed by averaging the `ATMO` values that lie outside the overlapping region and are lower than the maximum averaged mass within the overlapping region with a straight line connecting the maximum `BEX` value and the closest but higher `ATMO` value. In a corresponding fashion, the `BEX` values that lie outside the overlapping region and are above the minimum averaged mass within the overlapping region are averaged with a straight line connecting the minimum `ATMO` value and the closest but lower `BEX` value. An example mass sensitivity curve is displayed in Fig. 4.6 alongside the overall model resulting from both the smoothing procedure from Section 4.4.1, which produces a discontinuity, and the averaging procedure described here, which does not. We note that the discrepancy between the two evolutionary models for a given mass are often $\gtrsim$1 mag and therefore cannot result from the slight differences arising from the independent calculation of the `BEX` evolutionary tracks. In the event that a magnitude value is too small (i.e. too bright) to be interpolated by the `ATMO` evolutionary models, we simply set the mass value to 75 M_J. This does not have any

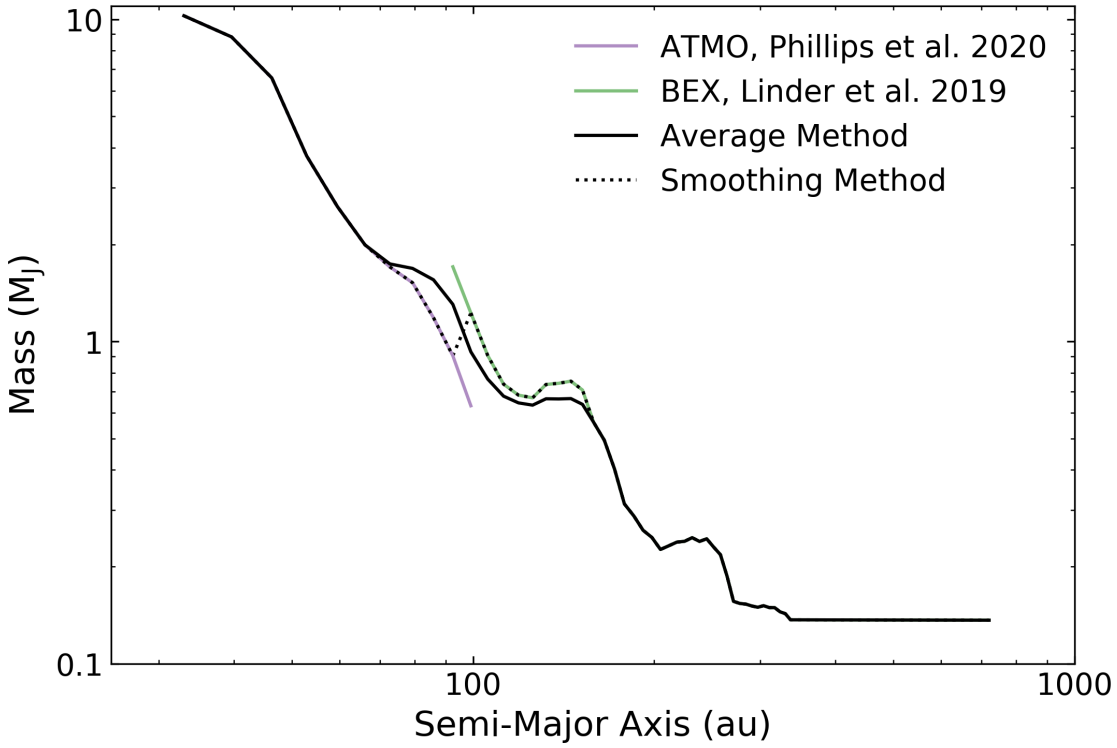

Figure 4.6: Mass sensitivity curves for a single example object within the sample. The difference between the `ATMO` (purple) and `BEX` (green) models causes a sharp discontinuity using a smoothing procedure similar to that described in Section 4.4.1 (dotted black), however when the described averaging method is used (solid black) this discontinuity is not produced.

effect on the overall mass sensitivity limits, which are at much lower masses. Finally, in the event that a magnitude value is too large (i.e. too faint) to be interpolated by the `BEX` evolutionary models, we set the mass value to the minimum calculated mass value of the contrast curve.

4.5.2 QMESS Detection Probabilities

Following the calculation of mass sensitivity limits for each of the objects we estimate detection probability maps using the QMESS (Quick Multi-purpose Exoplanet Simulation System, Bonavita et al. 2012; Bonavita et al. 2013). Its predecessor, MESS, is a Monte Carlo tool used for the statistical analysis of direct imaging survey results. It combines the information on the target stars with instrument detection limits to estimate the probability of detection for a given synthetic planet population, ultimately generating detection probability maps. Its faster QMESS evolution (Bonavita et al. 2013), which is used in this instance, allows for a substantial gain in computational time, achieved by abandoning the Monte Carlo approach in favour of a simple grid based one. The new approach uses a previously

generated map to estimate the range of possible projected separations corresponding to each value of semi-major axis in the grid, thus skipping the time consuming orbit projection module used in the original code. This projection map is generated taking into account a fine grid of uniformly distributed orbital parameters, and enables the calculation of the probability that an object at a given physical separation can be observed at a projected separation that puts it in an instrument's field of view.

QMESS allows for a high level of flexibility in terms of the possible assumptions on the synthetic planet population to be used when determining the detection probability. However, in this case we use the default setup, which uses flat distributions in log space for both the mass and semi-major axis and a Gaussian eccentricity distribution with $\mu = 0$ and $\sigma = 0.3$ (following the approach of Hogg et al. 2010, see Bonavita et al. 2013 for details). The detection probability maps generated for this study range from $0.01 - 75\ M_J$ and $1 - 1000$ au, with a resolution of 500 in each dimension.

4.5.3 *JWST* Mass Sensitivity

To assess the broader, population based, mass sensitivity limits of *JWST* we present mean detection probability maps for the βPMG and TWA samples in Fig. 4.7, the total combined sample separated by spectral class in Fig. 4.8, and the total combined sample in Fig. 4.9.

4.5.3.1 β Pictoris and TW Hya

The detection probability maps for βPMG and TWA shown in Fig. 4.7 clearly display an increase in sensitivity towards the lowest mass companions with increasing wavelength. In the mid-infrared the SEDs of low mass (cooler) planetary objects peak, whereas a stellar SED continues to diminish. As such, the overall relative magnitude contrast between these two objects will decrease. This increase in detection probability therefore indicates that the favourable decrease in contrast towards longer wavelengths outweighs the difference between the NIRCam and MIRI contrast limits as shown in Fig. 4.5. The dramatic improvement between the F356W and F444W filters is primarily due to the F356W band lying directly on a CH_4 absorption feature, across which significantly less flux is emitted. Comparing the measured flux between these two filters will therefore be useful in elim-

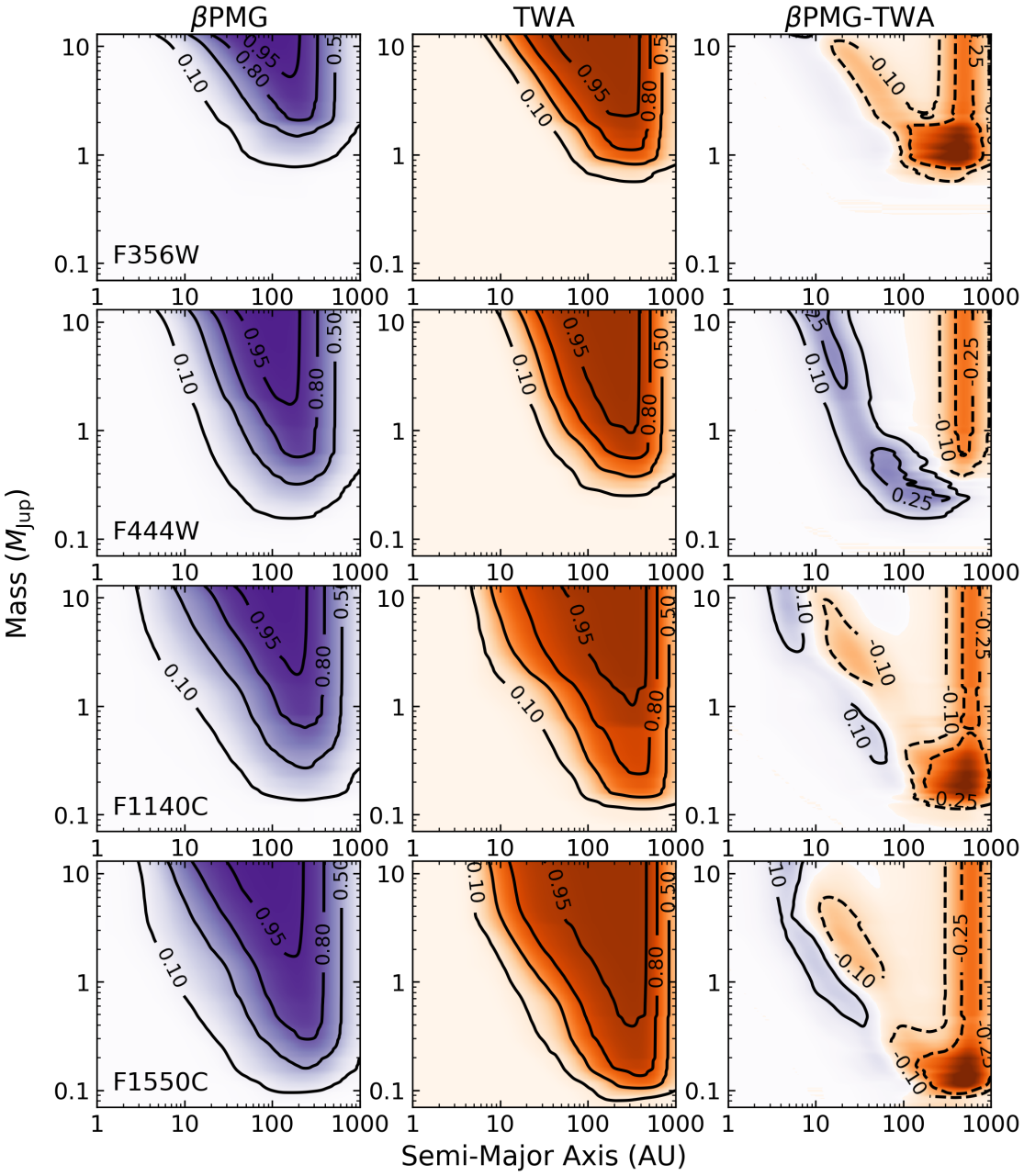

Figure 4.7: Mean detection probability maps produced using the QMESS (Bonavita et al. 2013). From top to bottom each row corresponds to the F356W, F444W, F1140C, and F1550C *JWST* filters. The first two columns correspond to the mean probability maps for all objects within the βPMG (purple) and TWA (orange) samples, contours signify the 10%, 50%, 80%, and 95% detection thresholds. The final column is equal to the difference of the βPMG and TWA columns, solid contours signify detection threshold differences of 25%, 10%, and dashed contours signify differences of −10% and −25%. Irrespective of the moving group the MIRI F1140C and F1550C filters provide the best sensitivity, reaching masses as low as 0.1 M_J. Between the two moving groups, TWA is generally sensitive to the lowest mass companions at wide separations, whilst βPMG is generally more sensitive to companions at shorter separations.

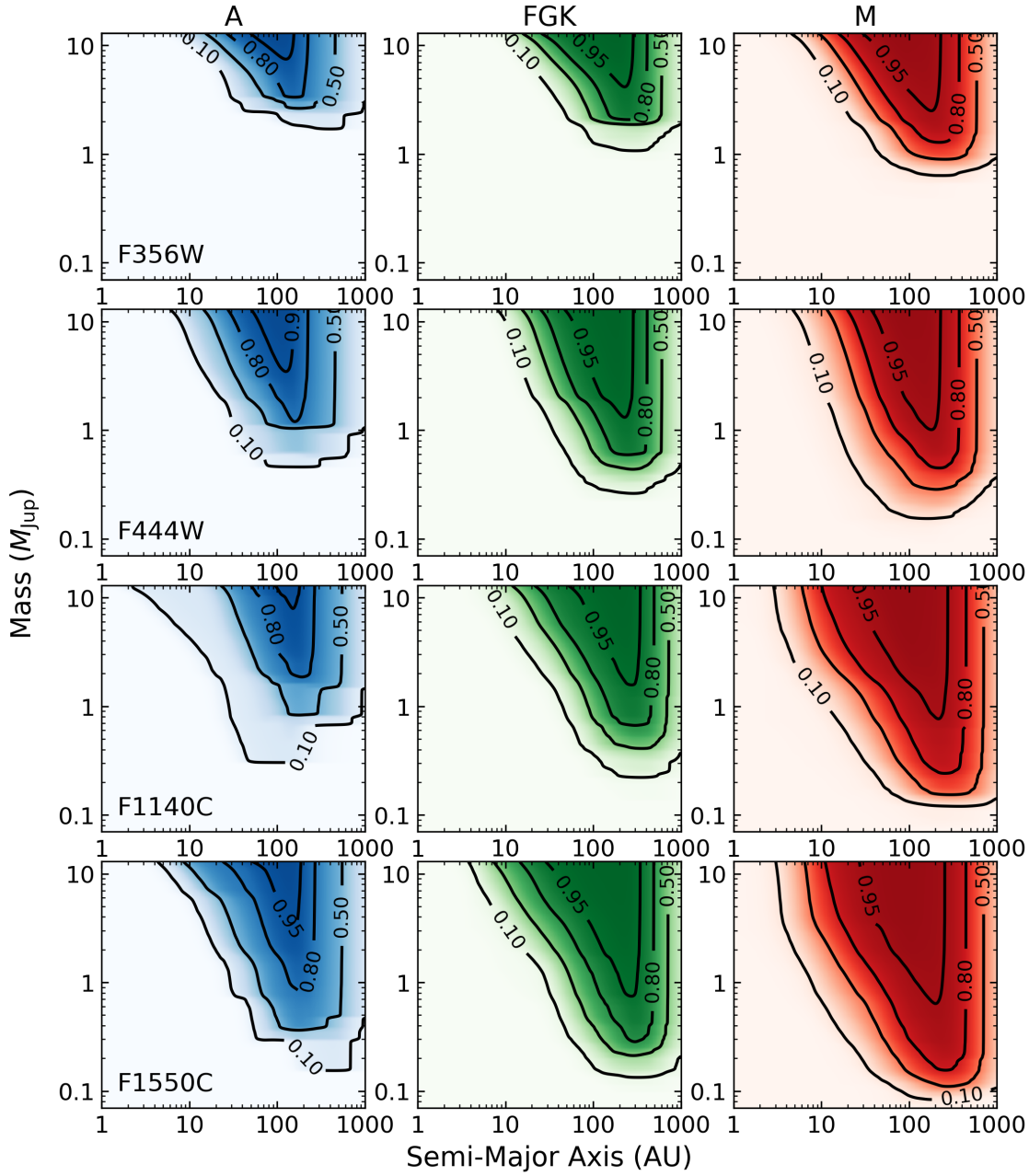

Figure 4.8: Mean detection probability maps produced using the QMESS (Bonavita et al. 2013). From top to bottom each row corresponds to the F356W, F444W, F1140C, and F1550C *JWST* filters. From left to right each column corresponds to the mean probability maps for stars of spectral class A (blue), F/G/K (green), and M (red) across both the βPMG and TWA samples. Contours signify the 10%, 50%, 80%, and 95% detection thresholds. Similarly to Fig. 4.7, the MIRI F1140C and F1550C filters provide the best sensitivity. A clear trend with sensitivity and spectral type is also observed, with M stars providing the best mass sensitivity due to their relatively fainter magnitudes than earlier spectral type objects within the moving groups.

inating background stars, which should not exhibit such a decrease in the F356W band. In terms of overall mass sensitivity, the 50% probability contour for the best performing F1550C filter reaches a minimum mass of ~0.2M_J from 200 – 300 au for βPMG, and a minimum mass of ~0.1M_J from 200 – 600 au for TWA. At ages of 24 and 10 Myr, corresponding to βPMG and TWA respectively, these mass limits correspond to objects with a temperature of ~250 K as determined from the `BEX` evolutionary models.

The rightmost column in Fig. 4.7 displays the difference in detection probabilities between the βPMG and TWA samples. Irrespective of the chosen filter, the TWA sample typically performs better at the widest separations. This is a natural result of the objects in the TWA sample being located further away on average than those in the βPMG sample (see Fig. 4.1); the angular separations probed in an observation of a more distant object correspond to larger physical separations. Similarly, the βPMG targets perform slightly better than the TWA targets at the smallest separations as the sharp reduction in the limiting contrast at shorter angular separations occurs at a shorter physical separation for objects closer to us. In the majority of filters the TWA sample is most sensitive to the lowest mass companions due to its younger age of 10±3 Myr compared to 24±3 Myr for βPMG. At this younger age potential exoplanets will have more recently formed and will therefore be hotter and more luminous (e.g. Baraffe et al. 2003, Phillips et al. 2020), making them easier to detect. Interestingly, this is not the case for the F444W filter, in which the βPMG targets perform better. This indicates that at this wavelength, for these βPMG and TWA samples, the increase in measurable flux due to a planet being physically closer to us outweighs the increase due to youth.

4.5.3.2 Spectral Class

If the entire sample is instead separated in terms of spectral class, rather than YMG membership, we observe a similar increase in sensitivity towards the lowest masses at longer wavelengths (Fig. 4.8). For the A star sample there are slight discontinuities in the probability map resulting from the limited sample size compared to the other spectral classes (see Fig. 4.1). Between spectral classes there is a general increase in the overall mass sensitivity at all separations for later type stars. Specifically, the 50% probability contour for the best performing F1550C filter reaches a minimum mass of: ~0.4 M_J from 100 – 400 au

for A stars, ~0.2 M_J from 200 – 400 au for F/G/K stars, and ~0.1 M_J from 200 – 500 au for M stars. Given these stars are at similar distances, earlier type stars are much brighter and will impart more noise into the final image, therefore restricting the minimum detectable mass. As the vast majority of the selected TWA sample are M stars (Fig. 4.1), this further explains why it outperforms the βPMG sample in the mean detection probability maps (Fig. 4.7).

Thus far, M stars have presented relatively poor targets for detecting exoplanets through direct imaging, with multiple studies indicating that at wide separations giant planets are particularly less frequent around lower mass stars (Bowler 2016; Nielsen et al. 2019). However, the observations informing these studies were not sensitive to the potential population of sub-Jupiter mass companions which can be readily imaged by *JWST*. Furthermore, albeit for a sample of objects at much shorter separations, the occurrence rate of sub-Jupiter mass companions as estimated from the *Kepler* mission does not decline towards later spectral types (Howard et al. 2012; Fressin et al. 2013). In these respects M stars represent some of the best potential targets for directly imaging the lowest mass exoplanets to date. This is distinctly different to ground-based direct imaging observations, where M stars are typically too faint to enable precise adaptive optics wavefront corrections, resulting in sub optimal coronagraphic suppression (Hardy and Thompson 2000). In fact, *JWST* Guaranteed Time Observer (GTO) program 1184 (PI: J. Schlieder) is already scheduled to perform a small NIRCam survey over nine young and nearby M stars during Cycle 1. The results from this program will not only provide valuable scientific information on the occurrence rates of sub-Jupiter companions at wide separations, but will also serve as a valuable comparison to the simulated sensitivities shown in this study.

4.5.3.3 Comparison to Completed Surveys

To compare the predicted sensitivities of *JWST* with the capabilities of current state-of-the-art instruments, we show the overall mean detection probability map of our sample in the F444W and F1550C filters alongside the already measured detection thresholds from the Gemini Planet Imager Exoplanet Survey (GPIES) (Nielsen et al. 2019) and the SpHere INfrared survey for Exoplanets (SHINE) (Vigan et. al, Submitted) in Fig. 4.9. These surveys represent the most sensitive to date, utilising advanced instrumentation and sophisticated

post-processing techniques. Fig. 4.9 demonstrates that whilst *JWST* will provide very little to no improvement towards imaging the closest separation exoplanets from 1 – 10 au, it offers a dramatic increase in sensitivity at the widest separations. In particular, beyond 100 au it will be possible to image companions down to ~0.1 M_J in the F1550C filter – more than an order of magnitude smaller than achieved with GPIES and SHINE. It is critical to emphasise that even though it is possible to make these comparisons, differences in the individual samples result in explicit biases in the final completeness maps. In particular, as a significant number of the objects in both the GPIES and SHINE samples are at distances further than the βPMG or TWA objects in our sample, their detection probabilities are more suppressed at the shortest separations. In reality, the sensitivity of both GPIES and SHINE is greatly superior at these separations due to the smaller inner working angle of the respective GPI (Macintosh et al. 2014) and SPHERE (Beuzit et al. 2019) instruments. Nevertheless, the improvement in mass sensitivity at the largest separations provided by *JWST* is predominantly due to its greater sensitivity and unique wavelength coverage, and not a result of our sample selection.

At wide separations, the predominant model of planetary formation is that of disk fragmentation through gravitational instability (Boss 1997). However, recent observational surveys have demonstrated that, in general, wide separations planets of >1 M_J are rare (Vigan et al. 2017; Nielsen et al. 2019; Vigan et al. Submitted). Furthermore, population synthesis models have shown that at separations beyond 50 au, where *JWST* is most sensitive, companions of $\lesssim$1 M_J are extremely uncommon (Forgan and Rice 2013; Forgan et al. 2015; Vigan et al. 2017). As a result, a large number of targets will likely be necessary to sample the population of sub-Jupiter mass companions at wide separations at a high degree of statistical certainty. Performing such a survey with *JWST* could be prohibitively expensive. Even in a favourable situation, where every target has a corresponding reference five times brighter than itself, an observing program of the full TWA and βPMG sample shown here would require over 500 hours of *JWST* telescope time (~8% of the entire Cycle 1 call) due to the time intensive nature of the small-grid dithered reference observations. Nevertheless, this cost could be mitigated somewhat by reducing the sample size, or scheduling observations in sequence and sharing reference stars between targets in a similar fashion to the aforementioned GTO survey of nearby M stars. In addi-

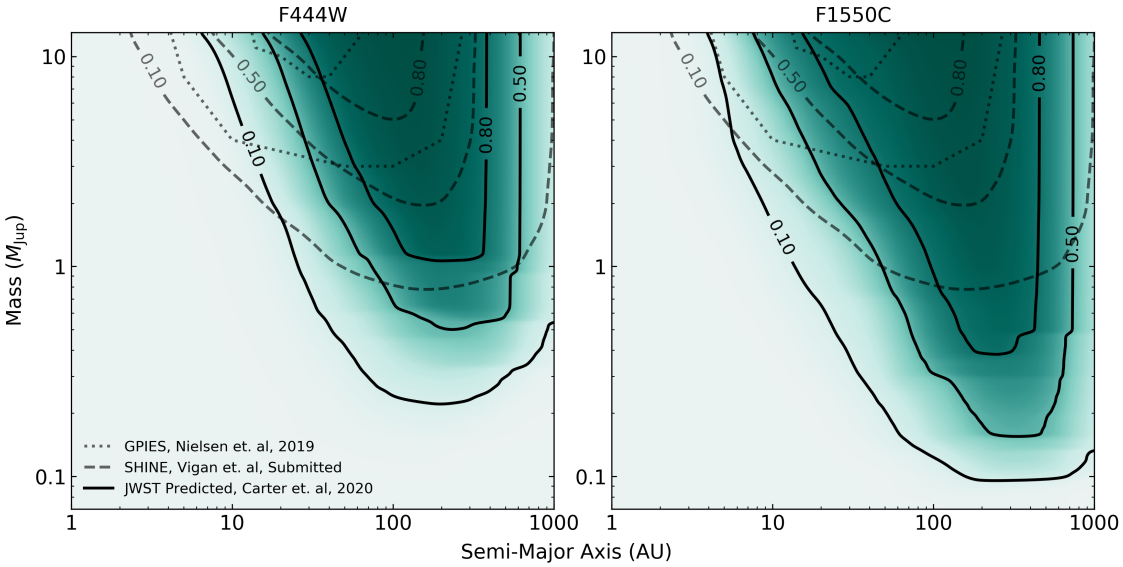

Figure 4.9: Mean detection probability map for the full βPMG and TWA sample in the F444W (*left*) and F1550C (*right*) filters. Solid contours signify the the 10%, 50%, 80%, and 95% detection thresholds of this study, dotted contours signify the 10% and 50% thresholds for the GPIES survey (Nielsen et al. 2019), and dashed contours signify the 10%, 50%, and 80% thresholds for the SHINE survey (Vigan et. al, Submitted).

tion, *JWST* likely presents the only opportunity to explore this parameter space until the *Nancy Grace Roman Space Telescope* (Spergel et al. 2015) or the next generation of 30 – 40 m ground based telescopes (e.g. Skidmore et al. 2015; Tamai et al. 2016; Fanson et al. 2018) have finished construction and commissioning.

Aside from detecting new companions, *JWST* will be an excellent complementary observatory to current and future ground based instruments. From the ground, large scale surveys are more realisable, and the mass sensitivity maps shown in Fig. 4.9 demonstrate that many of the detected objects from these surveys will likely be observable with *JWST* also. This is particularly noteworthy as the wavelength coverage offered by *JWST* is much greater than that offered from the ground, enabling much more detailed atmospheric characterisations of these objects.

4.6 Conclusion

We present in this work the most sophisticated simulated mass sensitivity limits for *JWST* coronagraphy to date, with a particular focus on members of the nearby young moving groups TW Hya and β Pictoris. Of the two samples, TW Hya members are slightly more sensitive to the lowest mass companions due to their younger age, whilst β Pictoris mem-

bers are slightly more sensitive to closer separation companions because they are less distant. When separating our sample by spectral class, we find that the typically less luminous M star population provides sensitivity to the lowest mass companions. This is a stark contrast to ground-based observations, for which M stars are often too faint to facilitate the crucial adaptive optics corrections necessary for high contrast imaging (Hardy and Thompson 2000). Irrespective of spectral class or moving group, we identify the MIRI F1550C filter as the most sensitive to the lowest mass exoplanets. Across the full simulated sample, we find that *JWST* will be capable of imaging ~1 M_J companions from 10 – 100 au, and ~0.1 M_J companions beyond 100 au. These limits represent significant improvements over current state-of-the-art ground-based instruments such as SPHERE (Beuzit et al. 2019) and GPI (Macintosh et al. 2014) which are currently sensitive to ~1 M_J companions. As a result, a survey of nearby young moving group members with *JWST* would be able to provide robust constraints on the presence and frequency of sub-Jupiter mass exoplanets beyond 100 au for the first time. Such measurements will be informative to planetary formation simulations, in addition to modelling of the overall population distribution. However, depending on the number of targets in the survey sample, this could be particularly time intensive. Even without such a survey, the mass sensitivity and wavelength coverage of *JWST* make it an excellent tool for characterising exoplanets discovered from the ground.

Finally, we eagerly await the launch of *JWST*, at which point it will be possible to update and refine the contrast model shown in this study by the true on-sky coronagraphic observations. Such a comparison is a specific goal of the Director's Discretionary Early Release Science Program 1386, *High Contrast Imaging of Exoplanets and Exoplanetary Systems with JWST* (PI: S. Hinkley), and will dramatically improve our understanding of the significance of observational factors such as pointing offset, thermal drift, target-reference slew distance, and dither strategy.

Chapter 5

Conclusion

5.1 Summary of Previous Chapters

Throughout this thesis I have presented a variety of studies towards the detection and characterisation of exoplanets. Particularly, I focus on the future capabilities of *JWST* and the advances it will provide. Below I briefly detail the studies presented in each chapter.

In Chapter 2, I characterise the atmosphere of the hot Jupiter exoplanet WASP-6b through transmission spectrum observations with *HST*, *VLT*, *Spitzer*, and *TESS*. Additionally, the effects of the estimated stellar heterogeneity of WASP-6 on our observations are also considered. Irrespective of our assumptions for the significance of stellar heterogeneity, Na, K and H_2O are clearly detected, and the elemental oxygen abundance is constrained to $[O/H] \simeq -0.9 \pm 0.3$ relative to solar. However, the retrieved [Na/H] and [K/H] abundances are distinctly affected by this correction due to its degeneracy with the scattering opacity of haze species within the atmosphere. These results also show WASP-6b is one of the most favourable objects for future characterisation with *JWST*, despite the presence of haze in its atmosphere.

In Chapter 3, I present a collection of three studies that employ `PandExo` simulations to determine the capabilities of *JWST* towards observing predicted forward model spectra of transiting exoplanets. The first of these studies investigates the significance of spectral variations due to wind-driven chemistry in hot Jupiter atmospheres. These processes act

to enrich the upper atmosphere with CH_4 and homogenise its vertical CH_4 abundance profile. Furthermore, this increased CH_4 abundance leads to significant deviations in the resultant transmission and emission spectra which are significantly larger than the *JWST* precision. For the second study, transmission spectra were produced from a 3D global circulation model including fully radiative clouds. Even in the most significantly cloudy case, the absorption due to specific cloud species can be observed with *JWST* and readily distinguished from a purely "grey" opacity model. The final study looked the effects of model assumptions towards the variation of the C/O ratio within forward model transmission spectra for both a hot Jupiter- and warm Neptune-like atmosphere. For both a C/O=0.1 and a C/O=2.0, the generated forward models are substantially different dependent on whether the C/H ratio or O/H ratio was varied to reach this C/O ratio. In all cases these variations are observable with *JWST*. As an ensemble, these studies demonstrate that careful consideration must be given to the underlying model assumptions when comparing forward models to actual *JWST* observations.

Finally, in Chapter 4, I utilise state-of-the-art simulations of *JWST* performance, in combination with the latest evolutionary and population synthesis models, to present the most sophisticated simulated mass sensitivity limits of *JWST* coronagraphy to date. In particular, these efforts are focused towards observations of members within the nearby young moving groups β Pictoris and TW Hydrae. These limits indicate that whilst *JWST* will provide little improvement towards imaging exoplanets at close separations, at wide separations the increase in sensitivity is dramatic. Beyond ~100 au, *JWST* will be capable of directly imaging companions as small as ~0.1 M_J, at least an order of magnitude improvement over the leading ground-based instruments. Probing this unexplored parameter space will be of immediate value to modelling efforts focused on planetary formation and population synthesis. *JWST* will also serve as an excellent complement to ground based observatories through its unique ability to characterise previously detected companions across the near- to mid-infrared for the first time.

5.2 Future Work

The work presented in this thesis is certainly not exhaustive, and continued observations of exoplanets with current instrumentation, or refining of the estimated *JWST* performance, will be crucial up until launch. Fortunately, these efforts are being made right now, with new transiting exoplanetary discoveries being made almost daily with telescopes such as *NGTS* (Wheatley et al. 2018) and *TESS* (Ricker et al. 2015), and a more modest influx of directly imaged companions with instruments such as GPI (Macintosh et al. 2014) and SPHERE (Beuzit et al. 2019). Additionally, characterisation of these objects is still ongoing, particularly for transiting exoplanets at the near-UV to optical wavelengths which are inaccessible to *JWST* (e.g. Wakeford et al. 2020).

5.2.1 The Exoplanet Early Release Science Programs

Upon *JWST*'s launch, the first publicly available exoplanetary data that can be compared to current simulated data will be from the Early Release Science (ERS) programs 1366 (*The Transiting Exoplanet Community Early Release Science Program*, (Bean et al. 2018)) and 1386 (*High Contrast Imaging of Exoplanets and Exoplanetary Systems with JWST*, (Hinkley et al. 2017)).

As part of ERS program 1366, the hot Jupiter WASP-79b (Smalley et al. 2012) will be characterised in transmission across a range of *JWST* modes to tightly constrain its atmospheric composition for comparison to state-of-the-art forward models. In addition, these measurements will enable the assessment of cross-instrument systematics and identify the optimal *JWST* observing mode for transiting observations. The hot Jupiter WASP-43b (Hellier et al. 2011) will also be observed with MIRI LRS for a continuous ~24 hour period, to capture its full phase curve variations at mid-infrared wavelengths. This observation will allow us to better constrain the 3D composition and structure of its atmosphere, in addition to searching for the presence of clouds. Furthermore, given the extremely long observation duration, this phase curve would provide a powerful estimate of the long baseline *JWST* systematics. Finally, the ultra-hot Jupiter WASP-18b (Hellier et al. 2009) will be observed at secondary eclipse with the NIRISS SOSS mode to constrain its thermal structure and search for opacity due to the production of H- ions. As the star WASP-18

has a relatively bright *J*-band magnitude of 8.4, this observation will also be a valuable probe of the systematic effects at high levels of detector saturation.

Within ERS program 1386, the recently discovered wide separation exoplanet HIP 65426b (Chauvin et al. 2017) will be characterised through coronagraphic imaging in a range of filters from the near- to mid-infrared with NIRCam and MIRI. These will be the first ever observations of a directly imaged exoplanet at these wavelengths and can offer insights into this object's formation history, cloud coverage, and overall atmospheric composition. Furthermore, these observations will provide the first estimates of the true on-sky contrast capabilities of *JWST* and will be a powerful comparison to the work displayed in Chapter 4. The exoplanet / brown dwarf VHS 1256-1257b (Gauza et al. 2015) will also be characterised in the near- to mid-infrared, however given its large angular separation this will be performed using direct spectroscopy with NIRSpec and MIRI from 0.6-28 μm. Given the significantly larger resolution (R>1000 at all wavelengths) compared to the coronagraphic observations, these observations will be an incredibly powerful comparison to forward model and retrieval analyses. Finally, the debris disk around HD 141569A (Weinberger et al. 1999) will also be characterised across the near- to mid-infrared with NIRCam and MIRI coronagraphic imaging. This will provide constraints on the water-ice abundance in the disk rings themselves, as well as being the first direct observations ever of the rising Wien tail of a disk SED. Additionally, these observations will be a valuable test of *JWST* PSF subtraction and post-processing methods of an image with diffuse emission across a large pixel area.

As a co-investigator of both of these programs, I plan to continue my preparatory efforts towards observations of exoplanets with *JWST* until launch, and then support and contribute to the data analysis and interpretation efforts as soon as the data are available.

The Appendices

A.1 WASP-6b Transmission Spectrum Supplement

A.1.1 STIS and *Spitzer* Light Curves

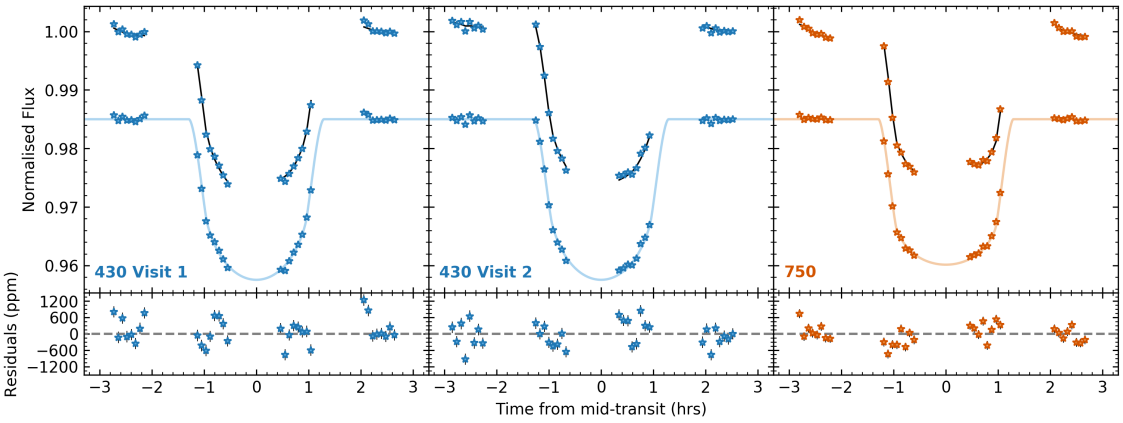

Figure A.1: Normalised white light curves and residuals of WASP-6b for the STIS 430 and STIS 750 grism observations as labelled. In each panel the upper light curve is the raw flux with black line indicating the GP transit plus systematic model fit, whilst the lower is the light curve after removal of the GP systematic component overplotted with the best fitting transit model from Mandel and Agol (2002). All lower panels display residuals following subtraction of the corresponding corrected light curves by their respective best fitting models.

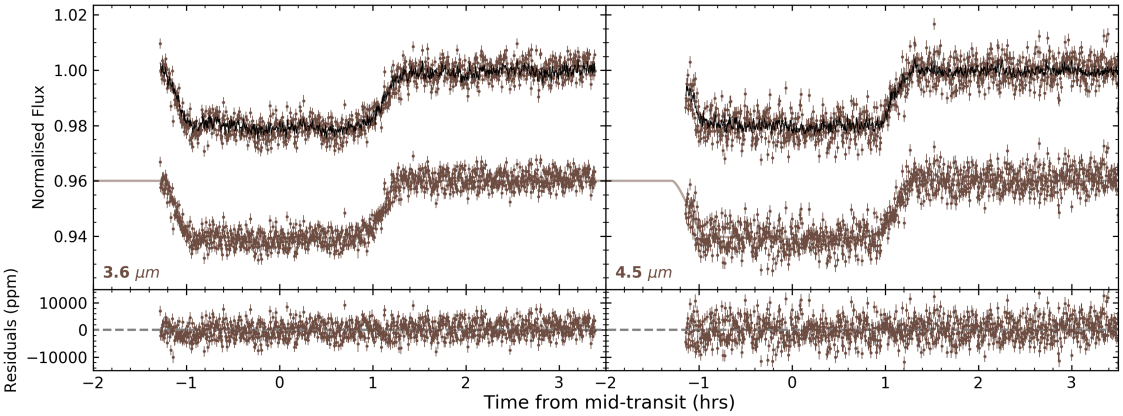

Figure A.2: As in Figure A.1 but for the *Spitzer* IRAC observations as labelled.

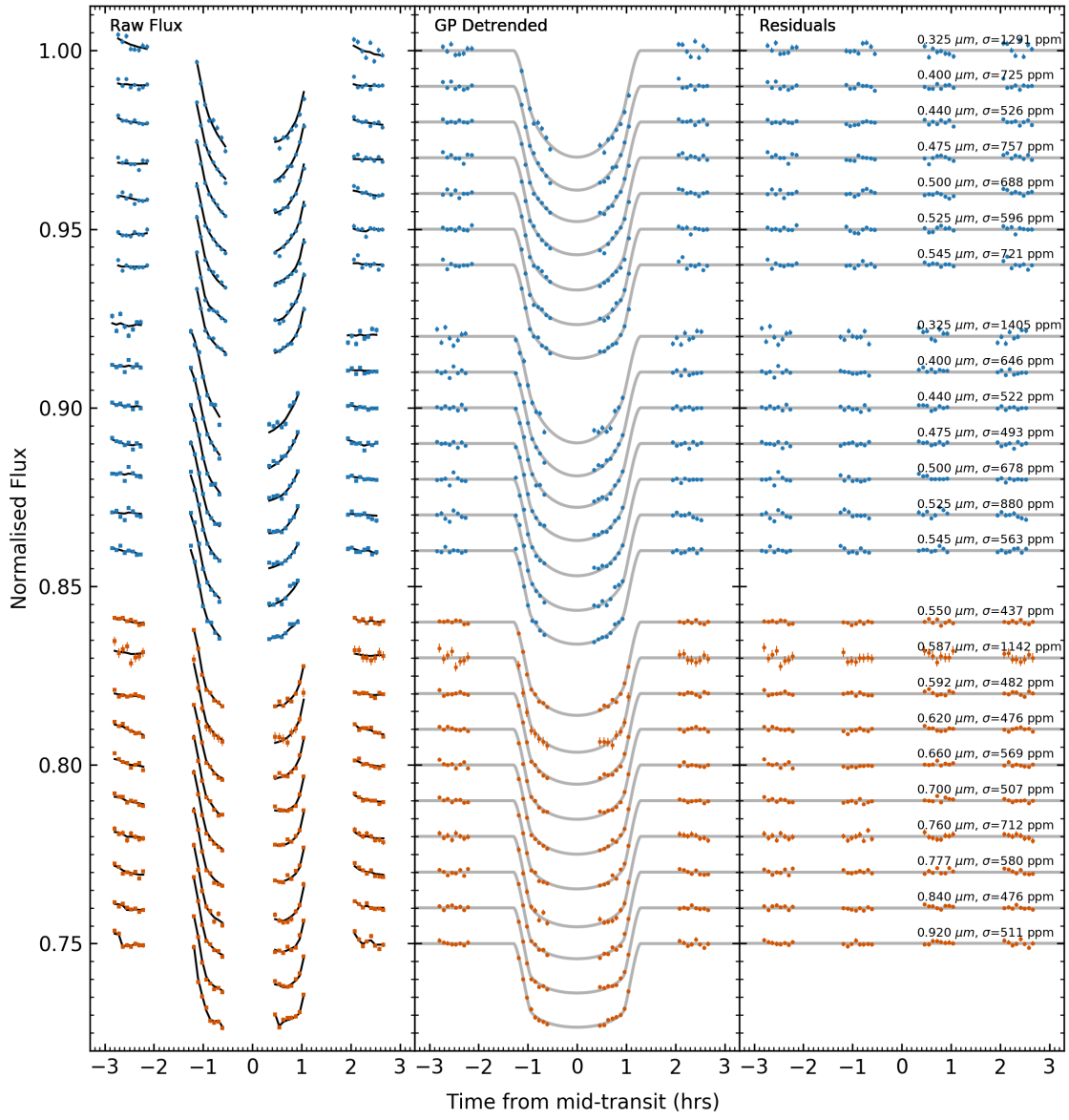

Figure A.3: Normalised spectrophotometric light curves for both STIS 430 datasets (top, middle groups) and the STIS 750 dataset (bottom group) of WASP-6b, light curves are offset from one another by an arbitrary constant. *Left:* Raw extracted light curves with black lines indicating the GP transit plus systematic model fit. *Centre:* Light curves after removal of GP systematic component. The best fitting transit models from Mandel and Agol (2002) are displayed in grey. *Right:* Residuals following subtraction of best fitting model.

A.1.2 Spectroscopic Light Curve Fits

Wavelength (μm)	R_p/R_*	$R_p/R_{*,TESS}$	$R_p/R_{*,AIT}$	c_1	c_2	c_3	c_4
FORS2 G600B							
0.4493–0.4653	$0.14563^{+0.00084}_{-0.00085}$	$0.14464^{+0.00085}_{-0.00089}$	$0.14408^{+0.00084}_{-0.00087}$	$0.563^{+0.020}_{-0.020}$	0.1783	-	-
0.4653–0.4813	$0.14611^{+0.00069}_{-0.00070}$	$0.14505^{+0.00070}_{-0.00071}$	$0.14454^{+0.00070}_{-0.00071}$	$0.547^{+0.017}_{-0.017}$	0.1882	-	-
0.4813–0.4973	$0.14578^{+0.00067}_{-0.00066}$	$0.14474^{+0.00067}_{-0.00067}$	$0.14422^{+0.00067}_{-0.00066}$	$0.507^{+0.016}_{-0.016}$	0.2015	-	-
0.4973–0.5133	$0.14671^{+0.00070}_{-0.00071}$	$0.14567^{+0.00071}_{-0.00072}$	$0.14514^{+0.00071}_{-0.00072}$	$0.520^{+0.017}_{-0.017}$	0.1951	-	-
0.5133–0.5293	$0.14609^{+0.00065}_{-0.00065}$	$0.14508^{+0.00065}_{-0.00066}$	$0.14456^{+0.00064}_{-0.00066}$	$0.464^{+0.016}_{-0.016}$	0.2298	-	-
0.5293–0.5453	$0.14757^{+0.00074}_{-0.00073}$	$0.14655^{+0.00074}_{-0.00073}$	$0.14599^{+0.00073}_{-0.00070}$	$0.426^{+0.018}_{-0.018}$	0.2111	-	-
0.5453–0.5613	$0.14631^{+0.00064}_{-0.00063}$	$0.14531^{+0.00064}_{-0.00063}$	$0.14483^{+0.00065}_{-0.00062}$	$0.427^{+0.015}_{-0.016}$	0.2332	-	-
0.5613–0.5773	$0.14639^{+0.00076}_{-0.00076}$	$0.14542^{+0.00075}_{-0.00077}$	$0.14491^{+0.00074}_{-0.00077}$	$0.395^{+0.019}_{-0.019}$	0.2347	-	-
0.5773–0.5853	$0.14603^{+0.00096}_{-0.00098}$	$0.14509^{+0.00096}_{-0.00098}$	$0.14462^{+0.00095}_{-0.00099}$	$0.437^{+0.024}_{-0.025}$	0.2348	-	-
0.5853–0.5933	$0.14938^{+0.00125}_{-0.00116}$	$0.14836^{+0.00125}_{-0.00116}$	$0.14790^{+0.00123}_{-0.00115}$	$0.355^{+0.030}_{-0.036}$	0.2579	-	-
0.5933–0.6013	$0.14671^{+0.00095}_{-0.00093}$	$0.14578^{+0.00097}_{-0.00094}$	$0.14526^{+0.00096}_{-0.00095}$	$0.342^{+0.024}_{-0.025}$	0.2477	-	-
0.6013–0.6173	$0.14576^{+0.00066}_{-0.00066}$	$0.14481^{+0.00068}_{-0.00066}$	$0.14431^{+0.00067}_{-0.00066}$	$0.384^{+0.017}_{-0.017}$	0.2367	-	-
FORS2 G600RI							
0.5293–0.5453	$0.14587^{+0.00128}_{-0.00128}$	$0.14492^{+0.00128}_{-0.00127}$	$0.14436^{+0.00127}_{-0.00127}$	$0.469^{+0.031}_{-0.032}$	0.2113	-	-
0.5453–0.5613	$0.14682^{+0.00061}_{-0.00073}$	$0.14581^{+0.00062}_{-0.00072}$	$0.14530^{+0.00062}_{-0.00070}$	$0.422^{+0.017}_{-0.016}$	0.2332	-	-
0.5613–0.5773	$0.14670^{+0.00115}_{-0.00125}$	$0.14573^{+0.00115}_{-0.00130}$	$0.14523^{+0.00114}_{-0.00124}$	$0.397^{+0.029}_{-0.032}$	0.2346	-	-
0.5773–0.5853	$0.14678^{+0.00074}_{-0.00076}$	$0.14581^{+0.00074}_{-0.00076}$	$0.14532^{+0.00074}_{-0.00075}$	$0.420^{+0.020}_{-0.020}$	0.2348	-	-
0.5853–0.5933	$0.14790^{+0.00090}_{-0.00094}$	$0.14694^{+0.00089}_{-0.00092}$	$0.14646^{+0.00089}_{-0.00093}$	$0.393^{+0.024}_{-0.025}$	0.2582	-	-
0.5933–0.6013	$0.14586^{+0.00067}_{-0.00066}$	$0.14491^{+0.00067}_{-0.00069}$	$0.14442^{+0.00066}_{-0.00067}$	$0.408^{+0.018}_{-0.018}$	0.2476	-	-
0.6013–0.6173	$0.14638^{+0.00055}_{-0.00052}$	$0.14545^{+0.00055}_{-0.00052}$	$0.14497^{+0.00054}_{-0.00053}$	$0.380^{+0.014}_{-0.015}$	0.2367	-	-
0.6173–0.6253	$0.14542^{+0.00062}_{-0.00061}$	$0.14450^{+0.00062}_{-0.00061}$	$0.14400^{+0.00061}_{-0.00060}$	$0.376^{+0.017}_{-0.017}$	0.2431	-	-
0.6253–0.6333	$0.14688^{+0.00100}_{-0.00093}$	$0.14591^{+0.00100}_{-0.00092}$	$0.14546^{+0.00102}_{-0.00094}$	$0.334^{+0.026}_{-0.030}$	0.2495	-	-
0.6333–0.6413	$0.14598^{+0.00072}_{-0.00068}$	$0.14508^{+0.00074}_{-0.00068}$	$0.14462^{+0.00071}_{-0.00070}$	$0.359^{+0.019}_{-0.021}$	0.2513	-	-
0.6413–0.6493	$0.14583^{+0.00056}_{-0.00058}$	$0.14488^{+0.00057}_{-0.00057}$	$0.14442^{+0.00056}_{-0.00057}$	$0.319^{+0.016}_{-0.016}$	0.2539	-	-
0.6493–0.6573	$0.14529^{+0.00083}_{-0.00077}$	$0.14439^{+0.00086}_{-0.00080}$	$0.14390^{+0.00083}_{-0.00077}$	$0.279^{+0.022}_{-0.027}$	0.3395	-	-
0.6573–0.6653	$0.14600^{+0.00054}_{-0.00051}$	$0.14508^{+0.00056}_{-0.00052}$	$0.14461^{+0.00056}_{-0.00053}$	$0.314^{+0.014}_{-0.015}$	0.2562	-	-
0.6653–0.6733	$0.14586^{+0.00074}_{-0.00071}$	$0.14493^{+0.00075}_{-0.00070}$	$0.14449^{+0.00073}_{-0.00071}$	$0.321^{+0.020}_{-0.022}$	0.2524	-	-
0.6733–0.6813	$0.14563^{+0.00059}_{-0.00057}$	$0.14475^{+0.00059}_{-0.00057}$	$0.14427^{+0.00059}_{-0.00058}$	$0.314^{+0.016}_{-0.018}$	0.2523	-	-
0.6813–0.6893	$0.14497^{+0.00068}_{-0.00062}$	$0.14408^{+0.00067}_{-0.00063}$	$0.14362^{+0.00067}_{-0.00062}$	$0.321^{+0.018}_{-0.020}$	0.2549	-	-
0.6893–0.6973	$0.14378^{+0.00055}_{-0.00056}$	$0.14287^{+0.00058}_{-0.00056}$	$0.14242^{+0.00056}_{-0.00056}$	$0.334^{+0.016}_{-0.016}$	0.2505	-	-
0.6973–0.7053	$0.14509^{+0.00071}_{-0.00067}$	$0.14420^{+0.00071}_{-0.00067}$	$0.14374^{+0.00071}_{-0.00066}$	$0.304^{+0.020}_{-0.024}$	0.2527	-	-
0.7053–0.7133	$0.14491^{+0.00056}_{-0.00055}$	$0.14402^{+0.00056}_{-0.00056}$	$0.14358^{+0.00057}_{-0.00055}$	$0.308^{+0.015}_{-0.017}$	0.2499	-	-
0.7133–0.7213	$0.14489^{+0.00053}_{-0.00054}$	$0.14399^{+0.00056}_{-0.00056}$	$0.14352^{+0.00054}_{-0.00055}$	$0.309^{+0.015}_{-0.016}$	0.2463	-	-
0.7213–0.7293	$0.14557^{+0.00061}_{-0.00059}$	$0.14470^{+0.00064}_{-0.00060}$	$0.14424^{+0.00061}_{-0.00062}$	$0.269^{+0.017}_{-0.020}$	0.2477	-	-
0.7293–0.7373	$0.14453^{+0.00054}_{-0.00055}$	$0.14365^{+0.00053}_{-0.00055}$	$0.14319^{+0.00054}_{-0.00055}$	$0.284^{+0.016}_{-0.016}$	0.2501	-	-
0.7373–0.7453	$0.14614^{+0.00058}_{-0.00059}$	$0.14524^{+0.00058}_{-0.00059}$	$0.14479^{+0.00058}_{-0.00058}$	$0.264^{+0.017}_{-0.017}$	0.2475	-	-
0.7453–0.7533	$0.14487^{+0.00058}_{-0.00061}$	$0.14400^{+0.00059}_{-0.00061}$	$0.14353^{+0.00059}_{-0.00060}$	$0.282^{+0.017}_{-0.017}$	0.2488	-	-
0.7533–0.7613	$0.14429^{+0.00071}_{-0.00072}$	$0.14344^{+0.00073}_{-0.00072}$	$0.14300^{+0.00070}_{-0.00071}$	$0.286^{+0.020}_{-0.022}$	0.2457	-	-
0.7613–0.7693	$0.14744^{+0.00108}_{-0.00108}$	$0.14656^{+0.00110}_{-0.00105}$	$0.14617^{+0.00107}_{-0.00106}$	$0.274^{+0.030}_{-0.033}$	0.2515	-	-
0.7693–0.7773	$0.14577^{+0.00061}_{-0.00060}$	$0.14488^{+0.00061}_{-0.00061}$	$0.14445^{+0.00060}_{-0.00061}$	$0.240^{+0.018}_{-0.019}$	0.2549	-	-
0.7773–0.7853	$0.14428^{+0.00063}_{-0.00060}$	$0.14345^{+0.00063}_{-0.00062}$	$0.14299^{+0.00063}_{-0.00061}$	$0.245^{+0.018}_{-0.020}$	0.2489	-	-
0.7853–0.7933	$0.14495^{+0.00092}_{-0.00083}$	$0.14408^{+0.00095}_{-0.00083}$	$0.14363^{+0.00093}_{-0.00083}$	$0.244^{+0.024}_{-0.026}$	0.2456	-	-
0.7933–0.8013	$0.14368^{+0.00071}_{-0.00070}$	$0.14287^{+0.00074}_{-0.00070}$	$0.14243^{+0.00070}_{-0.00069}$	$0.274^{+0.020}_{-0.022}$	0.2474	-	-
0.8013–0.8093	$0.14417^{+0.00093}_{-0.00097}$	$0.14334^{+0.00093}_{-0.00097}$	$0.14291^{+0.00096}_{-0.00095}$	$0.250^{+0.027}_{-0.032}$	0.2472	-	-
0.8093–0.8173	$0.14464^{+0.00085}_{-0.00076}$	$0.14385^{+0.00084}_{-0.00077}$	$0.14341^{+0.00083}_{-0.00077}$	$0.254^{+0.022}_{-0.024}$	0.2475	-	-
0.8173–0.8253	$0.14501^{+0.00087}_{-0.00083}$	$0.14420^{+0.00087}_{-0.00085}$	$0.14377^{+0.00085}_{-0.00085}$	$0.241^{+0.024}_{-0.028}$	0.2442	-	-
0.8253–0.8333	$0.14477^{+0.00063}_{-0.00064}$	$0.14394^{+0.00061}_{-0.00062}$	$0.14352^{+0.00063}_{-0.00064}$	$0.266^{+0.018}_{-0.019}$	0.2507	-	-
TESS							
0.6000–1.0000	$0.14405^{+0.00074}_{-0.00061}$	$0.14322^{+0.00073}_{-0.00061}$	$0.14276^{+0.00072}_{-0.00061}$	0.6590	−0.4538	0.9531	−0.4668

Table A.1: Measured spectrophotometric transit depths of WASP-6b for the G600B and G600RI datasets in addition to the weighted average transit depth of the *TESS* photometry. Transit depths calculated following an activity correction based on the *TESS* and *AIT* photometry are also independently shown.

Wavelength (μm)	R_P/R_*	$R_P/R_{*,TESS}$	$R_P/R_{*,AIT}$	c_1	c_2	c_3	c_4
STIS 430							
0.3250–0.4000	$0.14758^{+0.00128}_{-0.00136}$	$0.14644^{+0.00136}_{-0.00147}$	$0.14583^{+0.00164}_{-0.00145}$	0.4458	−0.4545	1.4520	−0.5362
0.4000–0.4400	$0.14714^{+0.00073}_{-0.00075}$	$0.14610^{+0.00085}_{-0.00103}$	$0.14554^{+0.00072}_{-0.00068}$	0.3943	−0.1849	1.1642	−0.4810
0.4400–0.4750	$0.14586^{+0.00069}_{-0.00073}$	$0.14486^{+0.00067}_{-0.00069}$	$0.14430^{+0.00070}_{-0.00071}$	0.4227	−0.0653	0.9769	−0.4525
0.4750–0.5000	$0.14581^{+0.00104}_{-0.00093}$	$0.14469^{+0.00105}_{-0.00097}$	$0.14470^{+0.00106}_{-0.00108}$	0.4290	0.1635	0.5462	−0.2798
0.5000–0.5250	$0.14607^{+0.00084}_{-0.00089}$	$0.14509^{+0.00089}_{-0.00090}$	$0.14460^{+0.00084}_{-0.00084}$	0.5095	−0.1362	0.8108	−0.3523
0.5250–0.5450	$0.14647^{+0.00078}_{-0.00081}$	$0.14547^{+0.00078}_{-0.00083}$	$0.14493^{+0.00111}_{-0.00128}$	0.4855	0.0726	0.5461	−0.2855
0.5450–0.5700	$0.14520^{+0.00069}_{-0.00073}$	$0.14419^{+0.00073}_{-0.00078}$	$0.14378^{+0.00071}_{-0.00071}$	0.5293	−0.0370	0.6028	−0.2840
STIS 750							
0.5500–0.5868	$0.14549^{+0.00085}_{-0.00087}$	$0.14461^{+0.00082}_{-0.00086}$	$0.14409^{+0.00084}_{-0.00085}$	0.5334	0.0001	0.5262	−0.2553
0.5868–0.5918	$0.14724^{+0.00181}_{-0.00185}$	$0.14629^{+0.00181}_{-0.00179}$	$0.14581^{+0.00184}_{-0.00189}$	0.5755	−0.1509	0.7106	−0.3503
0.5918–0.6200	$0.14451^{+0.00087}_{-0.00087}$	$0.14355^{+0.00084}_{-0.00081}$	$0.14311^{+0.00085}_{-0.00083}$	0.5635	−0.0259	0.4825	−0.2387
0.6200–0.6600	$0.14506^{+0.00110}_{-0.00133}$	$0.14414^{+0.00111}_{-0.00138}$	$0.14367^{+0.00110}_{-0.00138}$	0.5951	−0.0778	0.4802	−0.2411
0.6600–0.7000	$0.14494^{+0.00094}_{-0.00096}$	$0.14413^{+0.00095}_{-0.00099}$	$0.14365^{+0.00092}_{-0.00092}$	0.6087	−0.1196	0.4761	−0.2288
0.7000–0.7599	$0.14501^{+0.00086}_{-0.00094}$	$0.14411^{+0.00089}_{-0.00093}$	$0.14372^{+0.00086}_{-0.00090}$	0.6251	−0.1738	0.4843	−0.2277
0.7599–0.7769	$0.14743^{+0.00125}_{-0.00127}$	$0.14660^{+0.00125}_{-0.00126}$	$0.14625^{+0.00123}_{-0.00120}$	0.6373	−0.2154	0.4876	−0.2239
0.7769–0.8400	$0.14472^{+0.00104}_{-0.00106}$	$0.14390^{+0.00108}_{-0.00108}$	$0.14349^{+0.00103}_{-0.00105}$	0.6354	−0.2178	0.4696	−0.2167
0.8400–0.9200	$0.14443^{+0.00085}_{-0.00085}$	$0.14367^{+0.00086}_{-0.00086}$	$0.14328^{+0.00085}_{-0.00086}$	0.6486	−0.2801	0.4821	−0.2159
0.9200–1.0300	$0.14365^{+0.00124}_{-0.00119}$	$0.14294^{+0.00122}_{-0.00118}$	$0.14257^{+0.00121}_{-0.00120}$	0.6332	−0.2595	0.4444	−0.2039
WFC3 G141							
1.1308–1.1493	$0.14344^{+0.00065}_{-0.00064}$	$0.14262^{+0.00064}_{-0.00061}$	$0.14230^{+0.00064}_{-0.00062}$	0.5850	−0.2405	0.4859	−0.2567
1.1493–1.1678	$0.14282^{+0.00060}_{-0.00062}$	$0.14198^{+0.00066}_{-0.00074}$	$0.14165^{+0.00066}_{-0.00069}$	0.5739	−0.1975	0.4283	−0.2336
1.1678–1.1863	$0.14332^{+0.00066}_{-0.00066}$	$0.14242^{+0.00073}_{-0.00075}$	$0.14212^{+0.00077}_{-0.00077}$	0.5691	−0.1734	0.3892	−0.2181
1.1863–1.2048	$0.14400^{+0.00085}_{-0.00083}$	$0.14322^{+0.00080}_{-0.00082}$	$0.14296^{+0.00080}_{-0.00081}$	0.5643	−0.1534	0.3583	−0.2049
1.2048–1.2233	$0.14212^{+0.00055}_{-0.00053}$	$0.14136^{+0.00054}_{-0.00051}$	$0.14109^{+0.00052}_{-0.00052}$	0.5392	−0.0570	0.2359	−0.1550
1.2233–1.2418	$0.14379^{+0.00058}_{-0.00051}$	$0.14301^{+0.00056}_{-0.00051}$	$0.14274^{+0.00054}_{-0.00052}$	0.5287	−0.0068	0.1678	−0.1276
1.2418–1.2603	$0.14388^{+0.00052}_{-0.00052}$	$0.14308^{+0.00051}_{-0.00052}$	$0.14278^{+0.00050}_{-0.00051}$	0.5186	0.0422	0.0995	−0.0998
1.2603–1.2788	$0.14316^{+0.00061}_{-0.00063}$	$0.14234^{+0.00059}_{-0.00060}$	$0.14204^{+0.00061}_{-0.00061}$	0.5153	0.0714	0.0602	−0.0882
1.2788–1.2973	$0.14292^{+0.00061}_{-0.00062}$	$0.14212^{+0.00072}_{-0.00069}$	$0.14185^{+0.00070}_{-0.00066}$	0.5137	0.1156	−0.0193	−0.0577
1.2973–1.3158	$0.14356^{+0.00056}_{-0.00054}$	$0.14279^{+0.00055}_{-0.00053}$	$0.14248^{+0.00056}_{-0.00052}$	0.4957	0.1714	−0.0897	−0.0212
1.3158–1.3343	$0.14402^{+0.00049}_{-0.00049}$	$0.14333^{+0.00056}_{-0.00053}$	$0.14304^{+0.00055}_{-0.00052}$	0.4904	0.2140	−0.1587	0.0094
1.3343–1.3528	$0.14494^{+0.00053}_{-0.00052}$	$0.14418^{+0.00052}_{-0.00052}$	$0.14387^{+0.00053}_{-0.00053}$	0.4814	0.2785	−0.2558	0.0510
1.3528–1.3713	$0.14481^{+0.00050}_{-0.00051}$	$0.14400^{+0.00050}_{-0.00053}$	$0.14374^{+0.00049}_{-0.00051}$	0.4826	0.3004	−0.3031	0.0739
1.3713–1.3898	$0.14443^{+0.00061}_{-0.00061}$	$0.14362^{+0.00061}_{-0.00062}$	$0.14333^{+0.00063}_{-0.00062}$	0.4781	0.3553	−0.3914	0.1116
1.3898–1.4083	$0.14450^{+0.00059}_{-0.00058}$	$0.14376^{+0.00062}_{-0.00060}$	$0.14352^{+0.00060}_{-0.00060}$	0.4754	0.4040	−0.4798	0.1539
1.4083–1.4268	$0.14436^{+0.00068}_{-0.00072}$	$0.14355^{+0.00071}_{-0.00075}$	$0.14328^{+0.00069}_{-0.00070}$	0.4814	0.4162	−0.5192	0.1739
1.4268–1.4453	$0.14510^{+0.00056}_{-0.00059}$	$0.14432^{+0.00056}_{-0.00058}$	$0.14402^{+0.00055}_{-0.00058}$	0.4909	0.4304	−0.5695	0.2001
1.4453–1.4638	$0.14472^{+0.00051}_{-0.00050}$	$0.14394^{+0.00058}_{-0.00057}$	$0.14368^{+0.00059}_{-0.00055}$	0.5020	0.4428	−0.6133	0.2215
1.4638–1.4823	$0.14352^{+0.00051}_{-0.00050}$	$0.14272^{+0.00058}_{-0.00055}$	$0.14247^{+0.00057}_{-0.00056}$	0.5176	0.4336	−0.6300	0.2323
1.4823–1.5008	$0.14408^{+0.00060}_{-0.00061}$	$0.14344^{+0.00068}_{-0.00070}$	$0.14316^{+0.00070}_{-0.00067}$	0.5378	0.4095	−0.6377	0.2437
1.5008–1.5193	$0.14422^{+0.00063}_{-0.00062}$	$0.14352^{+0.00060}_{-0.00060}$	$0.14327^{+0.00060}_{-0.00061}$	0.5610	0.3679	−0.6216	0.2451
1.5193–1.5378	$0.14381^{+0.00060}_{-0.00062}$	$0.14304^{+0.00061}_{-0.00064}$	$0.14276^{+0.00062}_{-0.00062}$	0.5891	0.3711	−0.6882	0.2845
1.5378–1.5563	$0.14388^{+0.00088}_{-0.00065}$	$0.14308^{+0.00098}_{-0.00072}$	$0.14278^{+0.00084}_{-0.00070}$	0.6200	0.3216	−0.6681	0.2839
1.5563–1.5748	$0.14267^{+0.00077}_{-0.00071}$	$0.14214^{+0.00107}_{-0.00093}$	$0.14187^{+0.00102}_{-0.00094}$	0.6541	0.2446	−0.6119	0.2700
1.5748–1.5933	$0.14323^{+0.00090}_{-0.00087}$	$0.14253^{+0.00082}_{-0.00075}$	$0.14228^{+0.00085}_{-0.00080}$	0.6734	0.1558	−0.5064	0.2283
1.5933–1.6118	$0.14314^{+0.00064}_{-0.00064}$	$0.14246^{+0.00068}_{-0.00067}$	$0.14222^{+0.00067}_{-0.00067}$	0.7158	0.1056	−0.5040	0.2401
1.6118–1.6303	$0.14361^{+0.00072}_{-0.00073}$	$0.14293^{+0.00062}_{-0.00062}$	$0.14270^{+0.00062}_{-0.00062}$	0.7518	0.0128	−0.4181	0.2107
1.6303–1.6488	$0.14303^{+0.00065}_{-0.00067}$	$0.14243^{+0.00073}_{-0.00076}$	$0.14219^{+0.00073}_{-0.00076}$	0.7736	−0.0330	−0.3973	0.2099

Table A.2: As in Table A.1, except for the STIS 430, STIS 750 and WFC3 G141 datasets.

A.2 *JWST* Coronagraphic Simulations Supplement

A.2.1 Target Sample

A.2.2 Correlation Matrix Contrast Estimation

For a typical coronagraphic, or high-contrast, imaging observation it is often useful to calculate the radial contrast profile between the final noise-subtracted image and the flux of the target star. As there is usually only a single final image, this profile is typically calculated using spatial statistical properties such as the mean or variance over a range of concentric annuli. However, as the *JWST* exposure time calculator `Pandeia`'s noise calculations are based on a correlation matrix infrastructure, a different method must be used for its coronagraphic simulations.

For a default `Pandeia` coronagraphic simulation, an ensemble of reference subtracted target images will be generated from a number of random draws over telescope and instrument states. An average contrast profile for these images can be determined by first calculating

$$N = aCa^T, \tag{1}$$

where N is the noise matrix, C is the covariance matrix of the ensemble of images, and a is a smoothing aperture matrix. By taking the square root of the diagonal of N, one can obtain σ, the 2-dimensional noise map from the ensemble of images. This noise map is then normalised by the peak flux of an off-axis simulated image of the target, S, also smoothed by the same aperture a, to produce a corresponding 2-d dimensional contrast map. Finally, the radial contrast profile, or contrast curve, is determined by taking the mean within concentric annuli of the final σ/S contrast map.

Common Name	2MASS Identifier	Distance (pc)	Spectral Type	m_{F356W}	m_{F444W}	m_{F1140C}	m_{F1550C}
HD 203	00065008-2306271	40.0 ± 0.1	F2IV	5.03	5.03	5.54	5.49
RBS 38	00172353-6645124	36.81 ± 0.04	M2.5V	7.59	7.48	8.19	7.99
GJ 2006 A	00275023-3233060	34.9 ± 0.1	M3.5Ve	7.78	7.65	8.35	8.16
Barta 161 12	01351393-0712517	37.3 ± 0.1	M4.3	7.91	7.78	8.47	8.28
TYC 1208-468-1	01373940+1835332	52.1 ± 0.3	K3Ve	6.51	6.52	7.27	7.11
HD 14082 A	02172527+2844423	39.8 ± 0.1	F5V	4.88	4.88	5.84	5.78
J0224+2031	02241739+2031513	68.7 ± 0.8	M6	11.29	11.14	11.88	11.70
AG Tri A	02272924+3058246	41.1 ± 0.1	K8	6.99	7.02	7.67	7.53
EPIC 211046195	03350208+2342356	51.2 ± 0.4	M8.5	10.88	10.73	11.38	11.20
51 Eri	04373613-0228248	29.8 ± 0.1	F0V	4.32	4.32	4.82	4.78
J0443+0002	04433761+0002051	21.1 ± 0.1	M9γ	10.54	10.40	10.90	10.75
Gl 182	04593483+0147007	24.4 ± 0.02	M0Ve	6.07	6.04	6.81	6.64
CD-57 1054	05004714-5715255	26.9 ± 0.02	M0.5e	6.05	6.02	6.81	6.64
V1841 Ori	05004928+1527006	53.4 ± 0.1	K2IV	7.54	7.57	8.23	8.08
HIP 23418 ABCD	05015881+0958587	23.85 ± 0.05	M3V	6.05	5.92	6.76	6.57
J0506+0439	05061292+0439272	27.8 ± 0.04	M4.0	7.86	7.72	8.42	8.23
AF Lep	05270477-1154033	26.87 ± 0.02	F7	4.78	4.78	5.35	5.28
J0529-3239	05294468-3239141	29.87 ± 0.04	M4.5	8.05	7.91	8.60	8.41
J0531-0303	05315786-0303367	38.6 ± 0.2	M5	8.27	8.13	8.82	8.63
V1311 Ori AB	05320450-0305291	34.6 ± 0.7	M2Ve	6.82	6.75	7.47	7.28
J0532-0301	05320596-0301159	38.4 ± 0.1	M5	9.43	9.29	10.13	9.94
Beta Pic	05471708-5103594	19.8 ± 0.1	A6V	3.19	3.19	2.83	2.79
GSC 06513-00291	06131330-2742054	32.7 ± 0.2	M3.5V	6.93	6.80	7.56	7.37
AO Men	06182824-7202416	39.26 ± 0.05	K4Ve	6.63	6.66	7.30	7.17
TWA 22 A	10172689-5354265	19.6 ± 0.1	M5	7.39	7.24	7.96	7.77
alf Cir	14423039-6458305	15.9 ± 0.1	A7V	2.08	1.93	3.48	3.29
V343 Nor A	15385757-5742273	40.1 ± 0.1	K0V	5.42	5.44	6.33	6.23
J1657-5343	16572029-5343316	50.6 ± 0.3	M3V	7.64	7.55	8.26	8.07
HD 155555 A	17172550-6657039	30.51 ± 0.03	G5IV	4.40	4.42	5.17	5.07
CD-54 7336	17295506-5415487	67.8 ± 0.2	K1V	7.33	7.35	7.88	7.78
HD 160305	17414903-5043279	65.7 ± 0.2	F9V	6.96	6.97	7.39	7.32
HD 161247	17453733-2824269	76.2 ± 0.7	F3V	6.76	6.76	7.22	7.16
UCAC3 74-428746	17483374-5306118	77.1 ± 0.3	M2	9.11	9.00	9.71	9.51
UCAC4 331-124196	17520173-2357571	63.5 ± 0.2	M2	8.32	8.25	8.61	8.42
HD 164249 A	18030341-5138564	49.6 ± 0.1	F5V	5.71	5.71	6.16	6.10
HD 165189	18064990-4325297	44.6 ± 0.3	A6V	4.14	4.14	4.68	4.64
V4046 Sgr	18141047-3247344	72.4 ± 0.3	K6V	7.05	7.08	5.66	5.52
HD 167847 B	18183181-3503026	83.2 ± 0.4	G5	6.99	7.00	7.69	7.60
HD 168210	18195221-2916327	79.4 ± 0.3	G5V	6.96	6.97	7.52	7.43
J1842-5554	18420483-5554126	51.7 ± 0.2	M4.5	9.54	9.40	10.13	9.94
HIP 92024 A	18452691-6452165	28.3 ± 0.2	A7	4.08	4.08	3.85	3.81
HD 173167	18480637-6213470	50.6 ± 0.1	F5V	6.05	6.05	6.51	6.44
CD-31 16041	18504448-3147472	49.6 ± 0.1	K7V	7.36	7.35	8.05	7.88
HIP 92680	18530587-5010499	47.1 ± 0.1	G9IV	6.23	6.25	6.84	6.74
TYC 6872-1011-1	18580415-2953045	74.2 ± 0.4	M0V	7.81	7.80	8.45	8.28
J1908-1603	19082195-1603249	69.4 ± 0.7	M5.4	11.10	10.95	11.64	11.46
HIP 95270	19225894-5432170	48.2 ± 0.1	F5.5	5.82	5.82	6.26	6.20
J1923-4606	19233820-4606316	71.1 ± 0.2	M0V	8.13	8.14	8.79	8.63
J1935-2846	19355595-2846343	56.5 ± 1.6	M9	12.02	11.87	11.32	11.14
J1956-3207	19560438-3207376	51.2 ± 0.1	M0V	7.73	7.72	8.40	8.23
HIP 99273	20090521-2613265	50.1 ± 0.1	F5V	5.89	5.89	6.37	6.31
J2033-2556	20333759-2556521	43.4 ± 0.2	M4.5V	8.56	8.41	9.13	8.94
J2043-2433 AB	20434114-2433534	42.5 ± 0.2	M3.7	7.53	7.42	8.18	7.98
AU Mic	20450949-3120266	9.725 ± 0.005	M1Ve	4.04	3.99	5.07	4.89
HD 198472	20524162-5316243	63.1 ± 0.2	F5.5V	6.51	6.51	6.92	6.86
HIP 103311 AB	20554767-1706509	46.0 ± 0.1	F8V	5.66	5.67	6.21	6.14
J2110-1920	21100461-1920302	34.3 ± 0.5	M5	7.28	7.14	7.87	7.68
J2135-4218	21354554-4218343	48.9 ± 0.3	M4.5	10.49	10.34	11.01	10.82
J2208+1144	22085034+1144131	37.0 ± 0.2	M4.3	8.79	8.65	9.32	9.13
HD 213429	22311828-0633183	25.5 ± 0.4	F8V	4.54	4.54	5.17	5.10
CPD-72 2713	22424896-7142211	36.66 ± 0.03	K7V	6.73	6.74	7.44	7.28
HIP 112312 A	22445794-3315015	20.86 ± 0.02	M4IVe	6.66	6.53	7.31	7.12
BD-13 6424	23323085-1215513	27.37 ± 0.04	M0V	6.40	6.35	7.15	6.97
J2335-3401	23355015-3401477	38.0 ± 0.2	M6	10.39	10.24	10.79	10.61

Table A.3: Properties for all objects within the βPMG sample as obtained from the Gagné et al. (2018b) compilation. The apparent magnitudes are calculated for each individual object using its corresponding synthetic SED and the *JWST* PCEs as described in Section 4.4.

Common Name	2MASS Identifier	Distance (pc)	Spectral Type	m_{F356W}	m_{F444W}	m_{F1140C}	m_{F1550C}
TWA 39 A	10120908-3124451	49.3 ± 0.4	M4Ve	7.62	7.48	6.93	6.74
TWA 34	10284580-2830374	61.4 ± 0.3	M6γ	9.11	8.96	9.05	8.86
TWA 7	10423011-3340162	34.0 ± 0.1	M4pec	6.73	6.64	7.38	7.19
J1058-2346	10585054-2346206	44.1 ± 0.1	M6γe	9.09	8.94	9.60	9.41
TWA 1	11015191-3442170	60.1 ± 0.1	M3epec	6.84	6.86	5.26	5.10
TWA 43	11084400-2804504	53.1 ± 0.5	A2Vn	5.04	5.04	5.33	5.32
TWA 2 A	11091380-3001398	46.1 ± 1.4	M1.5IVe	6.54	6.47	7.24	7.05
TWA 3 A	11102788-3731520	36.6 ± 0.2	M4pec	6.29	6.16	4.64	4.45
TWA 12	11210549-3845163	65.5 ± 0.2	M2IVe	8.00	7.93	8.59	8.40
TWA 13 A	11211723-3446454	59.9 ± 0.1	M1Ve	7.52	7.49	8.14	7.97
TWA 5 Aa	11315526-3436272	49.4 ± 0.1	M2.5	6.51	6.42	7.19	7.00
TWA 30 A	11321831-3019518	48.0 ± 0.3	M5pec	8.56	8.42	7.87	7.68
TWA 8 A	11324124-2651559	46.3 ± 0.2	M3IVe	7.30	7.19	7.94	7.74
TWA 33	11393382-3040002	48.7 ± 0.2	M4.5e	8.58	8.44	7.94	7.75
TWA 26	11395113-3159214	49.7 ± 0.6	M9γ	10.86	10.73	11.40	11.25
TWA 9 A	11482422-3728491	76.4 ± 0.4	K7IVe	7.64	7.67	8.28	8.13
TWA 45	11592786-4510192	71.0 ± 1.6	M4.5	8.84	8.70	9.37	9.18
TWA 35	12002750-3405371	72.8 ± 0.5	M4	8.45	8.31	9.01	8.82
TWA 36	12023799-3328402	63.4 ± 0.3	M5	9.57	9.43	10.12	9.93
TWA 23 A	12072738-3247002	55.7 ± 0.3	M3Ve	7.58	7.47	8.19	7.99
TWA 27 A	12073346-3932539	64.4 ± 0.7	M8γ	11.13	10.98	10.29	10.11
TWA 25	12153072-3948426	53.1 ± 0.2	K9IV-Ve	7.22	7.19	7.87	7.70
TWA 44	12175920-3734433	76.5 ± 0.5	M5γe	10.42	10.27	10.93	10.74
TWA 32 A	12265135-3316124	63.8 ± 1.4	M5.5γ	9.33	9.18	8.59	8.40
TWA 20 A	12313807-4558593	81.7 ± 0.3	M3IVe	8.29	8.18	8.86	8.66
TWA 10	12350424-4136385	57.6 ± 0.2	M2Ve	8.06	7.95	8.64	8.44
TWA 46	12354615-4115531	56.9 ± 0.5	M3	8.98	8.87	9.53	9.33
TWA 11 A	12360103-3952102	71.9 ± 0.7	A0	5.40	5.40	4.97	4.98
TWA 47	12371238-4021480	63.7 ± 0.4	M2.5Ve	8.36	8.25	8.94	8.74
TWA 29	12451416-4429077	83.3 ± 3.5	M9.5γ	12.77	12.62	13.88	13.70

Table A.4: As in Table A.3, but for the TWA sample.

Bibliography

Agúndez, Marcelino, Vivien Parmentier, Olivia Venot, Franck Hersant, and Franck Selsis. 2014. 'Pseudo 2D chemical model of hot-Jupiter atmospheres: application to HD 209458b and HD 189733b.' A&A 564, A73 (April): A73.

Aigrain, S., F. Pont, and S. Zucker. 2012. 'A simple method to estimate radial velocity variations due to stellar activity using photometry.' MNRAS 419 (February): 3147–3158.

Alam, M. K., N. Nikolov, M. López-Morales, et al. 2018. 'The HST PanCET Program: Hints of Na I and Evidence of a Cloudy Atmosphere for the Inflated Hot Jupiter WASP-52b.' AJ 156, 298 (December): 298.

Allard, France, Peter H. Hauschildt, David R. Alexander, Akemi Tamanai, and Andreas Schweitzer. 2001. 'The Limiting Effects of Dust in Brown Dwarf Model Atmospheres.' ApJ 556, no. 1 (July): 357–372.

Ambikasaran, S., D. Foreman-Mackey, L. Greengard, D. W. Hogg, and M. O'Neil. 2014. 'Fast Direct Methods for Gaussian Processes.' *arXiv* (March).

Angerhausen, Daniel, Alfred Krabbe, and Christof Iserlohe. 2006. 'Near-infrared integral-field spectroscopy of HD209458b.' In Proc. SPIE, vol. 6269, 62694S. Society of Photo-Optical Instrumentation Engineers (SPIE) Conference Series. June.

Appenzeller, I., K. Fricke, W. Fürtig, et al. 1998. 'Successful commissioning of FORS1 - the first optical instrument on the VLT.' *The Messenger* 94 (December): 1–6.

Asplund, M., N. Grevesse, A. J. Sauval, and P. Scott. 2009. 'The Chemical Composition of the Sun.' ARA&A 47 (September): 481–522.

Auvergne, M., P. Bodin, L. Boisnard, et al. 2009. 'The CoRoT satellite in flight: description and performance.' A&A 506, no. 1 (October): 411–424.

Bagnasco, Giorgio, Manfred Kolm, Pierre Ferruit, et al. 2007. 'Overview of the near-infrared spectrograph (NIRSpec) instrument on-board the James Webb Space Telescope (JWST).' In Proc. SPIE, 6692:66920M. Society of Photo-Optical Instrumentation Engineers (SPIE) Conference Series. September.

Bailer-Jones, C. A. L., J. Rybizki, M. Fouesneau, G. Mantelet, and R. Andrae. 2018. 'Estimating Distance from Parallaxes. IV. Distances to 1.33 Billion Stars in Gaia Data Release 2.' AJ 156, no. 2, 58 (August): 58.

Bakos, G., R. W. Noyes, G. Kovács, et al. 2004. 'Wide-Field Millimagnitude Photometry with the HAT: A Tool for Extrasolar Planet Detection.' PASP 116, no. 817 (March): 266–277.

Baraffe, I., G. Chabrier, T. S. Barman, F. Allard, and P. H. Hauschildt. 2003. 'Evolutionary models for cool brown dwarfs and extrasolar giant planets. The case of HD 209458.' A&A 402 (May): 701–712.

Baraffe, Isabelle, Derek Homeier, France Allard, and Gilles Chabrier. 2015. 'New evolutionary models for pre-main sequence and main sequence low-mass stars down to the hydrogen-burning limit.' A&A 577, A42 (May): A42.

Barstow, J. K., S. Aigrain, P. G. J. Irwin, and D. K. Sing. 2017. 'A Consistent Retrieval Analysis of 10 Hot Jupiters Observed in Transmission.' ApJ 834, 50 (January): 50.

Batalha, Natasha E., and M. R. Line. 2017. 'Information Content Analysis for Selection of Optimal JWST Observing Modes for Transiting Exoplanet Atmospheres.' AJ 153, no. 4, 151 (April): 151.

Batalha, Natasha E., Avi Mandell, Klaus Pontoppidan, et al. 2017. 'PandExo: A Community Tool for Transiting Exoplanet Science with JWST & HST.' PASP 129, no. 976 (June): 064501.

Baudino, Jean-Loup, Paul Mollière, Olivia Venot, et al. 2017. 'Toward the Analysis of JWST Exoplanet Spectra: Identifying Troublesome Model Parameters.' ApJ 850, no. 2, 150 (December): 150.

Bean, J. L., J.-M. Désert, P. Kabath, et al. 2011. 'The Optical and Near-infrared Transmission Spectrum of the Super-Earth GJ 1214b: Further Evidence for a Metal-rich Atmosphere.' ApJ 743, 92 (December): 92.

Bean, Jacob L., Kevin B. Stevenson, Natalie M. Batalha, et al. 2018. 'The Transiting Exoplanet Community Early Release Science Program for JWST.' PASP 130, no. 993 (November): 114402.

Beichman, Charles A., John Krist, John T. Trauger, et al. 2010. 'Imaging Young Giant Planets From Ground and Space.' PASP 122, no. 888 (February): 162.

Bell, Cameron P. M., Eric E. Mamajek, and Tim Naylor. 2015. 'A self-consistent, absolute isochronal age scale for young moving groups in the solar neighbourhood.' MNRAS 454, no. 1 (November): 593–614.

Berdyugina, S. V. 2005. 'Starspots: A Key to the Stellar Dynamo.' *Living Reviews in Solar Physics* 2, 8 (December): 8.

Beuzit, J. -L., A. Vigan, D. Mouillet, et al. 2019. 'SPHERE: the exoplanet imager for the Very Large Telescope.' A&A 631, A155 (November): A155.

Biller, Beth A., Michael C. Liu, Zahed Wahhaj, et al. 2013. 'The Gemini/NICI Planet-Finding Campaign: The Frequency of Planets around Young Moving Group Stars.' ApJ 777, no. 2, 160 (November): 160.

Bloemhof, E. E., R. G. Dekany, M. Troy, and B. R. Oppenheimer. 2001. 'Behavior of Remnant Speckles in an Adaptively Corrected Imaging System.' ApJL 558, no. 1 (September): L71–L74.

Bohlin, Ralph C., and Susana E. Deustua. 2019. 'CALSPEC: WFC3 IR Grism Spectrophotometry.' *arXiv e-prints,* arXiv:1903.11985 (March): arXiv:1903.11985.

Bohlin, Ralph C., Szabolcs Mészáros, Scott W. Fleming, et al. 2017. 'A New Stellar Atmosphere Grid and Comparisons with HST/STIS CALSPEC Flux Distributions.' AJ 153, no. 5, 234 (May): 234.

Bonavita, M., G. Chauvin, S. Desidera, et al. 2012. 'MESS (multi-purpose exoplanet simulation system). A Monte Carlo tool for the statistical analysis and prediction of exoplanet search results.' A&A 537, A67 (January): A67.

Bonavita, M., E. J. W. de Mooij, and R. Jayawardhana. 2013. 'Quick-MESS: A Fast Statistical Tool for Exoplanet Imaging Surveys.' PASP 125, no. 929 (July): 849.

Boro Saikia, S., C. J. Marvin, S. V. Jeffers, et al. 2018. 'Chromospheric activity catalogue of 4454 cool stars. Questioning the active branch of stellar activity cycles.' A&A 616, A108 (August): A108.

Borucki, W. J., and A. L. Summers. 1984. 'The photometric method of detecting other planetary systems.' *Icarus* 58, no. 1 (April): 121–134.

Borucki, William, David Koch, Natalie Batalha, et al. 2009. 'KEPLER: Search for Earth-Size Planets in the Habitable Zone.' In *Transiting Planets,* edited by Frédéric Pont, Dimitar Sasselov, and Matthew J. Holman, 253:289–299. IAU Symposium. February.

Boss, A. P. 1997. 'Giant planet formation by gravitational instability.' *Science* 276 (January): 1836–1839.

Bouchy, F., S. Udry, M. Mayor, et al. 2005. 'ELODIE metallicity-biased search for transiting Hot Jupiters. II. A very hot Jupiter transiting the bright K star HD 189733.' A&A 444 (December): L15–L19.

Bowler, Brendan P. 2016. 'Imaging Extrasolar Giant Planets.' PASP 128, no. 968 (October): 102001.

Bowler, Brendan P., Michael C. Liu, Evgenya L. Shkolnik, and Motohide Tamura. 2015. 'Planets around Low-mass Stars (PALMS). IV. The Outer Architecture of M Dwarf Planetary Systems.' ApJS 216, no. 1, 7 (January): 7.

Brande, Jonathan, Thomas Barclay, Joshua E. Schlieder, Eric D. Lopez, and Elisa V. Quintana. 2020. 'The Feasibility of Directly Imaging Nearby Cold Jovian Planets with MIRI/JWST.' AJ 159, no. 1, 18 (January): 18.

Brandt, Timothy D., Masayuki Kuzuhara, Michael W. McElwain, et al. 2014. 'The Moving Group Targets of the SEEDS High-contrast Imaging Survey of Exoplanets and Disks: Results and Observations from the First Three Years.' ApJ 786, no. 1, 1 (May): 1.

Burrows, A., M. Marley, W. B. Hubbard, et al. 1997. 'A Nongray Theory of Extrasolar Giant Planets and Brown Dwarfs.' ApJ 491, no. 2 (December): 856–875.

Canipe, Alicia Michelle, Massimo Robberto, and Bryan Hilbert. 2017. 'A New Non-Linearity Correction Method for the JWST Near-Infrared Camera.' In *American Astronomical Society Meeting Abstracts #230,* 230:114.02. American Astronomical Society Meeting Abstracts. June.

Carter, Aarynn L., Nikolay Nikolov, David K. Sing, et al. 2020. 'Detection of Na, K, and H_2O in the hazy atmosphere of WASP-6b.' MNRAS 494, no. 4 (April): 5449–5472.

Cartier, Kimberly M. S., Thomas G. Beatty, Ming Zhao, et al. 2017. 'Near-infrared Emission Spectrum of WASP-103b Using Hubble Space Telescope/Wide Field Camera 3.' AJ 153, no. 1, 34 (January): 34.

Cassan, A., D. Kubas, J. -P. Beaulieu, et al. 2012. 'One or more bound planets per Milky Way star from microlensing observations.' Nature 481, no. 7380 (January): 167–169.

Charbonneau, David, Timothy M. Brown, David W. Latham, and Michel Mayor. 2000. 'Detection of Planetary Transits Across a Sun-like Star.' ApJL 529, no. 1 (January): L45–L48.

Charbonneau, David, Timothy M. Brown, Robert W. Noyes, and Ronald L. Gilliland. 2002. 'Detection of an Extrasolar Planet Atmosphere.' ApJ 568, no. 1 (March): 377–384.

Charnay, B., B. Bézard, J. -L. Baudino, et al. 2018. 'A Self-consistent Cloud Model for Brown Dwarfs and Young Giant Exoplanets: Comparison with Photometric and Spectroscopic Observations.' ApJ 854, no. 2, 172 (February): 172.

Chauvin, G., S. Desidera, A. -M. Lagrange, et al. 2017. 'Discovery of a warm, dusty giant planet around HIP 65426.' A&A 605, L9 (September): L9.

Chauvin, G., A. -M. Lagrange, C. Dumas, et al. 2004. 'A giant planet candidate near a young brown dwarf. Direct VLT/NACO observations using IR wavefront sensing.' A&A 425 (October): L29–L32.

Chauvin, G., A. Vigan, M. Bonnefoy, et al. 2015. 'The VLT/NaCo large program to probe the occurrence of exoplanets and brown dwarfs at wide orbits. II. Survey description, results, and performances.' A&A 573, A127 (January): A127.

Cheetham, A. C., M. Samland, S. S. Brems, et al. 2019. 'Spectral and orbital characterisation of the directly imaged giant planet HIP 65426 b.' A&A 622, A80 (February): A80.

Claret, A. 2000. 'A new non-linear limb-darkening law for LTE stellar atmosphere models. Calculations for -5.0 <= log[M/H] <= +1, 2000 K <= T_{eff} <= 50000 K at several surface gravities.' A&A 363 (November): 1081–1190.

Cooper, Curtis S., and Adam P. Showman. 2006. 'Dynamics and Disequilibrium Carbon Chemistry in Hot Jupiter Atmospheres, with Application to HD 209458b.' ApJ 649, no. 2 (October): 1048–1063.

Cowan, Nicolas B., and Eric Agol. 2011. 'The Statistics of Albedo and Heat Recirculation on Hot Exoplanets.' ApJ 729, no. 1, 54 (March): 54.

Curtis, Jason L., Marcel A. Agüeros, Eric E. Mamajek, Jason T. Wright, and Jeffrey D. Cummings. 2019. 'TESS Reveals that the Nearby Pisces-Eridanus Stellar Stream is only 120 Myr Old.' AJ 158, no. 2, 77 (August): 77.

Cutri, R. M., and et al. 2013. 'VizieR Online Data Catalog: AllWISE Data Release (Cutri+ 2013).' *VizieR Online Data Catalog*, II/328 (November): II/328.

Deeg, Hans J., and Juan Antonio Belmonte. 2018. *Handbook of Exoplanets.*

Deming, D., H. Knutson, J. Kammer, et al. 2015. 'Spitzer Secondary Eclipses of the Dense, Modestly-irradiated, Giant Exoplanet HAT-P-20b Using Pixel-level Decorrelation.' ApJ 805, 132 (June): 132.

Deming, D., A. Wilkins, P. McCullough, et al. 2013. 'Infrared Transmission Spectroscopy of the Exoplanets HD 209458b and XO-1b Using the Wide Field Camera-3 on the Hubble Space Telescope.' ApJ 774, 95 (September): 95.

Domingo, V., B. Fleck, and A. I. Poland. 1995. 'The SOHO Mission: an Overview.' Sol. Phys. 162, nos. 1-2 (December): 1–37.

Doyle, A. P., B. Smalley, P. F. L. Maxted, et al. 2013. 'Accurate spectroscopic parameters of WASP planet host stars.' MNRAS 428 (February): 3164–3172.

Doyon, René, John B. Hutchings, Mathilde Beaulieu, et al. 2012. 'The JWST Fine Guidance Sensor (FGS) and Near-Infrared Imager and Slitless Spectrograph (NIRISS).' In Proc. SPIE, vol. 8442, 84422R. Society of Photo-Optical Instrumentation Engineers (SPIE) Conference Series. September.

Drummond, B., N. J. Mayne, J. Manners, et al. 2018a. 'Observable Signatures of Wind-driven Chemistry with a Fully Consistent Three-dimensional Radiative Hydrodynamics Model of HD 209458b.' ApJL 855, no. 2, L31 (March): L31.

Drummond, B., P. Tremblin, I. Baraffe, et al. 2016. 'The effects of consistent chemical kinetics calculations on the pressure-temperature profiles and emission spectra of hot Jupiters.' A&A 594, A69 (October): A69.

Drummond, Benjamin, Aarynn L. Carter, Eric Hébrard, et al. 2019. 'The carbon-to-oxygen ratio: implications for the spectra of hydrogen-dominated exoplanet atmospheres.' MNRAS 486, no. 1 (June): 1123–1137.

Drummond, Benjamin, Nathan J. Mayne, James Manners, et al. 2018b. 'The 3D Thermal, Dynamical, and Chemical Structure of the Atmosphere of HD 189733b: Implications of Wind-driven Chemistry for the Emission Phase Curve.' ApJ 869, no. 1, 28 (December): 28.

Eastman, Jason, B. Scott Gaudi, and Eric Agol. 2013. 'EXOFAST: A Fast Exoplanetary Fitting Suite in IDL.' PASP 125, no. 923 (January): 83.

Edwards, J. M. 1996. 'Efficient Calculation of Infrared Fluxes and Cooling Rates Using the Two-Stream Equations.' *Journal of the Atmospheric Sciences* 53 (13): 1921–1932.

Edwards, J. M., and A. Slingo. 1996. 'Studies with a flexible new radiation code. I: Choosing a configuration for a large-scale model.' *Quarterly Journal of the Royal Meteorological Society* 122 (531): 689–719.

Espinoza, Néstor, and Andrés Jordán. 2016. 'Limb darkening and exoplanets - II. Choosing the best law for optimal retrieval of transit parameters.' MNRAS 457, no. 4 (April): 3573–3581.

Evans, T. M., S. Aigrain, N. Gibson, et al. 2015. 'A uniform analysis of HD 209458b Spitzer/IRAC light curves with Gaussian process models.' MNRAS 451 (July): 680–694.

Evans, T. M., D. K. Sing, T. Kataria, et al. 2017. 'An ultrahot gas-giant exoplanet with a stratosphere.' Nature 548 (August): 58–61.

Evans, Thomas M., Frédéric Pont, David K. Sing, et al. 2013. 'The Deep Blue Color of HD 189733b: Albedo Measurements with Hubble Space Telescope/Space Telescope Imaging Spectrograph at Visible Wavelengths.' ApJL 772, no. 2, L16 (August): L16.

Evans, Thomas M., David K. Sing, Jayesh M. Goyal, et al. 2018. 'An Optical Transmission Spectrum for the Ultra-hot Jupiter WASP-121b Measured with the Hubble Space Telescope.' AJ 156, no. 6, 283 (December): 283.

Evans, Thomas M., David K. Sing, Hannah R. Wakeford, et al. 2016. 'Detection of H_2O and Evidence for TiO/VO in an Ultra-hot Exoplanet Atmosphere.' ApJL 822, no. 1, L4 (May): L4.

Fanson, James, Patrick J. McCarthy, Rebecca Bernstein, et al. 2018. 'Overview and status of the Giant Magellan Telescope project.' In Proc. SPIE, 10700:1070012. Society of Photo-Optical Instrumentation Engineers (SPIE) Conference Series. July.

Fleury, B., M. S. Gudipati, B. L. Henderson, and M. Swain. 2019. 'Photochemistry in Hot H_2-dominated Exoplanet Atmospheres.' ApJ 871, 158 (February): 158.

Foreman-Mackey, D., D. W. Hogg, D. Lang, and J. Goodman. 2013. 'emcee: The MCMC Hammer.' PASP 125 (March): 306.

Forgan, Duncan, Richard J. Parker, and Ken Rice. 2015. 'The dynamical fate of self-gravitating disc fragments after tidal downsizing.' MNRAS 447, no. 1 (February): 836–845.

Forgan, Duncan, and Ken Rice. 2013. 'Towards a population synthesis model of objects formed by self-gravitating disc fragmentation and tidal downsizing.' MNRAS 432, no. 4 (July): 3168–3185.

Fortney, J. J., K. Lodders, M. S. Marley, and R. S. Freedman. 2008. 'A Unified Theory for the Atmospheres of the Hot and Very Hot Jupiters: Two Classes of Irradiated Atmospheres.' ApJ 678, no. 2 (May): 1419–1435.

Fortney, Jonathan J. 2005. 'The effect of condensates on the characterization of transiting planet atmospheres with transmission spectroscopy.' MNRAS 364, no. 2 (December): 649–653.

Fressin, François, Guillermo Torres, David Charbonneau, et al. 2013. 'The False Positive Rate of Kepler and the Occurrence of Planets.' ApJ 766, no. 2, 81 (April): 81.

Fu, Guangwei, Drake Deming, Joshua Lothringer, et al. 2020. 'The Hubble PanCET program: Transit and Eclipse Spectroscopy of the Strongly Irradiated Giant Exoplanet WASP-76b.' *arXiv e-prints*, arXiv:2005.02568 (May): arXiv:2005.02568.

Gagné, Jonathan, Jacqueline K. Faherty, and Eric E. Mamajek. 2018a. 'Volans-Carina: A New 90 Myr Old Stellar Association at 85 pc.' ApJ 865, no. 2, 136 (October): 136.

Gagné, Jonathan, Eric E. Mamajek, Lison Malo, et al. 2018b. 'BANYAN. XI. The BANYAN Σ Multivariate Bayesian Algorithm to Identify Members of Young Associations with 150 pc.' ApJ 856, no. 1, 23 (March): 23.

Gaia Collaboration, A. G. A. Brown, A. Vallenari, et al. 2018. 'Gaia Data Release 2. Summary of the contents and survey properties.' A&A 616, A1 (August): A1.

Gaia Collaboration, T. Prusti, J. H. J. de Bruijne, et al. 2016. 'The Gaia mission.' A&A 595, A1 (November): A1.

Galicher, R., C. Marois, B. Macintosh, et al. 2016. 'The International Deep Planet Survey. II. The frequency of directly imaged giant exoplanets with stellar mass.' A&A 594, A63 (October): A63.

Gandhi, Siddharth, and Nikku Madhusudhan. 2017. 'GENESIS: new self-consistent models of exoplanetary spectra.' MNRAS 472, no. 2 (December): 2334–2355.

Gao, Peter, Daniel P. Thorngren, Graham K. H. Lee, et al. 2020. 'Aerosol composition of hot giant exoplanets dominated by silicates and hydrocarbon hazes.' *Nature Astronomy* (May).

Gardner, Jonathan P., John C. Mather, Mark Clampin, et al. 2006. 'The James Webb Space Telescope.' Space Sci. Rev. 123, no. 4 (April): 485–606.

Garhart, Emily, Drake Deming, Avi Mandell, et al. 2020. 'Statistical Characterization of Hot Jupiter Atmospheres Using Spitzer's Secondary Eclipses.' AJ 159, no. 4, 137 (April): 137.

Gauza, Bartosz, Victor J. S. Béjar, Antonio Pérez-Garrido, et al. 2015. 'Discovery of a Young Planetary Mass Companion to the Nearby M Dwarf VHS J125601.92-125723.9.' ApJ 804, no. 2, 96 (May): 96.

Gibson, N. P., S. Aigrain, F. Pont, et al. 2012a. 'Probing the haze in the atmosphere of HD 189733b with Hubble Space Telescope/WFC3 transmission spectroscopy.' MNRAS 422 (May): 753–760.

Gibson, N. P., S. Aigrain, S. Roberts, et al. 2012b. 'A Gaussian process framework for modelling instrumental systematics: application to transmission spectroscopy.' MNRAS 419 (January): 2683–2694.

Gibson, N. P., N. Nikolov, D. K. Sing, et al. 2017. 'VLT/FORS2 comparative transmission spectroscopy II: Confirmation of a cloud deck and Rayleigh scattering in WASP-31b, but no potassium?' MNRAS 467 (June): 4591–4605.

Gibson, Neale P., Ernst J. W. de Mooij, Thomas M. Evans, et al. 2019. 'Revisiting the potassium feature of WASP-31b at high resolution.' MNRAS 482, no. 1 (January): 606–615.

Gillon, M., D. R. Anderson, A. H. M. J. Triaud, et al. 2009. 'Discovery and characterization of WASP-6b, an inflated sub-Jupiter mass planet transiting a solar-type star.' A&A 501 (July): 785–792.

Girard, Julien H., William Blair, Brian Brooks, et al. 2018. 'Making good use of JWST's coronagraphs: tools and strategies from a user's perspective.' In Proc. SPIE, 10698:106983V. Society of Photo-Optical Instrumentation Engineers (SPIE) Conference Series. August.

Goyal, J. M., N. Mayne, D. K. Sing, et al. 2019a. 'Erratum: A library of ATMO forward model transmission spectra for hot Jupiter exoplanets.' MNRAS (March).

Goyal, J. M., H. R. Wakeford, N. J. Mayne, et al. 2019b. 'Fully scalable forward model grid of exoplanet transmission spectra.' MNRAS 482 (February): 4503–4513.

Goyal, Jayesh M., Nathan Mayne, David K. Sing, et al. 2018. 'A library of ATMO forward model transmission spectra for hot Jupiter exoplanets.' MNRAS 474, no. 4 (March): 5158–5185.

Gravity Collaboration, S. Lacour, M. Nowak, et al. 2019. 'First direct detection of an exoplanet by optical interferometry. Astrometry and K-band spectroscopy of HR 8799 e.' A&A 623, L11 (March): L11.

Greenbaum, Alexandra Z., Laurent Pueyo, Jean-Baptiste Ruffio, et al. 2018. 'GPI Spectra of HR 8799 c, d, and e from 1.5 to 2.4 μm with KLIP Forward Modeling.' AJ 155, no. 6, 226 (June): 226.

Greene, Thomas P., Michael R. Line, Cezar Montero, et al. 2016. 'Characterizing Transiting Exoplanet Atmospheres with JWST.' ApJ 817, no. 1, 17 (January): 17.

Griffith, C. A. 2014. 'Disentangling degenerate solutions from primary transit and secondary eclipse spectroscopy of exoplanets.' *Philosophical Transactions of the Royal Society of London Series A* 372 (March): 20130086–20130086.

Haemmerlé, L., P. Eggenberger, S. Ekström, et al. 2019. 'Stellar models and isochrones from low-mass to massive stars including pre-main sequence phase with accretion.' A&A 624, A137 (April): A137.

Haisch, Jr., Karl E., Elizabeth A. Lada, and Charles J. Lada. 2001. 'Disk Frequencies and Lifetimes in Young Clusters.' ApJL 553, no. 2 (June): L153–L156.

Hardy, John W., and Laird Thompson. 2000. 'Adaptive Optics for Astronomical Telescopes.' *Physics Today* 53, no. 4 (April): 69.

Hayek, W., D. Sing, F. Pont, and M. Asplund. 2012. 'Limb darkening laws for two exoplanet host stars derived from 3D stellar model atmospheres. Comparison with 1D models and HST light curve observations.' A&A 539, A102 (March): A102.

He, Chao, Sarah M. Hörst, Nikole K. Lewis, et al. 2018. 'Photochemical Haze Formation in the Atmospheres of Super-Earths and Mini-Neptunes.' *The Astronomical Journal* 156, no. 1, 38 (July): 38.

Hellier, C., D. R. Anderson, A. Collier Cameron, et al. 2011. 'WASP-43b: the closest-orbiting hot Jupiter.' A&A 535, L7 (November): L7.

Hellier, Coel, D. R. Anderson, A. Collier Cameron, et al. 2009. 'An orbital period of 0.94days for the hot-Jupiter planet WASP-18b.' Nature 460, no. 7259 (August): 1098–1100.

Helling, Ch., and W. Lucas. 2009. 'Gas-phase mean opacities for varying [M/H], N/O and C/O.' MNRAS 398, no. 2 (September): 985–994.

Helling, Ch., P. Woitke, and W. -F. Thi. 2008. 'Dust in brown dwarfs and extra-solar planets. I. Chemical composition and spectral appearance of quasi-static cloud layers.' A&A 485, no. 2 (July): 547–560.

Henry, Gregory W., Geoffrey W. Marcy, R. Paul Butler, and Steven S. Vogt. 2000. 'A Transiting "51 Peg-like" Planet.' ApJL 529, no. 1 (January): L41–L44.

Hinkley, Sasha, Isabelle Baraffe, Beth Biller, et al. 2017. *High Contrast Imaging of Exoplanets and Exoplanetary Systems with JWST.* JWST Proposal ID 1386. Cycle 0 Early Release Scienc, November.

Hinkley, Sasha, Ben R. Oppenheimer, Rémi Soummer, et al. 2007. 'Temporal Evolution of Coronagraphic Dynamic Range and Constraints on Companions to Vega.' ApJ 654, no. 1 (January): 633–640.

Hogg, D. W., A. D. Myers, and J. Bovy. 2010. 'Inferring the Eccentricity Distribution.' ApJ 725 (December): 2166–2175.

Hörst, Sarah M., Chao He, Nikole K. Lewis, et al. 2018. 'Haze production rates in super-Earth and mini-Neptune atmosphere experiments.' *Nature Astronomy* 2 (March): 303–306.

Howard, Andrew W., Geoffrey W. Marcy, Stephen T. Bryson, et al. 2012. 'Planet Occurrence within 0.25 AU of Solar-type Stars from Kepler.' ApJS 201, no. 2, 15 (August): 15.

Huitson, C. M., D. K. Sing, F. Pont, et al. 2013. 'An HST optical-to-near-IR transmission spectrum of the hot Jupiter WASP-19b: detection of atmospheric water and likely absence of TiO.' MNRAS 434 (October): 3252–3274.

Husnoo, N., F. Pont, T. Mazeh, et al. 2012. 'Observational constraints on tidal effects using orbital eccentricities.' MNRAS 422 (June): 3151–3177.

Husser, T. -O., S. Wende-von Berg, S. Dreizler, et al. 2013. 'A new extensive library of PHOENIX stellar atmospheres and synthetic spectra.' A&A 553, A6 (May): A6.

Ibgui, L., A. Burrows, and D. S. Spiegel. 2010. 'Tidal Heating Models for the Radii of the Inflated Transiting Giant Planets WASP-4b, WASP-6b, WASP-12b, WASP-15b, and TrES-4.' ApJ 713 (April): 751–763.

Jayasinghe, T., C. S. Kochanek, K. Z. Stanek, et al. 2018. 'The ASAS-SN catalogue of variable stars I: The Serendipitous Survey.' MNRAS 477 (July): 3145–3163.

Jensen-Clem, Rebecca, Dimitri Mawet, Carlos A. Gomez Gonzalez, et al. 2018. 'A New Standard for Assessing the Performance of High Contrast Imaging Systems.' AJ 155, no. 1, 19 (January): 19.

Jordán, A., N. Espinoza, M. Rabus, et al. 2013. 'A Ground-based Optical Transmission Spectrum of WASP-6b.' ApJ 778, 184 (December): 184.

Kammer, J. A., H. A. Knutson, M. R. Line, et al. 2015. 'Spitzer Secondary Eclipse Observations of Five Cool Gas Giant Planets and Empirical Trends in Cool Planet Emission Spectra.' ApJ 810, 118 (September): 118.

Kastner, J. H., B. Zuckerman, D. A. Weintraub, and T. Forveille. 1997. 'X-ray and molecular emission from the nearest region of recent star formation.' *Science* 277 (January): 67–71.

Kawashima, Yui, Renyu Hu, and Masahiro Ikoma. 2019. 'Detectable Molecular Features above Hydrocarbon Haze via Transmission Spectroscopy with JWST: Case Studies of GJ 1214b-, GJ 436b-, HD 97658b-, and Kepler-51b-like Planets.' ApJL 876, no. 1, L5 (May): L5.

Kawashima, Yui, and Masahiro Ikoma. 2019. 'Theoretical Transmission Spectra of Exoplanet Atmospheres with Hydrocarbon Haze: Effect of Creation, Growth, and Settling of Haze Particles. II. Dependence on UV Irradiation Intensity, Metallicity, C/O Ratio, Eddy Diffusion Coefficient, and Temperature.' ApJ 877, no. 2, 109 (June): 109.

Kirk, J., P. J. Wheatley, T. Louden, et al. 2017. 'Rayleigh scattering in the transmission spectrum of HAT-P-18b.' MNRAS 468, no. 4 (July): 3907–3916.

Kirk, J., P. J. Wheatley, T. Louden, et al. 2018. 'LRG-BEASTS III: ground-based transmission spectrum of the gas giant orbiting the cool dwarf WASP-80.' MNRAS 474, no. 1 (February): 876–885.

Kirk, James, Mercedes Lopez-Morales, Peter J. Wheatley, et al. 2019. 'LRG-BEASTS: transmission spectroscopy and retrieval analysis of the highly-inflated Saturn-mass planet WASP-39b.' *arXiv e-prints,* arXiv:1908.02358 (August): arXiv:1908.02358.

Knutson, Heather A., David Charbonneau, Lori E. Allen, et al. 2007. 'A map of the day-night contrast of the extrasolar planet HD 189733b.' Nature 447, no. 7141 (May): 183–186.

Knutson, Heather A., Diana Dragomir, Laura Kreidberg, et al. 2014. 'Hubble Space Telescope Near-IR Transmission Spectroscopy of the Super-Earth HD 97658b.' ApJ 794, no. 2, 155 (October): 155.

Kovács, Géza, and Tamás Kovács. 2019. 'Secondary eclipse of the hot Jupiter WASP-121b at 2 μm.' A&A 625, A80 (May): A80.

Kreidberg, Laura. 2015. 'batman: BAsic Transit Model cAlculatioN in Python.' PASP 127, no. 957 (November): 1161.

Kurucz, R. L. 1993. 'VizieR Online Data Catalog: Model Atmospheres (Kurucz, 1979).' *VizieR Online Data Catalog* 6039 (October).

Lafrenière, David, René Doyon, Christian Marois, et al. 2007. 'The Gemini Deep Planet Survey.' ApJ 670, no. 2 (December): 1367–1390.

Lajoie, Charles-Philippe, Rémi Soummer, Laurent Pueyo, et al. 2016. 'Small-grid dithers for the JWST coronagraphs.' In *Proceedings of the SPIE, Volume 9904, id. 99045K 8 pp. (2016).* Vol. 9904, 99045K. Society of Photo-Optical Instrumentation Engineers (SPIE) Conference Series.

Lavvas, P. P., A. Coustenis, and I. M. Vardavas. 2008. 'Coupling photochemistry with haze formation in Titan's atmosphere, Part I: Model description.' Planet. Space Sci. 56, no. 1 (January): 27–66.

Lavvas, P., and T. Koskinen. 2017. 'Aerosol Properties of the Atmospheres of Extrasolar Giant Planets.' ApJ 847, no. 1, 32 (September): 32.

Lecavelier Des Etangs, A., F. Pont, A. Vidal-Madjar, and D. Sing. 2008. 'Rayleigh scattering in the transit spectrum of HD 189733b.' A&A 481, no. 2 (April): L83–L86.

Lee, G. K. H., K. Wood, I. Dobbs-Dixon, A. Rice, and Ch. Helling. 2017. 'Dynamic mineral clouds on HD 189733b. II. Monte Carlo radiative transfer for 3D cloudy exoplanet atmospheres: combining scattering and emission spectra.' *Astronomy and Astrophysics* 601, A22 (May): A22.

Lee, G., I. Dobbs-Dixon, Ch. Helling, K. Bognar, and P. Woitke. 2016. 'Dynamic mineral clouds on HD 189733b. I. 3D RHD with kinetic, non-equilibrium cloud formation.' A&A 594, A48 (October): A48.

Liang, Mao-Chang, Sara Seager, Christopher D. Parkinson, Anthony Y. -T. Lee, and Yuk L. Yung. 2004. 'On the Insignificance of Photochemical Hydrocarbon Aerosols in the Atmospheres of Close-in Extrasolar Giant Planets.' ApJL 605, no. 1 (April): L61–L64.

Lightkurve Collaboration, J. V. d. M. Cardoso, C. Hedges, et al. 2018. *Lightkurve: Kepler and TESS time series analysis in Python.* Astrophysics Source Code Library, December.

Linder, Esther F., Christoph Mordasini, Paul Mollière, et al. 2019. 'Evolutionary models of cold and low-mass planets: cooling curves, magnitudes, and detectability.' A&A 623, A85 (March): A85.

Lines, S., J. Manners, N. J. Mayne, et al. 2018a. 'Exonephology: transmission spectra from a 3D simulated cloudy atmosphere of HD 209458b.' MNRAS 481, no. 1 (November): 194–205.

Lines, S., N. J. Mayne, I. A. Boutle, et al. 2018b. 'Simulating the cloudy atmospheres of HD 209458 b and HD 189733 b with the 3D Met Office Unified Model.' A&A 615, A97 (July): A97.

Louden, Tom, Peter J. Wheatley, Patrick G. J. Irwin, James Kirk, and Ian Skillen. 2017. 'A precise optical transmission spectrum of the inflated exoplanet WASP-52b.' MNRAS 470, no. 1 (September): 742–754.

Luger, R., E. Kruse, D. Foreman-Mackey, E. Agol, and N. Saunders. 2018. 'An Update to the EVEREST K2 Pipeline: Short Cadence, Saturated Stars, and Kepler-like Photometry Down to Kp = 15.' AJ 156, 99 (September): 99.

Luger, Rodrigo, Eric Agol, Ethan Kruse, et al. 2016. 'EVEREST: Pixel Level Decorrelation of K2 Light Curves.' AJ 152, no. 4, 100 (October): 100.

Lyot, Bernard. 1932. 'Étude de la couronne solaire en dehors des éclipses. Avec 16 figures dans le texte.' ZAp 5 (January): 73.

Macintosh, B., J. R. Graham, T. Barman, et al. 2015. 'Discovery and spectroscopy of the young jovian planet 51 Eri b with the Gemini Planet Imager.' *Science* 350, no. 6256 (October): 64–67.

Macintosh, Bruce, James R. Graham, Patrick Ingraham, et al. 2014. 'First light of the Gemini Planet Imager.' *Proceedings of the National Academy of Science* 111, no. 35 (September): 12661–12666.

Madhusudhan, N. 2012. 'C/O Ratio as a Dimension for Characterizing Exoplanetary Atmospheres.' *Astrophys. J* 758, 36 (October): 36.

Madhusudhan, N., J. Harrington, K. B. Stevenson, et al. 2011a. 'A high C/O ratio and weak thermal inversion in the atmosphere of exoplanet WASP-12b.' Nature 469 (January): 64–67.

Madhusudhan, N., and S. Seager. 2009. 'A Temperature and Abundance Retrieval Method for Exoplanet Atmospheres.' ApJ 707, no. 1 (December): 24–39.

———. 2010. 'On the Inference of Thermal Inversions in Hot Jupiter Atmospheres.' ApJ 725, no. 1 (December): 261–274.

Madhusudhan, Nikku. 2019. 'Exoplanetary Atmospheres: Key Insights, Challenges, and Prospects.' ARA&A 57 (August): 617–663.

Madhusudhan, Nikku, Olivier Mousis, Torrence V. Johnson, and Jonathan I. Lunine. 2011b. 'Carbon-rich Giant Planets: Atmospheric Chemistry, Thermal Inversions, Spectra, and Formation Conditions.' ApJ 743, no. 2, 191 (December): 191.

Malik, Matej, Luc Grosheintz, João M. Mendonça, et al. 2017. 'HELIOS: An Open-source, GPU-accelerated Radiative Transfer Code for Self-consistent Exoplanetary Atmospheres.' AJ 153, no. 2, 56 (February): 56.

Malo, Lison, René Doyon, Gregory A. Feiden, et al. 2014. 'BANYAN. IV. Fundamental Parameters of Low-mass Star Candidates in Nearby Young Stellar Kinematic Groups—Isochronal Age Determination using Magnetic Evolutionary Models.' ApJ 792, no. 1, 37 (September): 37.

Mamajek, Eric E., and Lynne A. Hillenbrand. 2008. 'Improved Age Estimation for Solar-Type Dwarfs Using Activity-Rotation Diagnostics.' ApJ 687, no. 2 (November): 1264–1293.

Mandel, Kaisey, and Eric Agol. 2002. 'Analytic Light Curves for Planetary Transit Searches.' ApJL 580, no. 2 (December): L171–L175.

Marleau, G. -D., and A. Cumming. 2014. 'Constraining the initial entropy of directly detected exoplanets.' MNRAS 437, no. 2 (January): 1378–1399.

Marley, M. S., A. S. Ackerman, J. N. Cuzzi, and D. Kitzmann. 2013. 'Clouds and hazes in exoplanet atmospheres.' In *Comparative Climatology of Terrestrial Planets*, edited by S. J. Mackwell, A. A. Simon-Miller, J. W. Harder, and M. A. Bullock, 367–391. Space Science Series. Phoenix: University of Arizona Press.

Marley, Mark S., Jonathan J. Fortney, Olenka Hubickyj, Peter Bodenheimer, and Jack J. Lissauer. 2007. 'On the Luminosity of Young Jupiters.' ApJ 655, no. 1 (January): 541–549.

Marois, Christian, David Lafrenière, René Doyon, Bruce Macintosh, and Daniel Nadeau. 2006. 'Angular Differential Imaging: A Powerful High-Contrast Imaging Technique.' ApJ 641, no. 1 (April): 556–564.

Marois, Christian, Bruce Macintosh, Travis Barman, et al. 2008. 'Direct Imaging of Multiple Planets Orbiting the Star HR 8799.' *Science* 322, no. 5906 (November): 1348.

Mawet, D., J. Milli, Z. Wahhaj, et al. 2014. 'Fundamental Limitations of High Contrast Imaging Set by Small Sample Statistics.' ApJ 792, no. 2, 97 (September): 97.

Mayne, Nathan J., Isabelle Baraffe, David M. Acreman, et al. 2014. 'The unified model, a fully-compressible, non-hydrostatic, deep atmosphere global circulation model, applied to hot Jupiters. ENDGame for a HD 209458b test case.' A&A 561, A1 (January): A1.

Mayor, Michel, and Didier Queloz. 1995. 'A Jupiter-mass companion to a solar-type star.' Nature 378, no. 6555 (November): 355–359.

McCullough, P. R., N. Crouzet, D. Deming, and N. Madhusudhan. 2014. 'Water Vapor in the Spectrum of the Extrasolar Planet HD 189733b. I. The Transit.' ApJ 791, no. 1, 55 (August): 55.

McCullough, P., and J. MacKenty. 2012. *Considerations for using Spatial Scans with WFC3.* Technical report. May.

Meingast, Stefan, João Alves, and Verena Fürnkranz. 2019. 'Extended stellar systems in the solar neighborhood . II. Discovery of a nearby 120° stellar stream in Gaia DR2.' A&A 622, L13 (February): L13.

Mészáros, Sz., C. Allende Prieto, B. Edvardsson, et al. 2012. 'New ATLAS9 and MARCS Model Atmosphere Grids for the Apache Point Observatory Galactic Evolution Experiment (APOGEE).' AJ 144, no. 4, 120 (October): 120.

Mikal-Evans, Thomas, David K. Sing, Jayesh M. Goyal, et al. 2019. 'An emission spectrum for WASP-121b measured across the 0.8-1.1 μm wavelength range using the Hubble Space Telescope.' MNRAS 488, no. 2 (September): 2222–2234.

Miles, Brittany E., Andrew J. I. Skemer, Caroline V. Morley, et al. 2020. 'Observations of Disequilibrium CO Chemistry in the Coldest Brown Dwarfs.' *arXiv e-prints,* arXiv:2004.10770 (April): arXiv:2004.10770.

Milli, J., T. Banas, D. Mouillet, et al. 2016. 'Speckle lifetime in XAO coronagraphic images: temporal evolution of SPHERE coronagraphic images.' In Proc. SPIE, vol. 9909, 99094Z. Society of Photo-Optical Instrumentation Engineers (SPIE) Conference Series. July.

Mollière, P., R. van Boekel, C. Dullemond, Th. Henning, and C. Mordasini. 2015. 'Model Atmospheres of Irradiated Exoplanets: The Influence of Stellar Parameters, Metallicity, and the C/O Ratio.' ApJ 813, no. 1, 47 (November): 47.

Mordasini, Christoph. 2018. 'Planetary Population Synthesis.' In *Handbook of Exoplanets,* 143.

Morley, Caroline V., Jonathan J. Fortney, Eliza M. -R. Kempton, et al. 2013. 'Quantitatively Assessing the Role of Clouds in the Transmission Spectrum of GJ 1214b.' ApJ 775, no. 1, 33 (September): 33.

Morley, Caroline V., Jonathan J. Fortney, Mark S. Marley, et al. 2012. 'Neglected Clouds in T and Y Dwarf Atmospheres.' ApJ 756, no. 2, 172 (September): 172.

Morley, Caroline V., Mark S. Marley, Jonathan J. Fortney, et al. 2014. 'Water Clouds in Y Dwarfs and Exoplanets.' ApJ 787, no. 1, 78 (May): 78.

Morley, Caroline V., Andrew J. Skemer, Katelyn N. Allers, et al. 2018. 'An L Band Spectrum of the Coldest Brown Dwarf.' ApJ 858, no. 2, 97 (May): 97.

Morrell, Sam, and Tim Naylor. 2019. 'Exploring the M-dwarf Luminosity–Temperature–Radius Relationships using Gaia DR2.' *arXiv e-prints,* arXiv:1908.03025 (August): arXiv:1908.03025.

Moses, J. I., M. R. Line, C. Visscher, et al. 2013a. 'Compositional Diversity in the Atmospheres of Hot Neptunes, with Application to GJ 436b.' ApJ 777, no. 1, 34 (November): 34.

Moses, J. I., N. Madhusudhan, C. Visscher, and R. S. Freedman. 2013b. 'Chemical Consequences of the C/O Ratio on Hot Jupiters: Examples from WASP-12b, CoRoT-2b, XO-1b, and HD 189733b.' ApJ 763, no. 1, 25 (January): 25.

Moses, Julianne I., C. Visscher, J. J. Fortney, et al. 2011. 'Disequilibrium Carbon, Oxygen, and Nitrogen Chemistry in the Atmospheres of HD 189733b and HD 209458b.' ApJ 737, no. 1, 15 (August): 15.

Nielsen, Eric L., Robert J. De Rosa, Bruce Macintosh, et al. 2019. 'The Gemini Planet Imager Exoplanet Survey: Giant Planet and Brown Dwarf Demographics from 10 to 100 au.' AJ 158, no. 1, 13 (July): 13.

Nielsen, Eric L., Michael C. Liu, Zahed Wahhaj, et al. 2013. 'The Gemini NICI Planet-Finding Campaign: The Frequency of Giant Planets around Young B and A Stars.' ApJ 776, no. 1, 4 (October): 4.

Nikolov, N., D. K. Sing, A. S. Burrows, et al. 2015. 'HST hot-Jupiter transmission spectral survey: haze in the atmosphere of WASP-6b.' MNRAS 447 (February): 463–478.

Nikolov, N., D. K. Sing, J. J. Fortney, et al. 2018. 'An absolute sodium abundance for a cloud-free 'hot Saturn'exoplanet.' *Nature* 557 (7706): 526–529.

Nikolov, N., D. K. Sing, N. P. Gibson, et al. 2016. 'VLT FORS2 Comparative Transmission Spectroscopy: Detection of Na in the Atmosphere of WASP-39b from the Ground.' ApJ 832, 191 (December): 191.

Öberg, Karin I., and Edwin A. Bergin. 2016. 'Excess C/O and C/H in Outer Protoplanetary Disk Gas.' ApJL 831, no. 2, L19 (November): L19.

Öberg, Karin I., Ruth Murray-Clay, and Edwin A. Bergin. 2011. 'The Effects of Snowlines on C/O in Planetary Atmospheres.' ApJL 743, no. 1, L16 (December): L16.

Parmentier, Vivien, Jonathan J. Fortney, Adam P. Showman, Caroline Morley, and Mark S. Marley. 2016. 'Transitions in the Cloud Composition of Hot Jupiters.' ApJ 828, no. 1, 22 (September): 22.

Parmentier, Vivien, Adam P. Showman, and Yuan Lian. 2013. '3D mixing in hot Jupiters atmospheres. I. Application to the day/night cold trap in HD 209458b.' A&A 558, A91 (October): A91.

Patruno, A., and M. Kama. 2017. 'Neutron star planets: Atmospheric processes and irradiation.' A&A 608, A147 (December): A147.

Pepper, Joshua, Richard W. Pogge, D. L. DePoy, et al. 2007. 'The Kilodegree Extremely Little Telescope (KELT): A Small Robotic Telescope for Large-Area Synoptic Surveys.' PASP 119, no. 858 (August): 923–935.

Perrin, Marshall D., Laurent Pueyo, Kyle Van Gorkom, et al. 2018. 'Updated optical modeling of JWST coronagraph performance contrast, stability, and strategies.' In Proc. SPIE, 10698:1069809. Society of Photo-Optical Instrumentation Engineers (SPIE) Conference Series. August.

Perrin, Marshall D., Anand Sivaramakrishnan, Charles-Philippe Lajoie, et al. 2014. 'Updated point spread function simulations for JWST with WebbPSF.' In Proc. SPIE, 9143:91433X. Society of Photo-Optical Instrumentation Engineers (SPIE) Conference Series.

Phillips, Mark W., Pascal Tremblin, Isabelle Baraffe, et al. 2020. 'A new set of atmosphere and evolution models for cool T-Y brown dwarfs and giant exoplanets.' *arXiv e-prints*, arXiv:2003.13717 (March): arXiv:2003.13717.

Pinhas, A., B. V. Rackham, N. Madhusudhan, and D. Apai. 2018. 'Retrieval of planetary and stellar properties in transmission spectroscopy with AURA.' MNRAS 480 (November): 5314–5331.

Pollacco, D. L., I. Skillen, A. Collier Cameron, et al. 2006. 'The WASP Project and the SuperWASP Cameras.' PASP 118 (October): 1407–1418.

Pollack, J. B., O. Hubickyj, P. Bodenheimer, et al. 1996. 'Formation of the Giant Planets by Concurrent Accretion of Solids and Gas.' *Icarus* 124 (November): 62–85.

Pont, F., H. Knutson, R. L. Gilliland, C. Moutou, and D. Charbonneau. 2008. 'Detection of atmospheric haze on an extrasolar planet: the 0.55-1.05 μm transmission spectrum of HD 189733b with the HubbleSpaceTelescope.' MNRAS 385, no. 1 (March): 109–118.

Pontoppidan, Klaus M., Timothy E. Pickering, Victoria G. Laidler, et al. 2016. 'Pandeia: a multi-mission exposure time calculator for JWST and WFIRST.' In Proc. SPIE, 9910:991016. Society of Photo-Optical Instrumentation Engineers (SPIE) Conference Series. July.

Powell, Diana, Xi Zhang, Peter Gao, and Vivien Parmentier. 2018. 'Formation of Silicate and Titanium Clouds on Hot Jupiters.' *The Astrophysical Journal* 860, no. 1, 18 (June): 18.

Rackham, Benjamin V., Dániel Apai, and Mark S. Giampapa. 2018. 'The Transit Light Source Effect: False Spectral Features and Incorrect Densities for M-dwarf Transiting Planets.' ApJ 853, no. 2, 122 (February): 122.

———. 2019. 'The Transit Light Source Effect. II. The Impact of Stellar Heterogeneity on Transmission Spectra of Planets Orbiting Broadly Sun-like Stars.' AJ 157, no. 3, 96 (March): 96.

Rackham, Benjamin, Néstor Espinoza, Dániel Apai, et al. 2017. 'ACCESS I: An Optical Transmission Spectrum of GJ 1214b Reveals a Heterogeneous Stellar Photosphere.' ApJ 834, no. 2, 151 (January): 151.

Redfield, Seth, Michael Endl, William D. Cochran, and Lars Koesterke. 2008. 'Sodium Absorption from the Exoplanetary Atmosphere of HD 189733b Detected in the Optical Transmission Spectrum.' ApJL 673, no. 1 (January): L87.

Ressler, M. E., K. G. Sukhatme, B. R. Franklin, et al. 2015. 'The Mid-Infrared Instrument for the James Webb Space Telescope, VIII: The MIRI Focal Plane System.' PASP 127, no. 953 (July): 675.

Ricker, G. R., J. N. Winn, R. Vanderspek, et al. 2014. 'Transiting Exoplanet Survey Satellite (TESS).' In *Space Telescopes and Instrumentation 2014: Optical, Infrared, and Millimeter Wave*, 9143:914320. Proc. SPIE. August.

Ricker, George R., Joshua N. Winn, Roland Vanderspek, et al. 2015. 'Transiting Exoplanet Survey Satellite (TESS).' *Journal of Astronomical Telescopes, Instruments, and Systems* 1, 014003 (January): 014003.

Rieke, G. H., G. S. Wright, T. Böker, et al. 2015. 'The Mid-Infrared Instrument for the James Webb Space Telescope, I: Introduction.' PASP 127, no. 953 (July): 584.

Rieke, Marcia J., Douglas Kelly, and Scott Horner. 2005. 'Overview of James Webb Space Telescope and NIRCam's Role.' In Proc. SPIE, edited by James B. Heaney and Lawrence G. Burriesci, 5904:1–8. Society of Photo-Optical Instrumentation Engineers (SPIE) Conference Series. August.

Rouan, Daniel, Jacques Baudrand, Anthony Boccaletti, et al. 2007. 'The Four Quadrant Phase Mask Coronagraph and its avatars.' *Comptes Rendus Physique* 8, nos. 3-4 (April): 298–311.

Ruane, G., D. Mawet, J. Kastner, et al. 2017. 'Deep Imaging Search for Planets Forming in the TW Hya Protoplanetary Disk with the Keck/NIRC2 Vortex Coronagraph.' AJ 154, no. 2, 73 (August): 73.

Sallum, Steph, and Andy Skemer. 2019. 'Comparing nonredundant masking and filled-aperture kernel phase for exoplanet detection and characterization.' *Journal of Astronomical Telescopes, Instruments, and Systems* 5, 018001 (January): 018001.

Samland, M., P. Mollière, M. Bonnefoy, et al. 2017. 'Spectral and atmospheric characterization of 51 Eridani b using VLT/SPHERE.' A&A 603, A57 (July): A57.

Seager, S. 2003. 'The search for extrasolar Earth-like planets.' *Earth and Planetary Science Letters* 208, nos. 3-4 (March): 113–124.

Seager, S., and D. D. Sasselov. 2000. 'Theoretical Transmission Spectra during Extrasolar Giant Planet Transits.' ApJ 537 (July): 916–921.

Sedaghati, E., H. M. J. Boffin, R. J. MacDonald, et al. 2017. 'Detection of titanium oxide in the atmosphere of a hot Jupiter.' Nature 549 (September): 238–241.

Shappee, B. J., J. L. Prieto, D. Grupe, et al. 2014. 'The Man behind the Curtain: X-Rays Drive the UV through NIR Variability in the 2013 Active Galactic Nucleus Outburst in NGC 2617.' ApJ 788, 48 (June): 48.

Sheppard, Kyle B., Avi M. Mandell, Patrick Tamburo, et al. 2017. 'Evidence for a Dayside Thermal Inversion and High Metallicity for the Hot Jupiter WASP-18b.' ApJL 850, no. 2, L32 (December): L32.

Showman, A. P., and T. Guillot. 2002. 'Atmospheric circulation and tides of "51 Pegasus b-like" planets.' A&A 385 (April): 166–180.

Sing, D. K. 2010. 'Stellar limb-darkening coefficients for CoRot and Kepler.' A&A 510, A21 (February): A21.

Sing, D. K., J.-M. Désert, J. J. Fortney, et al. 2011a. 'Gran Telescopio Canarias OSIRIS transiting exoplanet atmospheric survey: detection of potassium in XO-2b from narrowband spectrophotometry.' A&A 527, A73 (March): A73.

Sing, D. K., J. J. Fortney, N. Nikolov, et al. 2016. 'A continuum from clear to cloudy hot-Jupiter exoplanets without primordial water depletion.' Nature 529 (January): 59–62.

Sing, D. K., F. Pont, S. Aigrain, et al. 2011b. 'Hubble Space Telescope transmission spectroscopy of the exoplanet HD 189733b: high-altitude atmospheric haze in the optical and near-ultraviolet with STIS.' MNRAS 416, no. 2 (September): 1443–1455.

Sivaramakrishnan, Anand, Christopher D. Koresko, Russell B. Makidon, Thomas Berkefeld, and Marc J. Kuchner. 2001. 'Ground-based Coronagraphy with High-order Adaptive Optics.' ApJ 552, no. 1 (May): 397–408.

Sivaramakrishnan, Anand, David Lafrenière, K. E. Saavik Ford, et al. 2012. 'Non-redundant Aperture Masking Interferometry (AMI) and segment phasing with JWST-NIRISS.' In Proc. SPIE, vol. 8442, 84422S. Society of Photo-Optical Instrumentation Engineers (SPIE) Conference Series. September.

Sivaramakrishnan, Anand, Peter G. Tuthill, Michael J. Ireland, et al. 2009. 'Planetary system and star formation science with non-redundant masking on JWST.' In Proc. SPIE, vol. 7440, 74400Y. Society of Photo-Optical Instrumentation Engineers (SPIE) Conference Series.

Skemer, Andrew J., Mark S. Marley, Philip M. Hinz, et al. 2014. 'Directly Imaged L-T Transition Exoplanets in the Mid-infrared.' ApJ 792, no. 1, 17 (September): 17.

Skidmore, Warren, TMT International Science Development Teams, and TMT Science Advisory Committee. 2015. 'Thirty Meter Telescope Detailed Science Case: 2015.' *Research in Astronomy and Astrophysics* 15, no. 12, 1945 (December): 1945.

Smalley, B., D. R. Anderson, A. Collier-Cameron, et al. 2012. 'WASP-78b and WASP-79b: two highly-bloated hot Jupiter-mass exoplanets orbiting F-type stars in Eridanus.' A&A 547, A61 (November): A61.

Snellen, I. A. G., S. Albrecht, E. J. W. de Mooij, and R. S. Le Poole. 2008. 'Ground-based detection of sodium in the transmission spectrum of exoplanet HD 209458b.' A&A 487, no. 1 (August): 357–362.

Soderblom, David R. 2010. 'The Ages of Stars.' ARA&A 48 (September): 581–629.

Soummer, Rémi. 2005. 'Apodized Pupil Lyot Coronagraphs for Arbitrary Telescope Apertures.' ApJL 618, no. 2 (January): L161–L164.

Soummer, Rémi, J. Brendan Hagan, Laurent Pueyo, et al. 2011. 'Orbital Motion of HR 8799 b, c, d Using Hubble Space Telescope Data from 1998: Constraints on Inclination, Eccentricity, and Stability.' ApJ 741, no. 1, 55 (November): 55.

Soummer, Rémi, Charles-Philippe Lajoie, Laurent Pueyo, et al. 2014. 'Small-grid dithering strategy for improved coronagraphic performance with JWST.' In *Proceedings of the SPIE, Volume 9143, id. 91433V 9 pp. (2014).* 9143:91433V. Society of Photo-Optical Instrumentation Engineers (SPIE) Conference Series.

Soummer, Rémi, Laurent Pueyo, and James Larkin. 2012. 'Detection and Characterization of Exoplanets and Disks Using Projections on Karhunen-Loève Eigenimages.' ApJL 755, no. 2, L28 (August): L28.

Southworth, John. 2011. 'Homogeneous studies of transiting planets: an online catalogue.' *arXiv e-prints*, arXiv:1108.2976 (August): arXiv:1108.2976.

Spake, J. J., D. K. Sing, T. M. Evans, et al. 2018. 'Helium in the eroding atmosphere of an exoplanet.' *Nature* 557 (7703): 68–70.

Sparks, William B., and Holland C. Ford. 2002. 'Imaging Spectroscopy for Extrasolar Planet Detection.' ApJ 578, no. 1 (October): 543–564.

Spergel, D., N. Gehrels, C. Baltay, et al. 2015. 'Wide-Field InfrarRed Survey Telescope-Astrophysics Focused Telescope Assets WFIRST-AFTA 2015 Report.' *arXiv e-prints*, arXiv:1503.03757 (March): arXiv:1503.03757.

Spiegel, David S., and Adam Burrows. 2012. 'Spectral and Photometric Diagnostics of Giant Planet Formation Scenarios.' ApJ 745, no. 2, 174 (February): 174.

Stevenson, Kevin B., Jacob L. Bean, Nikku Madhusudhan, and Joseph Harrington. 2014. 'Deciphering the Atmospheric Composition of WASP-12b: A Comprehensive Analysis of its Dayside Emission.' ApJ 791, no. 1, 36 (August): 36.

Stolker, T., S. P. Quanz, K. O. Todorov, et al. 2020. 'MIRACLES: atmospheric characterization of directly imaged planets and substellar companions at 4-5 μm. I. Photometric analysis of β Pic b, HIP 65426 b, PZ Tel B, and HD 206893 B.' A&A 635, A182 (March): A182.

Stone, Jordan M., Andrew J. Skemer, Philip M. Hinz, et al. 2018. 'The LEECH Exoplanet Imaging Survey: Limits on Planet Occurrence Rates under Conservative Assumptions.' AJ 156, no. 6, 286 (December): 286.

Tamai, Roberto, Michele Cirasuolo, Juan Carlos González, Bertrand Koehler, and Mauro Tuti. 2016. 'The E-ELT program status.' In Proc. SPIE, vol. 9906, 99060W. Society of Photo-Optical Instrumentation Engineers (SPIE) Conference Series. July.

Tody, Doug. 1993. 'IRAF in the Nineties.' In *Astronomical Data Analysis Software and Systems II*, edited by R. J. Hanisch, R. J. V. Brissenden, and J. Barnes, 52:173. Astronomical Society of the Pacific Conference Series. January.

Tregloan-Reed, J., J. Southworth, M. Burgdorf, et al. 2015. 'Transits and starspots in the WASP-6 planetary system.' MNRAS 450 (June): 1760–1769.

Tremblin, P., D. S. Amundsen, P. Mourier, et al. 2015. 'Fingering Convection and Cloudless Models for Cool Brown Dwarf Atmospheres.' ApJL 804, no. 1, L17 (May): L17.

Tsai, Shang-Min, James R. Lyons, Luc Grosheintz, et al. 2017. 'VULCAN: An Open-source, Validated Chemical Kinetics Python Code for Exoplanetary Atmospheres.' ApJS 228, no. 2, 20 (February): 20.

Udalski, A., B. Paczynski, K. Zebrun, et al. 2002. 'The Optical Gravitational Lensing Experiment. Search for Planetary and Low-Luminosity Object Transits in the Galactic Disk. Results of 2001 Campaign.' *AcA* 52 (March): 1–37.

van Dokkum, P. G. 2001. 'Cosmic-Ray Rejection by Laplacian Edge Detection.' PASP 113 (November): 1420–1427.

Van Gorkom, Kyle, Laurent Pueyo, Charles-Philippe Lajoie, and JWST Coronagraphs Working Group. 2016. 'Improving JWST Coronagraphic Performance with Accurate Image Registration.' In *American Astronomical Society Meeting Abstracts #228*, 228:317.03. American Astronomical Society Meeting Abstracts. June.

Venot, O., E. Hébrard, M. Agúndez, et al. 2012. 'A chemical model for the atmosphere of hot Jupiters.' A&A 546, A43 (October): A43.

Vigan, A., M. Bonavita, B. Biller, et al. 2017. 'The VLT/NaCo large program to probe the occurrence of exoplanets and brown dwarfs at wide orbits. IV. Gravitational instability rarely forms wide, giant planets.' A&A 603, A3 (June): A3.

Visscher, Channon, and Julianne I. Moses. 2011. 'Quenching of Carbon Monoxide and Methane in the Atmospheres of Cool Brown Dwarfs and Hot Jupiters.' ApJ 738, no. 1, 72 (September): 72.

Wakeford, H. R., and D. K. Sing. 2015. 'Transmission spectral properties of clouds for hot Jupiter exoplanets.' A&A 573, A122 (January): A122.

Wakeford, H. R., D. K. Sing, D. Deming, et al. 2018. 'The Complete Transmission Spectrum of WASP-39b with a Precise Water Constraint.' AJ 155, 29 (January): 29.

Wakeford, H. R., D. K. Sing, K. B. Stevenson, et al. 2020. 'Into the UV: A Precise Transmission Spectrum of HAT-P-41b Using Hubble's WFC3/UVIS G280 Grism.' AJ 159, no. 5, 204 (May): 204.

Wakeford, H. R., K. B. Stevenson, N. K. Lewis, et al. 2017a. 'HST PanCET program: A Cloudy Atmosphere for the Promising JWST Target WASP-101b.' ApJL 835, L12 (January): L12.

Wakeford, H. R., T. J. Wilson, K. B. Stevenson, and N. K. Lewis. 2019. 'Exoplanet Atmosphere Forecast: Observers Should Expect Spectroscopic Transmission Features to be Muted to 33%.' *Research Notes of the American Astronomical Society* 3, no. 1, 7 (January): 7.

Wakeford, Hannah R., David K. Sing, Tiffany Kataria, et al. 2017b. 'HAT-P-26b: A Neptune-mass exoplanet with a well-constrained heavy element abundance.' *Science* 356, no. 6338 (May): 628–631.

Weinberger, A. J., E. E. Becklin, G. Schneider, et al. 1999. 'The Circumstellar Disk of HD 141569 Imaged with NICMOS.' ApJL 525, no. 1 (November): L53–L56.

Weisskopf, M. C., B. Brinkman, C. Canizares, et al. 2002. 'An Overview of the Performance and Scientific Results from the Chandra X-Ray Observatory.' PASP 114, no. 791 (January): 1–24.

Werner, M. W., T. L. Roellig, F. J. Low, et al. 2004. 'The Spitzer Space Telescope Mission.' ApJS 154, no. 1 (September): 1–9.

Wheatley, Peter J., Richard G. West, Michael R. Goad, et al. 2018. 'The Next Generation Transit Survey (NGTS).' MNRAS 475, no. 4 (April): 4476–4493.

Wolszczan, A., and D. A. Frail. 1992. 'A planetary system around the millisecond pulsar PSR1257 + 12.' Nature 355, no. 6356 (January): 145–147.

Wong, Ian, Avi Shporer, Tansu Daylan, et al. 2020. 'Systematic Phase Curve Study of Known Transiting Systems from Year 1 of the TESS Mission.' *arXiv e-prints*, arXiv:2003.06407 (March): arXiv:2003.06407.

Wright, Edward L., Peter R. M. Eisenhardt, Amy K. Mainzer, et al. 2010. 'The Wide-field Infrared Survey Explorer (WISE): Mission Description and Initial On-orbit Performance.' AJ 140, no. 6 (December): 1868–1881.

Yung, Y. L., M. Allen, and J. P. Pinto. 1984. 'Photochemistry of the atmosphere of Titan - Comparison between model and observations.' ApJS 55 (July): 465–506.

Zahnle, K., M. S. Marley, R. S. Freedman, K. Lodders, and J. J. Fortney. 2009. 'Atmospheric Sulfur Photochemistry on Hot Jupiters.' ApJL 701, no. 1 (August): L20–L24.

Zhou, Y., D. Apai, B. W. P. Lew, and G. Schneider. 2017. 'A Physical Model-based Correction for Charge Traps in the Hubble Space Telescope's Wide Field Camera 3 Near-IR Detector and Its Applications to Transiting Exoplanets and Brown Dwarfs.' AJ 153, 243 (June): 243.

Zuckerman, B. 2019. 'The Nearby, Young, Argus Association: Membership, Age, and Dusty Debris Disks.' ApJ 870, no. 1, 27 (January): 27.

Zuckerman, B., Inseok Song, M. S. Bessell, and R. A. Webb. 2001. 'The β Pictoris Moving Group.' ApJL 562, no. 1 (November): L87–L90.

Zurlo, A., A. Vigan, R. Galicher, et al. 2016. 'First light of the VLT planet finder SPHERE. III. New spectrophotometry and astrometry of the HR 8799 exoplanetary system.' A&A 587, A57 (March): A57.